



Computational Studies of Non-Precious Catalysts for the Oxygen Reduction Reaction

Reda, Mateusz Krzysztof

Publication date:
2018

Document Version
Publisher's PDF, also known as Version of record

[Link back to DTU Orbit](#)

Citation (APA):
Reda, M. K. (2018). *Computational Studies of Non-Precious Catalysts for the Oxygen Reduction Reaction*. Technical University of Denmark.

General rights

Copyright and moral rights for the publications made accessible in the public portal are retained by the authors and/or other copyright owners and it is a condition of accessing publications that users recognise and abide by the legal requirements associated with these rights.

- Users may download and print one copy of any publication from the public portal for the purpose of private study or research.
- You may not further distribute the material or use it for any profit-making activity or commercial gain
- You may freely distribute the URL identifying the publication in the public portal

If you believe that this document breaches copyright please contact us providing details, and we will remove access to the work immediately and investigate your claim.

Computational Studies of
Non-Precious Catalysts for
the Oxygen Reduction Reaction

PhD thesis

Department of Energy Conversion and Storage
Technical University of Denmark

Mateusz Reda

Computational Studies of Non-Precious Catalysts for the Oxygen Reduction Reaction

Author

Mateusz Reda

E-mail: mared@dtu.dk

Supervisors

Professor Tejs Vegge

Department of Energy Conversion and Storage

Technical University of Denmark

E-mail: teve@dtu.dk

Associate Professor Heine Anton Hansen

Department of Energy Conversion and Storage

Technical University of Denmark

E-mail: heih@dtu.dk

Atomic Scale Modelling and Materials

DTU Energy

Technical University of Denmark

Frederiksborgvej 399

4000 Roskilde

Denmark

Tel.: (+45) 46 77 58 00

Web: www.energy.dtu.dk

E-mail: info@energy.dtu.dk

Release date: March 31, 2018

ISBN: 978-87-92986-74-0

*It is the glory of God to hide things
but the glory of kings to investigate them.*

Prov. 25:2 (GW)

Abstract

Proton Exchange Membrane Fuel Cells (PEMFCs) are electrochemical devices capable of direct conversion of chemical energy into electricity. They are a promising alternative power supply for future automobile applications, with advantages such as higher energy conversion efficiency and lower emission of pollutants. A few problems stand in the way to the commercialization of the PEMFC technology. Among them, the slow kinetics of the cathodic Oxygen Reduction Reaction (ORR) is arguably the biggest.

Currently, the best known ORR catalysts are based on rare and expensive platinum, which price contributes significantly to the overall cost of the fuel cell stack. There are two main strategies to solve this problem: (i) decrease the platinum content, at the same time maximizing the catalyst activity, *e.g.*, by alloying Pt with other metals; (ii) use a non-precious catalyst made of earth-abundant elements. In this thesis, the second possibility is investigated computationally using Density Functional Theory.

Three main groups of non-precious ORR catalysts are studied: N-doped graphene (NG), iron carbide-supported NG ($\text{Fe}_3\text{C}/\text{NG}$) and a catalyst containing porphyrin-like FeN_4 moiety embedded in the graphene structure (Fe-N-C). First, solvation and spectator effects, immanently present in the catalytic environment in NG, are studied. It is shown that including explicit water solvation and bound atomic oxygen spectators is essential for the correct description of the oxygen reduction reaction on NG, and then also on $\text{Fe}_3\text{C}/\text{NG}$ catalyst.

The modeled catalytic activity of the $\text{Fe}_3\text{C}/\text{NG}$ heterostructure towards oxygen reduction reaction is found superior to that of the iron-supported NG (Fe/NG) and iron carbide-supported graphene ($\text{Fe}_3\text{C}/\text{G}$). This is consistent with experimental evidence in the literature. Differences between Fe and Fe_3C supports are shown to result from their electron-donating properties. Heterostructures comprising supports with electron-donating properties between Fe and Fe_3C are predicted to reach or exceed the Pt(111) surface activity.

Finally, the experimentally observed enhancement of the Fe-N-C catalyst activity in phosphoric acid solutions is shown to result from the phosphate anion adsorption on one side of the FeN_4 moiety. Owing to the fact that Fe-N-C catalyst is a 2-dimensional material, the other side of the FeN_4 moiety is still available for O_2 adsorption. Phosphate ligand is found to slightly modify binding energies of the ORR intermediates, promoting the oxygen reduction reaction. This opens a new possibility of tuning the catalytic activity by manipulating the electrolyte composition.

Resumé

Proton Exchange Membrane brændselsceller (PEMFCs) er elektrokemiske apparater, som er i stand til at omdanne kemisk energi til elektricitet. De er lovende som alternativ energitilførsel i fremtidige automobiler og har fordele som højere energiomdannelseseffektivitet og lavere udledning af forurenede gasser. Nogle udfordringer skal løses før PEMFC teknologien bliver kommercialiseret, den største deriblandt er formentlig den langsomme kinetik i katodereaktionen, der reducerer ilt (ORR).

De bedst kendte katalysatorer for ORR er, på nuværende tidspunkt, baseret på det sjældne og dyre platin, hvis pris bidrager betragteligt til de overordnede omkostninger ved en brændselscellestak. Der er to hovedstrategier til at løse dette problem: (i) formindsk indholdet af platin og på samme tid maksimer katalysatoren aktivitet f.eks. ved at legere Pt med andre metaller; (ii) benyt en katalysator bestående af uædle metaller og/eller elementer med høj forekomst på Jorden. I denne afhandling vil den anden mulighed blive undersøgt med tæthedsfunktionalteori (DFT) beregninger.

Tre hovedgrupper af uædle ORR katalysatorer er blevet undersøgt: N-doped grafen (NG), NG understøttet af jernkarbid ($\text{Fe}_3\text{C}/\text{NG}$) og en katalysator bestående af et porphyrin-lignende molekyle indgraveret i grafen (Fe-N-C). Som det første bliver opløsnings og tilskuereffekter undersøgt, de er altid til stede i de katalytiske omgivelser for NG. Det bliver vist at inkludering af eksplicit vand, der repræsenterer opløsningseffekter og tilskuere af adsorberede iltatomer er nødvendige for en korrekt beskrivelse af ORR på NG og $\text{Fe}_3\text{C}/\text{NG}$ katalysatorerne.

Den modellerede katalytiske ORR aktivitet af $\text{Fe}_3\text{C}/\text{NG}$ heterostrukturen er højere end aktiviteten af jern-understøttet NG (Fe/NG) og jernkarbid-understøttet grafen ($\text{Fe}_3\text{C}/\text{G}$). Dette er konsistent med eksperimentelle beviser fra litteraturen. Forskelle mellem Fe and Fe_3C supportter viser sig at stamme fra deres egenskab til at donere elektroner. Heterostrukturer opbygget af supportmaterialer med et elektrondoneringspotentialer svarende til et gennemsnit mellem Fe og Fe_3C forudsiges at have en overfladeaktivitet på højde med eller større end Pt(111).

Slutteligt vises det at den eksperimentelt observerede forbedring af Fe-N-C katalysatorens aktivitet i fosforsyreopløsninger skyldes adsorption af en fosfatanion på den ene side af FeN_4 -enheden. Da Fe-N-C katalysatoren er et 2-dimensionelt materiale er den anden side af FeN_4 -enheden stadig tilgængelig til adsorbering af O_2 . Det vises at fosfatligander ændrer bindingsenergiene for de intermediære produkter i ORR. Dette fremmer ORR og åbner en ny mulighed for at justere den katalytiske aktivitet ved at manipulere kompositionen af elektrolytten.

Preface

This thesis is submitted in candidacy for the Ph.D. degree from Technical University of Denmark (DTU). The work presented here has been conducted at Section for Atomic Scale Modelling and Materials (ASC) under Department of Energy Conversion and Storage (DTU Energy), from April 2015 to March 2018. The project was supervised by Prof. Tejs Vegge, Section Leader of ASC, and co-supervised by Assoc. Prof. Heine Anton Hansen. The work was financially supported by the Innovation Fund Denmark through the project: *Initiative Towards Non-Precious Metal Polymer Fuel Cells* (NonPrecious), no. 4106-00012A.

Mateusz Reda
Kgs. Lyngby, March 2018

Acknowledgements

I would like to thank my supervisor, Prof. Tejs Vegge, for his guidance over the course of my Ph.D. studies, his incredible ability to make sense out of seemingly unrelated pieces of information, as well as his sensitivity to others' needs. I would also like to thank my co-supervisor, Assoc. Prof. Heine A. Hansen, for being always available and ready to explain the intricacies of theoretical electrocatalysis.

Many thanks to all colleagues from the ASC Section for creating enjoyable scientific and social environment. I will especially remember: Arghya and Jaysree for their hospitality; "Witching Hour adventure" with Christian; Jin's perpetual giggle; Niels and Nicolai for showing a lively interest in my lunches; Rune for being an acute observer; Simon for his deliberate drivels spoken with all seriousness; Steen for his always-positive attitude. Special thanks to Katrine, Henrik, Rune, Steen, and Vladimir for proofreading the manuscript and providing valuable suggestions for improvements.

Unspeakable thanks to my wife, Ewelinka, and my Parents.

List of publications

The following publications — included in App. B — have been prepared during this Ph.D. project.

Paper 1

DFT study of stabilization effects on N-doped graphene for ORR catalysis

Mateusz Reda, Heine Anton Hansen, Tejs Vegge
Catalysis Today, 2018
In press.

Paper 2

Enhanced Oxygen Reduction Activity by Selective Anion Adsorption on Non-Precious Metal Catalysts

Kaspar Holst-Olesen, Mateusz Reda, Heine Anton Hansen, Tejs Vegge, Matthias Arenz
Nature Communications, 2018
Under review.

Paper 3

DFT Study of the Oxygen Reduction Reaction on Carbon-Coated Iron and Iron Carbide

Mateusz Reda, Heine Anton Hansen, Tejs Vegge
To be submitted.

Contents

Abstract	i
Resumé	ii
Preface	iii
Acknowledgements	iv
List of publications	v
List of Figures	ix
List of Tables	xi
1 Introduction	1
1.1 Fuel cell technology	1
1.2 The Oxygen Reduction Reaction (ORR)	2
1.2.1 Cathodic reactions and the overpotential	2
1.2.2 The ORR mechanism	3
1.2.3 The ideal catalyst and the scaling relations	4
1.2.4 Paths to affordable PEM fuel cells	9
1.3 Active sites on non-precious ORR catalysts	10
1.3.1 Metal-nitrogen-carbon catalysts (M-N-C)	10
1.3.2 Nitrogen-doped carbon	13
1.3.3 Encapsulated non-precious metal catalysts	15
1.3.4 Other non-precious ORR catalysts	16
1.4 Thesis outline	16
2 Computational Methods	18
2.1 Density Functional Theory	18
2.1.1 Born-Oppenheimer approximation	18
2.1.2 Hohenberg-Kohn theorems	18
2.1.3 Kohn-Sham scheme	19
2.1.4 BEEF-vdW functional	22
2.2 From DFT energy to Gibbs free energy	23
2.2.1 Gas phase molecules	24
2.2.2 Adsorbates	24
2.2.3 Gibbs free energy corrections	25

2.3	Solvation	26
2.3.1	Explicit solvation by H ₂ O molecules	26
2.3.2	Implicit solvation	29
2.4	General computational details	30
3	Stabilization effects on N-doped graphene	31
3.1	Introduction	31
3.1.1	Background	31
3.1.2	N-doped graphene model	32
3.1.3	Stabilization energy definitions	32
3.2	Stabilization effects	33
3.2.1	Free nitrogen	33
3.2.2	Solvation	35
3.2.3	Synergy of the two effects	37
3.2.4	Solvation on different materials	37
3.3	Discussion: O(sp) band filling	39
3.3.1	Stabilization due to free nitrogen	41
3.3.2	Stabilization due to water	42
3.4	Increasing dimensionality	44
3.4.1	Additional water layers on the adsorbate side	44
3.4.2	Adding more N-graphene layers	45
3.4.3	Water layer on both sides of N-graphene	45
3.5	Case study: ORR on N-graphene (6.25%N) with explicit water	46
3.6	Conclusions	49
4	Carbon-coated iron carbide and iron	50
4.1	Introduction	50
4.2	Structures of the interfaces	50
4.2.1	Fe ₃ C/graphene	50
4.2.2	Fe/graphene	51
4.2.3	Nitrogen doping	54
4.3	ORR catalyst models	55
4.4	The water layer	55
4.5	Free energy diagrams and the 2D volcano	58
4.6	Multiple graphene layers	68
4.7	Summary	69
5	Fe-N-C activity enhancement by selective anion adsorption	70
5.1	Introduction	70
5.2	Results	71
5.2.1	Experiment summary	71
5.2.2	Computational approach	75
5.2.3	Discussion	75
5.3	Conclusion	78
6	Conclusions and outlook	79
6.1	Conclusions	79

6.2 Outlook	80
A Supplementary material	82
A.1 Implicit and explicit solvation of anions at the Fe-N-C catalyst .	82
References	84
B Papers	99
B.1 Paper 1	99
B.2 Paper 2	112
B.3 Paper 3	135

List of Figures

1.1	Schematic of a PEM fuel cell.	2
1.2	Typical ORR polarization curve.	3
1.3	Timeline showing limited improvements in ORR performance over the past decade.	4
1.4	Theoretical free energy diagrams of two model ORR catalysts.	6
1.5	Scaling relations for the adsorption energies of *OOH and *O on the (111) metal surfaces.	7
1.6	ORR volcano curve.	8
1.7	Strategies proposed to circumvent the unfavorable *OH-*OOH scaling relation.	9
1.8	Fe-N-C active sites deduced by Dodelet <i>et al.</i>	11
1.9	Fe-N-C active site models considered by Zitolo <i>et al.</i>	12
1.10	Fe-N-C active sites in Zelenay’s catalyst.	12
1.11	Five main types of nitrogen doping in carbon materials.	13
1.12	ORR mechanism on N-doped carbon as proposed by Guo <i>et al.</i>	14
1.13	ORR $4e^-$ associative pathway on N-doped graphene with a Stone-Wales defect.	15
1.14	Cl ₂ -etching/H ₂ -restoring method.	16
3.1	N-doped graphene structure example.	32
3.2	First adsorption energy vs. N/*ads ratio at different nitrogen concentrations.	33
3.3	Oxygen adsorption energy as a function of N–N distance for systems with 1 N/*O and 2 N/*O.	34
3.4	Top views of the optimized structures of pristine N-graphene and ORR intermediates with single water layer.	35
3.5	Atomic oxygen adsorption energy on N-doped graphene as a function of N–N distance.	36
3.6	Structures exhibiting significant *O solvation energies.	38
3.7	Adsorbed oxygen projected density of states.	40
3.8	Bader charge on atoms in three N-graphene systems.	41
3.9	Average $\Delta_{\text{ads}}E(\text{O})$ vs. average Bader charge on *O	42
3.10	ORR intermediate adsorption energies for different solvation models.	43
3.11	Side views of N-graphene structures with double water layer.	45
3.12	ORR intermediate adsorption energies for different numbers of N-graphene layers.	46
3.13	Oxygen reduction reaction free energy diagrams at $U = 0.8 V_{\text{RHE}}$ for N-graphene (6.25%N).	48

4.1	Fe ₃ C and Fe interface models.	52
4.2	OH adsorption energy on graphene as a function of strain.	53
4.3	Water layer structures for the Fe ₃ C/NG system.	56
4.4	Water layer structures for the Fe ₃ C/G and Fe/G systems.	57
4.5	Water layer structures for Pt(111).	58
4.6	ORR free energy diagrams at for Pt(111) and NG.	59
4.7	ORR free energy diagrams for Fe ₃ C/G and Fe ₃ C/NG.	60
4.8	ORR free energy diagrams for Fe/G and Fe/NG.	61
4.9	ORR free energy diagrams for 2×NG and Fe ₃ C/2×NG.	62
4.10	Correlation between oxygen adsorption Gibbs free energy and a Bader charge.	64
4.11	Theoretical ORR overpotential as a function of $\Delta_{\text{ads}}G(\text{OH})$ and $\Delta_{\text{ads}}G(\text{O})$	65
4.12	ORR free energy diagrams for NG (2N/ads) and Fe ₃ C/NG (2N/ads).	66
4.13	ORR free energy diagrams for 3×NG and Fe ₃ C/3×NG.	67
5.1	Polycrystalline platinum RDE polarization curves.	71
5.2	Fe-N-C RDE polarization curves.	72
5.3	Effect of electrolyte molarity.	73
5.4	Effect of adding H ₃ PO ₄	74
5.5	Thermodynamic cycle for calculation of the Gibbs free energy of A ⁿ⁻ anion adsorption from solution.	76
5.6	Anion adsorption Gibbs free energy on Pt(111) vs. electrode potential.	76
5.7	Free energy diagram of the oxygen reduction reaction on Fe-N-C catalyst.	77
A.1	Side views of the optimized structures of OH ⁻ and HSO ₄ ⁻ anions adsorbed on Fe-N-C catalyst model with explicit solvation.	83

List of Tables

4.1	ORR intermediates adsorption Gibbs free energies at $U = 0$ V _{RHE} .	63
A.1	Adsorption Gibbs free energies of OH ⁻ and HSO ₄ ⁻ anions.	82

Chapter 1

Introduction

1.1 Fuel cell technology

Fuel cells are devices that directly convert chemical energy in fuels into electrical energy through an electrochemical reaction. The intermediate steps of producing heat and mechanical work, which are typical of many conventional power generation methods, are avoided. Fuel cells are theoretically much more efficient than heat engines, as they are not constrained by thermodynamic limitations such as the Carnot efficiency. For example, direct utilization of hydrogen in an internal combustion engine has an efficiency of about 10-20%, while the ideal thermodynamic efficiency of a H₂-O₂ fuel cell is about 83% at 25°C [1].

There are several types of fuel cells, most commonly classified based on the type of electrolyte used [1, 2]. The present thesis focuses on issues associated with the Proton-Exchange Membrane Fuel Cells (PEMFC, Fig. 1.1). With low operating temperature (60–80°C) and short startup time, this type is potentially attractive for light transport (*e.g.* cars) and certain portable applications. PEM fuel cells are particularly suitable for operation on pure hydrogen, which requires efficient H₂ storage — a generally non-trivial task. However, integrated fuel processors exist, which allow for on-site hydrogen generation from conventional fuels such as natural gas or gasoline. There is also a special kind of PEM fuel cell, which utilizes liquid methanol as a fuel directly, eliminating problematic H₂ gas storage or hydrocarbon conversion. The so-called Direct Methanol Fuel Cell (DMFC) is seen as a promising power supply for future portable electronics, like cameras and notebook computers [2].

Unfortunately, PEM fuel cell technology suffers from a serious issue, which is sluggish kinetics of the Oxygen Reduction Reaction (ORR) taking place at the fuel cell cathode [4]. Over the past two decades, a considerable insight was gained into the reasons behind this phenomenon, and the key findings are summarized in the next section of the thesis.

Currently, the greatest challenge in commercializing PEM fuel cells is finding a durable and inexpensive material, which would efficiently catalyze the cathodic oxygen reduction reaction. This issue is widely addressed in the re-

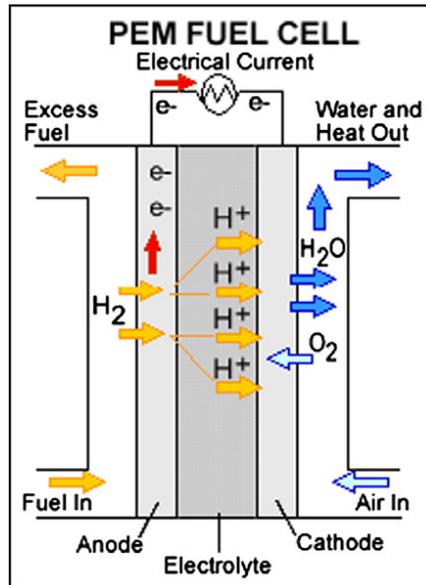


Figure 1.1: Schematic of a proton exchange membrane fuel cell [3].

search community. The approach is both experimental and theoretical, with the present thesis being an example of the latter.

1.2 The Oxygen Reduction Reaction (ORR)

1.2.1 Cathodic reactions and the overpotential

PEM fuel cells work under acidic conditions. The overall oxygen reduction reaction equation at the cathode is



where the protons are produced at the PEMFC anode and travel to the cathode through the proton-exchange membrane. U_{eq} is the equilibrium potential (vs. the standard hydrogen electrode, or SHE) at 25°C and 1 bar of O_2 and H_2 . It represents a cell potential in the absence of net flow of current and determines the theoretical upper bound for the voltage achievable in a single H_2 - O_2 cell. It is worth mentioning that at lower potentials an undesirable side reaction of oxygen reduction to hydrogen peroxide may occur



One particularly useful quantity that describes fuel cell under working conditions is the overpotential

$$\eta = U_{\text{eq}} - U \quad (1.3)$$

where U is the electrode potential when a current is being drawn from the cell. Overpotential represents the amount of potential that has to be sacrificed to put a cell into operation. The larger the overpotential, the lower the cell

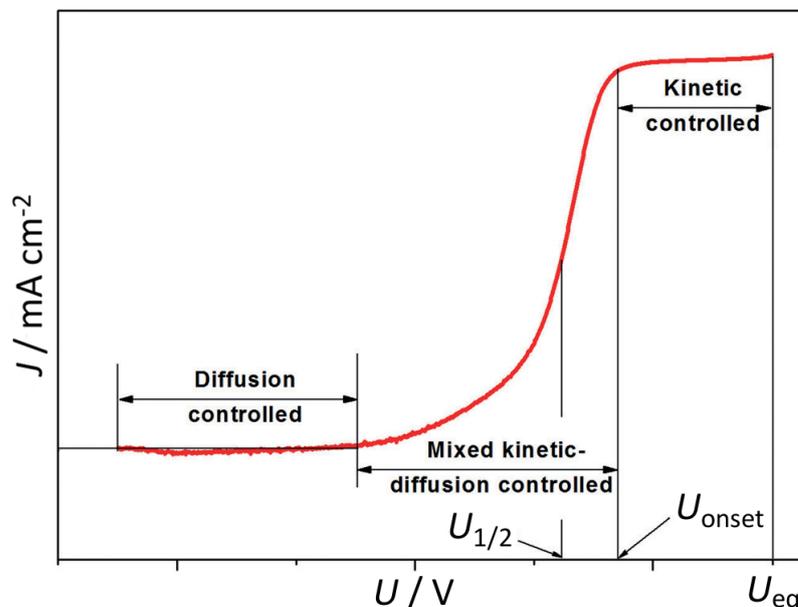


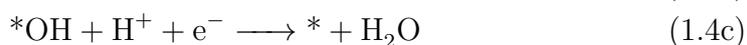
Figure 1.2: Typical ORR polarization curve [5]. $U_{1/2}$ – half-wave potential, U_{onset} – onset potential, U_{eq} – equilibrium potential.

efficiency, but also the more current can be drawn from the cell. A typical polarization curve, *i.e.* the plot of current density vs. U , is shown in Fig. 1.2.

The slow kinetics of the ORR can be understood as a large overpotential required to draw the reaction. Currently, the best platinum-based catalysts allow achieving satisfactory current densities at about $\eta = 300\text{--}400$ mV, while platinum group metal free (PGM-free) catalysts require *ca.* 100 mV more [5–7]. Fig. 1.3 shows that, despite the significant effort, only minimal improvements have been achieved over the past decade in decreasing the required ORR overpotential.

1.2.2 The ORR mechanism

The reactions (1.1) and (1.2) occur on the catalyst surface, on specific spots called active sites (denoted by an asterisk). Two mechanisms are usually considered. If the oxygen molecule dissociates before reduction, a resulting reaction sequence is called the $4e^-$ dissociative mechanism



The dissociative mechanism is often unattended due to large O_2 dissociation barriers found on various materials [9, 10].

Alternatively, the oxygen molecule may be reduced directly, which results

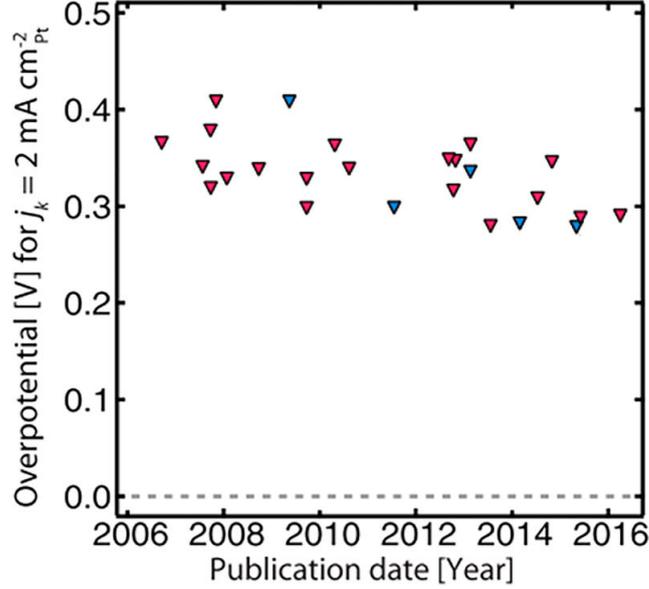
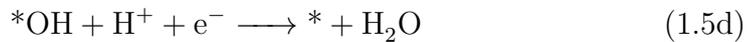
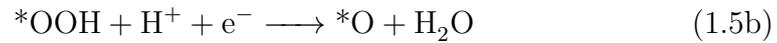


Figure 1.3: Timeline showing limited improvements in ORR performance over the past decade [8].

in the associative mechanism



The above sequence is called a $4e^-$ associative pathway. Competitively to reaction (1.5b), a proton may attack the oxygen directly bound to the surface. The resulting $2e^-$ associative pathway leads to H_2O_2 evolution

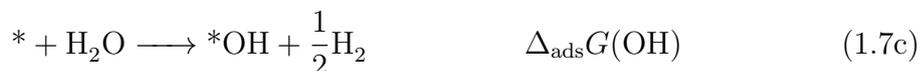


1.2.3 The ideal catalyst and the scaling relations

From now on, the H_2 - O_2 fuel cell will be considered. At $T = 25^\circ\text{C}$ and $p_{\text{H}_2} = p_{\text{O}_2} = 1 \text{ bar}$, the overall reaction taking place in this type of fuel cell is



where H_2 and O_2 are in gas phase, H_2O is in liquid phase, and ΔG is the reaction Gibbs free energy. The $4e^-$ associative mechanism includes three intermediate surface species: $* \text{OOH}$, $* \text{O}$ and $* \text{OH}$. Let their adsorption Gibbs free energies be defined relative to water



Sometimes an initial step of molecular oxygen adsorption is considered



By definition of the reversible hydrogen electrode (RHE), at 0 V_{RHE} the reaction



is in equilibrium ($\Delta G = 0$). Unless otherwise stated, the RHE reference for the electrode potential will be used in the remaining part of the thesis. Eq. (1.8) allows to rewrite equations (1.6) and (1.7a–c) in the following form



where $\Delta G_{\text{X}}(0 \text{ V})$ are the Gibbs free energies of the consecutive states along the ORR at 0 V , relative to the Gibbs free energy of $(* + 2 \text{H}_2\text{O})$, denoted as $\Delta G_{\text{H}_2\text{O}}$. The effect of applied potential (U) on the Gibbs free energy can be approximated [9] by

$$\Delta G(U) = \Delta G(0 \text{ V}) - neU \quad (1.10)$$

where n – number of electrons transferred, e – elementary positive charge. The free energies of the ORR steps [Eq. (1.5)] can then be calculated as



The above procedure of calculating potential-dependent Gibbs free energies of electrochemical reactions based on the energies of the corresponding chemical reactions is called the Computational Hydrogen Electrode (CHE) scheme [9].

An example free energy diagram (FED) of the ORR proceeding on a special type of catalyst is shown in Fig. 1.4a. This theoretical material binds the ORR intermediates at $U = 0 \text{ V}$ with the following adsorption energies:

$$\Delta_{\text{ads}}G(\text{OOH}) = 3.69 \text{ eV}$$

$$\Delta_{\text{ads}}G(\text{O}) = 2.46 \text{ eV}$$

$$\Delta_{\text{ads}}G(\text{OH}) = 1.23 \text{ eV}$$

Increasing the electrode potential causes each intermediate to bind less strongly [Eq. (1.10)]. Arbitrarily close to the equilibrium potential ($U_{\text{eq}} = 1.23 \text{ V}$), the whole reaction path is downhill in free energy (exergonic), and the reaction can proceed without hindrance (assuming no kinetic barriers between the steps).

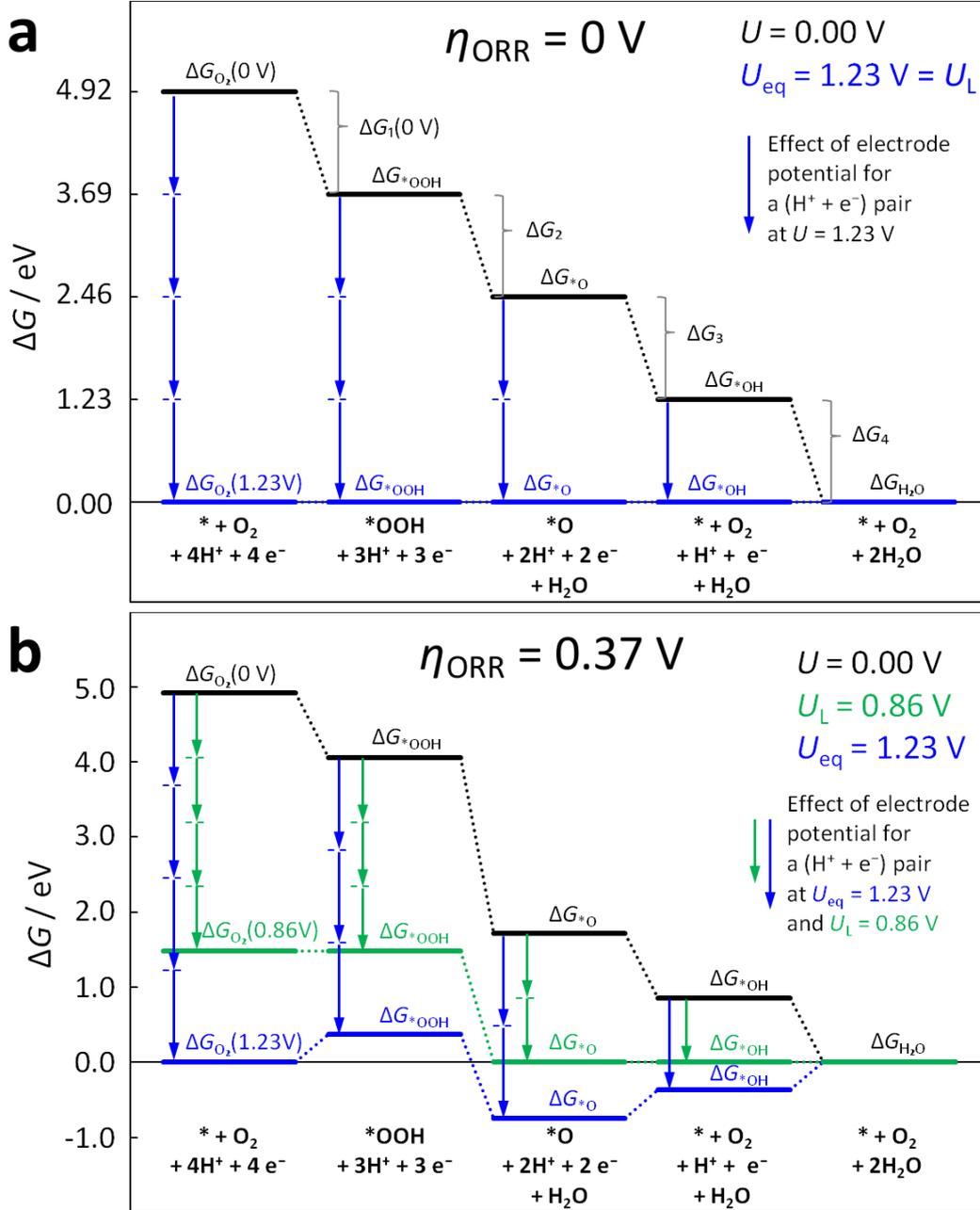


Figure 1.4: Theoretical free energy diagrams of two model ORR catalysts at $U = 0 \text{ V}$, U_{eq} (the equilibrium potential) and U_{L} (the limiting potential — the highest potential at which the whole reaction path is exergonic): (a) the ideal catalyst, (b) the best catalyst obeying scaling relations [Eqs. (1.12) and (1.13)]. The symbols shown in the figure are defined in Eq. (1.9)–(1.11).

The theoretical ORR overpotential is $\eta_{\text{ORR}} = 0 \text{ V}$. Such a material would be the ideal ORR catalyst.

One might expect that, given the large variety of known and described materials, it should be possible to find a few that would be close to fulfilling the ideal catalyst requirement. However, using Density Functional Theory (DFT), linear relationships between adsorption energies of species binding with the surface through a specified atom were found [11]. This observation applies in particular to the ORR intermediates, both on metal and oxide surfaces [12, 13]. These relationships are known in the literature as the “scaling relations” [8], and for *OOH, *O and *OH species adsorbed on the (111) surface of various metals they are as follows (see also Fig. 1.5):

$$\Delta_{\text{ads}}G(\text{OOH}) = \Delta_{\text{ads}}G(\text{OH}) + 3.2 \text{ eV} \quad (1.12)$$

$$\Delta_{\text{ads}}G(\text{O}) = 2 \Delta_{\text{ads}}G(\text{OH}) \quad (1.13)$$

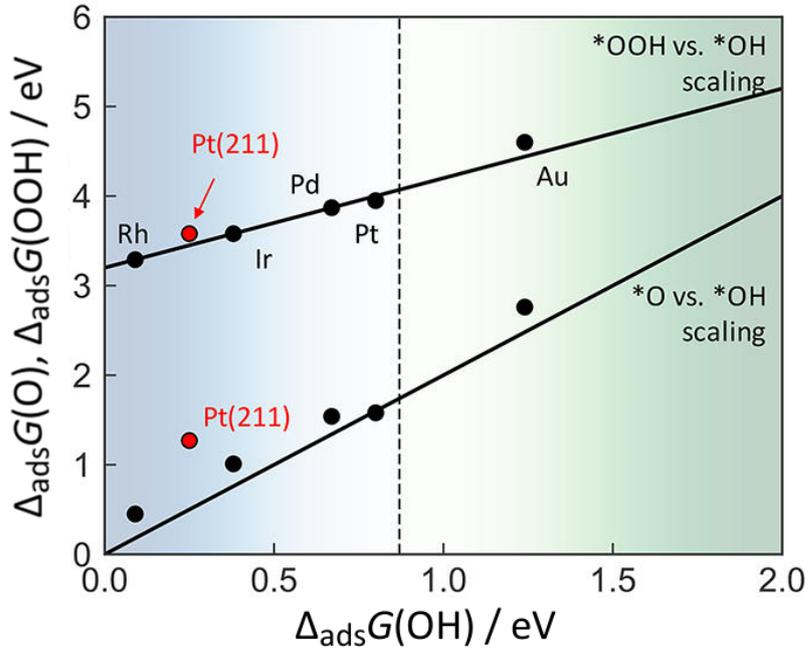


Figure 1.5: Scaling relations for the adsorption energies of *OOH and *O on the (111) metal surfaces (black circles) vs. *OH adsorption energy as a descriptor [8]. The solid lines correspond to $\Delta_{\text{ads}}G(\text{OOH}) = \Delta_{\text{ads}}G(\text{OH}) + 3.2 \text{ eV}$ and $\Delta_{\text{ads}}G(\text{O}) = 2 \Delta_{\text{ads}}G(\text{OH})$. Vertical dashed line marks $\Delta_{\text{ads}}G(\text{OH})$ of the best catalyst obeying the scaling relations.

The above scaling relations imply that only one variable is independent [*e.g.* $\Delta_{\text{ads}}G(\text{OH})$]. They also impose a restriction on how good the ORR catalyst can be, due to the unfavorable relation between *OH and *OOH adsorption energies (for the ideal catalyst: $\Delta_{\text{ads}}G(\text{OOH}) = \Delta_{\text{ads}}G(\text{OH}) + 2.46 \text{ eV}$). The free energy diagram of the best catalyst obeying the scaling relations is shown in Fig. 1.4b. At the equilibrium potential, Gibbs free energies of some steps along the ORR path are positive, which means there is a thermodynamic

barrier to oxygen reduction. The step with the highest free energy is called the potential-limiting step. In the case of the best ORR catalyst obeying the scaling relations, $\Delta G_1(U_{\text{eq}}) = \Delta G_2(U_{\text{eq}}) = \Delta G_3(U_{\text{eq}}) = 0.37 \text{ eV}$, and all these three steps equally limit the highest ORR potential, at which the whole reaction path is downhill in free energy. For the ORR path to become exergonic, the electrode potential has to decrease by $\eta_{\text{ORR}} = 0.37 \text{ V}$, which is the theoretical overpotential for this catalyst. Its value compares well with the overpotentials of the best-known catalysts shown in Fig. 1.3. The quantity

$$U_{\text{L}} = U_{\text{eq}} - \eta_{\text{ORR}} \quad (1.14)$$

is called the limiting potential, and it is the highest potential at which full reaction path is exergonic.

Materials that bind ORR intermediates both weaker and stronger than the best catalyst obeying scaling relations exhibit higher theoretical overpotentials. On materials exhibiting stronger binding, $^*\text{OH}$ reduction to water is the potential-limiting step. On materials exhibiting weaker binding, O_2 reduction to $^*\text{OOH}$ is the potential-limiting step. The U_{L} vs. $\Delta_{\text{ads}}G(\text{OH})$ dependence (with the latter being the ORR intermediates binding energy descriptor) forms a volcano curve, and expresses the Sabatier principle for the ORR (Fig. 1.6).

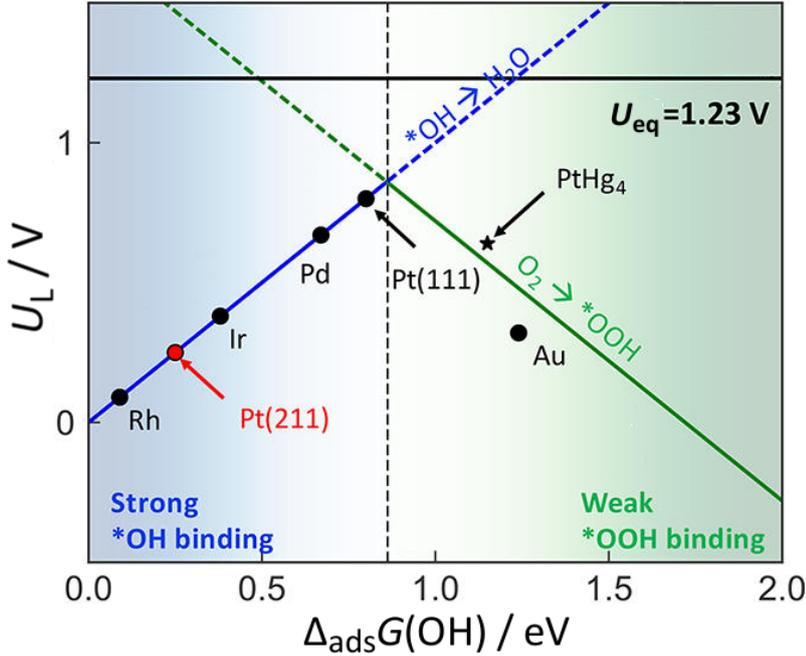


Figure 1.6: ORR volcano curve as a function of the limiting potential vs. OH adsorption energy [8]. The vertical dashed line marks $\Delta_{\text{ads}}G(\text{OH})$ of the best catalyst obeying the scaling relations, which is at the top of the volcano.

Above, the theoretical approach to catalytic oxygen electroreduction adopted in this work was described. It is based solely on the thermodynamic analysis of the reaction steps. A review of the computationally more demanding kinetic analysis of the ORR under electrochemical conditions can be found in a recent paper by Kulkarni *et al.* [8].

1.2.4 Paths to affordable PEM fuel cells

The high ORR overpotential, together with other issues like the catalyst price and its instability during operation, has a serious implication: as of today, PEMFC technology is too expensive to compete with the internal combustion engine for the automobile market. The most active ORR electrocatalysts are currently based on rare and expensive platinum. Consequently, the catalyst contributes about 46% to the PEM fuel cell stack cost [6].

There are a few approaches which could make the PEMFC technology competitive. The most optimistic and forward-looking one is to find a catalyst not subject to the ORR scaling relations. A few strategies were proposed to achieve that, and they usually involve the third dimension (*e.g.*, *via* confinement, surface functionalization, or electrolyte engineering, Fig. 1.7). However, an experimental proof of concept is still pending.

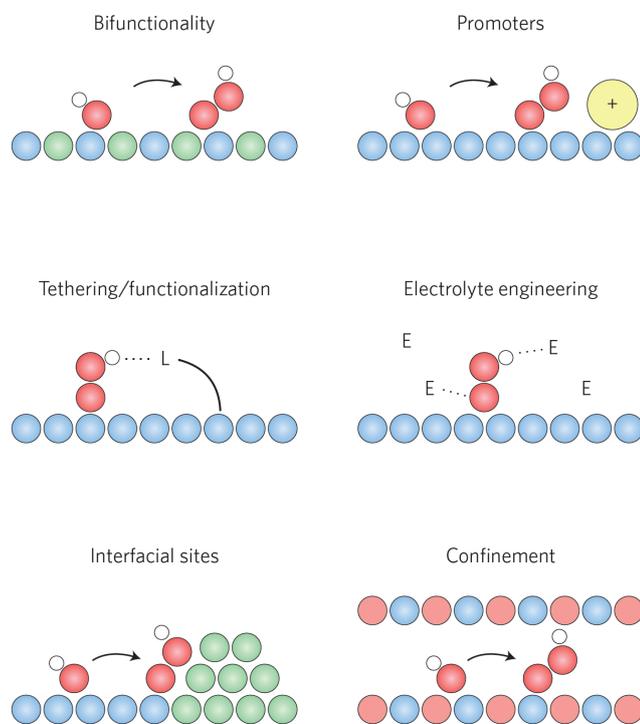


Figure 1.7: Strategies proposed to circumvent the unfavorable $*\text{OH}-*\text{OOH}$ scaling relation [14].

Another widely addressed approach is to maximize the activity of the platinum-based catalysts, at the same time minimizing the platinum metal content. Both goals can be achieved, *e.g.*, by alloying platinum with other (less expensive) transition metals. Several review articles describe this matter comprehensively [4, 15–17].

Finally, ORR catalysts may entirely consist of earth-abundant elements, such as carbon, boron, nitrogen, iron, cobalt, etc. Like in case of Pt-based materials, the major activity limitation of non-precious ORR catalysts is the $*\text{OH}-*\text{OOH}$ scaling relation. The highest theoretical activity of both groups

of catalysts is the same; however, the inherently lower material cost makes the non-precious materials particularly interesting. This group of catalysts is studied in the present thesis.

In the next section, a few notable non-precious ORR catalysts are reviewed, with a special emphasis on the nature of the active site.

1.3 Active sites on non-precious ORR catalysts

Certainly, there exist a countless number of ways to synthesize a catalytic material. Taking an example of just one method of a non-precious ORR catalyst synthesis — pyrolysis — a chemist can control such variables as: pyrolysis temperature, pressure and time, temperature program, type of precursors/additives and their concentration, pyrolysis atmosphere (*e.g.*, argon, nitrogen, ammonia), pre- and post-processing methods etc. All of these factors influence such characteristics of the end product as the activity, durability/stability (under various chemical and electrochemical conditions and over different periods of time), particle size and morphology, etc.

However, the multitude of so obtained materials active towards the ORR contain only a few general types of active sites, with activity determined by the closest chemical environment. Owing to the locality of the adsorption phenomena [18], the active sites can be satisfactorily simulated by quantum-mechanical methods, such as DFT, capable of describing systems containing up to several hundred atoms.

Below, the current understanding of the catalytic site structures in three different classes of materials is presented. The types of catalysts are metal-nitrogen-carbon (M-N-C) materials, nitrogen-doped carbon and encapsulated non-precious metal catalysts.

1.3.1 Metal-nitrogen-carbon catalysts (M-N-C)

The first premise that materials made of earth-abundant elements are capable of catalyzing oxygen electroreduction reaction comes from Jasinski, who discovered that cobalt phthalocyanine is active towards ORR in alkaline media [19]. Until today, catalysts with moieties containing transition metal atom, nitrogen, and carbon (M-N-C) are considered one the most promising groups of cathodic materials for future commercial use in low-cost fuel cells [5].

Currently, the most active M-N-C catalysts for ORR are synthesized by pyrolysis from iron, nitrogen and carbon-containing precursors. Noteworthy breakthroughs were made by Proietti (Dodelet group) *et al.* [20] and Sa *et al.* [7], with volumetric ORR activities of their materials being 230 and 320 A cm⁻³, respectively (U.S. Department of Energy target 2017 for non-precious catalytic materials: 300 A cm⁻³). However, the long-term stability of the former catalyst under operating conditions is still unsatisfactory, and the stability of the latter was not investigated in the acidic conditions. One of the most

probable reasons behind the activity loss over time is the dissolution of iron in acidic environment [21].

However, remarkable stability was achieved in case of a catalyst reported by Wu *et al.* (Zelenay group) [22]. With the onset potential of 0.93 V and the half-wave potential of 0.81 V, it exhibited remarkable stability in a 700 h fuel cell lifetime test at 0.40 V, as well as during voltage cycling between 0.6 and 1.0 V (up to 30 000 cycles). This activity is very good by the standards of non-precious materials; however, it still does not reach the activity of platinum-based catalysts, even with an order of magnitude higher catalyst loading.

A significant effort has been made to resolve the active sites structures in the Fe-N-C materials [6, 21, 23–28]. Dodelet *et al.* used Mössbauer spectroscopy to identify various iron forms present in their catalyst samples. By studying the correlation between each form content and ORR kinetic current density, they deduced that catalytically active sites are porphyrin-like FeN_4C centers (Fig. 1.8a) and N-coordinated $\text{FeN}_{2+2}/\text{C}$ structures ($\text{N-FeN}_{2+2}/\text{C}$, Fig. 1.8b).

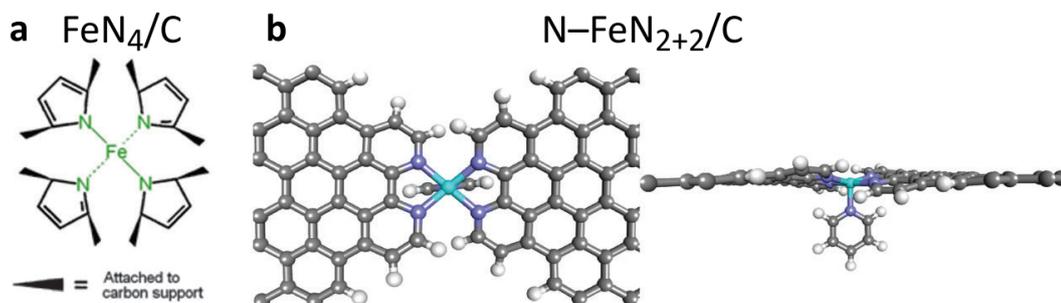


Figure 1.8: Fe-N-C active sites deduced by Dodelet *et al.*: (a) porphyrin-like FeN_4C structure [23], (b) $\text{N-FeN}_{2+2}/\text{C}$ structure, where N-coordination is modeled by axial pyridine group [25].

Zitolo *et al.* analyzed a similarly synthesized catalyst by X-ray absorption near-edge spectroscopy (XANES), and simulated XANES spectra of Fe for a series of possible active site structures [26]. By comparing experimental and theoretical spectra, they achieved the best match for a porphyrin-like $\text{FeN}_4\text{C}_{12}$ moiety (Fig. 1.9), similar to the FeN_4C structure suggested by Dodelet *et al.* (Fig. 1.8a).

Carbon-embedded nitrogen-coordinated iron active sites were recently directly visualized with aberration-corrected scanning transmission electron microscopy in Zelenay’s catalyst (Fig. 1.10a) [6]. The material was found to contain a considerably higher concentration of Fe associated with edges and steps than with basal-plane, which is consistent with earlier DFT modeling by Holby *et al.* [27, 28]. According to their computations, the edge-hosted FeN_4 structure spontaneously evolves OH ligand, and the OH-coordinated moiety acts as the catalytic site, exhibiting a limiting potential of 0.80 V on the associative pathway.

There is no definitive consensus yet on the exact structure and environment of the active sites in Fe-N-C catalysts. However, both experimental and the-

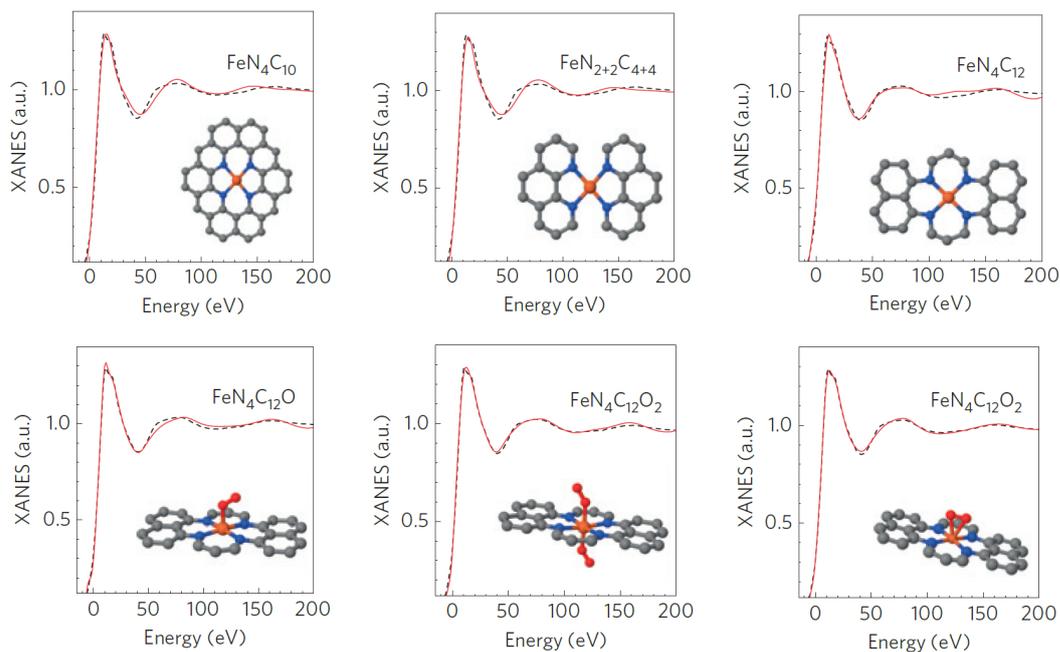


Figure 1.9: Fe-N-C active site models considered by Zitolo *et al.* [26]. Experimental XANES spectrum of Fe (black dashed line) is presented together with theoretical simulation (solid red line) for the considered structure. For $\text{FeN}_4\text{C}_{12}$, the experimental spectrum is correctly reproduced up to 90 eV above the absorption edge. The best match is achieved for $\text{FeN}_4\text{C}_{12}\text{O}_2$ structures (end-on and side-on adsorbate configuration).

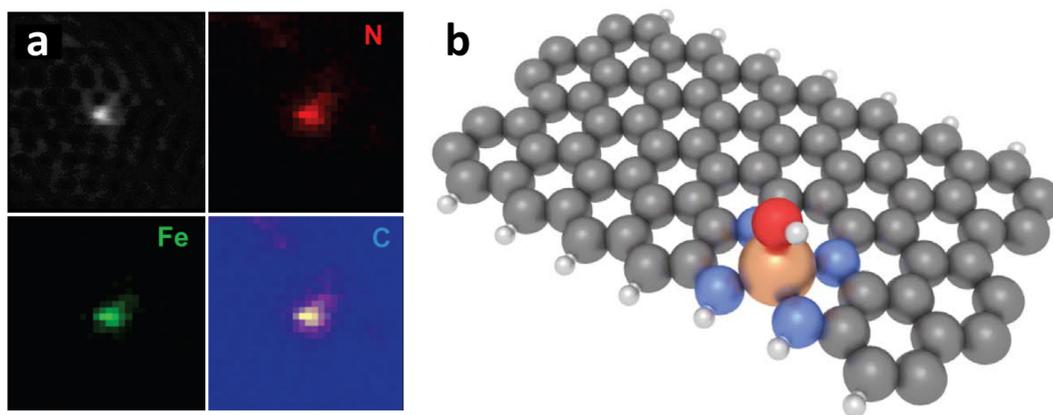


Figure 1.10: Fe-N-C active sites in Zelenay's catalyst [6]. (a) High-angle annular dark-field scanning transmission electron microscopy (HAADF-STEM) representing the first direct observation of the proposed Fe-N-C active site. Individual Fe atom embedded in a few-layer graphene sheet exists together with nitrogen. (b) Proposed active site structure: edge-hosted FeN_4 moiety with OH ligand.

oretical evidence has so far consistently confirmed that nitrogen-coordinated iron moieties (most probably FeN_4) embedded in a carbon structure are directly responsible for the ORR catalytic activity in these systems. It is most likely that various structures are present in the experimental conditions, and the chemical environment causes differences in their activity and stability. Further experimental and computational research is required to determine which types of structures are the most desirable, and how to synthesize them with high efficiency and selectivity.

1.3.2 Nitrogen-doped carbon

The class of nitrogen-doped carbon catalysts includes materials like N-doped graphene, carbon nanotubes, and porous carbon nanostructures. These materials are inherently insensitive to acid leaching owing to the lack of metal atom in the active site structure. The pure N-doped carbon activity appears in all its glory in alkaline media, often exceeding the activity of platinum [29]. However, some amount of nitrogen is found nearly in every notable non-precious ORR catalyst [5], including encapsulated metal structures described in the next section.

It is well known that a nitrogen dopant embedded in a carbon structure facilitates oxygenated species adsorption on adjacent carbon atoms, rather than acting directly as an adsorption site [30]. There are five main types of N-doping in carbon (Fig. 1.11), each associated with specific N 1s X-ray absorption energy [31]. Significant experimental effort was dedicated to determine which type of doping was responsible for the ORR activity [31–38]. The results were often contradictory, oscillating between graphite-like (carbon substitution in a graphene basal plane) and pyridine-like (as part of a 6-member ring found in a graphene sheet edge).

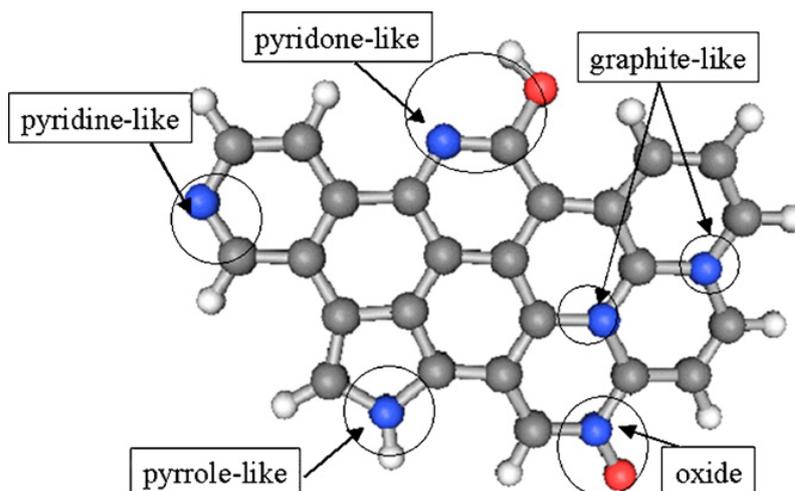


Figure 1.11: Five main types of nitrogen doping in carbon materials [31].

The discussion has been settled by Guo *et al.*, who used a well-controlled method of N-doping to obtain pyridinic-N and graphitic-N sites on highly ori-

ented pyrolytic graphite (HOPG). They have rigorously demonstrated that the ORR activity correlates with pyridinic-N content, while there is no correlation between the activity and graphitic-N content. The proposed ORR mechanism is shown in Fig. 1.12.

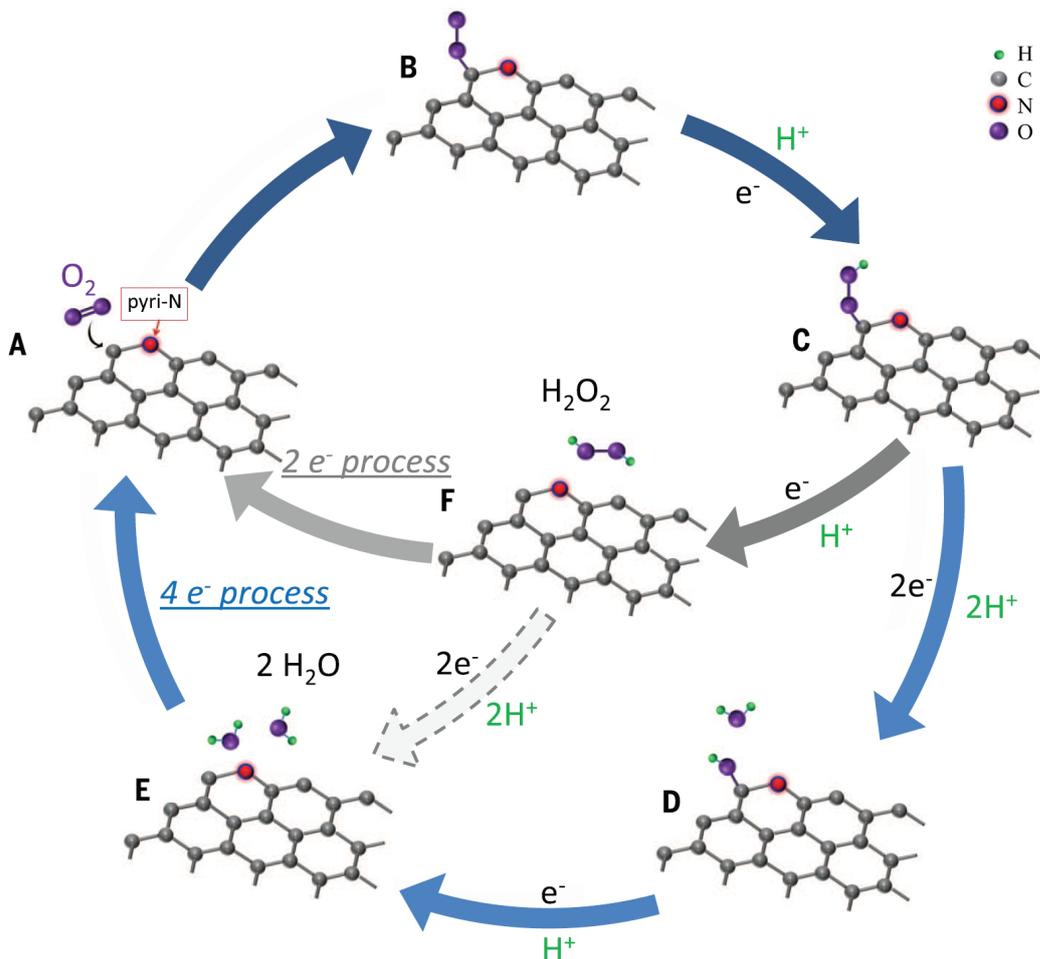


Figure 1.12: ORR mechanism on N-doped carbon as proposed by Guo *et al.* [39]. Pyridine-like nitrogen facilitates oxygen reduction reaction on the neighboring carbon atom.

However, graphitic-N-doping is still a possible explanation of a significant activity of some ORR catalysts. DFT calculations by Siahrostami *et al.* have shown that certain combinations of graphene basal plane defects and N-substitutions can exhibit low theoretical ORR overpotentials, comparable to that of the Pt(111) surface [40]. An N-doped version of the Stone-Wales defect was found particularly active and stable (Fig. 1.13). This type of defect was also most frequently observed in their N-doped mesoporous carbon catalyst. Graphitic nitrogen was concluded a likely source of the catalyst activity, as it represented 69% of all nitrogen species.

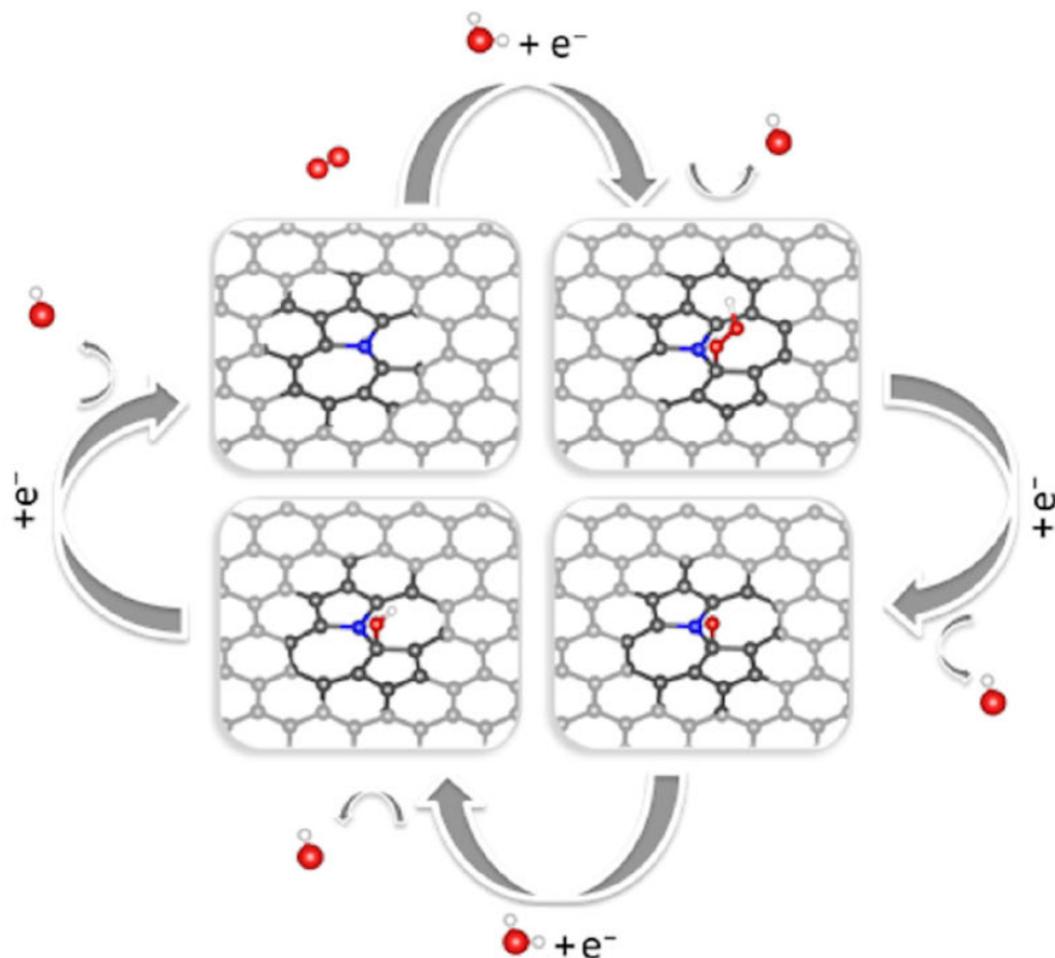


Figure 1.13: ORR $4e^-$ associative pathway on N-doped graphene with a Stone-Wales defect, as proposed by To *et al.* [40].

1.3.3 Encapsulated non-precious metal catalysts

Encapsulated non-precious metal catalysts consist of metal or carbide nanoparticles (core) encased in graphitic layers (shell). The role of the inner metallic particles is to activate the outer graphitic layers towards ORR. The carbon cover protects the nanoparticles from being leached out by the acidic electrolyte and provides direct adsorption sites for the ORR intermediates. It often contains various types of nitrogen embedded in the carbon structure [41–43].

Examples of reported materials of this type include Fe and Fe-Co alloy confined in carbon nanotubes (in short: Fe@CNT and FeCo@CNT) obtained by Deng *et al.* [41, 44], slightly similar Fe@CNT structure obtained by Chung *et al.* [45], and iron carbide encased in graphitic layers (Fe₃C@C) synthesized by Hu *et al.* [46]. Soon after these catalysts were first reported, Dodelet *et al.* noted that a new type of the ORR catalytic site was likely discovered [47].

Shortly after that, Varnell *et al.* confirmed this presumption by using a novel Cl₂-etching and H₂-restoring procedure at 900°C [42]. They prepared

a catalyst containing both FeN_4C sites and confined Fe. Gaseous chlorine treatment transformed all iron forms in the sample into chlorides, which led to catalyst deactivation. Subsequent reduction by hydrogen restored the catalytic activity entirely; however, the Mössbauer spectrum of the treated sample showed no evidence of the presence of nitrogen-coordinated iron (Fig. 1.14). Accordingly, the activity was ascribed to the encapsulated Fe heterostructure.

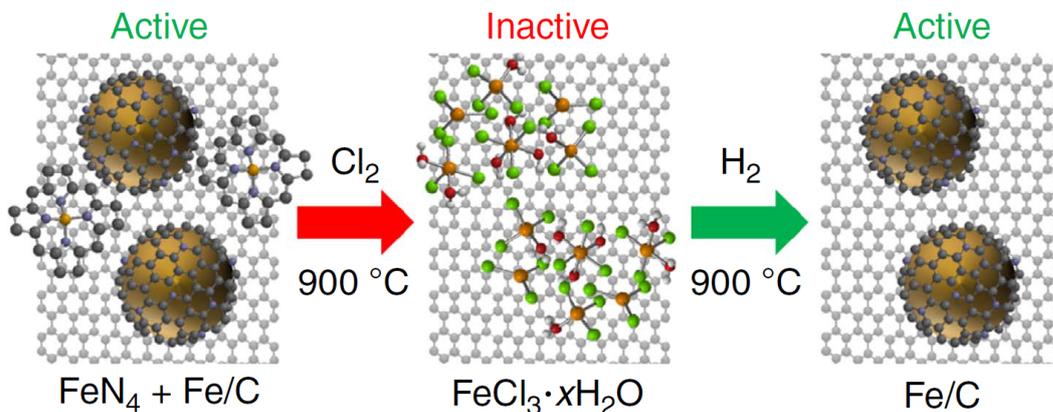


Figure 1.14: Cl_2 -etching/ H_2 -restoring method confirming the catalytic activity of the encapsulated iron heterostructure towards ORR [42].

1.3.4 Other non-precious ORR catalysts

The above summary of ORR catalysts includes arguably the most promising materials for future commercial applications in PEMFC. However, its purpose was mainly to introduce materials that are considered in the present thesis and is by no means intended to be comprehensive. A large number of other earth-abundant ORR catalysts grouped into classes, such as transition metal-nitrogen-carbon catalysts, doped nanotubes/graphenes/porous carbon, metal carbides/nitrides/oxides/chalcogenides, metal-organic frameworks and coupled inorganic/carbon and carbon/carbon systems, can be found in recent review articles [4, 5, 29].

1.4 Thesis outline

This thesis consists of seven chapters. The remaining six chapters are outlined below.

Chapter 2 introduces computational methods employed throughout this thesis.

Chapter 3 is based on Paper 1 and presents a computational study of two effects stabilizing ORR intermediates on basal plane N-doped graphene. A resulting ORR reaction environment is discussed.

Chapter 4 is based on Paper 3 and presents a computational study of experimentally known ORR catalyst, which comprises iron carbide-supported graphitic layers. A consistency between computational and experimental data allows formulating a guideline for the future search for more effective support materials.

Chapter 5 is based on Paper 2 and presents a combined experimental and computational study of the Fe-N-C catalyst activity increase in phosphoric acid. The effect is theoretically explained by selective anion adsorption, which demonstrates that species present in the electrolyte may enhance catalytic activity.

Chapter 6 summarizes the key findings and discusses possible routes of further study.

Chapter 2

Computational Methods

2.1 Density Functional Theory

Density Functional Theory (DFT) is, as of today, the most popular method to solve the non-relativistic, time-independent Schrödinger equation for systems containing about 10–1000 atoms in solid-state physics. Here, the theory will be briefly introduced.

2.1.1 Born-Oppenheimer approximation

At the beginning, we will assume that the motion of nuclei and electrons can be treated independently. The electrons are almost 2000 times lighter than the lightest existing nucleus (proton). This usually allows us to assume that electrons adapt their configuration to that of the nuclei at all times. The practical implication of this so-called Born-Oppenheimer approximation is that we can split system's Hamiltonian into the nuclear and electronic part, and treat positions of the nuclei in the electronic part as parameters, and not as dynamic quantum variables.

The electronic Schrödinger equation with the Hamiltonian written explicitly in atomic units reads

$$\left(-\frac{1}{2} \sum_{i=1}^N \nabla_i^2 + \sum_{I=1}^M \sum_{i=1}^N \frac{Z_I}{|\mathbf{R}_I - \mathbf{r}_i|} + \sum_{i<j}^N \frac{1}{|\mathbf{r}_i - \mathbf{r}_j|} \right) \Psi = E\Psi \quad (2.1)$$

where $\mathbf{r} = \{\mathbf{r}_i, i = 1, \dots, N\}$ is the set of N electronic coordinates, $\mathbf{R} = \{\mathbf{R}_i, i = 1, \dots, M\}$ is the set of M nuclear coordinates and Z_I are the charges of the nuclei. The first term in the Hamiltonian is the kinetic energy of the electrons, the second term is the electron–nuclei interaction, and the third term is the electron–electron interaction.

2.1.2 Hohenberg-Kohn theorems

In Density Functional Theory, the key role is played by the electron density, which in terms of the wavefunction can be written as

$$\rho(\mathbf{r}) = N \int \cdots \int |\Psi(\mathbf{r}, \mathbf{r}_2, \dots, \mathbf{r}_N)|^2 d\mathbf{r}_2 \dots d\mathbf{r}_N \quad (2.2)$$

Density Functional Theory is founded on two Hohenberg-Kohn theorems.

Theorem 1. The external potential $v_{\text{ext}}(\mathbf{r})$ is unequivocally determined by the electron density $\rho(\mathbf{r})$, besides a trivial additive constant.

In other words, if we knew the electron density of the system, we would have all the information about its ground state, *i.a.* full many-body wavefunction Ψ and the kinetic $T[\rho]$, potential $V[\rho]$, and total $E[\rho]$ energies. Here by $X[\rho]$ we mean that property X is a functional of the electron density. We can thus write

$$E[\rho] = T[\rho] + V_{\text{ne}}[\rho] + V_{\text{ee}}[\rho] = \int \rho(\mathbf{r})v_{\text{ext}}(\mathbf{r})d\mathbf{r} + F_{\text{HK}}[\rho] \quad (2.3)$$

where $V_{\text{ne}}[\rho]$ and $V_{\text{ee}}[\rho]$ refer to the potential energies of the electron-nuclei and electron-electron interactions, and $F_{\text{HK}}[\rho]$ is called the universal density functional

$$F_{\text{HK}}[\rho] = T[\rho] + V_{\text{ee}}[\rho] \quad (2.4)$$

Theorem 2. Total energy $\tilde{E}[\tilde{\rho}]$ obtained with a trial electron density $\tilde{\rho}$ is always greater or equal to the ground state energy E . Equality holds only if the trial density is the actual electron density of the system.

This is the DFT analog of the variational principle in wave-function based quantum mechanics. It states that if we knew the form of the universal density functional [Eq. (2.4)], we would be able to obtain $\rho(\mathbf{r})$ with arbitrary precision by minimizing $E[\rho]$ (in some basis or without it).

To keep Hohenberg-Kohn theorems in force, it is sufficient if the electron density fulfills the following three conditions

$$\rho(\mathbf{r}) \geq 0, \quad N = \int \rho(\mathbf{r})d\mathbf{r}, \quad \int |\nabla \sqrt{\rho(\mathbf{r})}|^2 d\mathbf{r} < \infty \quad (2.5)$$

Some interesting features of the electron density are:

- it is a non-negative function [first expression in Eq. (2.5)],
- it integrates over the whole space to the number of electrons in the system [second expression in Eq. (2.5)],
- it has cusps at the location of nuclei,
- density gradient at a nucleus is closely related to the nucleus identity.

2.1.3 Kohn-Sham scheme

Having established foundations for DFT, we will discuss its practical implementation. Currently, almost all DFT calculations are based on the Kohn-Sham scheme, briefly described below.

Consider the system of interest being described by a set of non-interacting electrons moving in an effective Kohn-Sham potential $v_{\text{KS}}(\mathbf{r})$. The potential is constructed so as to ensure the density of non-interacting electrons is equal to the true many-body electron density. The Hamiltonian of this reference system is

$$\hat{\mathcal{H}}_{\text{R}} = \sum_{i=1}^N \left[-\frac{1}{2} \nabla_i^2 + v_{\text{KS}}(\mathbf{r}_i) \right] \quad (2.6)$$

where the first term is the kinetic energy operator of the non-interacting electrons. The advantages of this formulation are as follows:

1. Wavefunction for a system of non-interacting electrons is just a Slater determinant of one-electron orbitals. Considering the closed shell situation for simplicity, we have $N/2$ doubly occupied orbitals, and the wavefunction is

$$\Phi(\mathbf{r}) = \frac{1}{\sqrt{(\frac{N}{2})!}} \text{SD}[\varphi_1(\mathbf{r}_1)\varphi_2(\mathbf{r}_2) \dots \varphi_{N/2}(\mathbf{r}_{N/2})] \quad (2.7)$$

2. Within the same assumption (closed-shell electronic structure), the electron density is

$$\rho(\mathbf{r}) = 2 \sum_{i=1}^{N/2} |\varphi_i(\mathbf{r})|^2 \quad (2.8)$$

3. The orbitals (called Kohn-Sham orbitals) are computed by solving one-electron equations

$$\left[-\frac{1}{2} \nabla^2 + v_{\text{KS}}(\mathbf{r}) \right] \varphi_i(\mathbf{r}) = \varepsilon_i \varphi_i(\mathbf{r}) \quad (2.9)$$

It should be noted though these orbitals may have no physical meaning.

4. The exact expression for the kinetic energy of non-interacting electrons is known

$$T_{\text{R}}[\rho] = 2 \sum_{i=1}^{N/2} \langle \varphi_i | -\frac{1}{2} \nabla^2 | \varphi_i \rangle \quad (2.10)$$

By a slight modification of Eq. (2.3) we can write an expression for the total energy functional of our system, the Kohn-Sham (KS) functional

$$\begin{aligned} E_{\text{KS}}[\rho] &= T_{\text{R}}[\rho] + V_{\text{ne}}[\rho] + J[\rho] + E_{\text{XC}}[\rho] \\ &= 2 \sum_{i=1}^{N/2} \langle \varphi_i | -\frac{1}{2} \nabla^2 | \varphi_i \rangle + \int \rho(\mathbf{r}) v_{\text{ext}}(\mathbf{r}) d\mathbf{r} \\ &\quad + \frac{1}{2} \iint \frac{\rho(\mathbf{r})\rho(\mathbf{r}')}{|\mathbf{r} - \mathbf{r}'|} d\mathbf{r} d\mathbf{r}' + E_{\text{XC}}[\rho] \end{aligned} \quad (2.11)$$

where

$$J[\rho] = \frac{1}{2} \iint \frac{\rho(\mathbf{r})\rho(\mathbf{r}')}{|\mathbf{r} - \mathbf{r}'|} d\mathbf{r}d\mathbf{r}' \quad (2.12)$$

is a classical Coulomb interaction of charge density $\rho(\mathbf{r})$ with itself. Notice that it contains interaction of an electron with an average charge density of all the electrons, which means it also includes an unphysical interaction of an electron with itself.

By this, we have divided the energy of the system into two parts. The first part contains all the contributions that are well-known and can be calculated exactly ($T_{\text{R}}[\rho]$, $V_{\text{ne}}[\rho]$, $J[\rho]$). The second part is an exchange-correlation term

$$E_{\text{XC}}[\rho] := T[\rho] - T_{\text{R}}[\rho] + V_{\text{ee}}[\rho] - J[\rho] \quad (2.13)$$

It is the smallest energetic contribution that includes all the ignorance about the system. Its role is to:

- fix the kinetic energy,
- take into account Pauli repulsion,
- cancel the interaction of an electron with itself, introduced in Eq. (2.12),
- include the remainder of the electrostatic interaction between electrons (many-electron picture).

The exchange-correlation energy is usually thought of as the interaction between electron density $\rho(\mathbf{r})$ and a fictitious charge depletion $\tilde{\rho}_{\text{XC}}(\mathbf{r}, \mathbf{r}')$ called the exchange-correlation hole

$$E_{\text{XC}}[\rho] = \frac{1}{2} \iint \frac{\rho(\mathbf{r})\tilde{\rho}_{\text{XC}}(\mathbf{r}, \mathbf{r}')}{|\mathbf{r} - \mathbf{r}'|} d\mathbf{r}d\mathbf{r}' \quad (2.14)$$

To obtain Kohn-Sham orbitals from Eq. (2.9), we need to know the Kohn-Sham potential $v_{\text{KS}}(\mathbf{r})$. We can use the 2nd Hohenberg-Kohn theorem to minimize the functional in Eq. (2.11) with a constraint that electron density is normalized to N [second expression in Eq. (2.5)]

$$\frac{\delta}{\delta\rho(\mathbf{r})} \left(E_{\text{KS}}[\rho] - \mu \int \rho(\mathbf{r})d\mathbf{r} \right) = 0 \quad (2.15)$$

We obtain the effective Kohn-Sham potential

$$v_{\text{KS}}(\mathbf{r}) = v_{\text{ext}}(\mathbf{r}) + \int \frac{\rho(\mathbf{r}')}{|\mathbf{r} - \mathbf{r}'|} d\mathbf{r}' + v_{\text{XC}}(\mathbf{r}) \quad (2.16)$$

with

$$v_{\text{XC}}(\mathbf{r}) = \frac{\delta E_{\text{XC}}[\rho]}{\delta\rho(\mathbf{r})} \quad (2.17)$$

Notice that the Kohn-Sham potential, which enters Eq. (2.9), depends itself on its solution through the electron density. Therefore the problem has to be solved self-consistently in an iterative procedure:

1. Make an initial guess for the electron density,
2. Calculate the Kohn-Sham potential, Eq. (2.16),
3. Solve N one-electron problems, Eq. (2.9),
4. Calculate the electron density, Eq. (2.8),
5. Compare the new density with the old one. If the difference is greater than the convergence criterion, go back to point 2.

2.1.4 BEEF-vdW functional

Density functional theory is exact for the ground state. However, since the expression for the exact exchange-correlation functional is not known, we have to search for better and better approximations that will bring us closer and closer to the exact solution. Many such approximations have been developed and classified in what is known as the Jacob's ladder [48]. The 2nd rung of this ladder is the Generalized Gradient Approximation (GGA), where the information about electron density and its gradient is used. Currently, this class of functionals seems to be the best compromise between accuracy and computational cost for most of the solid-state physics applications.

Two very popular functionals which belong to this rung are PBE [49] (for general purposes) and RPBE [50] (mainly for surface adsorption). These functionals, however, do not account for non-local van der Waals interactions like dispersion forces. Systems considered in the present thesis contain explicit water layers interacting with a hydrophobic surface of the catalyst, as well as multiple graphene layers, stacked one on another. In such systems, dispersion forces can play a significant role. For this reason, a BEEF-vdW functional [51], is employed, in which vdW-DF2 [52] non-local correlation is used. This approach proved to be successful in predicting adsorption bond energies both to transition metal surfaces [53] and carbon-based materials, at the same time offering a very good description of metal/graphene heterostructures, such as Ni(111)/graphene [51] (systems comprising metal/graphene heterostructures are investigated in Chapter 4). It also gives a unique possibility of adsorption energy error estimation [54]. In what follows, the idea behind the BEEF-vdW functional is introduced.

Exchange-correlation energy functional can be separated into the exchange and correlation parts

$$E_{XC}^{\text{GGA}}[\rho, \nabla\rho] = E_X^{\text{GGA}}[\rho, \nabla\rho] + E_C^{\text{GGA}}[\rho, \nabla\rho] \quad (2.18)$$

Here we emphasize that the functional of interest is a GGA functional. Each component can be expressed as a function of energy density ε . The exchange part can, therefore, take the following form

$$E_X^{\text{GGA}}[\rho, \nabla\rho] = \int \varepsilon_X^{\text{GGA}}(\rho(\mathbf{r}), \nabla\rho(\mathbf{r})) \, d\mathbf{r} \quad (2.19)$$

It is convenient to express the GGA exchange energy density $\varepsilon_X^{\text{GGA}}$ as a product of the uniform electron gas exchange energy density $\varepsilon_X^{\text{LDA}}$ [55] and an exchange enhancement factor $F_X(s)$. The acronym LDA stands for the Local Density Approximation, which is the 1st rung of the Jacob's ladder. Function s is called the reduced density gradient

$$s(\rho, \nabla\rho) = \frac{|\nabla\rho|}{2k_F\rho} = \frac{|\nabla\rho|}{2(3\pi^2)^{1/3}\rho^{4/3}} \quad (2.20)$$

where k_F is the Fermi wave vector. The exchange GGA functional now reads

$$E_X^{\text{GGA}}[\rho, \nabla\rho] = \int \varepsilon_X^{\text{LDA}}(\rho) F_X(s(\rho, \nabla\rho)) d\mathbf{r} \quad (2.21)$$

In BEEF-vdW the enhancement factor is expanded in a basis of M_X Legendre polynomials $B_m(t(s))$ in a transformed reduced density gradient $t(s)$

$$F_X^{\text{BEEF-vdW}}(s(\rho, \nabla\rho)) = \sum_{m=0}^{M_X-1} a_m B_m(t(s)), \quad t(s) = \frac{2s^2}{4+s^2} - 1 \quad (2.22)$$

Electron correlation effects are modeled as a linear combination of a purely local Perdew-Wang [56] LDA correlation functional $E_C^{\text{LDA}}[\rho]$, semilocal Perdew-Burke-Ernzerhof (PBE) [49] correlation $E_C^{\text{PBE}}[\rho, \nabla\rho]$, and vdW-DF2 [52] type non-local correlation. The purpose of the latter is to account for non-covalent, intermolecular interactions called collectively the van der Waals interactions. The total BEEF-vdW exchange-correlation functional reads

$$E_{XC}^{\text{BEEF-vdW}} = \sum_{m=0}^{M_X-1} a_m \int \varepsilon_X^{\text{LDA}} B_m(t(s)) d\mathbf{r} + \alpha_C E_C^{\text{LDA}} + (1 - \alpha_C) E_C^{\text{PBE}} + E_C^{\text{NL}} \quad (2.23)$$

Expansion coefficients a_m and correlation mixing parameter α_C are adjustable parameters of the model which can be found in the original paper [51].

Error estimation is achieved by generating an ensemble of several thousand functionals with perturbed values of a_m and α_C . The perturbation is performed in such a way that the standard deviation in quantity calculated using the ensemble of functionals corresponds to the predicted computational error. It should be noted however that this method cannot account for systematic errors. Error estimation feature of BEEF-vdW has not been employed in the calculations conducted under this thesis.

2.2 From DFT energy to Gibbs free energy

Constant temperature and pressure are the most common conditions at which chemical and electrochemical reactions occur in practical applications. This equally applies to the oxygen reduction reaction in fuel cells. In this thesis,

ORR is modeled at $T = 298.15$ K and the partial pressure of oxygen and hydrogen of $p_{\text{O}_2} = p_{\text{H}_2} = 1$ bar. Gibbs free energy is the thermodynamic potential that decreases for a spontaneous process (and reaches the minimum at equilibrium) at fixed (T, p)

$$G = H - TS = U + pV - TS \quad (2.24)$$

Direct output of a DFT calculation is the ground state energy of a given configuration of atoms. To model ORR on a catalyst surface, it is necessary to convert the DFT energy (E_{DFT}) into the Gibbs free energy. Below, the process is described both for gas phase molecules and adsorbates on the catalyst surface.

2.2.1 Gas phase molecules

Gibbs free energies of the gas-phase reactants are calculated according to the following equations [57]

$$\begin{aligned} G(T, p) &= H(T) - TS(T, p) = \\ &= \left[E_{\text{DFT}} + E_{\text{ZPE}} + \int_0^{298.15 \text{ K}} c_p(T) dT \right] \\ &\quad - T \left[S(298.15 \text{ K}, p^\circ) - k_{\text{B}} \ln \frac{p}{p^\circ} \right] \end{aligned} \quad (2.25)$$

$$E_{\text{ZPE}} = \sum_i \frac{\varepsilon_i}{2} \quad (2.26)$$

where: E_{ZPE} – the zero-point energy (calculated from the vibrational spectroscopy data), ε_i – the energy associated with a vibrational mode i , $c_p(T)$ – heat capacity at constant pressure, p° – standard pressure (1 bar). With the exception of E_{DFT} , all the properties are taken from the literature [58–60].

Gibbs free energy of liquid water is equal to the Gibbs free energy of water in the gas phase at the equilibrium vapor pressure (0.032 bar at 298.15 K [60]). Mole fraction-based activity of water in the electrolyte is assumed to be $a_{\text{H}_2\text{O}} = 1$.

2.2.2 Adsorbates

Gibbs free energies of the adsorbates are calculated from the partition function [57] with the following assumptions:

- pV term in Eq. (2.24) is negligible,
- the adsorbate has only vibrational degrees of freedom,
- the vibrations can be approximated as quantum harmonic oscillations.

$$G(T) \cong U(T) - TS(T) = [E_{\text{DFT}} + E_{\text{ZPE}} + U_{\text{vib}}(T)] - TS_{\text{vib}}(T) \quad (2.27)$$

$$U_{\text{vib}}(T) = \sum_i \frac{\varepsilon_i}{\exp\left(\frac{\varepsilon_i}{k_{\text{B}}T}\right) - 1} \quad (2.28)$$

$$S_{\text{vib}}(T) = k_{\text{B}} \sum_i \left\{ \frac{\varepsilon_i}{k_{\text{B}}T \left[\exp\left(\frac{\varepsilon_i}{k_{\text{B}}T}\right) - 1 \right]} - \ln \left[1 - \exp\left(-\frac{\varepsilon_i}{k_{\text{B}}T}\right) \right] \right\} \quad (2.29)$$

Vibrational frequency calculations are performed *via* the finite difference approach, perturbing only the adsorbate atoms. E_{ZPE} is calculated as in Eq. (2.26).

2.2.3 Gibbs free energy corrections

The above procedure applied to the reaction of liquid water formation [Eq. (1.6)] results in the Gibbs free energy of -4.18 eV. Significant deviation from the experimental value is often attributed to the poor representation of the O_2 energy at the DFT/GGA level, which is due to the complicated electronic structure of the oxygen molecule [61, 62]. To avoid O_2 calculation, ΔG_{ORR} is fixed to the experimental value of -4.92 eV. This also ensures that the key value in the simulation, $U_{\text{eq}}(\text{H}_2\text{O})$ [Eq. (1.1)], is correct. Similarly, whenever the $2e^-$ associative pathway [Eq. (1.5a, e)] is considered, the H_2O_2 formation energy is fixed at the experimental value to ensure the correct value of $U_{\text{eq}}(\text{H}_2\text{O}_2)$ [Eq. (1.2)].

Moreover, Christensen *et al.* have found systematic errors in DFT/BEEF-vdW description of the hydrogen and water molecules, as well as the peroxide bond [63, 64]. Based on their work, the following corrections are added to the corresponding Gibbs free energies of H_2 , H_2O and $^*\text{OOH}$ in Eq. (1.7)

$$\Delta G(\text{H}_2) = 0.09 \text{ eV} \quad (2.30\text{a})$$

$$\Delta G(\text{H}_2\text{O}) = -0.03 \text{ eV} \quad (2.30\text{b})$$

$$\Delta G(\text{O}-\text{O}) = 0.20 \text{ eV}. \quad (2.30\text{c})$$

2.3 Solvation

Oxygen reduction reaction in PEM fuel cells occurs at the solid/liquid interface between the ORR catalyst and the aqueous environment. Water molecules at the interface interact with ORR intermediates adsorbed on the catalyst surface and can alter their binding energy compared to that in the vacuum. The inclusion of solvation effects in ORR modeling requires involving additional computational resources and is still often omitted. In such cases, the effect is usually assumed to be transferable from the Pt(111) surface [9, 65, 66]. While this assumption seems to be justified for other metal (111) surfaces, in Chapter 3 it is shown not to apply to the basal plane N-doped graphene and a few similar surfaces.

2.3.1 Explicit solvation by H₂O molecules

There are a few ways to include solvation effects at the solid/liquid interfaces. A complete *ab initio* treatment requires including many layers of explicit water molecules in the calculation and performing potential energy surface sampling (*e.g.*, using *ab initio* molecular dynamics) and statistical averaging [67]. This approach is particularly expensive due to a large number of steps required to obtain reliable statistical averages.

Another approach is to find the minimum energy structures of explicit water layers for each system along the ORR path (*, *OOH, *O and *OH) [9, 68–70]. It is assumed that these static structures represent electrode/solution interface accurately enough to produce reliable solvation energies. The main computational effort lies in finding a global minimum of the respective water layers. This can be achieved, *e.g.*, by performing relatively short molecular dynamics (MD) simulations (or, even better, a few MD runs starting from different initial configurations), optimizing a few lowest-energy structures obtained during the calculation, and using the lowest-energy one to calculate the solvation energy and to construct the ORR free energy diagram [69]. Another quite efficient global optimization algorithm suitable for finding optimal water layer is the minima hopping method [71]. It also relies on short MD runs combined with the additional feature of avoiding revisiting previously found local minima. As this method was extensively utilized for optimizing water structures in this thesis, it is briefly introduced below.

The minima hopping algorithm [71]

A region in configurational space containing all the configurations that will relax into a specific local minimum is called a basin. A union of several neighboring basins is called a super-basin. If one can arrive at the lowest minimum of a super-basin without crossing barriers much higher than the average difference in energy between local minima, such a super-basin is called a funnel.

Most algorithms for finding global minimum in molecular systems rely on thermodynamic principles, especially the Boltzmann factor $\exp(-\Delta E/k_B T)$, which makes it difficult for the system to escape any funnel during the avail-

able computer time. As a result, the system revisits many times neighboring configurations, which are close in energy.

The essence of the minima hopping method is making more violent escape moves from basins that were already visited. The algorithm with parameters used is as follows:

1. Initialize a current minimum `Mcurrent`
2. Start a short MD run with the kinetic energy `Ekinetic`. Stop in the `mdmin`-th minimum along the trajectory and relax the structure to find the closest local minimum `M`. Parameters used:
 Initial `Ekinetic`: $T = 4000$ K,
 `mdmin` = 2.
3. if `M` = `Mcurrent` or any other minimum visited previously, then increase the kinetic energy (`Ekinetic` = $1.1 * Ekinetic$) and go to point (2),
4. if `M` is a new minimum, then decrease the kinetic energy (`Ekinetic` = $(1/1.1) * Ekinetic$)
5. If `energy(M) - energy(Mcurrent) < Ediff` (initial `Ediff` = 2.5 eV), then:
 - add `Mcurrent` to the history list
 - accept the new minimum (`Mcurrent` = `M`)
 - decrease `Ediff`: `Ediff` = $0.98 * Ediff$
 Else reject the new minimum and increase `Ediff`:
 `Ediff` = $(1/0.98) * Ediff$
6. If the number of collected minima is unsatisfactory, go to point (2).

High temperature used during the molecular dynamics stage can cause undesirable dissociation or desorption of molecules subject to global optimization. This may result in the exploration of uninteresting parts of the configuration space. For example, during a search for the most favorable `*CO` adsorption site on a catalyst surface, the algorithm may spend much time exploring `{*C + *O}` or `{* + CO}` configurations. A recent modification to the minima hopping algorithm, implemented in Atomic Simulation Environment [72], allows to include Hookean constraints preventing molecules decomposing or leaving the catalyst surface [73]. However, dissociation or desorption of water molecules forming a water layer on catalyst surface occurred only sporadically, and the original minima hopping method was used in this work.

It has to be noted that, given limited time and computational resources, the minima hopping method does not ensure finding the global minimum on the potential energy surface. As a rule of thumb, the algorithm was stopped after finding 30–50 local minima (convergence criterion for finding local minimum: maximum force on each atom $f_{\max} < 0.05$ eV/Å). The lowest energy structure, as well as a few structures which energy was up to 0.1 eV higher than the lowest energy one (usually 2 to 5 structures in total), were then used for final

optimization ($f_{\max} < 0.01 \text{ eV/\AA}$). After this, the lowest energy structure was selected. For some systems, an extended minima hopping run was performed to find *ca.* 80 local minima. This rarely resulted in finding lower energy minima, but even in such events, the energy difference was less than 0.05 eV.

Adsorption energies of the ORR intermediates in the presence of water

Adsorption energies of the ORR intermediates in vacuum were defined in Eq. (1.7). Here, the adsorption energies in the presence of explicit water layer are discussed.

A catalyst surface without water or any ORR intermediate adsorbed will be denoted by an asterisk (*). An ORR intermediate bound to the surface will be represented by *X, where $X = \{\text{OOH}, \text{O}, \text{OH}, \text{O}_2\}$. Systems with water layer will be represented by *|NH₂O (or *X|NH₂O), where N denotes the number of water molecules included in the water layer. In the derivation below, energies E directly obtained from DFT calculations are used; however, they can be converted into Gibbs free energies as described in Section 2.2.

Consider the reaction of a water layer formation on the surface of a catalyst



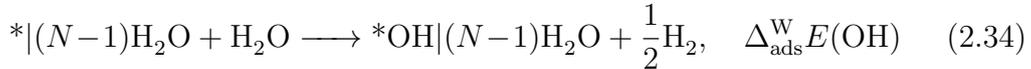
where WL stands for the water layer and ΔE_{WL} is

$$\Delta E_{\text{WL}} = E(*|\text{NH}_2\text{O}) - E(*) - N E(\text{H}_2\text{O}). \quad (2.32)$$

The average energy of a water molecule in the water layer is

$$E(\text{H}_2\text{O}_{\text{WL}}) = E(\text{H}_2\text{O}) + \frac{1}{N} \Delta E_{\text{WL}} = \frac{1}{N} [E(*|\text{NH}_2\text{O}) - E(*)]. \quad (2.33)$$

In the adopted approach, one water molecule is removed from the water layer per each adsorbate placed on the surface. The adsorption energy in the presence of water is calculated similarly as in Eq. (1.7), with a slight modification (example for OH intermediate)



where the superscript W denotes the presence of water and the energy of *|(N-1)H₂O is calculated as

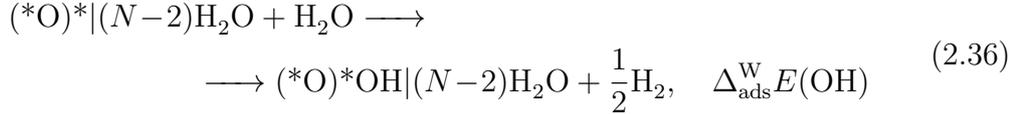
$$E[*|(N-1)\text{H}_2\text{O}] = E(*|\text{NH}_2\text{O}) - E(\text{H}_2\text{O}_{\text{WL}}). \quad (2.35)$$

The *|NH₂O and *OH|(N-1)H₂O structures are obtained using the minima hopping method as described above. Adsorption energies of the remaining ORR intermediates are calculated analogously.

In other words, the energy of a water molecule displaced upon insertion of adsorbate is assumed to be the average energy of H₂O in the water layer in the absence of any adsorbates. The sum of adsorbed species and water

molecules is kept fixed (N) to avoid a situation in which insertion of adsorbate into the system pushes a water molecule into a highly unstable position above a well-developed water layer.

In Chapters 3 and 4, the ORR in the presence of co-adsorbed spectator $^*\text{O}$ is studied. Also in this case, the principle of adsorption energy calculation is similar, *i.e.*, for the example of OH intermediate, the following reaction is considered



where the spectator is written in parentheses before the asterisk. The energy of $(^*\text{O})^*|(N-2)\text{H}_2\text{O}$ is calculated as

$$E[(^*\text{O})^*|(N-2)\text{H}_2\text{O}] = E[(^*\text{O})^*|(N-1)\text{H}_2\text{O}] - E(\text{H}_2\text{O}_{\text{WL}}). \quad (2.37)$$

To summarize, the following systems have to be optimized using the minima hopping algorithm to calculate the adsorption energies of the ORR intermediates in the presence of water:

no spectator	with $^*\text{O}$ spectator
$^* \text{NH}_2\text{O}$	$^* \text{NH}_2\text{O}$
	$(^*\text{O})^* (N-1)\text{H}_2\text{O}$
$^*\text{O} (N-1)\text{H}_2\text{O}$	$(^*\text{O})^*\text{O} (N-2)\text{H}_2\text{O}$
$^*\text{OH} (N-1)\text{H}_2\text{O}$	$(^*\text{O})^*\text{OH} (N-2)\text{H}_2\text{O}$
$^*\text{OOH} (N-1)\text{H}_2\text{O}$	$(^*\text{O})^*\text{OOH} (N-2)\text{H}_2\text{O}$

The number N is selected individually for each system depending on the surface area of the simulation cell and the number of molecular layers of H_2O to be included in the simulated water layer.

Adsorption free energies of the ORR intermediates in the presence of water, $\Delta_{\text{ads}}^{\text{W}}G(\text{X})$, are used to construct the ORR free energy diagram.

Solvation energy of an ORR intermediate can be calculated as a difference between adsorption energy in water and vacuum

$$\Delta_{\text{solv}}E(\text{X}) = -\Delta_{\text{stab}}^{\text{W}}E(\text{X}) = \Delta_{\text{ads}}^{\text{W}}E(\text{X}) - \Delta_{\text{ads}}E(\text{X}) \quad (2.38)$$

Here, $\Delta_{\text{stab}}^{\text{W}}E(\text{X})$ is the adsorbate stabilization energy caused by solvation (equal to the negative solvation energy).

2.3.2 Implicit solvation

Solvation methods described above treat liquid environment quantum-mechanically by including explicit water molecules in the system, which makes them relatively expensive. As opposed to that, an implicit solvation approach couples a quantum-mechanical description of the solute (here: catalyst + adsorbate) with an implicit description of the solvent as a continuum polarizable medium [74].

In the simplest formulation, only the electrostatic interaction between the solute and the solvent is considered. Solvent is described by a single parameter, *i.e.*, its relative permittivity. However, a generally applicable implicit solvation model has to take into account both electrostatic and van der Waals interactions, as well as the cavity formation energy. The model used in the present thesis, developed by Mathew *et al.* [74, 75], is known as VASPsol and is freely available as a patch to the Vienna *Ab initio* Simulation Package (VASP) source code. It adopts empirically parametrized non-electrostatic interactions and cavity formation energy related to a surface tension parameter.

Implicit solvation models have a few significant advantages over explicit solvent description methods. The benefits include much less demanding calculations, as well as the absence of errors resulting from statistical averaging due to incomplete sampling of solvent configurations. On the other hand, probably the greatest disadvantage of treating solvent as a continuum is the inability to describe effects resulting from the granular structure of the solvent, such as solvent-solute interaction *via* orbital overlap. This is suggested to be the reason for a poor prediction of the *O solvation on N-doped graphene surface using VASPsol model, described in details in Chapter 3.

2.4 General computational details

General computational details pertaining to each study in this thesis are listed below. Further details specific to each study can be found in relevant chapters.

All Density Functional Theory (DFT) calculations are done using Vienna *Ab initio* Simulation Package (VASP) [76–79] coupled with Atomic Simulation Environment (ASE) [72]. Core electrons are described with the Projector Augmented Wave method [80, 81], and the basis set for the electronic wavefunctions are plane waves below the 400 eV (explicit solvation) or 600 eV (implicit solvation) energy cutoff. Fermi smearing of electronic occupations with a width of 0.1 eV is used. Monkhorst-Pack [82] mesh for the Brillouin zone sampling, $(k_1, k_2, 1)$, is usually chosen such that $k_i v_i > 30$ for v_i being the corresponding lattice vector. However, more dense sampling ($k_i v_i > 40$) is used for N-doped graphene systems in Chapter 3. The vacuum layer region between periodic images of model systems is about 10 Å. Dipole correction is used to decouple electrostatic potentials on the two sides of the two-dimensional structure. Geometry optimization is performed until the maximum force on each atom drops below 0.01 eV/Å.

Chapter 3

Stabilization effects on N-doped graphene

This chapter is based on Paper 1 (included in Appendix B.1), and contains additional information about *O solvation effects on materials beyond N-doped graphene. The Reader does not have to refer to the paper as all the relevant information is included in the thesis.

3.1 Introduction

3.1.1 Background

The class of metal-free ORR catalysts is dominated by conductive carbon nanostructures, modified by various types of doping, especially nitrogen doping [5, 29]. In recent years, N-doped carbon nanotubes and graphene have been extensively studied both experimentally and computationally. Theoretical approaches investigated, among other things, effects such as the type of nitrogen doping (graphitic, pyridinic, pyrrolic) [83], morphology and concentration of N-dopants [84], structural defects [40, 85], curvature [85], solvation of *O₂ [86] and other ORR intermediates [69] by water, and the influence of additional nitrogen dopants on the *O₂ [86] and *O [65] stability.

In this chapter, the latter two effects are revisited and reassessed. Unoccupied nitrogen dopant in the cell, referred to as “free nitrogen”, is a nitrogen atom, where neighboring carbon atoms remain being empty adsorption sites. Such nitrogen is particularly interesting due to its selective stabilization of *O over *OH and *OOH [65]. Similarly, the presence of water was found to stabilize *O₂ adsorbate by 0.83 eV, twice as much as *OH [69]. Here, the influence of these two effects on all ORR intermediates is systematically studied as a function of nitrogen concentrations, the number of nitrogen atoms per adsorbate, and the number of water molecules per adsorbate. Bader charge analysis [87] and projected density of states (PDOS) calculations are performed to gain insight into the underlying phenomena and explain why different ORR intermediates respond differently to both effects. A case study of the oxygen reduction process on a selected catalytic system shows how these findings apply to the ORR modeling.

3.1.2 N-doped graphene model

All considered N-doped graphene (NG) models consist of graphitic nitrogen atoms uniformly dispersed in the graphene sheet. When a nitrogen atom is introduced into the system preserving its unit cell, it is placed in a position that maximizes the distance between nitrogen atoms. In that case, uniformity of N distribution cannot be strictly preserved. However, all the studied properties of the system are found to be insensitive to such deviations from uniformity. Non-uniform dopant distribution, such as nitrogen clustering, introduces another degree of freedom and is not studied in this work.

The considered NG model systems are referred to in the following format:

$$\text{NG}_{x_y}\text{N}/\text{ads}/z\text{H}_2\text{O},$$

where: x = nitrogen concentration (atomic ratio), y = N/*ads ratio, ads = considered adsorbate (O, OH, OOH or O₂ for a specific adsorbate, or “ads” for general considerations), z = H₂O/*ads ratio. For example, NG_{4.2%_2}N/O/11H₂O denotes graphene with 4.2% of nitrogen dopant, atomic oxygen adsorbate, N/*O ratio of 2 and H₂O/*O ratio of 11. This structure is shown in Fig. 3.1.

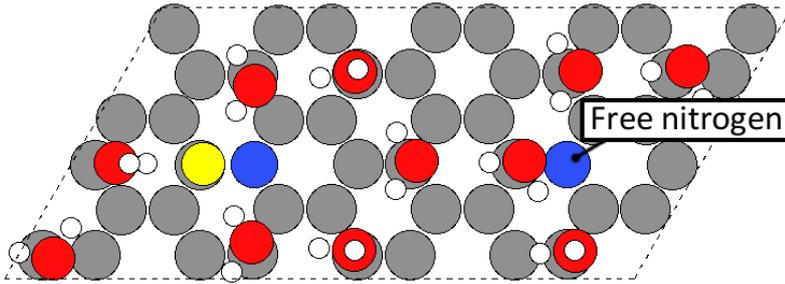


Figure 3.1: N-doped graphene structure example, denoted as NG_{4.2%_2}N/O/11H₂O. Color code for atoms: H – white, C – gray, N – blue, O – red. Oxygen adsorbate is highlighted in yellow.

3.1.3 Stabilization energy definitions

Adsorption energies are defined as the DFT energies of the reactions in Eq. (1.7), denoted as $\Delta_{\text{ads}}E(X)$, where $X = \{\text{OOH}, \text{O}, \text{OH}, \text{O}_2\}$. Superscripts are added when considering adsorption energies in the presence of free nitrogen [$\Delta_{\text{ads}}^{\text{N}}E(X)$], water [$\Delta_{\text{ads}}^{\text{W}}E(X)$] or both [$\Delta_{\text{ads}}^{\text{N+W}}E(X)$].

Stabilization by free nitrogen is the difference between the adsorption energy in 1 N/*ads system (no free nitrogen, *e.g.*, as in Fig. 3.2a, d) and >1 N/*ads systems (at least one free nitrogen, *e.g.*, as in Fig. 3.2b, c, e, f):

$$\Delta_{\text{stab}}^{\text{N}}E(X) = \Delta_{\text{ads}}E(X) - \Delta_{\text{ads}}^{\text{N}}E(X) \quad (3.1)$$

The energy of stabilization *via* solvation is the difference between ORR adsorption energies in vacuum and water and equals the negative solvation energy (for details, see Section 2.3.1):

$$\Delta_{\text{stab}}^{\text{W}}E(X) = -\Delta_{\text{solv}}E(X) = \Delta_{\text{ads}}E(X) - \Delta_{\text{ads}}^{\text{W}}E(X) \quad (3.2)$$

3.2 Stabilization effects

3.2.1 Free nitrogen

It is well known that a nitrogen dopant embedded in a graphene structure creates a net positive charge on adjacent carbon atoms, making their bonds with ORR intermediates stronger, and by this facilitating the ORR [30]. More recently, it was found that free nitrogen atoms which are located far away from the active site stabilize certain ORR adsorbates as well [65].

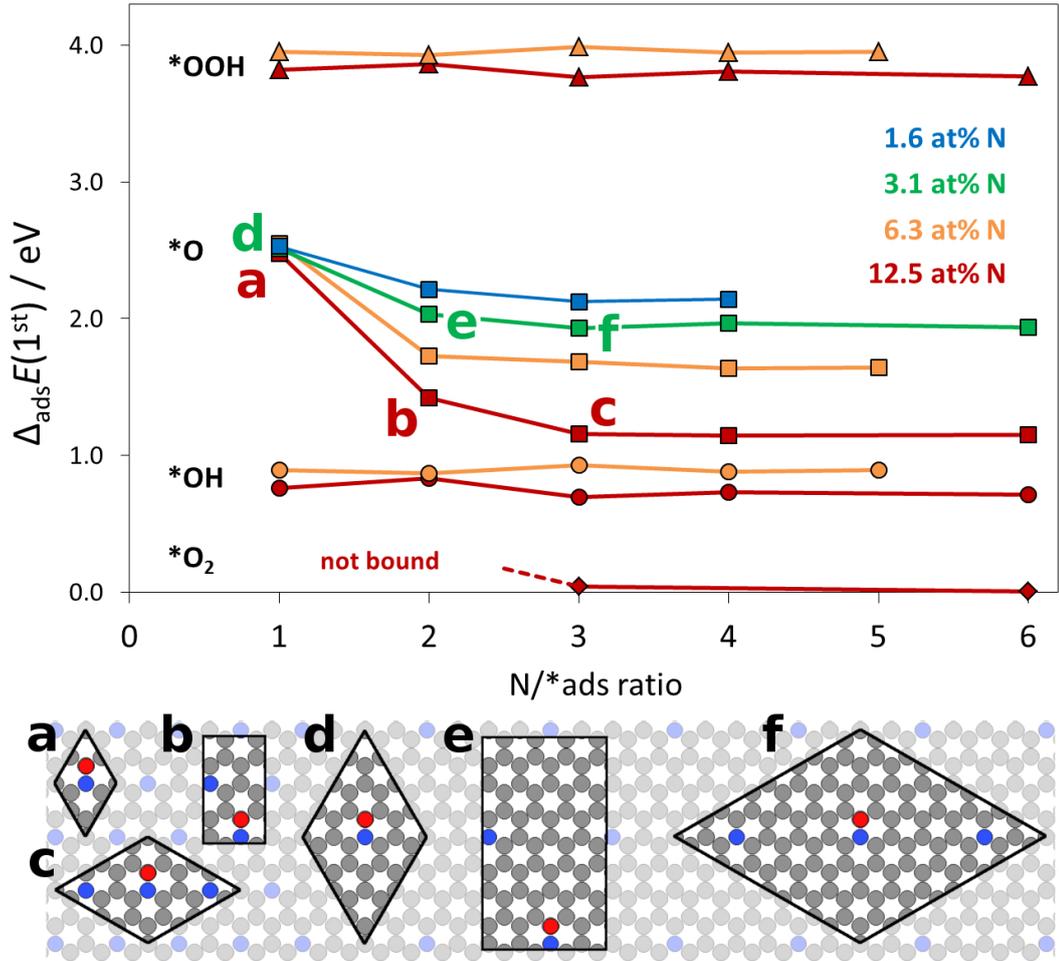


Figure 3.2: First adsorption energy, $\Delta_{\text{ads}}E(1^{\text{st}})$, vs. $N/*_{\text{ads}}$ ratio at different nitrogen concentrations; ads = {O, OH, OOH, O₂}. Sample unit cell structures are marked on the figure with letters (a)-(f). Color code for atoms is the same as in Fig. 3.1.

The effect of up to five free nitrogen atoms on the adsorption energy of ORR intermediates at different N concentrations is shown in Fig. 3.2. The OH and OOH adsorption energies are essentially independent of the $N/*_{\text{ads}}$ ratio; fluctuations of ± 0.05 eV are observed. By contrast, atomic oxygen is significantly stabilized by additional unoccupied nitrogen. This effect is most apparent when the first free nitrogen appears in the cell: oxygen binding

energy increases by up to 1.05 eV (for 12.5%N). Introduction of the second free nitrogen further stabilizes oxygen, especially at high nitrogen concentrations (0.26 eV stabilization of 3 N/*O relative to 2 N/*O at 12.5%N). A higher N/*O ratio than 3 has a marginal effect on the *O stability.

Stabilization by free N vanishes with decreasing nitrogen concentration. For systems with uniform N distribution, this is understandable. In these systems, nitrogen concentration is strictly related to N–N distance (d_{N-N}). In the limit of $d_{N-N} \rightarrow \infty$ (equivalent to 0%N), a local environment around the adsorption site is the same, irrespective of the N/*O ratio. Nonetheless, the influence of free nitrogen on oxygen binding proves to be a long-range effect. For instance, the stabilization of oxygen by two free nitrogen atoms at 1.6%N is around 0.4 eV, while the N–N distance is 14.8 Å. Moreover, a hyperbolic decay of $\Delta_{\text{stab}}^N E(O)$ with N–N distance is observed (Fig. 3.3). This brings to mind electrostatic (Coulomb) potential between point charges. A proposed explanation of this phenomenon is presented in Section 3.3.

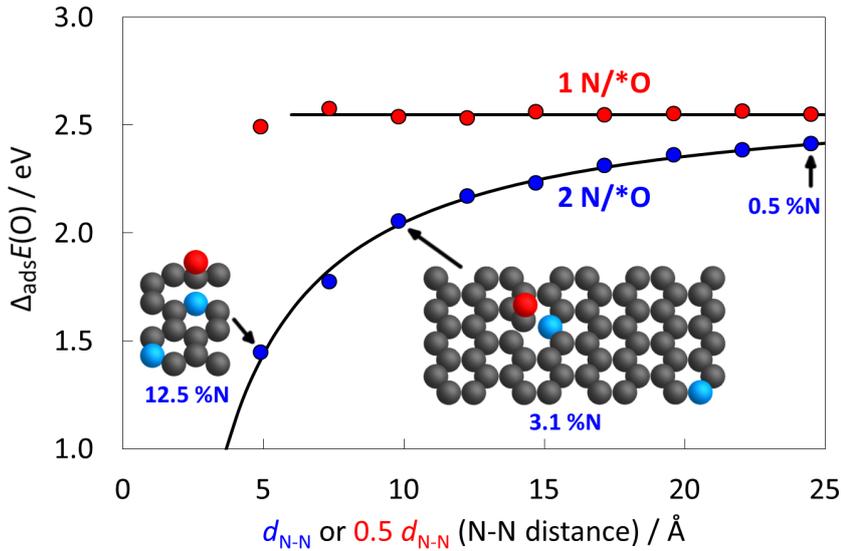


Figure 3.3: Oxygen adsorption energy as a function of N–N distance for systems with 1 N/*O (constant function) and 2 N/*O (hyperbola), showing the long-range character of the *O stabilization caused by a distant, free N. Color code for atoms: C – dark gray, N – blue, O – red.

The effect of stabilization by free nitrogen becomes even more significant for molecular oxygen, as the presence of at least two free nitrogen atoms ($N/*O_2 \geq 3$) appears to be a prerequisite for O_2 chemisorption at 12.5%N. Moreover, for the considered nitrogen concentrations, 12.5%N was the only one that ensured O_2 chemisorption, whereas lower concentrations did not. * O_2 is similar to *O in that its binding energy strongly depends on the presence of free nitrogen atoms in the cell.

3.2.2 Solvation

Binding energies of the ORR intermediates depend on the environment near the fuel cell cathode. This environment is characterized by such factors as the presence of water [9], pH of the electrolyte [67] and applied field [88]. Here the focus is on the solvation effect caused by the explicit water molecules.

The water effect is well-studied with Pt(111) as a catalyst [9, 68, 70] and is often assumed to be transferable to other classes of materials [65, 66]. There is some evidence, however, that $\Delta_{\text{stab}}^{\text{W}} E(\text{X})$ can vary a lot between different catalyst materials. For instance, water has a negligible effect on the stability of atomic oxygen found in fcc hollow sites on the Pt(111) surface [9], but oxygen adsorbed on top of a carbon atom in basal plane N-doped graphene is stabilized in an aqueous environment by about 0.5 eV [69].

Here, the influence of a single water layer on the ORR intermediates adsorption energies at different water-to-adsorbate ratios ($\text{H}_2\text{O}/^*\text{ads}$) is studied. Surface density of water in the employed model is 0.25 H_2O molecules per each atom in the N-graphene sheet, which corresponds to about 5% average expansive strain on the water layer relative to hexagonal ice. This model allows studying the solvation effect across many different N concentrations and $\text{H}_2\text{O}/^*\text{ads}$ ratios. Hexagonal water arrangements were found to be the most stable by the minima-hopping algorithm both for clean and adsorbate-covered N-graphene surfaces (sample structures are shown in Fig. 3.4). Unlike the case of the Pt(111) surface [89] and catalysts containing FeN_4 moieties [90], water molecules do not chemisorb on the active site of N-doped graphene. The average separation between the N-graphene sheet and water oxygen atoms is *ca.* 3.7 Å. The energy of a single water layer adhesion to graphene and N-graphene (6.25%N) is 79 and 82 meV per water molecule, respectively.

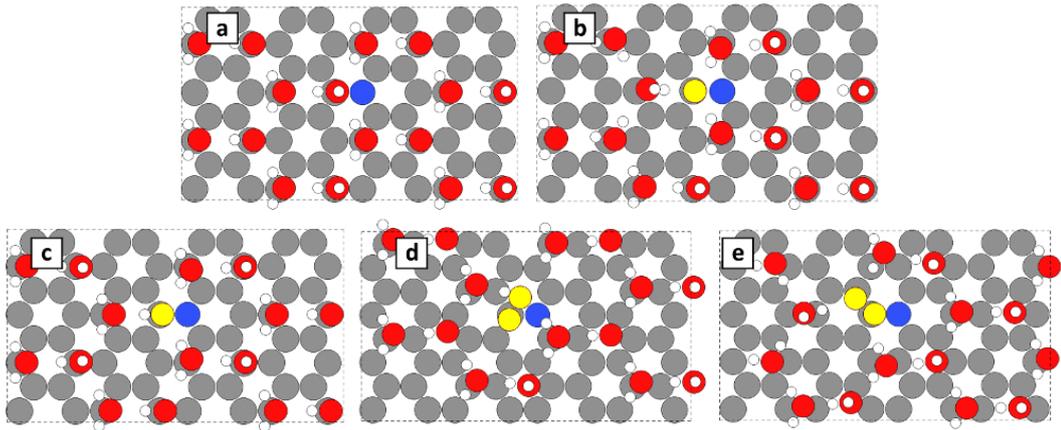


Figure 3.4: Top views of the optimized structures of pristine N-graphene and ORR intermediates with single water layer. N-graphene models are: (a) pristine N-doped graphene with 1.6%N, and NG_1.6%_1N/X/15H₂O with X being: (b) O, (c) OH, (d) OOH and (e) O₂. Color code for atoms is the same as in Fig. 3.1. Oxygen atoms belonging to the adsorbates are highlighted in yellow.

3. STABILIZATION EFFECTS ON N-DOPED GRAPHENE

For both $^*\text{OH}$ and $^*\text{OOH}$ intermediates, the solvation-based stabilization energy is $\Delta_{\text{stab}}^{\text{W}}E(\text{X}) = 0.19 \pm 0.02$ eV, irrespective of nitrogen concentration, $\text{H}_2\text{O}/^*\text{ads}$ ratio, and $\text{N}/^*\text{ads}$ ratio. The situation is different for $^*\text{O}$, where $\Delta_{\text{stab}}^{\text{W}}E(\text{O})$ depends on the $\text{H}_2\text{O}/^*\text{O}$ ratio. This is shown in Fig. 3.5, where both solvation and free nitrogen effects on $^*\text{O}$ adsorption energy are considered as a function of N concentration. For systems without free nitrogen, stabilization energy can be viewed as the difference between $1\text{N}/^*\text{O}$ and $1\text{N}/^*\text{O}+\text{H}_2\text{O}$ curves in Fig. 3.5. At low water-to-adsorbate ratios ($\text{H}_2\text{O}/^*\text{O} = 5$), the stabilization energy is 0.38 eV, and increases with increasing $\text{H}_2\text{O}/^*\text{O}$ until reaching a plateau (*ca.* 0.65 eV) at 11 $\text{H}_2\text{O}/^*\text{O}$. Increasing $\text{H}_2\text{O}/^*\text{O}$ further has practically no effect on the stabilization energy (*e.g.*, $\Delta_{\text{stab}}^{\text{W}}E(\text{O}) = 0.67$ eV at 31 $\text{H}_2\text{O}/^*\text{O}$). The plateau suggests that 2-3 coordination shells of water participate in $^*\text{O}$ stabilization. A similar analysis for systems with free nitrogen (the difference between $2\text{N}/^*\text{O}$ and $2\text{N}/^*\text{O}+\text{H}_2\text{O}$ curves in Fig. 3.5) leads to the same conclusion, though in this case stabilization energies are about 0.17 eV higher.

A similar trend is found for the $^*\text{O}_2$ adsorbate. The stabilization energy is 0.67 and 1.05 eV for systems with 5 $\text{H}_2\text{O}/^*\text{O}_2$ (NG_12.5%_3N/O₂/5H₂O) and 11 $\text{H}_2\text{O}/^*\text{O}_2$ (NG_12.5%_6N/O₂/11H₂O), respectively.

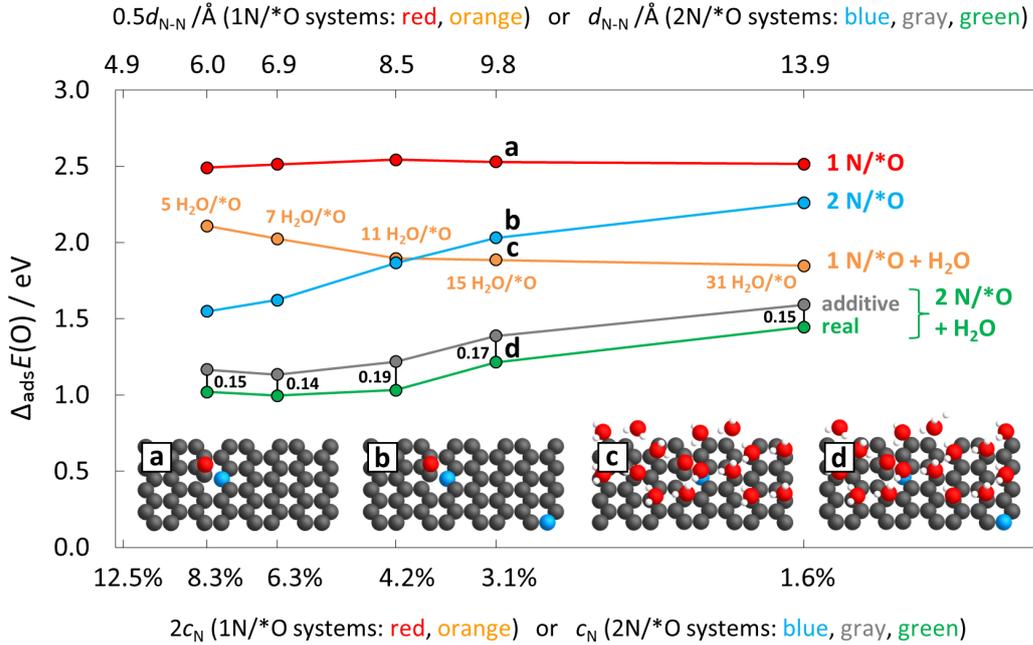


Figure 3.5: Atomic oxygen adsorption energy on N-doped graphene as a function of N–N distance (or N concentration) in the following scenarios: (i) in vacuum, $1\text{N}/^*\text{O}$ (red), (ii) in vacuum, $2\text{N}/^*\text{O}$ (blue), (iii) in water, $1\text{N}/^*\text{O}$ (orange), (iv) in water, $2\text{N}/^*\text{O}$ (green), (v) in water, $2\text{N}/^*\text{O}$, assuming additivity of the free N and H_2O stabilizing effects (gray). Sample structures for systems containing 64 atoms in N-graphene unit cell are shown as insets. Color code for atoms: H – white, C – dark gray, N – blue, O – red.

3.2.3 Synergy of the two effects

As mentioned above, the solvation effect becomes stronger in the presence of free nitrogen. Equivalently, free nitrogen effect becomes stronger in the presence of water, *i.e.*, the two effects synergistically stabilize *O. This can be expressed as

$$\Delta_{\text{stab}}^{\text{N+W}} E(\text{O}) = \Delta_{\text{stab}}^{\text{N}} E(\text{O}) + \Delta_{\text{stab}}^{\text{W}} E(\text{O}) + \Delta_{\text{stab}}^{\text{syn}} E(\text{O})$$

where the synergy component is $\Delta_{\text{stab}}^{\text{syn}} E(\text{O}) = 0.17 \pm 0.02$ eV (Fig. 3.5).

For high nitrogen concentration, the total stabilizing effect reaches a remarkably high value of 1.5 eV, and is approximately constant down to 4.2%N, due to the opposite changes of $\Delta_{\text{stab}}^{\text{N}} E(\text{O})$ and $\Delta_{\text{stab}}^{\text{W}} E(\text{O})$ with nitrogen concentration. Below 4.2%N, the solvation effect reaches its maximum and flattens, while the free nitrogen effect continues to vanish slowly. Even though the total stabilizing effect has to finally converge to the pure solvation effect at 0%N limit, the synergy component shows no clear evidence of fading over the considered nitrogen concentration range.

3.2.4 Solvation on different materials

Interestingly, the effect of strong *O solvation appears not to be limited to basal plane N-doped graphene. As long as the atomic oxygen is located in atop adsorption site on a 2nd row element, significant *O solvation is found on other types of materials (Fig. 3.6). Five cases are described below.

N-doped graphene with a Stone-Wales defect

An N-dopant can exist together with a Stone-Wales defect incorporated into the graphene structure. The utilized active site model (Fig. 3.6a) corresponds to the most catalytically active structure studied theoretically by Siahrostami *et al.* [40]. There are 18 H₂O molecules in the water layer, and 62 atoms in the defective N-graphene sheet, which means the water layer is slightly denser (0.29 H₂O per NG atom) than for the systems studied above. This results in a very small strain of about 0.35% (mixed expansive and compressive) on H₂O phase, relative to hexagonal ice layer. The calculated stabilization energy *via* solvation is 0.78 eV.

B-doped graphene

B-doped carbon materials have been considered as the ORR catalysts in the literature [91, 92]. While a boron dopant serves as the atop adsorption site for *OH and *OOH intermediates, the lowest energy configuration of *O is the bridge site between C and B [92]. This is confirmed in the present work — *O on B-doped graphene is located in the C–B bridge site both in systems with and without water layer. The energy of stabilization by water is in this case only 0.03 eV. However, if the oxygen is forced to bind on top of the boron atom, and the structure is optimized, the stabilization energy becomes 0.85 eV (Fig. 3.6b).

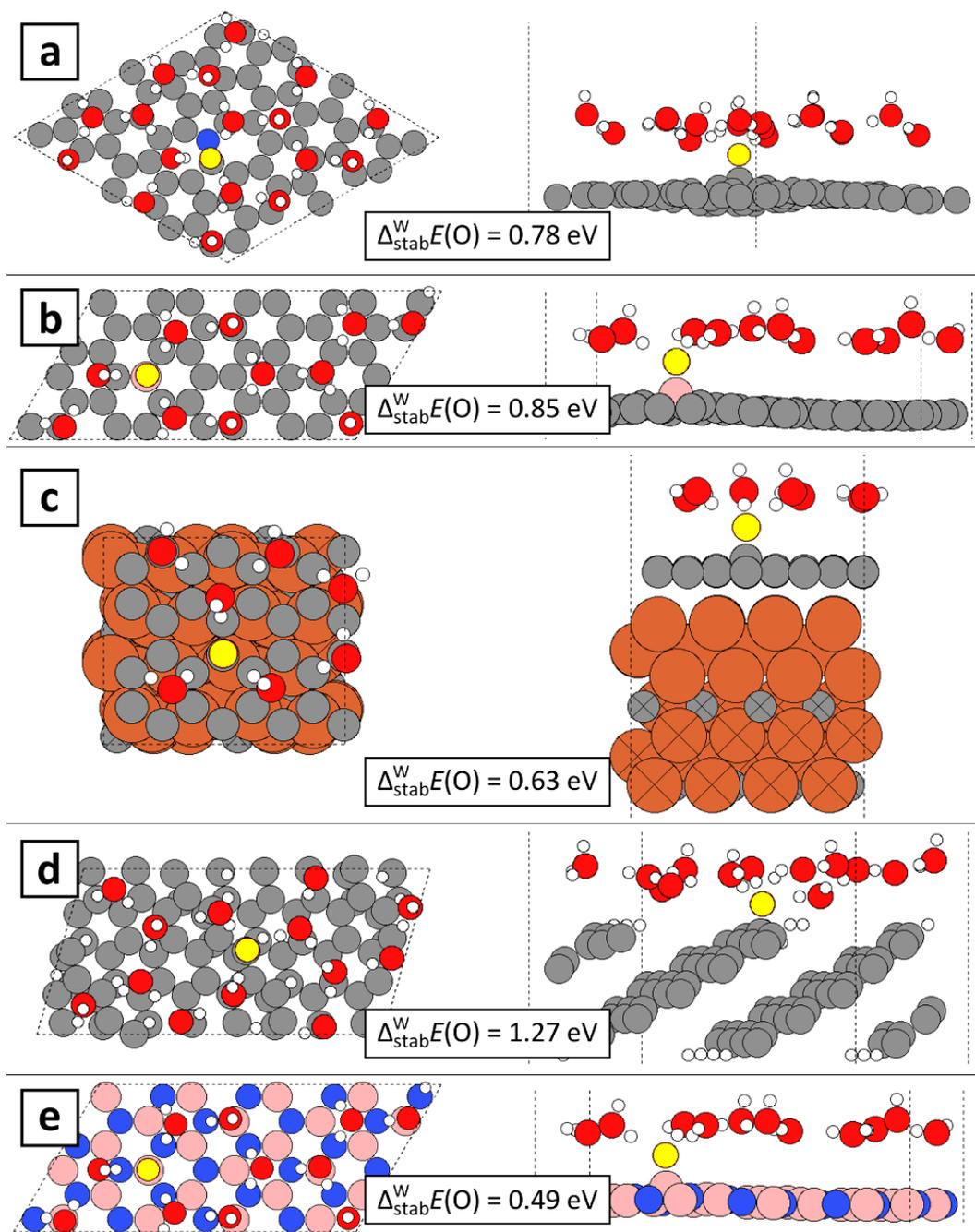


Figure 3.6: Structures exhibiting significant $*\text{O}$ solvation energies: (a) N-doped graphene with a Stone-Wales defect, (b) B-doped graphene, (c) Fe_3C -supported graphene, (d) hydrogen-terminated graphite step zigzag edges, (e) hexagonal boron nitride. Left column – top views, right column – side views. Water-induced stabilization energies are included in the figure. Color code for atoms: H – white, B – pink, C – gray, N – blue, O – red, Fe – orange. Oxygen adsorbates are highlighted in yellow. Crosses mark atoms fixed in bulk configuration during the structure optimization.

This clearly shows the difference in the role of water in the two situations. When *O is located in the bridge site, the oxygen is able to form two bonds with the surface; therefore no dangling bond is left, and surrounding water has almost no effect on the adsorbed oxygen. On the other hand, when *O is located on top of the boron atom, only a single bond between oxygen and the surface can be formed. A single, unpaired electron on the oxygen atom makes the system highly unstable, and the reaction with surrounding water increases its stability.

Fe₃C-supported graphene

*O stabilization by water on Fe₃C-supported graphene (0.63 eV, Fig. 3.6c) is similar to that on N-doped graphene. The Fe₃C/G model is described in details in Chapter 4.

Hydrogen-terminated graphite zigzag edges

Especially strong *O stabilization of almost 1.3 eV is found on hydrogen-terminated graphite zigzag step edges (Fig. 3.6d). It shows that the effect is not limited to the basal plane of graphene-based materials. This is particularly important in light of a recent finding that the edge-hosted pyridinic-N dopant is most likely responsible for the N-doped carbon materials activity towards ORR [39].

Hexagonal boron nitride (h-BN)

Supported hexagonal boron nitride has been suggested as a promising ORR catalyst in a theoretical study by Koitz *et al.* [66]. On an unsupported and non-solvated h-BN surface, the *O intermediate binds to the B–N bridge site. With metallic support, however, an adsorption site on top of the boron atom is preferred [66]. Oxygen stabilization in that site on unsupported h-BN is estimated by forcing *O to stay on top of the boron atom. The effect is smaller than for the other studied materials, but still significant (0.49 eV, Fig. 3.6e).

3.3 Discussion: O(sp) band filling

In this section, an insight into the origin of a strong *O and *O₂ stabilization by free nitrogen and solvation effects is provided. Fig. 3.7, showing the density of states projected onto adsorbed oxygen sp states for *O systems, forms the basis for the discussion. It illustrates that free nitrogen (transition from Fig. 3.7a to 3.7b) and water (Fig. 3.7a → 3.7c) cause the O(sp) band filling. When both effects cooperate, virtually all the O(sp) states are located below the Fermi level.

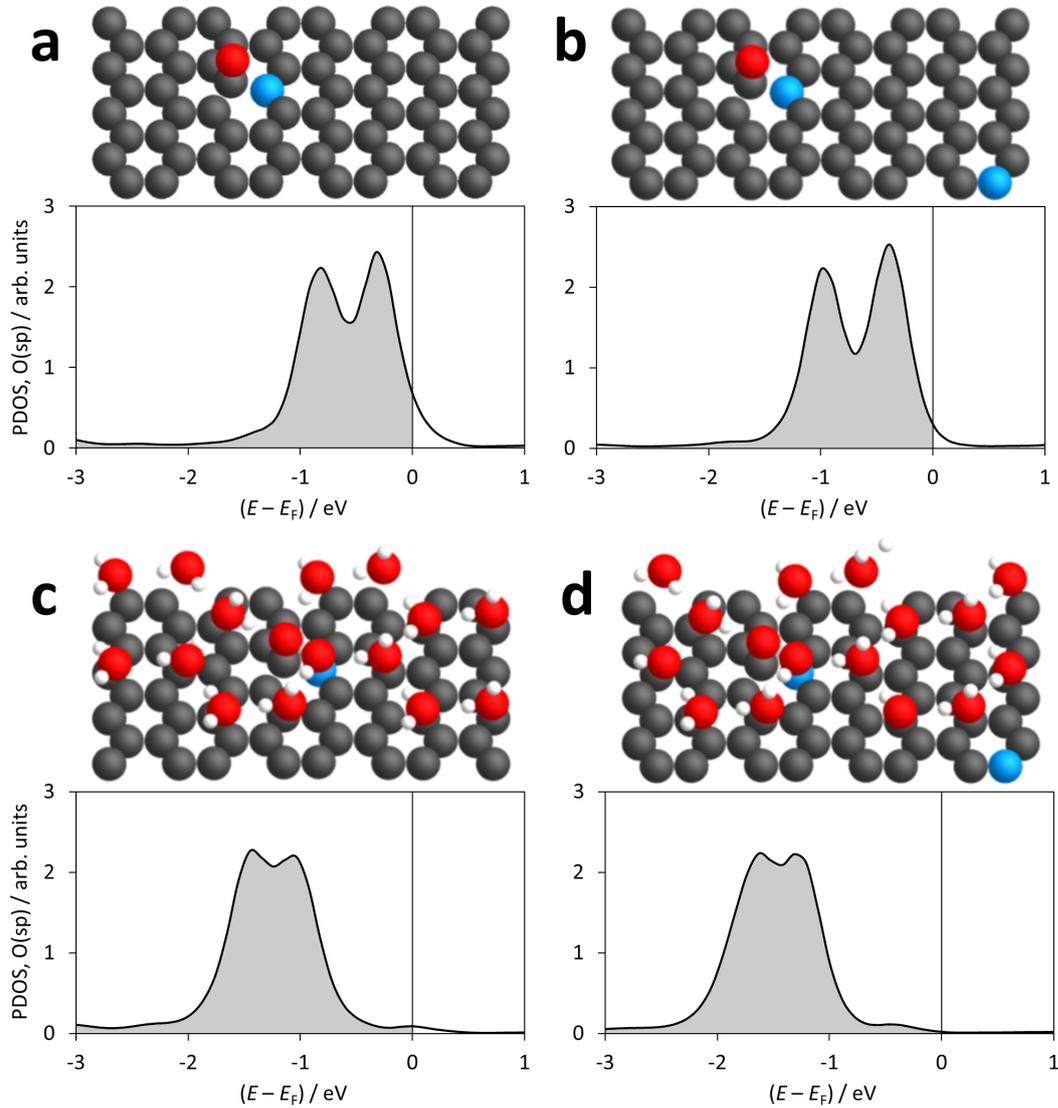


Figure 3.7: Adsorbed oxygen projected density of states for: (a) NG_1.6%_1N/O, (b) NG_3.1%_2N/O, (c) NG_1.6%_1N/O/15H₂O, (d) NG_3.1%_2N/O/15H₂O. The corresponding structures are included above the plots. Color code for atoms is the same as in Fig. 3.5.

3.3.1 Stabilization due to free nitrogen

Free nitrogen selectively stabilizes *O and *O_2 . Both adsorbates have one dangling bond, since carbon, which is already bound to three other atoms, can provide only a single bond to oxygen. It manifests itself as unfilled O(sp) states (Fig. 3.7a), which make *O and *O_2 quite reactive and unstable. The presence of free nitrogen in the system significantly stabilizes both adsorbates. In what follows, this effect is studied on the example of the *O adsorbate.

Fig. 3.8 shows the Bader charge on oxygen and nitrogen for *O systems with and without free nitrogen, as well as the Bader charge on nitrogen in a pristine N-graphene sheet. Free nitrogen (Fig. 3.8b) causes the electron density on oxygen to increase by $0.06 e^-$, compared to the system without free nitrogen (Fig. 3.8a). One possible reason for this increase could be electron density transfer from the introduced free nitrogen to oxygen *via* an inductive or mesomeric effect. In that case, we should see electron density depletion on free nitrogen. However, Fig. 3.8c shows that this does not occur, and the Bader charge on nitrogen in the absence of any adsorbate is the same as the charge on free nitrogen in the presence of *O . Another explanation is therefore proposed, *i.e.*, that free nitrogen disrupts graphene's stable aromatic structure, which allows the more electronegative oxygen atom to withdraw more electron density from the graphene carbon atoms.

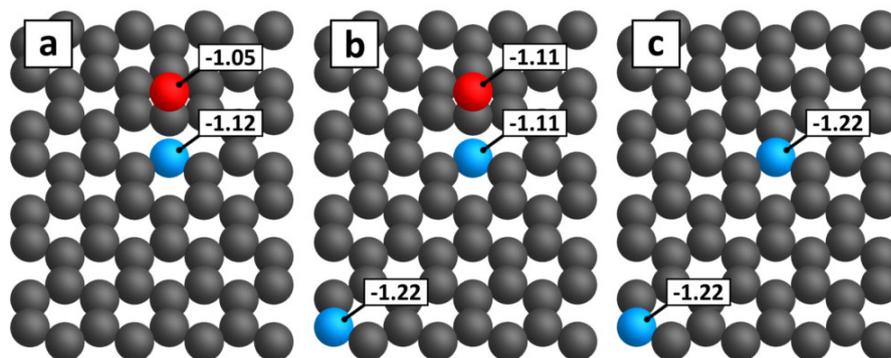


Figure 3.8: Bader charge on atoms in: (a) NG_1.6_1N/O, (b) NG_3.1_2N/O and (c) NG_3.1. Color code for atoms is the same as in Fig. 3.5.

The additional electron density on oxygen continues to fill non-fully occupied sp band (Fig. 3.7b). The system becomes more strongly polarized: oxygen gains a negative charge, and graphene carbon atoms become positively charged. This shows that, as graphene loses electrons in favor of oxygen, the system becomes partly ionic, while at the same time retaining covalent bonds between respective parts, as in the case of zwitterions. Variations in the Coulomb interaction between these ionic parts are suggested to be partly responsible for the variations in the stability of oxygen on the surface.

A correlation is found between the average Bader charge on oxygen and average oxygen binding energy for a set of NG_6.25% systems with varying N/ *O ratio (Fig. 3.9). In this case, the charge on oxygen is a measure of charge separation (varied by N/ *O ratio), while constant nitrogen concentra-

tion assures approximately constant distance between centers of positive and negative charges. The figure shows that the larger the charge donation into the O(sp) states, the more stable the system. It has to be also noted that above 2-3 N/*O ratio oxygen can no longer withdraw more electrons from the N-graphene sheet, and its adsorption energy stabilizes with respect to the number of free nitrogen atoms, as shown previously in Fig. 3.2.

It is worth noting that even though *O binding energy correlates with Bader charge on oxygen at a constant nitrogen concentration, these two properties do not correlate in general. For example, the Bader charge on oxygen is approximately constant (-1.10 ± 0.01) for the systems forming the 2 N/*O curve in Fig. 3.5, where the nitrogen concentration changes. In light of the proposed explanation, the observed decrease of the oxygen binding with decreasing nitrogen concentration is caused by the increase of the distance between fixed-charge ions. This dependence studied over a broader range of nitrogen concentrations reveals its hyperbolic character (Fig. 3.3), which is expected for electrostatically interacting systems.

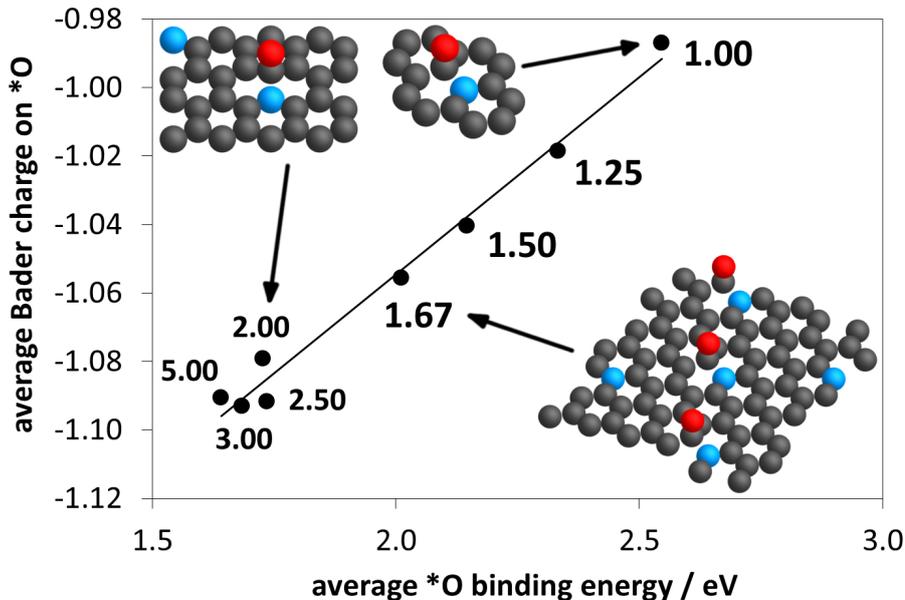


Figure 3.9: Average $\Delta_{\text{ads}}E(\text{O})$ vs. average Bader charge on *O at different N/*O ratios for a set of NG_6.25% systems. Color code for atoms is the same as in Fig. 3.5.

3.3.2 Stabilization due to water

Water stabilizes all the ORR intermediates (Fig. 3.10). However, its influence on *O and *O₂ is clearly stronger than on *OH and *OOH. As noted earlier, the difference between these two groups of adsorbates lies in the occupation of O(sp) states. *O and *O₂ have empty states, and their reactivity is thus much higher than that of *OH or *OOH.

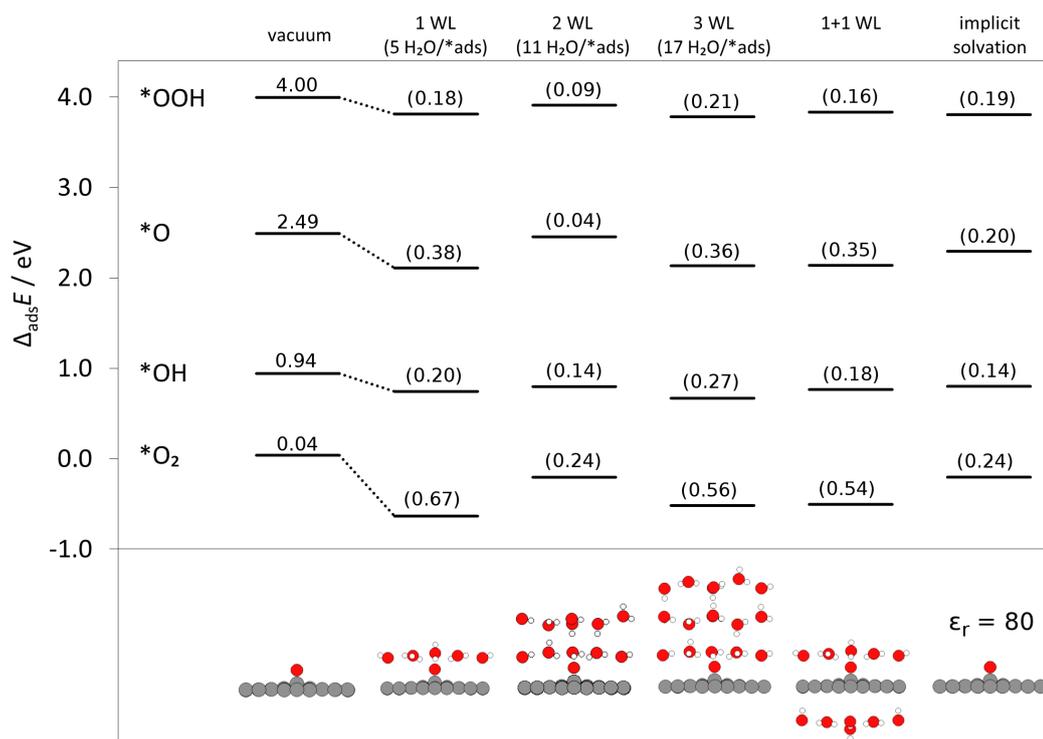


Figure 3.10: ORR intermediate adsorption energies for different solvation models: 1 to 3 water layers (WL), one water layer on each side, and continuum solvation model. Adsorption energies or stabilization ($\Delta_{\text{stab}}^{\text{W}} E(X)$, in parentheses) are included in eV above each $\Delta_{\text{ads}} E$ level. N-graphene models are: NG_12.5%_3N/ads for O₂ and NG_4.2%_1N/ads for *O, *OH, and *OOH. Side-view structures of *O systems are included below the plot. Color code for atoms: H – white, C – gray, O – red.

The strong stabilizing effect of water on atomic and molecular oxygen can be explained by bond formation between water molecules and adsorbed species. In this process, water fills oxygen empty states, as can be seen from the location of O(sp) band relative to Fermi level in vacuum (Fig. 3.7a and 3.7b) and in water (Fig. 3.7c and 3.7d). Bonds formed between *O and H₂O are about 0.18 Å shorter (average of three bonds) than hydrogen bonds between water and *OH, suggesting they are much stronger than regular hydrogen bonds.

Describing water as a continuum polarizable medium ($\epsilon_r = 80$) results in unsatisfactory *O and *O₂ stabilization energies. For the system with low H₂O/*ads ratio considered in Fig. 3.10, implicit solvation underestimates $\Delta_{\text{stab}}^{\text{W}} E(\text{O})$ and $\Delta_{\text{stab}}^{\text{W}} E(\text{O}_2)$ by 0.18 and 0.43 eV, respectively, relative to solvation by a single water layer. The situation becomes even worse for systems with a higher H₂O/*ads ratio. For example, *O solvation is underestimated by 0.40 eV in NG_4.2%_2N/O/11H₂O system. At the same time, implicit water reproduces *OH and *OOH solvation with deviations smaller than 0.1 eV. Continuum solvation models can capture polarization effects in the system, but since they neglect granular structure of the solvent, they cannot describe some solvent-adsorbate interactions, *e.g.* those resulting from the orbital overlap.

Inadequate description of the stabilization effect with the implicit solvation model confirms that the effect likely results from the water-oxygen bond formation. It also means that the implicit solvation is not particularly suitable for the ORR modeling on N-doped graphene.

3.4 Increasing dimensionality

The computational approach to catalyst modeling often requires reduction of the real system size or dimensionality due to limited computational resources. This approach usually leads to meaningful results due to the locality of adsorption phenomena [18], although it may be a source of error. Here, inaccuracy of the description of real 3-dimensional (N-graphene or N-graphite)/water interface by a 2-dimensional model is estimated. This is done by applying three different modifications, one at a time, to the base system, which is a single N-graphene + single water layer. The modifications are: (i) increasing the number of water layers (up to three) on the adsorbate side, (ii) including up to three N-graphene layers and (iii) including a water layer on the other side of the N-graphene sheet.

3.4.1 Additional water layers on the adsorbate side

ORR intermediate adsorption and solvation energies for different models of solvation are summarized in Fig. 3.10. Adding a second water layer on the adsorbate side destabilizes all the ORR adsorbates relative to the single water layer model. This is likely due to the high stability of the reference, where water molecules adopt a special configuration with twice as many interlayer hydrogen bonds as in hexagonal ice, as shown in Fig. 3.11a. The configuration is preserved to a large extent in systems with *OH and *OOH adsorbates (Fig. 3.11c and d), but differs significantly in *O and *O₂ systems (Fig. 3.11b and e), resulting in poor stabilization of the last two adsorbates. This special configuration of two water layers has been observed experimentally on graphene in ultrahigh vacuum [93] but is not expected to appear in experimental ORR setups, where the catalyst is immersed in a bulk electrolyte.

With three water layers, ORR adsorbate stability is similar to that with a single water layer within 0.11 eV. Although such differences may sometimes be non-negligible for ORR modeling, it can still be concluded that the first water layer has a decisive influence on the adsorbate solvation effects. A single water layer seems to be a reasonable compromise between accuracy and computational cost.

As discussed previously, in the single water layer model the H₂O/*O ratio influences *O solvation energy (Fig. 3.5). For example, increasing the H₂O/*O ratio from 5 to 15 increases $\Delta_{\text{stab}}^{\text{W}} E(\text{O})$ from 0.38 to 0.64 eV. A similar increase of the H₂O/*O ratio can be achieved by increasing the number of water layers from one (5 H₂O/*O) to three (17 H₂O/*O). Interestingly, $\Delta_{\text{stab}}^{\text{W}} E(\text{O})$ remains essentially constant in this process (0.38 and 0.36 eV, respectively). This

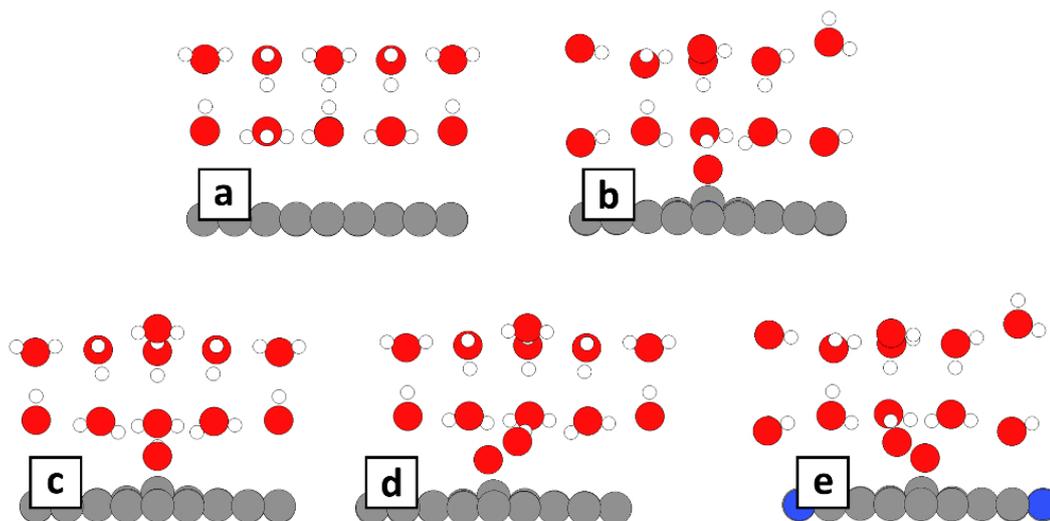


Figure 3.11: Side views of N-graphene structures with double water layer: pristine (a), and with the ORR intermediates: (b) $\ast\text{O}$, (c) $\ast\text{OH}$, (d) $\ast\text{OOH}$, (e) $\ast\text{O}_2$. N-graphene models are NG_4.2%_1N/ads for (a)–(d), and NG_12.5%_3N/O₂ for (e). Color code for atoms is the same as in Fig. 3.1.

suggests that from the practical point of view the effect of $\text{H}_2\text{O}/\ast\text{O}$ ratio on solvation energy is limited to the first water layer.

3.4.2 Adding more N-graphene layers

Energetically, the most favorable stacking of multiple N-graphene layers containing 4.2%N is AA stacking with nitrogen atoms located one above another. For this case, the BEEF-vdW functional predicts similar (within 0.05 Å) inter-layer distance as for graphite in the AB stacking. The adsorption and solvation energies for systems with single and multiple layers of N-graphene are summarized in Fig. 3.12. All solvation energies, as well as OH and OOH adsorption energies, are not affected by the presence of additional N-graphene layers. However, atomic and molecular oxygen adsorption energies exhibit non-monotonic variations with increasing number of N-graphene layers. Atomic oxygen binding becomes stronger by 0.08 and 0.06 eV, while molecular oxygen binding becomes weaker by 0.20 and 0.10 eV, for 2 and 3 graphene layers, respectively.

3.4.3 Water layer on both sides of N-graphene

Including a water layer on both sides of the N-graphene sheet marginally changes the $\ast\text{O}$, $\ast\text{OH}$ and $\ast\text{OOH}$ adsorption energy relative to having single water layer on the adsorbate side only (Fig. 3.10). The only affected ORR intermediate is O_2 , which binding energy weakens by about 0.13 eV. Though not dramatic, this effect should be remembered while modeling oxygen reduction reaction, as it is unlikely to have vacuum on one side of 2D catalyst in experimental conditions.

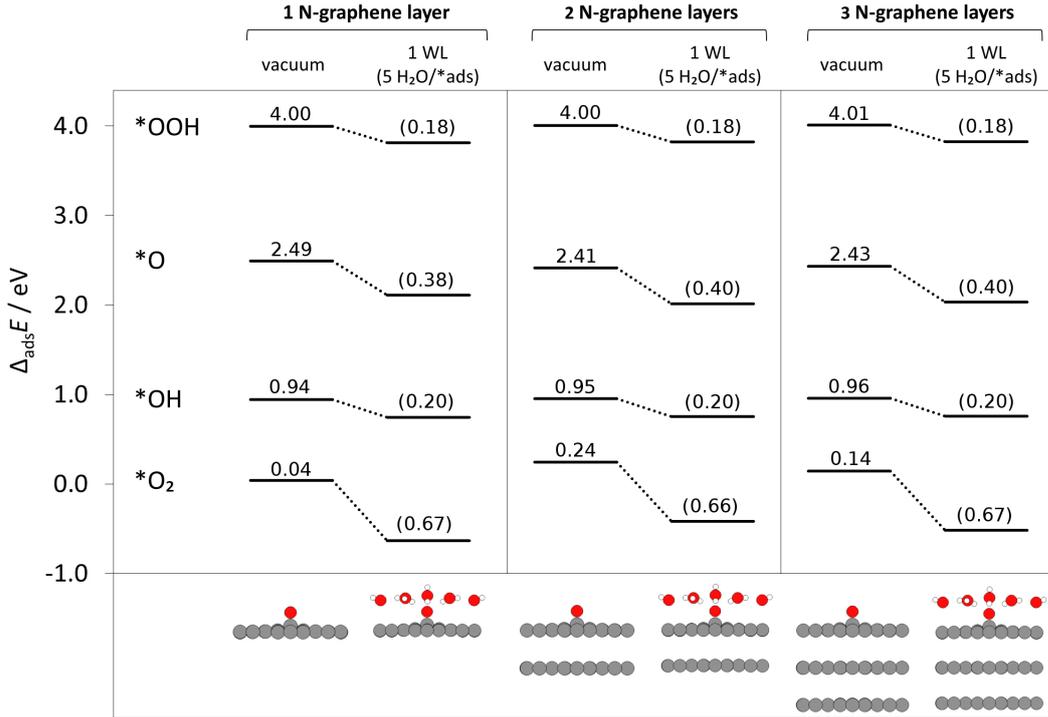


Figure 3.12: ORR intermediate adsorption energies for different numbers of N-graphene layers (1 to 3) in vacuum and with a single water layer. Adsorption energies and stabilization ($\Delta_{\text{stab}}^{\text{W}} E(X)$, in parentheses) are included in eV above each $\Delta_{\text{ads}} E$ level. N-graphene models are: NG_12.5%_3N/O₂ for *O₂ and NG_4.2%_1N/ads for *O, *OH and *OOH. Side-view structures of *O systems are included below the plot. Color code for atoms is the same as in Fig. 3.1.

3.5 Case study: ORR on N-graphene (6.25%N) with explicit water

To demonstrate how the above findings affect predicted ORR activity, the associative ORR pathway is modeled on N-doped graphene at 6.25%N. *O₂ intermediate is neglected, as there is strong evidence suggesting that the molecular oxygen adsorption is not necessarily required for the ORR to proceed on N-doped graphene [94].

First, a simple N-graphene model with one nitrogen and 15 carbon atoms in the unit cell is considered. A single water layer consists of 4 water molecules. The system's structure and free energy diagram at 0.8 V vs. RHE are shown in Fig. 3.13a. This system represents the simplest N-graphene/water interface model that could be used for ORR modeling at this nitrogen concentration. The predicted thermodynamic overpotential is 0.78 V. However, this model is relevant for ORR modeling only under the assumption that adsorbate binding energies do not depend on coverage (θ_{ads}). While this is true for *OH and *OOH adsorbates, at low *O coverage (or, equivalently, high N/*O ratio) atomic oxygen binds at least 0.8 eV stronger than at $\theta_{\text{ads}} = 1$ (Fig. 3.2). This will cause some nitrogen atoms in adjacent cells to remain unoccupied in order

for the *O system to achieve a lower energy structure.

In the second step, a $(\sqrt{2} \times \sqrt{2})$ version of the previous cell is considered. Now all the ORR steps are occurring in the presence of free nitrogen ($\theta_{\text{ads}} = 1/2$). The structure and the free energy diagram for this system are shown in Fig. 3.13b. This time *O binds so strong that its protonation becomes the potential-determining step. The resulting thermodynamic overpotential is 1.14 V.

Further increase of the N/*ads ratio results in even more stable *O, with practically no change of the *OH and *OOH levels (see Fig. 3.2). It suggests that some amount of *O will be present on the catalyst surface throughout the entire oxygen reduction process in the form of *O spectators. *O stability starts to decrease for $N/*O < 2$ as shown in Fig. 3.9. Entering that range would increase *O free energy in Fig. 3.13b, such that *O protonation may no longer be the potential-determining step. In other words, increasing *O coverage above 1/2 allows the catalyst to explore free energy paths with lower overall thermodynamic barriers. It is therefore suggested that at 6.25%N the oxygen reduction reaction occurs on basal plane N-doped graphene at *O coverages not lower than 1/2.

On the other hand, the coverage cannot be too close to 1. For example, introducing an *O spectator in the $(\sqrt{2} \times \sqrt{2})$ cell leaves only one catalytic site where the oxygen reduction reaction can take place, resulting in $\theta_{\text{ads}} = 1$. Adsorption of any ORR intermediate in such a position is highly unfavorable, as it significantly destabilizes spectator *O, which can no longer take advantage of the free nitrogen effect (which is about 0.8 eV at 6.25%N, see Fig. 3.2). As a consequence, to minimize the barriers along the ORR free energy diagram, the system seeks to adopt a configuration in which both the *O and free nitrogen are simultaneously present in the catalytic environment.

Summarizing, the optimal adsorbate coverage is in the range of $1/2 < \theta_{\text{ads}} < 1$. The simplest realization of this scenario is an N-graphene cell containing three nitrogen atoms. A carbon near the first of the N atoms is permanently bound with atomic oxygen, the second N atom is free throughout the process, and a carbon near the third N serves as an adsorption site for the ORR intermediates. The reaction occurs at $\theta_{\text{ads}} = 2/3$. The free energy diagram and the catalyst structure with *OH adsorbate is shown in Fig. 3.13c. The thermodynamic overpotential is found to be 0.94 V, with the potential-determining step being the *OOH formation on the surface.

It has to be noted that the predicted thermodynamic overpotential refers to the specific model studied here. In real systems, the distribution of nitrogen does not have to be regular, and nitrogen clustering may occur. It is likely that there exist different adsorbate coverages and different (*O spectator + free nitrogen + catalytic site) configurations, which result in a lower thermodynamic barrier for the ORR, and thus dominate the basal plane N-doped graphene activity towards the oxygen reduction.

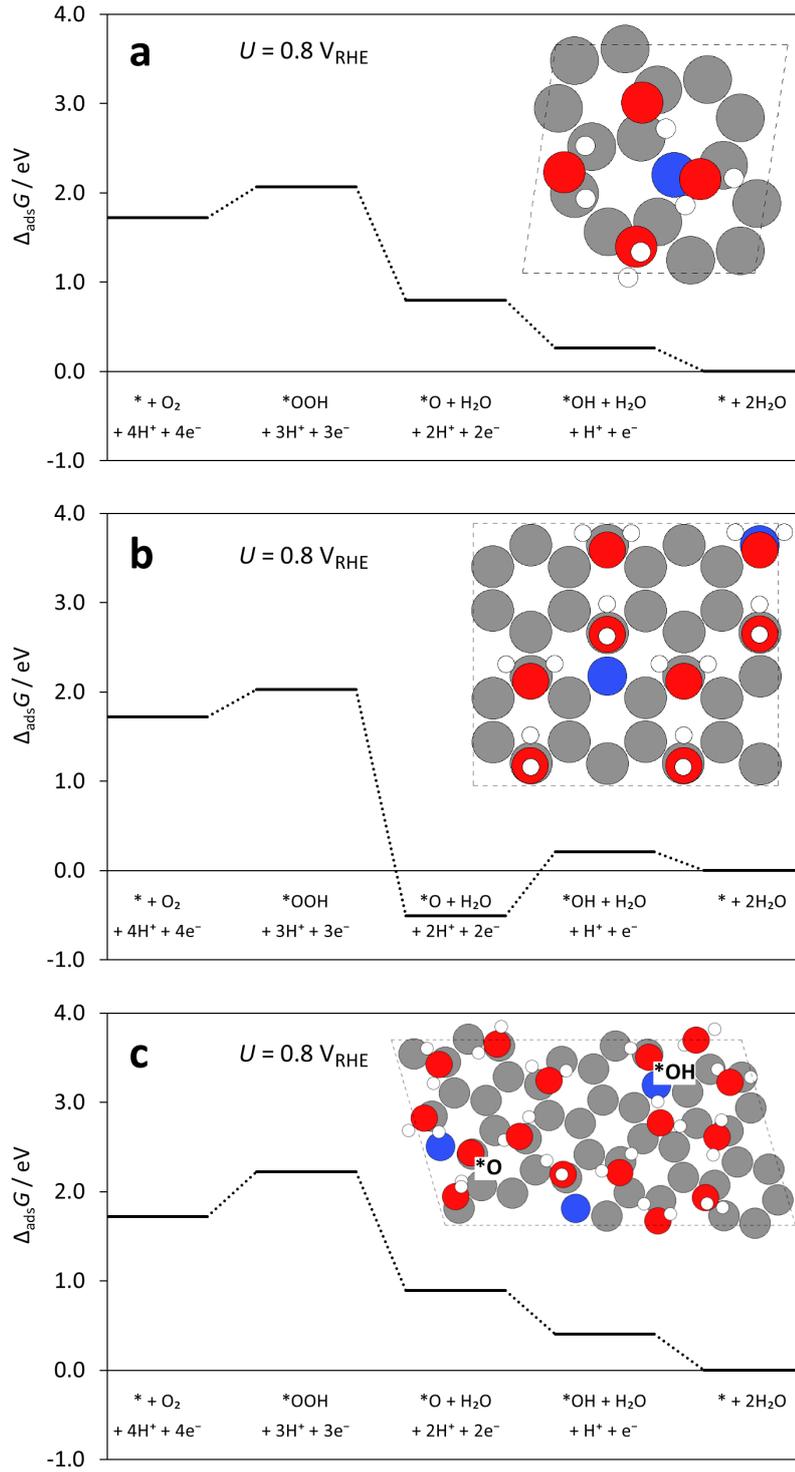


Figure 3.13: Oxygen reduction reaction free energy diagrams at $U = 0.8 V_{RHE}$ for N-graphene (6.25%N): (a) one N atom in the unit cell; ORR occurs at $\theta_{ads} = 1$; inset shows the structure of a pristine catalyst, (b) two N atoms in the unit cell; ORR occurs at $\theta_{ads} = 1/2$; inset shows the structure of a pristine catalyst, (c) three N atoms in the unit cell; one adsorbed atomic oxygen and one free nitrogen act as spectators; ORR occurs at $\theta_{ads} = 2/3$; inset shows the structure of $*OH$ in the catalytic environment defined by the spectators and a single water layer. Color code for atoms: H – white, C – gray, N – blue, O – red.

3.6 Conclusions

Two effects responsible for unusually high stabilization of the *O and *O_2 adsorbates on basal plane N-doped graphene (compared to conventional metal-based ORR catalysts) have been systematically studied. These are the effect of additional, free nitrogen in the N-graphene sheet and the solvation effect. The total stabilization energy from the two effects reaches values as high as 1.5 eV, including a 0.17 eV synergy component. Both effects are found to result from the high reactivity of *O and *O_2 adsorbates, caused by the presence of dangling bonds, which manifest themselves as unoccupied O(sp) states. Variations in the *O binding energy due to free nitrogen exhibit a long-range character, resembling electrostatic $1/r$ interactions between the charged parts of the system. The solvation effect is likely to be universal for materials where oxygen adsorbs on a 2nd row element in the atop position.

A case study of the oxygen reduction reaction at 6.25%N shows that the reaction occurs at an adsorbate surface coverage between $1/2 < \theta_{\text{ads}} < 1$, in the presence of *O and free nitrogen spectators.

Including explicit H_2O molecules is essential for the correct description of ORR intermediates adsorption energy on carbon materials. Continuum solvation models are unable to describe solvation of *O and *O_2 with sufficient accuracy, likely due to bond formation between these adsorbates and surrounding water molecules. The first water layer is found to have a decisive influence on the adsorbate solvation. Including a single water layer to account for solvation effects seems to be a reasonable compromise between accuracy and computational cost.

Chapter 4

Carbon-coated iron carbide and iron

This chapter is based on Paper 3, included in Appendix B.3. The chapter is self-contained, and the Reader does not have to refer to the paper.

4.1 Introduction

As noted in Section 1.3.3, metal-supported 2-dimensional materials are one of the most notable classes of non-precious ORR catalysts. Their activity can be tuned both by the choice of the 2D overlayer (*e.g.*, doped graphene, hexagonal boron nitride) and the support [5]. These interfaces have rarely been studied computationally, and studies are challenging due to certain computational difficulties, such as problems with the correct description of the support-overlayer interaction at a moderate computational cost [66, 95–98].

In this chapter, a computational model of Fe₃C@C catalyst (like the one synthesized by Hu *et al.* [46, 99–101]) is established, and its catalytic activity towards ORR is studied. Additionally, the activity of Fe/carbon interface is investigated, and the differences between catalytic and electronic properties of iron and iron carbide supports are used to propose a material, which is likely to outperform both Fe and Fe₃C.

4.2 Structures of the interfaces

Heterostructure interfaces are prepared using the Virtual NanoLab (VNL) software [102]. For all the systems containing iron, spin-polarized calculations are performed, as both iron and iron carbide are ferromagnetic.

4.2.1 Fe₃C/graphene

The iron carbide surface is modeled by use of the Fe₃C(010) facet. The choice was made as a compromise between the surface energy [103], the magnitude of the Fe₃C/graphene (Fe₃C/G) lattice mismatch and the system size, with the

aim to minimize all the three parameters. Fe₃C(010) facet surface energy is only about 13 meV/Å² (10%) higher than that of the most stable Fe₃C(001) facet. The unit cell contains 16 graphene carbon atoms placed horizontally on top of the iron carbide slab, such that the graphene basal plane is exposed to the liquid phase (Fig. 4.1a–c). The carbide phase is compressed (3.0%) to match the lattice of graphene. This is done to study the effect of support, without obscuring it by the effect of strained graphene. A similar approach was applied previously by Andersen *et al.* for graphene on different metal surfaces [96]. It has to be noted that the actual (experimental) strain in the system due to the interaction between the two phases is not known. The effect of uniaxial, biaxial and shear strain on the OH adsorption energy on graphene is illustrated in Fig. 4.2.

Considering the Fe₃C(010) plane, the atomic layer pattern repeats every 6 layers. This results in a number of possible cleavages with different surface properties. Starting from a carbon-rich Fe₃C surface, the stability of Fe₃C/graphene interface is analyzed as carbon atoms are removed from the Fe₃C surface to form a separate graphite phase (Fig. 4.1e). The process is described by the following reaction:



where x is the number of carbon atoms on the Fe₃C surface in the model unit cell. The lowest energy structure is found to contain no carbon atoms on the Fe₃C surface. Although removal of the third carbon atom requires energy input (12 meV/atom, which amounts to 0.3 meV/Å², or 5 mJ/m²), this barrier, as well as the actual carbon removal barrier, is expected to be surmountable in the pyrolytic synthesis conditions [46]. The system without non-graphitic carbon at the Fe₃C/graphene interface is therefore used to model this heterostructure.

Fe₃C slab consists of 7 atomic layers (6.8 Å), where the bottom 4 layers are fixed in the bulk configuration during the structure relaxation (Fig. 4.1a). The surface cell dimensions are (6.52, 0.00) × (0.93, 6.45) Å. This surface cell is used only to model the Fe₃C/(N-)graphene interface. The actual catalyst models, which are described in Section 4.3, consist of in-plane-extended versions of the cell described here. Graphene chemisorbs on Fe₃C with adhesion energy of 43 meV/(C atom), or 16.3 meV/Å² (260 mJ/m²), and the Fe₃C–graphene distance is found to be 2.3 Å. According to Bader charge analysis, each carbon atom in the graphene sheet withdraws 0.047 e[−] from the carbide phase on average. Increased availability of electrons in the graphene sheet is expected to increase the *O adsorbate stability, as it was shown in Chapter 3 in N-graphene systems with additional N dopant.

4.2.2 Fe/graphene

The iron surface is modeled by the lowest surface energy bcc-Fe(110) facet [104]. The slab consists of 3 atomic layers, where the two bottom layers are fixed in the bulk configuration during the structure relaxation (Fig. 4.1d). The surface cell vectors are (13.72, 0.00) × (−2.21, 6.13) Å, and each atomic layer

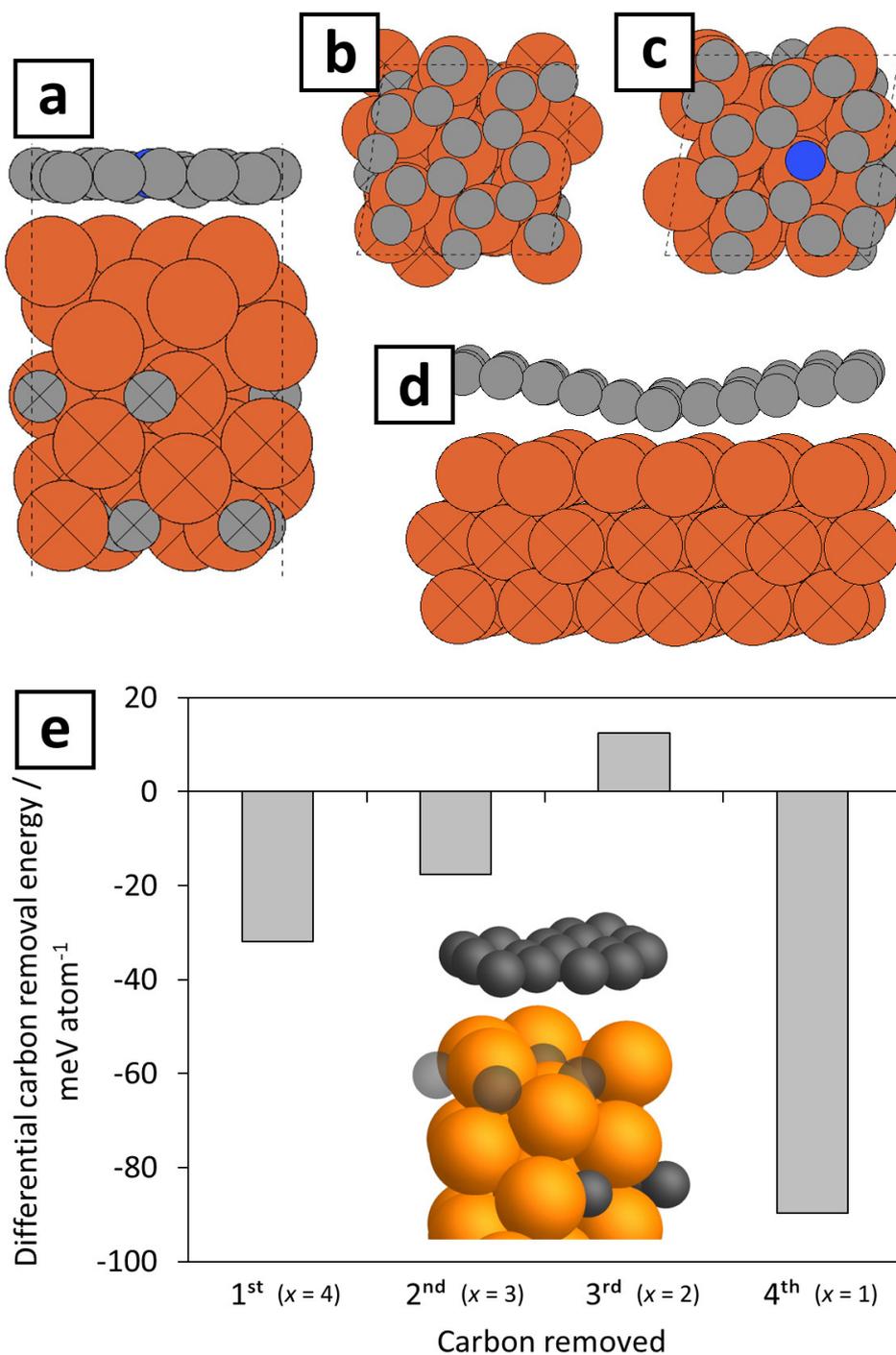


Figure 4.1: Fe_3C and Fe interface models: (a) $\text{Fe}_3\text{C}(010)/\text{N-graphene}$, side view; (b) $\text{Fe}_3\text{C}(010)/\text{graphene}$, top view; (c) $\text{Fe}_3\text{C}(010)/\text{N-graphene}$, top view; (d) $\text{Fe}(110)/\text{graphene}$, side view; (e) the differential energy of removing carbon atoms from the Fe_3C surface at the $\text{Fe}_3\text{C}/\text{G}$ interface; x is the parameter from Eq. (4.1); the four surface carbon atoms are shown as transparent in the inset. Crosses mark atoms which positions are fixed during structure relaxation. Color code for atoms: C – gray/black, N – blue, Fe – orange.

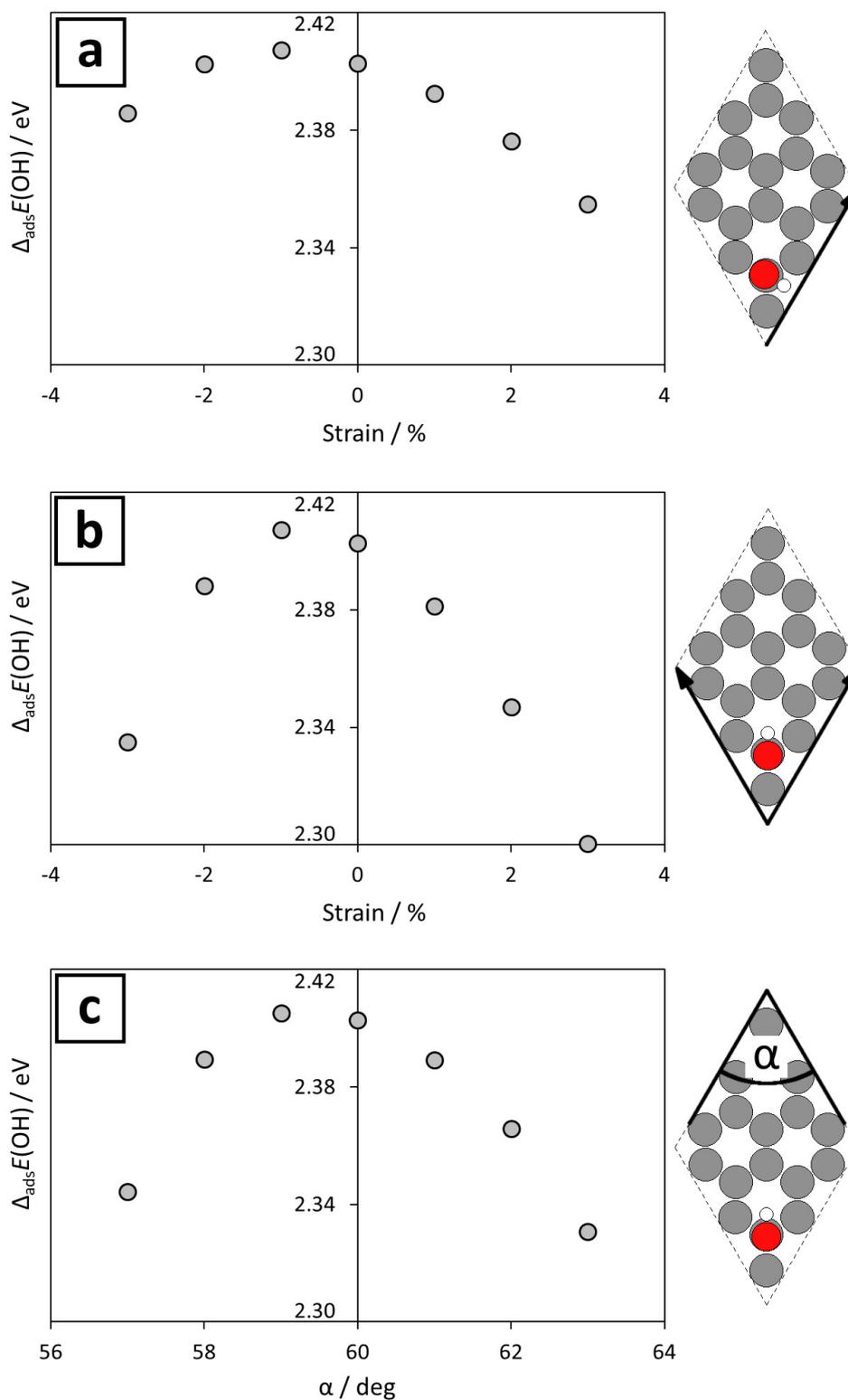


Figure 4.2: OH adsorption energy on graphene as a function of (a) uniaxial, (b) biaxial and (c) shear strain. The images show the unit cells, orientations of *OH and the varied lattice parameters. Color code for atoms: H – white, C – gray, O – red.

consists of 16 iron atoms. Iron and graphene lattices are matched by applying mixed expansive/compressive strain (2.0 %) to the iron phase. The unit cell contains 32 graphene carbon atoms placed on top of the iron slab.

According to the calculations, graphene chemisorption energy on bcc-Fe(110) surface is slightly positive, +2.3 meV/(C atom), which suggests this heterostructure is metastable relative to separate phases. A physisorbed state with a separation of 3.9 Å and adsorption energy of -38 meV/(C atom) was also found. The potential energy surface of a similar shape was previously observed for fcc-Ni(111)/graphene interface calculated using GGA functionals: PBE [96] and BEEF-vdW [51]. In this case, repeating the calculations at a higher level of theory (meta-GGA [96] or Random Phase Approximation [97]) results in evident binding of the chemisorbed state. The problem appearing with GGA functionals, also when including non-local interaction corrections, is attributed to an inaccurate simultaneous description of the covalent and dispersive forces in such weak binding systems [97]. Bearing that in mind, and having experimental evidence that bcc-Fe(110)/G forms a covalently bound heterostructure [105], the chemically bound bcc-Fe(110)/graphene interface is used as the ORR catalyst model.

A graphene sheet forms waves on the bcc-Fe(110) surface with corrugation amplitude of 1.0 Å (Fig. 4.1d). This effect was previously observed both in experiments and calculations and was found to result from a combination of lattice mismatch and strong interfacial interaction [105]. The shortest distance between iron and graphene is 2.2 Å.

A Bader charge analysis shows that each graphene carbon atom withdraws, on average, 0.041 e^- from the iron phase. This is significantly less than 0.07 e^- /(C atom) obtained by Taubert and Laasonen for iron nanoparticle enclosed in a fullerene [106]. The discrepancy is likely due to the larger separation between some parts of iron and graphene in the two dimensional Fe/G interface, caused by buckling of the graphene layer.

4.2.3 Nitrogen doping

The established Fe₃C/G and Fe/G interface models are subsequently modified by nitrogen doping. Replacing one carbon atom with nitrogen results in Fe₃C/N-graphene (Fe₃C/NG, Fig. 4.1c) and Fe/N-graphene (Fe/NG, Fig. 4.8b, inset) with 6.3 and 3.1 at%N in the graphene sheet, respectively. N-doped graphene is slightly more strongly bound to both supports. The chemisorption energies per N-graphene atom and the support-NG distances are -64 meV and 2.2 Å for the Fe₃C support, and -3.4 meV and 2.1 Å (NG wave trough) for the Fe support, respectively. A Bader charge transfer from the carbide and iron phases to the N-graphene phase is 0.048 and 0.038 e^- /(NG atom), respectively, which is only slightly different from the one obtained for the undoped systems.

4.3 ORR catalyst models

In Chapter 3, the spectator effect on the ORR intermediates stability is considered on unsupported N-graphene, and the presence of free nitrogen atoms is found to stabilize the *O intermediate significantly. On the one hand the lack of free nitrogen results in artificially weak *O binding, but on the other hand, too many free nitrogen atoms in the cell result in so strong *O binding that its reduction becomes the potential limiting step for the ORR. As a consequence, the reaction takes place in the presence of both *O and free nitrogen as spectators. Here, the same is found to be true for Fe₃C-supported N-graphene. To create such a reaction environment, the previously described Fe₃C/NG unit cell is extended in the surface plane to obtain a triple ($\sqrt{2} \times \sqrt{3}$) cell. The catalyst model contains 3 nitrogen atoms in the unit cell, of which *O occupies one, another one is free, and the last one serves as an active site for the ORR (Fig. 4.7b).

The catalytic properties of the Fe₃C/G interface are modeled using a double ($\sqrt{2} \times \sqrt{2}$) cell (Fig. 4.7a). The single cell resulted in the artificially lowered stability of the water layer inserted on top of the heterostructure (solvation model is described in details in Section 4.4).

The presence of free nitrogen is found not to influence the *O stability on Fe/NG interface. The previously described cell is thus also used as the catalyst model, both for N-doped and undoped systems.

For comparison, the same computational approach is used to model the oxygen reduction reaction on Pt(111) surface. The model consists of a 3×3 surface cell and three atomic layers of platinum. The bottom two layers are fixed in the bulk configuration during the structure relaxation.

4.4 The water layer

Explicit solvation model is utilized to account for solvation effects. It was shown in Chapter 3 that continuum solvation models cannot correctly describe interactions between water and adsorbed oxygen, hence including explicit H₂O molecules seems to be essential for the correct description of the ORR intermediates stability (especially for *O). Here, the number of water molecules included in each interface is enough to form at least a single water layer.

Global optimization of the water layer structure is performed using the minima hopping algorithm (Section 2.3.1). Here, the structure is determined for each ORR step in the appropriate environment (*e.g.*, in the presence of spectators, when relevant). The support has minimal effect on the optimal structure of water. For the time of minima hopping runs, the support is removed from the simulation cell, and the (N-)graphene structure is fixed. All the water molecules and adsorbate atoms, except for the one directly bound to the (N-)graphene sheet, are allowed to move during the global optimization. After finding at least 30 local minima, the support is reinserted to the lowest energy structure, as well as to the structures which energy is up to 0.1 eV higher than the lowest energy one. The final geometry optimization

is performed for these systems, allowing all the atoms to relax, except for the previously specified bottom part of the support slab. The lowest energy structure (Figs. 4.3 and 4.4) is used to construct the free energy diagram of the corresponding catalytic system.

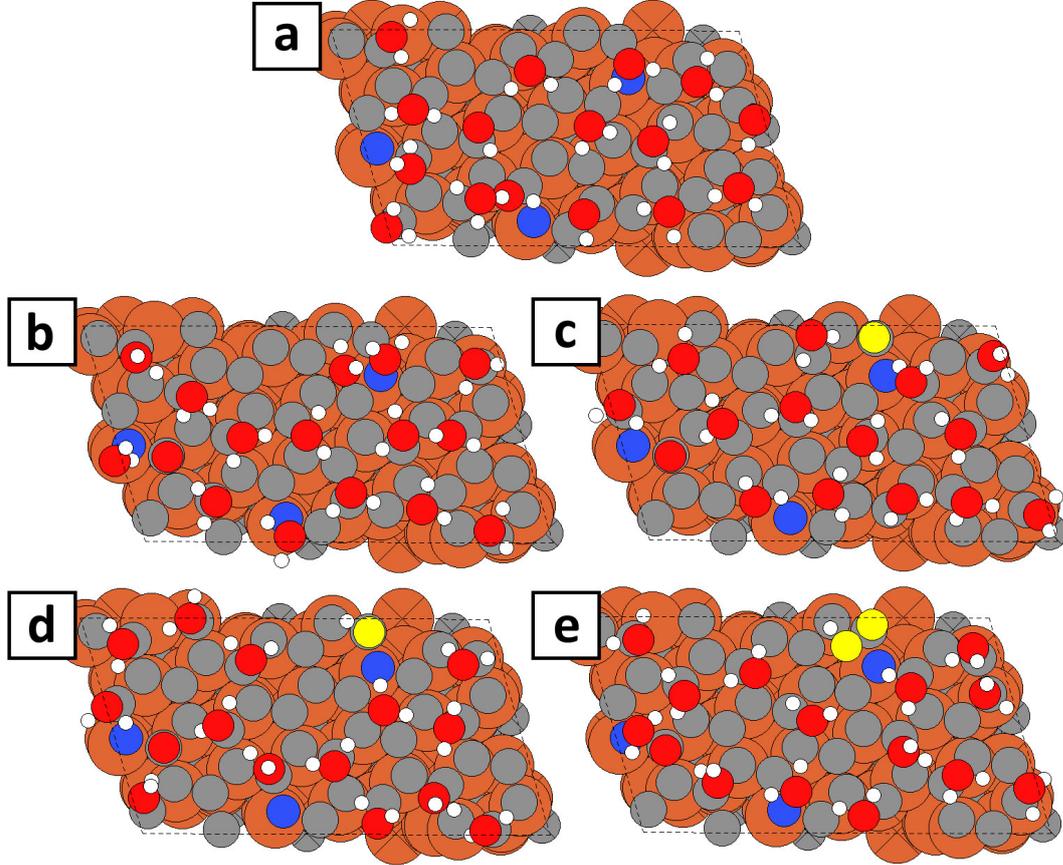


Figure 4.3: Water layer structures for the $\text{Fe}_3\text{C}/\text{NG}$ system. Same structures are used for NG and all (supported and unsupported) N-graphite systems. Water layer in (a) is shown in the absence of any adsorbate. The system in (b) consists of an empty active site $*$, one oxygen spectator, and one free nitrogen spectator. Systems with the same spectators, additionally comprising ORR intermediates at the active site are: (c) $*\text{O}$, (d) $*\text{OH}$, (e) $*\text{OOH}$. Crosses mark atoms which positions are fixed during structure relaxation. Color code for atoms: H – white, C – gray, N – blue, O – red, Fe – orange. Oxygen atoms belonging to the adsorbates at the active site are highlighted in yellow.

Only in a few cases, the water layer forms a regular hexagonal structure, similar to the one experimentally found on highly oriented pyrolytic graphite [107]. This is caused by difficulties in matching the support, graphene and hexagonal ice lattices at the same time at computationally affordable sizes of the unit cells. However, water layer stabilities relative to isolated H_2O molecules were found to be similar for all the considered systems, *i.e.*, 0.490 ± 0.010 eV/ H_2O molecule. Note that the difference between the water interaction energy with graphene and N-graphene (no support) was found to be only about 3 meV/ H_2O molecule (Section 3.2.2). Similar to unsupported

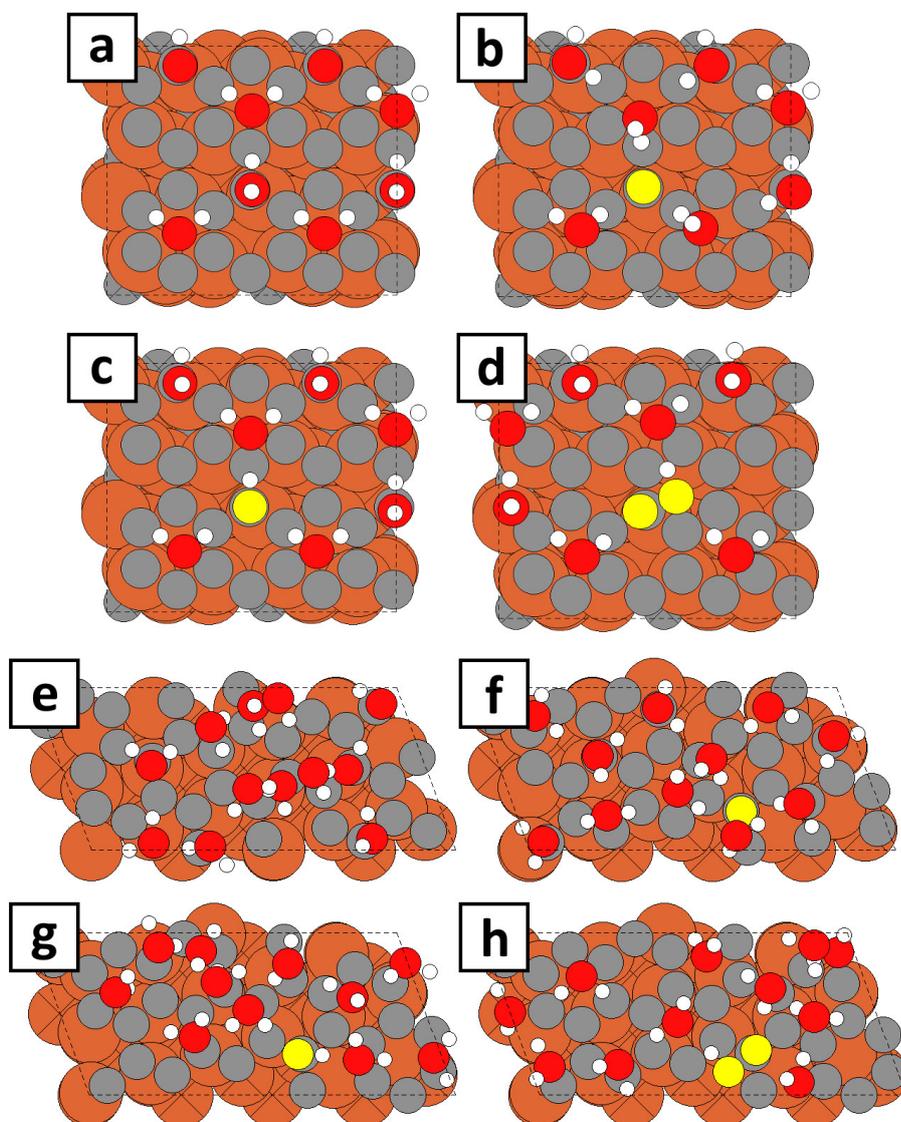


Figure 4.4: Water layer structures for $\text{Fe}_3\text{C}/\text{G}$: (a)-(d), and Fe/G : (e)-(h). The first four structures are also used for NG (2N/ads) and $\text{Fe}_3\text{C}/\text{NG}$ (2N/ads) systems. The last four structures are also used for Fe/NG system. Water layers in (a) and (e) are shown in the absence of any adsorbate. Systems with ORR intermediates at the active site: (b) and (f): $^*\text{O}$; (c) and (g): $^*\text{OH}$; (d) and (h): $^*\text{OOH}$. Color code for atoms is the same as in Fig. 4.3.

N-graphene, water molecules do not chemisorb on the active sites of $\text{Fe}_3\text{C}/(\text{N})\text{G}$ or $\text{Fe}/(\text{N})\text{G}$ interfaces. The presence of the aqueous environment stabilizes all ORR intermediates, $^*\text{OH}$ and $^*\text{OOH}$ by 0.18-0.35 eV, and $^*\text{O}$ by 0.63-0.95 eV, relative to vacuum.

Stability of ORR intermediates in an aqueous environment is higher than in vacuum by 0.18-0.35 eV for $^*\text{OH}$ and $^*\text{OOH}$, and by 0.63-0.95 eV for $^*\text{O}$, depending on the system considered. This compares well with the solvation energies on unsupported N-graphene (Section 3.2.2).

The water layer structure utilized to model solvation effects on the Pt(111) surface is similar to the one previously described in the literature [68, 70], *i.e.*, the half-dissociated water layer. The presence of $^*\text{OH}$ spectators in this model results from the fact that $^*\text{OH}$ reduction is the potential-determining step for the oxygen reduction reaction on Pt(111). The structures of ORR intermediates embedded in the half-dissociated water layer on Pt(111) are shown in Fig. 4.5.

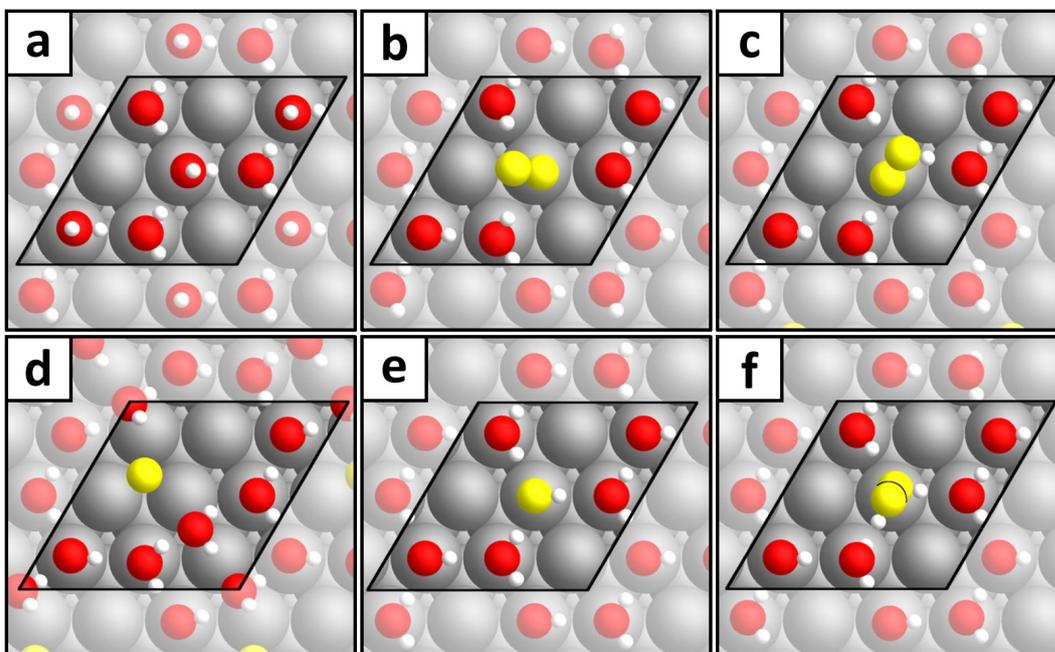


Figure 4.5: Structures of a single water layer (a) and ORR intermediates embedded in the half-dissociated water layer on Pt(111): (b) $^*\text{O}_2$, (c) $^*\text{OOH}$, (d) $^*\text{O}$, (e) $^*\text{OH}$ – the half-dissociated water layer, (f) H_2O_2^* . Color code for atoms: H – white, O – red, Pt – gray. Oxygen atoms belonging to the adsorbates at the active site are highlighted in yellow.

4.5 Free energy diagrams and the 2D volcano

Theoretical ORR free energy diagrams for the considered model catalysts at $U = 0.8 \text{ V}_{\text{RHE}}$ are shown in Figs. 4.6–4.9, and the adsorption Gibbs free energies (at $U = 0 \text{ V}_{\text{RHE}}$) are collected in Tab. 4.1.

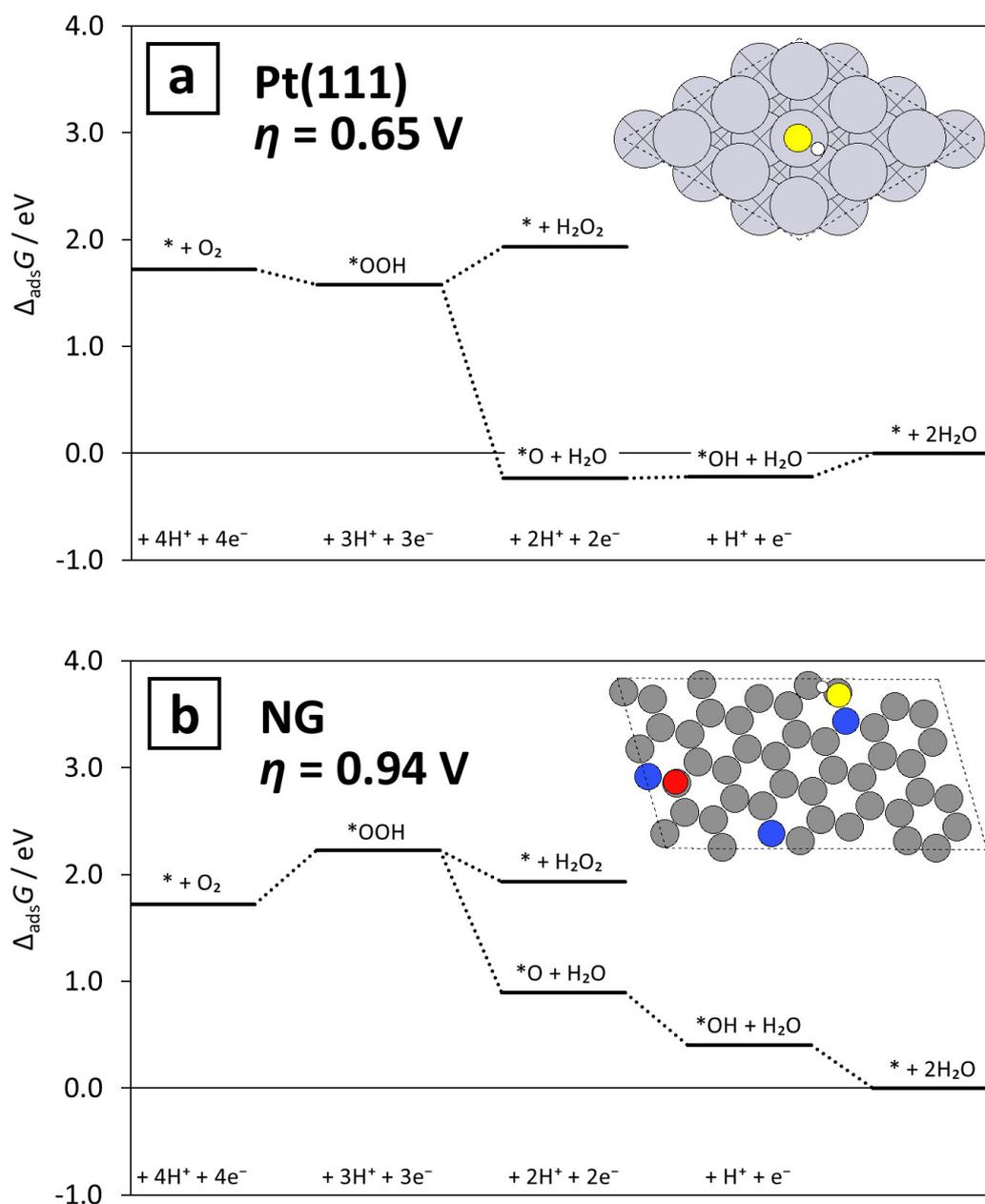


Figure 4.6: ORR free energy diagrams at $U = 0.8 \text{ V}_{\text{RHE}}$ for: (a) Pt(111), (b) NG. The insets show simulation cells of the corresponding systems with OH intermediate bound to the active site. The water layer is hidden for clarity. Crosses mark atoms which positions are fixed during structure relaxation. Color code for atoms: H – white, C – gray, N – blue, O – red (spectator) or yellow (adsorbate at the active site), Pt – light gray.

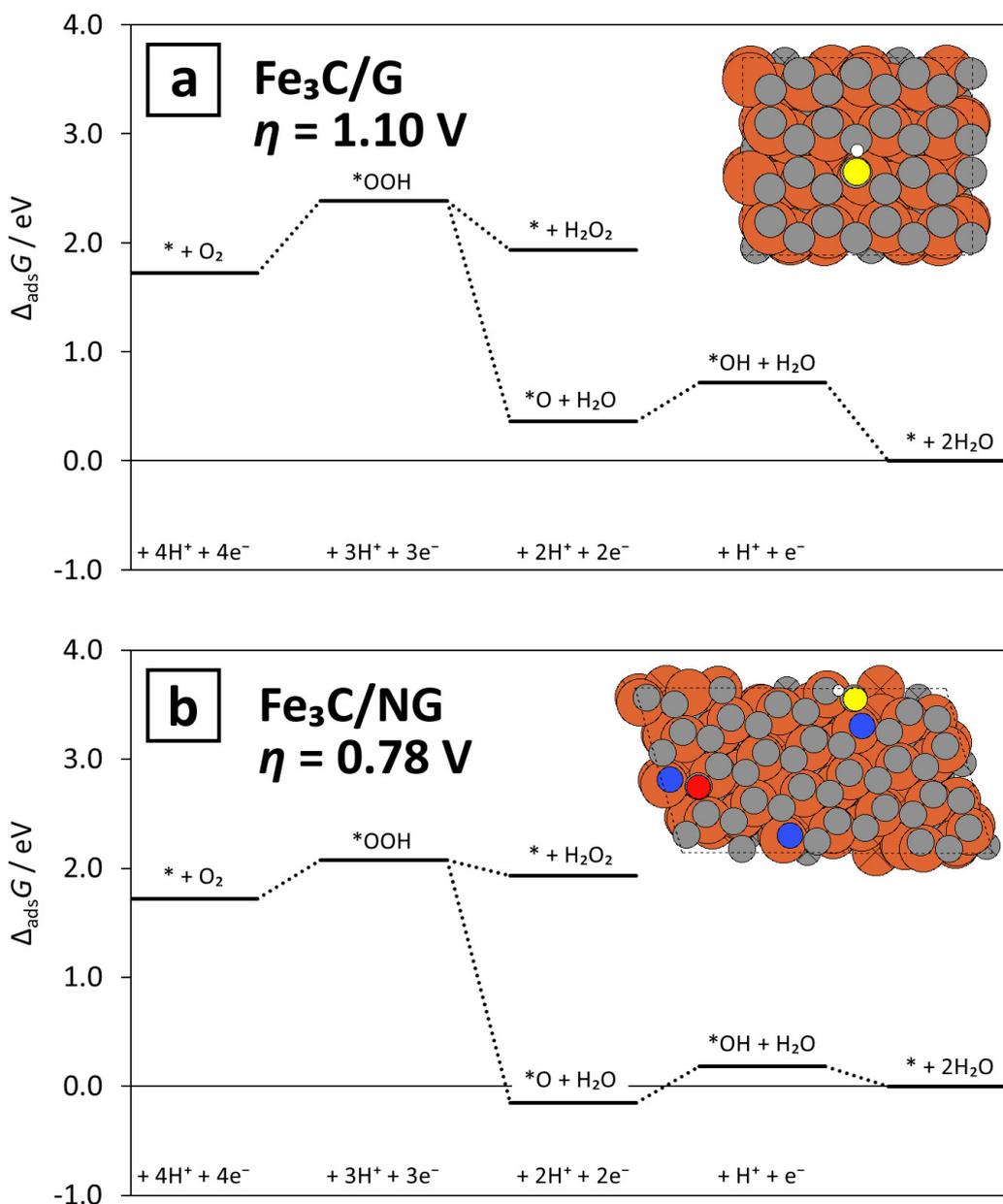


Figure 4.7: ORR free energy diagrams at $U = 0.8 \text{ V}_{\text{RHE}}$ for: (a) $\text{Fe}_3\text{C}/\text{G}$, (b) $\text{Fe}_3\text{C}/\text{NG}$. The insets show simulation cells of the corresponding systems with OH intermediate bound to the active site. The water layer is hidden for clarity. Crosses mark atoms which positions are fixed during structure relaxation. Color code for atoms: H – white, C – gray, N – blue, O – red (spectator) or yellow (adsorbate at the active site), Fe – orange.

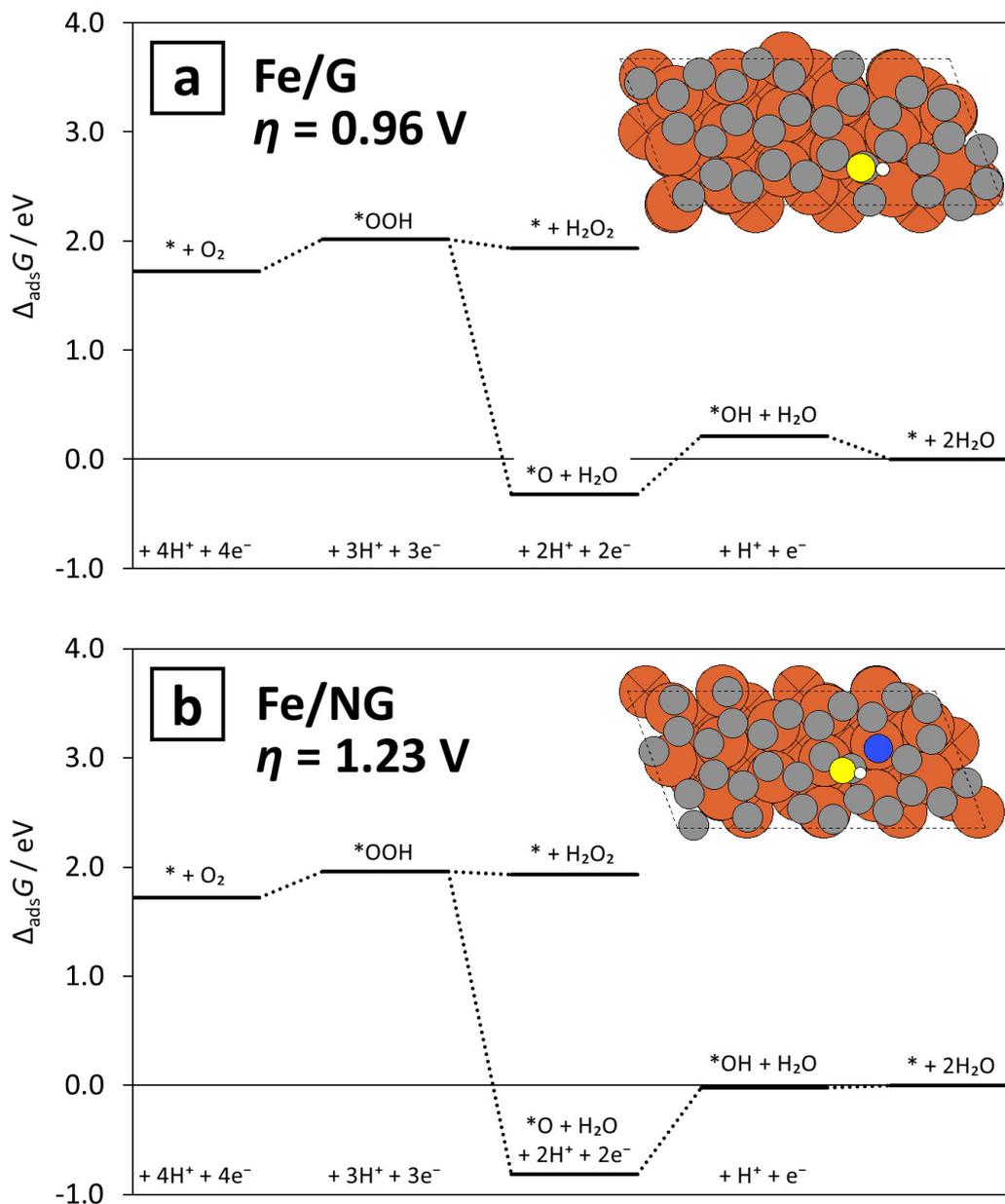


Figure 4.8: ORR free energy diagrams at $U = 0.8 \text{ V}_{\text{RHE}}$ for: (a) Fe/G, (b) Fe/NG. The insets show simulation cells of the corresponding systems with OH intermediate bound to the active site. The water layer is hidden for clarity. Crosses mark atoms which positions are fixed during structure relaxation. Color code for atoms is the same as in Fig. 4.7.

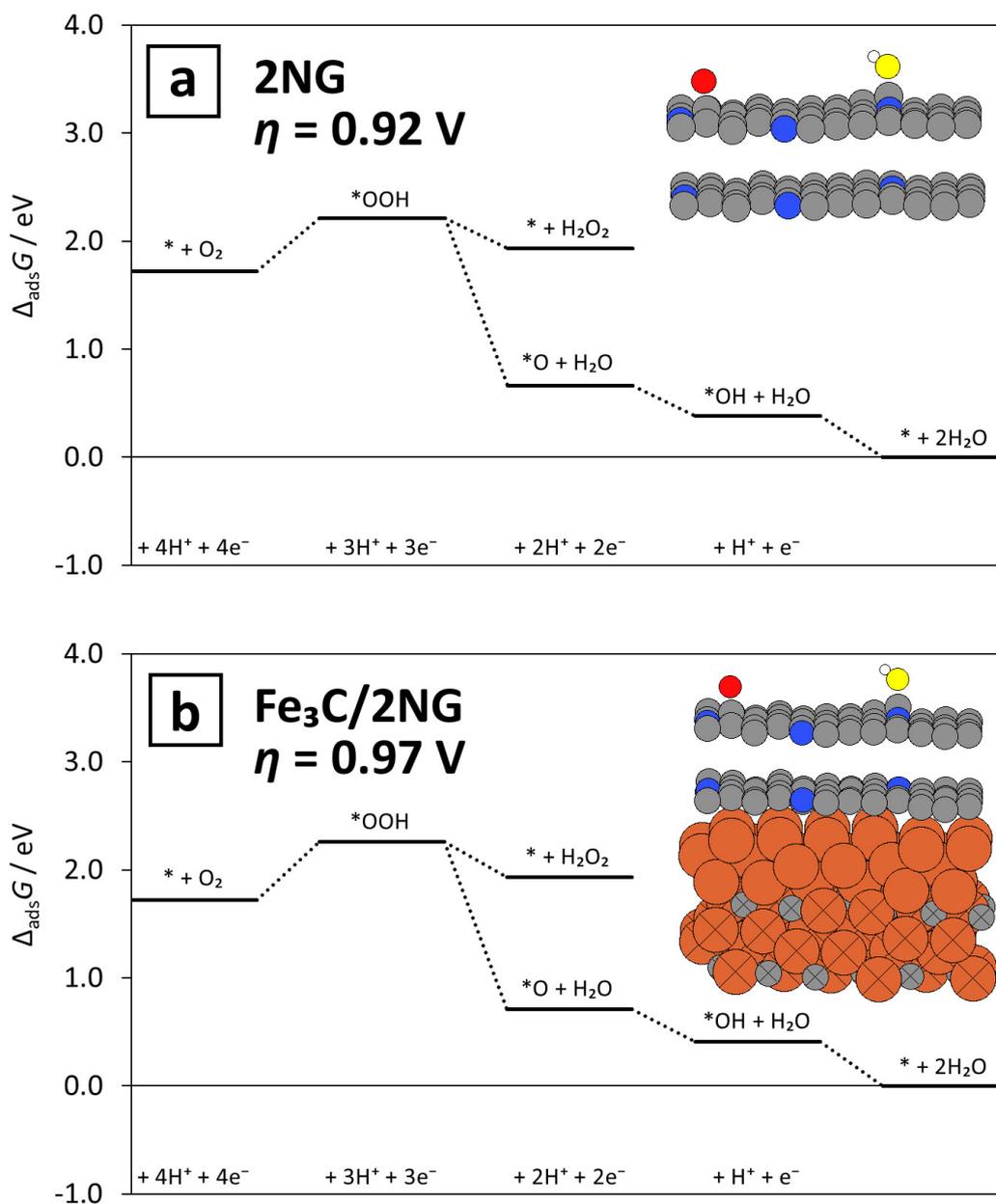


Figure 4.9: ORR free energy diagrams at $U = 0.8 \text{ V}_{\text{RHE}}$ for: (a) N-graphite with two NG layers (2×NG), (b) Fe₃C/N-graphite with two NG layers (Fe₃C/2×NG). The insets show simulation cells of the corresponding systems with OH intermediate bound to the active site. The water layer is hidden for clarity. Crosses mark atoms which positions are fixed during structure relaxation. Color code for atoms is the same as in Fig. 4.7.

Table 4.1: ORR intermediates adsorption Gibbs free energies at $U = 0 \text{ V}_{\text{RHE}}$ [Eq. (1.7)] and calculated ORR overpotentials (η_{ORR}) on the considered surfaces in the presence of water, after applying the Christensen’s corrections [Eq. (2.30a)].

System	Cell	$\Delta_{\text{ads}}G / \text{eV}$			$\eta_{\text{ORR}} / \text{V}$
		*OOH	*O	*OH	
Pt(111)	3×3	3.98	1.37	0.58	0.65
G	$\sqrt{2} \times \sqrt{2}$	5.98 ^a	3.65	2.58	2.19
Fe ₃ C/G	$\sqrt{2} \times \sqrt{2}$	4.79	1.96	1.51	1.10
Fe/G	1×1	4.41	1.28	1.01	0.96
NG	$\sqrt{2} \times \sqrt{3}$	4.63	2.50	1.20	0.94
Fe ₃ C/NG	$\sqrt{2} \times \sqrt{3}$	4.47	1.45	0.98	0.78
Fe/NG	1×1	4.36	0.78	0.78	1.23
NG (2N/ads)	$\sqrt{2} \times \sqrt{2}$	4.51	1.18	1.10	1.14
Fe ₃ C/NG (2N/ads)	$\sqrt{2} \times \sqrt{2}$	4.51	1.10	1.06	1.20
2×NG	$\sqrt{2} \times \sqrt{3}$	4.61	2.26	1.18	0.92
3×NG	$\sqrt{2} \times \sqrt{3}$	4.62	2.28	1.19	0.93
Fe ₃ C/2×NG	$\sqrt{2} \times \sqrt{3}$	4.66	2.31	1.21	0.97
Fe ₃ C/3×NG	$\sqrt{2} \times \sqrt{3}$	4.62	2.28	1.19	0.93

^a not bound; $\Delta_{\text{ads}}G$ estimated from $\Delta_{\text{ads}}G(\text{OOH}) = \Delta_{\text{ads}}G(\text{OH}) + 3.4 \text{ eV}$

It is clearly seen that the Fe₃C support significantly stabilizes all the ORR intermediates, *i.e.*, *OOH, *O and *OH, both on graphene (1.09, 1.68 and 1.07 eV, respectively) and N-graphene (0.15, 1.05 and 0.22 eV, respectively). The stabilizing effect is even stronger with the Fe support (1.47, 2.37 and 1.57 eV for graphene; 0.27, 1.71 and 0.42 eV for N-graphene, respectively). It is worth noting that the values for *O are much higher than those for the other ORR intermediates. As noted above, the electron density is transferred from the support to the (N-)graphene sheet. A correlation is found between Bader charge on oxygen and *O binding energy (Fig. 4.10). The electron density likely stabilizes the adsorbed oxygen by filling its empty sp states, as described in Chapter 3. Strong *O stabilization caused by support was observed earlier in Cu(111)/NG system [98].

Both Fe₃C and Fe supports significantly activate graphene surface towards ORR. The calculated ORR overpotential for Fe/G (Fig. 4.8a) and Fe₃C/G (Fig. 4.7a) is 0.31 and 0.45 V higher than for the Pt(111) surface (Fig. 4.6a), respectively. This agrees with the experimental results that encapsulated iron-based catalysts prepared from nitrogen-free precursors shows some but limited ORR activity [43, 46]. Interestingly, Fe/G heterostructure binds the *O intermediate so strong that its reduction to *OH becomes the potential-determining step — a situation rarely observed on transition metal surfaces [8]. The Fe/G,

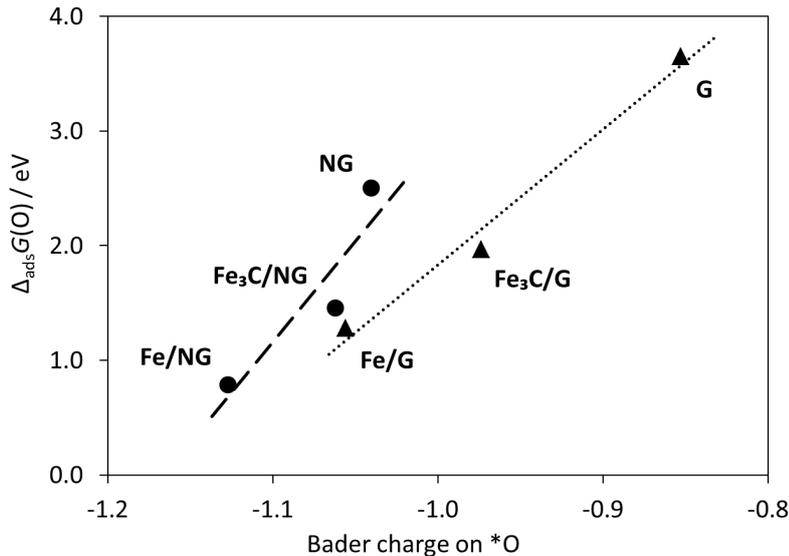


Figure 4.10: Correlation between oxygen adsorption Gibbs free energy and a Bader charge on *O for undoped (triangles, dotted line) and nitrogen-doped (circles, dashed line) systems.

as well as the $\text{Fe}_3\text{C}/\text{G}$ heterostructures do not appear to follow the scaling relation between *O and *OH adsorption energies determined for the transition metal (111) surfaces [$\Delta_{\text{ads}}G(\text{O}) = 2 \Delta_{\text{ads}}G(\text{OH})$, Eq. (1.13)]. This is visualized on a 2D ORR activity volcano plot (Fig. 4.11).

Unsupported N-doped graphene (Fig. 4.6b) belongs to the weak oxygen binding class of the ORR catalysts. Fe_3C support activates N-graphene towards ORR by making the bonds with ORR intermediates stronger, which decreases the calculated overpotential by 0.16 V (Fig. 4.7b). The resulting ORR overpotential is only 0.13 eV higher than that of the Pt(111) surface (Fig. 4.6a), lower than for any other heterostructure comprising undoped graphene investigated here. This is in line with experimental evidence that nitrogen plays an important role in the activity of the encapsulated iron-based catalyst [43].

As mentioned in Section 4.3, if the NG or $\text{Fe}_3\text{C}/\text{NG}$ structure contains sufficiently many unoccupied nitrogen atoms per adsorbate, *O binding energy is so strong that *O reduction becomes the ORR potential-determining step. This already happens with 2 nitrogen atoms per adsorbate, *i.e.*, with just one free nitrogen atom in the simulation cell (structures denoted as “NG (2N/ads)” and “ $\text{Fe}_3\text{C}/\text{NG}$ (2N/ads)” in Fig. 4.11; ORR free energy diagrams for these systems are shown in Fig. 4.12a and b). Under operational conditions, these structures immediately start to accumulate oxygen on the surface (*via* O_2 reduction or H_2O oxidation). This leads to destabilization of the next *O adsorbates, and the *O accumulation process is suspended as soon as another ORR step (*e.g.*, O_2 reduction to *OOH) starts to limit the ORR potential.

Fe/NG heterostructure (Fig. 4.8b) binds oxygen species, especially *O, even stronger than $\text{Fe}_3\text{C}/\text{NG}$. In this case, however, accumulation of *O on the

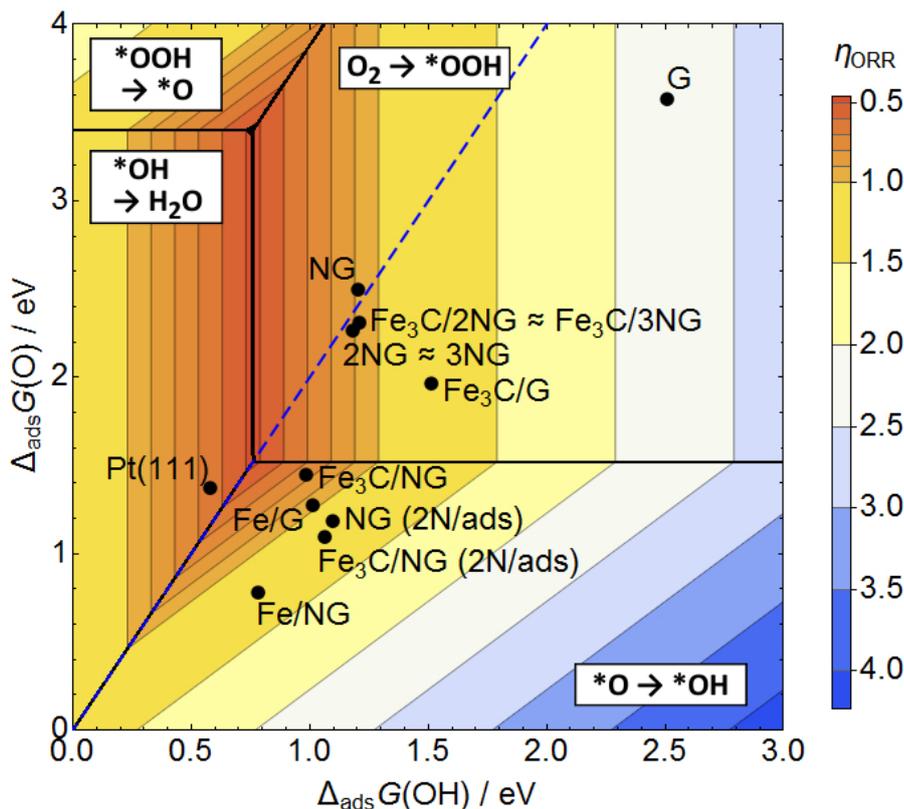


Figure 4.11: Theoretical ORR overpotential as a function of $\Delta_{\text{ads}}G(\text{OH})$ and $\Delta_{\text{ads}}G(\text{O})$. The scaling relation between $\ast\text{OH}$ and $\ast\text{OOH}$ adsorption energies, $\Delta_{\text{ads}}G(\text{OOH}) = \Delta_{\text{ads}}G(\text{OH}) + 3.4 \text{ eV}$, is determined from the data for the structures considered in this study (Tab. 4.1). The plot is divided into four areas (separated by solid black lines) based on the potential-determining steps, which are shown in the white boxes. The blue dashed line denotes the scaling relation between $\ast\text{O}$ and $\ast\text{OH}$ adsorption energies observed on the transition metal (111) surfaces [8].

surface does not destabilize next $\ast\text{O}$ adsorbates, and the process can continue until oxygen occupies each nitrogen (or, more precisely, any carbon atom next to each nitrogen) in the NG sheet. The theoretical overpotential required to reduce $\ast\text{O}$ is almost 0.6 V higher than for Pt(111), which means $\ast\text{O}$ effectively poisons the Fe/NG surface. This is again in agreement with experimental results, where the encapsulated iron-based catalyst's ORR activity was found to correlate with the Fe_3C phase content, but not with the Fe phases content [108]. Fe/NG shows poor ORR activity due to an unfavorable breaking of the scaling relation between $\ast\text{O}$ and $\ast\text{OH}$ adsorption energy (Fig. 4.11).

As noted in Chapter 3, atomic oxygen adsorbed on top of a catalytic site being the 2nd row element (C, B) is particularly unstable due to the presence of empty O(sp) states. It gains stability in the presence of water overlayer, free nitrogen atoms in the N-doped graphene sheet, and, as shown here, an electron donating support. Excessive stabilization of $\ast\text{O}$ is, however, unfavorable for the ORR efficiency, as it increases the energy required to reduce $\ast\text{O}$ to $\ast\text{OH}$. To

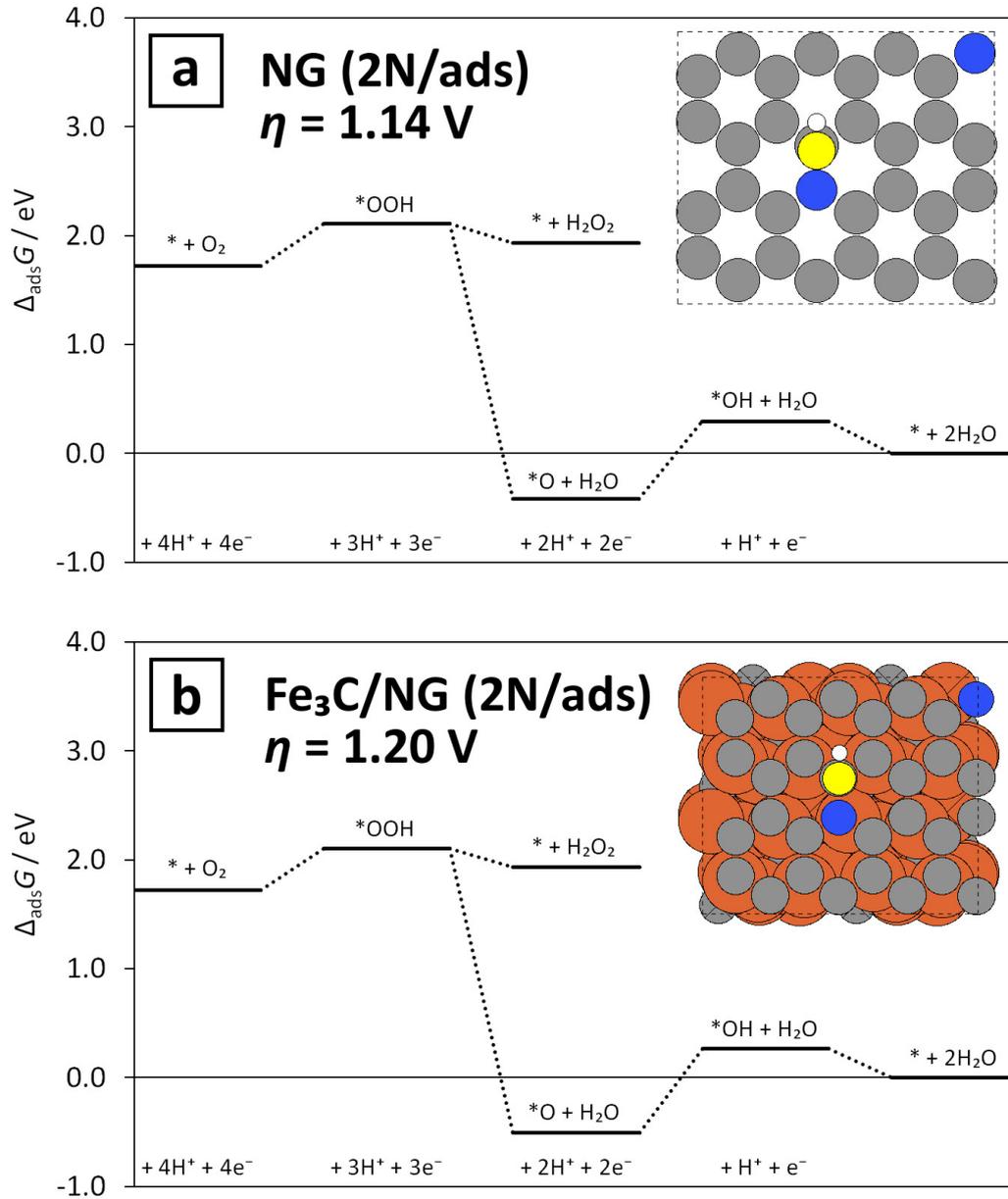


Figure 4.12: ORR free energy diagrams at $U = 0.8 V_{\text{RHE}}$ for: (a) N-graphene with two N atoms per adsorbate [NG (2N/ads)], (b) Fe₃C/N-graphene with two N atoms per adsorbate [Fe₃C/NG (2N/ads)]. The insets show simulation cells of the corresponding systems with OH intermediate bound to the active site. The water layer is hidden for clarity. Color code for atoms is the same as in Fig. 4.7.

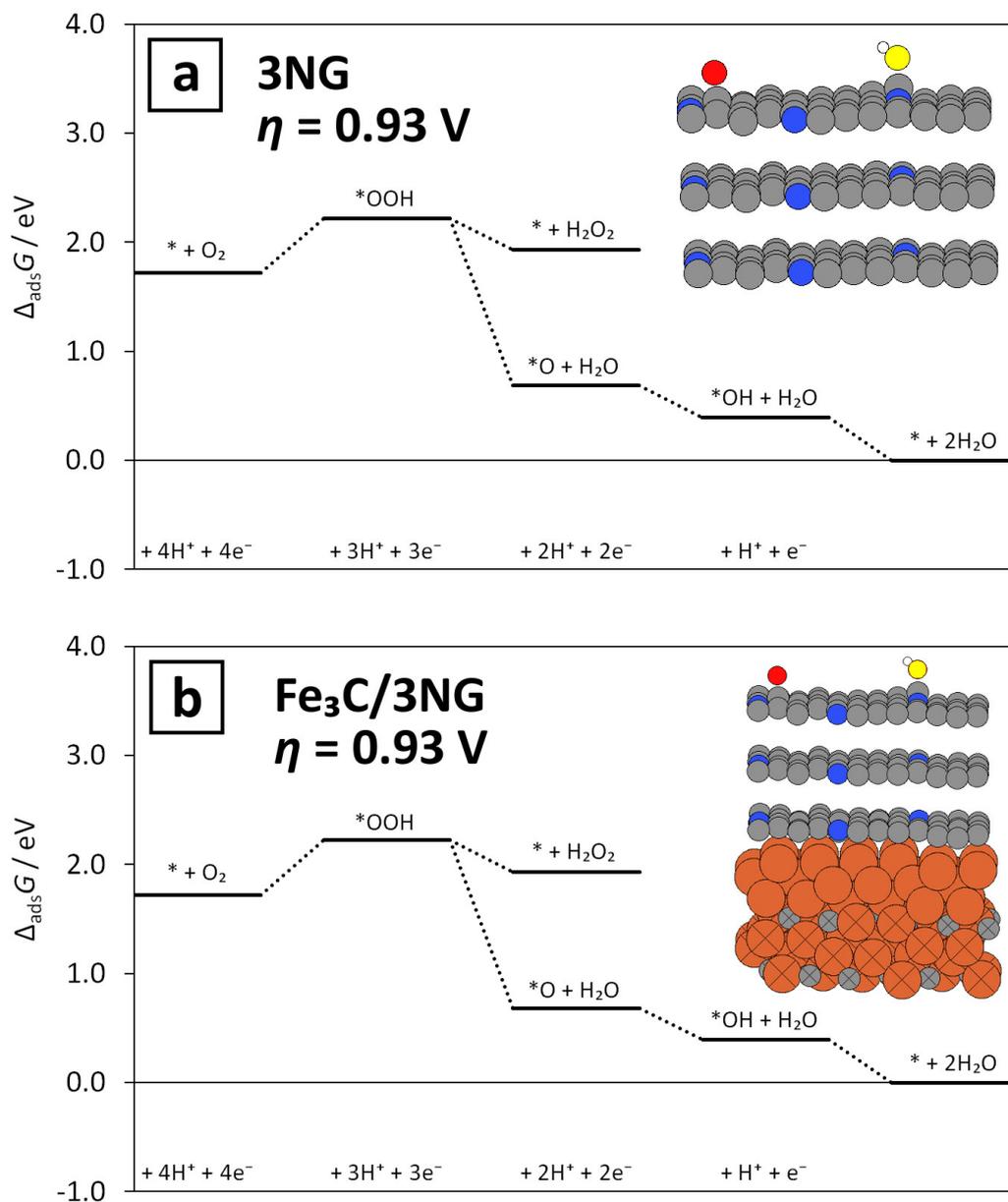


Figure 4.13: ORR free energy diagrams at $U = 0.8 \text{ V}_{\text{RHE}}$ for: (a) N-graphite with three N-graphene layers (3×NG), (b) Fe₃C/N-graphite with three N-graphene layers (Fe₃C/3×NG). The insets show simulation cells of the corresponding systems with OH intermediate bound to the active site. The water layer is hidden for clarity. Color code for atoms is the same as in Fig. 4.7.

solve this problem, *O has to be selectively destabilized. Since the spontaneous *O accumulation on the catalyst surface destabilizes the next *O adsorbates, the activity of NG and Fe_3C/NG systems increase. However, such an *O destabilization does not occur in case of Fe/NG system. Therefore, it cannot be expected that this effect will have a general application in establishing design rules for these systems.

Fe and Fe_3C supports differ in the amount of charge transferred to the N-graphene sheet, and subsequently to the *O adsorbate (Fig. 4.10). The Fe support donates enough charge to completely stabilize *O , even in the absence of free nitrogen. This results in the surface being fully covered by *O (all nitrogen atoms occupied) at the ORR-relevant potentials. Stronger electron donating supports than iron will most likely act similarly, causing the surface to be poisoned by *O as well. As opposed to that, Fe_3C support does not donate enough charge, and the presence of some amount of free nitrogen atoms is necessary. This leaves catalytic sites on the surface, where the ORR can proceed. Weaker electron donating supports than Fe_3C are expected to bind all the ORR adsorbates weaker, causing the drop in the ORR activity (moving it towards the pure NG activity). However, it can be expected that support with electron donating properties between Fe and Fe_3C will bind the ORR adsorbates stronger, but not strong enough to let *O entirely cover the N-graphene sheet. This may lead to a catalyst with ORR activity superior to that of the Fe_3C/NG heterostructure, possibly reaching or exceeding the activity of the $Pt(111)$ surface.

4.6 Multiple graphene layers

Preparing well defined (N-)graphene layers on the support is a difficult task. As seen from TEM images, Fe_3C -based catalyst is often coated by a few graphitic layers [46, 101, 108]. For this reason, the effect of adding more N-graphene layers to the Fe_3C/NG catalyst is studied here. The N-graphite model consists of two ($2\times NG$) or three ($3\times NG$) N-graphene sheets arranged in AA stacking, with nitrogen atoms located one above another. The catalytic environment is the same as for NG and Fe_3C/NG systems, *i.e.*, one *O and one free nitrogen act as spectators.

For the unsupported NG system, the addition of the second N-graphene layer stabilizes the *O intermediate by about 0.2 eV, but the *OOH and *OH binding energies remain almost unaffected (Tab. 4.1). The catalytic activity towards ORR does not change significantly, as the O_2 reduction to *OOH is the potential-determining step (Fig. 4.9a). The third N-graphene layer has a negligible effect on the adsorption energies of the ORR intermediates (Fig. 4.13a and Tab. 4.1).

In case of the Fe_3C/NG system, the catalytic activity drops rapidly upon addition of the second N-graphene layer (Fig. 4.9b). Both the calculated overpotential and the adsorption energies of the ORR intermediates become close to the values obtained with the unsupported systems. With three N-graphene layers, any dissimilarities between supported and unsupported systems vanish

(Fig. 4.13b and Tab. 4.1).

The study shows that in systems comprising multiple N-graphene layers, the support would not be expected to enhance the ORR activity. However, a strong correlation between Fe_3C content and the activity is found in the experiments [108], and this correlation is fully consistent with the active sites existing on a single graphitic layer on Fe_3C .

4.7 Summary

ORR activity of four heterostructures, *i.e.*, $\text{Fe}_3\text{C}(010)/\text{graphene}$, $\text{Fe}_3\text{C}(010)/\text{N-graphene}$, $\text{Fe}(110)/\text{graphene}$, and $\text{Fe}(110)/\text{N-graphene}$ is evaluated computationally and compared with earlier experimental studies. ORR intermediates solvation is taken into account by including an explicit water layer in each calculation. Both supports stabilize all the ORR intermediates; however, the effect of Fe is noticeably stronger. The $^*\text{O}$ intermediate is stabilized particularly strongly, and its binding energy is found to correlate with the charge on oxygen. Increasing O binding, as well as increasing negative charge on O, is found in the series: unsupported system < Fe_3C support < Fe support.

The most active heterostructure is $\text{Fe}_3\text{C}/\text{N-graphene}$. Like in case of an unsupported N-graphene system, $\text{Fe}_3\text{C}/\text{NG}$ accumulates $^*\text{O}$ on the surface, and the ORR takes place at the oxygen coverage between $0.5 < \theta_{\text{O}} < 1.0$. As opposed to that, Fe/NG system stabilizes $^*\text{O}$ intermediates so strong that its surface effectively becomes blocked by $^*\text{O}$ at ORR-relevant electrode potentials. The calculations are consistent with experimental evidence that: (i) Fe_3C support promotes ORR activity more than Fe support, (ii) N-doping is essential for achieving high ORR activity.

The Fe_3C -supported system activity quickly converges to that of the unsupported one with increasing number of graphitic layers. Even two N-graphene layers effectively isolate adsorbates from the influence of the support. Therefore, the experimental activity of the iron carbide encased in graphitic layers likely comes from Fe_3C -supported N-doped graphene monolayers. However, other effects like graphene defect promotion during synthesis caused by the presence of Fe_3C cannot be ruled out.

Finally, it is shown that electron donating support can increase the ORR activity of N-doped graphene (as in case of Fe_3C), but too strong electron donation properties of the support suppress the activity (as in case of Fe). It is suggested that a heterostructure consisting of NG layer supported on a stronger electron donating material than Fe_3C (but weaker than Fe) is likely to have similar or better ORR activity than the Pt(111) surface.

Chapter 5

Fe-N-C catalyst activity enhancement by selective anion adsorption

This chapter is based on Paper 2 included in Appendix B.2. The experimental part of the study was performed by Kaspar Holst-Olesen (University of Copenhagen), under the supervision of Prof. Matthias Arenz (University of Bern), and is summarized in the thesis. Reading the paper is advisable for a full understanding of the experimental details.

5.1 Introduction

It is a well-known fact that the oxygen reduction reaction on platinum is inhibited when certain acids are present in the electrolyte. This, in particular, applies to phosphoric [109–114], sulfuric and hydrochloric [115–119] acids. The poisoning mechanism is active site blocking by preferential adsorption of anions formed by acid deprotonation. Non-precious metal catalysts are much less studied in terms of activity loss caused by anions [120, 121]. Interestingly, Fe-N-C catalysts containing FeN₄ moieties are 2-dimensional materials, where species dissolved in the electrolyte can access both sides of the catalytic center. This opens a possibility of activity modification by ligand adsorption on the backside of the active site — an option which is not possible on 3D nanoparticles of traditional Pt-based catalysts.

Here, the effect of four different electrolytes (*i.e.*, H₃PO₄, HClO₄, H₂SO₄, and HCl) on the activity of Fe-N-C catalyst is investigated and compared to the known behavior of Pt. Most importantly, computational modeling reveals that the phosphoric acid not only does not poison Fe-N-C catalyst but even enhances its catalytic activity towards ORR. This result is consistent with electrochemical experiments conducted within the same study.

5.2 Results

5.2.1 Experiment summary

In Fig. 5.1, a well-known inhibiting effect of anion adsorption on the ORR on platinum is demonstrated in RDE measurements of a polycrystalline Pt (Pt-poly) disk in aqueous HClO_4 , H_2SO_4 , H_3PO_4 and HCl electrolytes, respectively. ORR half-wave potential ($U_{1/2}$) decreases significantly in the order $\text{HClO}_4 > \text{H}_2\text{SO}_4 > \text{H}_3\text{PO}_4 > \text{HCl}$. This change of $U_{1/2}$ can be associated with a decrease in ORR activity. However, the observed decrease in diffusion limited current (j_L) also suggests that the concentration of dissolved O_2 in the respective electrolytes decreases in the same order, except for HCl [122]. As the ORR is a first order reaction with respect to the oxygen concentration [123, 124], the observed ORR activity is a result of anion blocking as well as oxygen concentration.

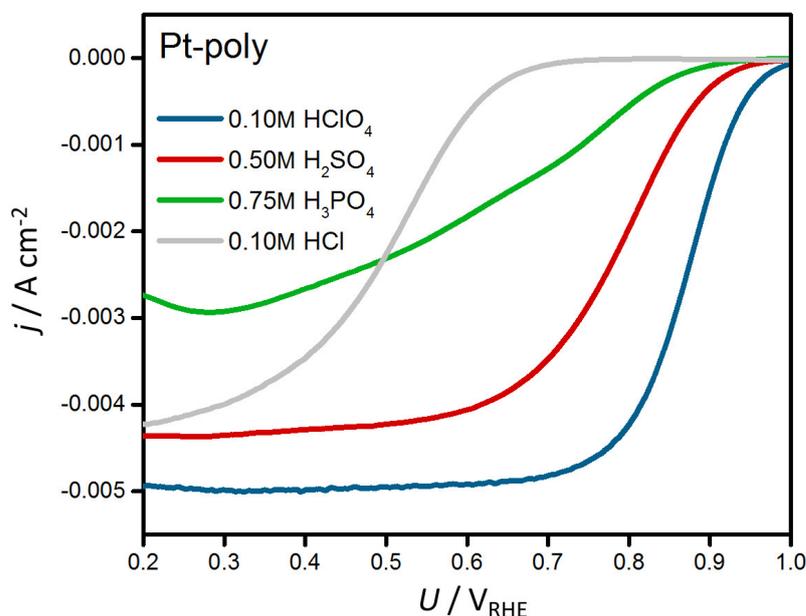


Figure 5.1: Polycrystalline platinum RDE polarization curves. Pt-poly disk in 0.10 M HClO_4 , 0.50 M H_2SO_4 , 0.75 M H_3PO_4 and 0.10 M HCl electrolyte saturated with O_2 at 900 rpm and 10 mV s^{-1} .

Fig. 5.2 shows the same measurement performed on a commercial Fe-N-C catalyst. It is evident that half-wave potentials are considerably less different (as compared to Pt) and all fall in the similar potential range. Noticeably, the polarization curve measured in H_3PO_4 electrolyte indicates a higher ORR activity at high potentials than in HClO_4 . In this case, it appears that the decrease in j_L follows the trend of the increasing electrolyte concentration. This indicates that low activity of Pt in H_3PO_4 (Fig. 5.1) is not only related to oxygen solubility but must also be due to other factors, *e.g.*, poisoning by anion adsorption.

To disentangle the influence of oxygen concentration and anion adsorption on the Fe-N-C catalyst, the molarity of the four electrolytes HClO_4 ,

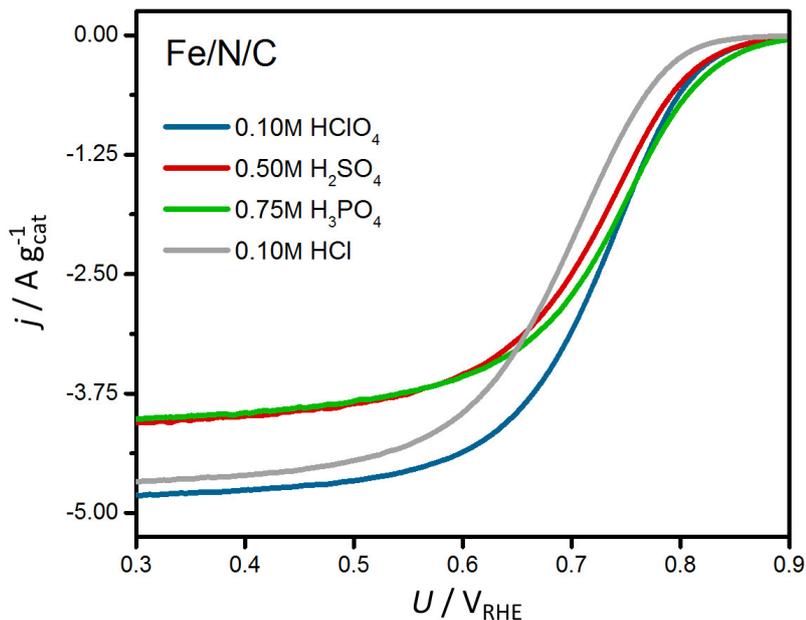


Figure 5.2: Fe-N-C RDE polarization curves. Fe-N-C in 0.10 M HClO_4 , 0.50 M H_2SO_4 and 0.75 M H_3PO_4 electrolyte purged with O_2 at 900 rpm and 10 mV s^{-1} . Total catalyst load is $800 \mu\text{g cm}^{-2}$.

H_2SO_4 , H_3PO_4 , and HCl was gradually increased and ORR polarization curves recorded. In Fig. 5.3a, j_L is used as a simple measure of the oxygen solubility and the viscosity of the electrolyte. It is seen that with increasing molarity, j_L and thus oxygen transport decreases. This trend is particularly prominent for phosphoric acid. Using the mass averaged ORR rate, j_k , as a measure of the ORR activity (Fig. 5.3b), it can be seen that in all acidic solutions the activity decreases with increasing electrolyte molarity in a similar manner as j_L . This suggests that increasing the molarity does not necessarily affect the catalytic activity of the Fe-N-C catalyst through site blocking. Instead, due to decreasing O_2 mass transport with increasing electrolyte molarity, the observed ORR rate decreases consistently with a first-order reaction with respect to O_2 concentration. Surprisingly, comparing the catalyst performance in HClO_4 and H_3PO_4 electrolytes, it is seen that higher ORR rates (Fig. 5.3b) are measured in the latter, despite the lower O_2 solubility (Fig. 5.3a). Such behavior is in sharp contrast to the observations on Pt catalysts, which always exhibit increased inhibition in the H_3PO_4 electrolyte. Therefore, the results not only demonstrate that anion adsorption behaves differently on the Fe-N-C catalyst than on a Pt-surface. A clear indication of a promotional effect of the anions in the H_3PO_4 electrolyte is observed for Fe-N-C. The results for the ORR in HCl electrolyte imply that Fe-N-C is not completely resistant to poisoning from species in the electrolyte solution, but that the promotional effect depends on the nature of the anions in the electrolyte.

In an effort to avoid the influence of oxygen solubility and electrolyte viscosity on the measured ORR rates, a different experiment was conducted as well; minute amounts of H_3PO_4 were added to a 0.1 M HClO_4 electrolyte so-

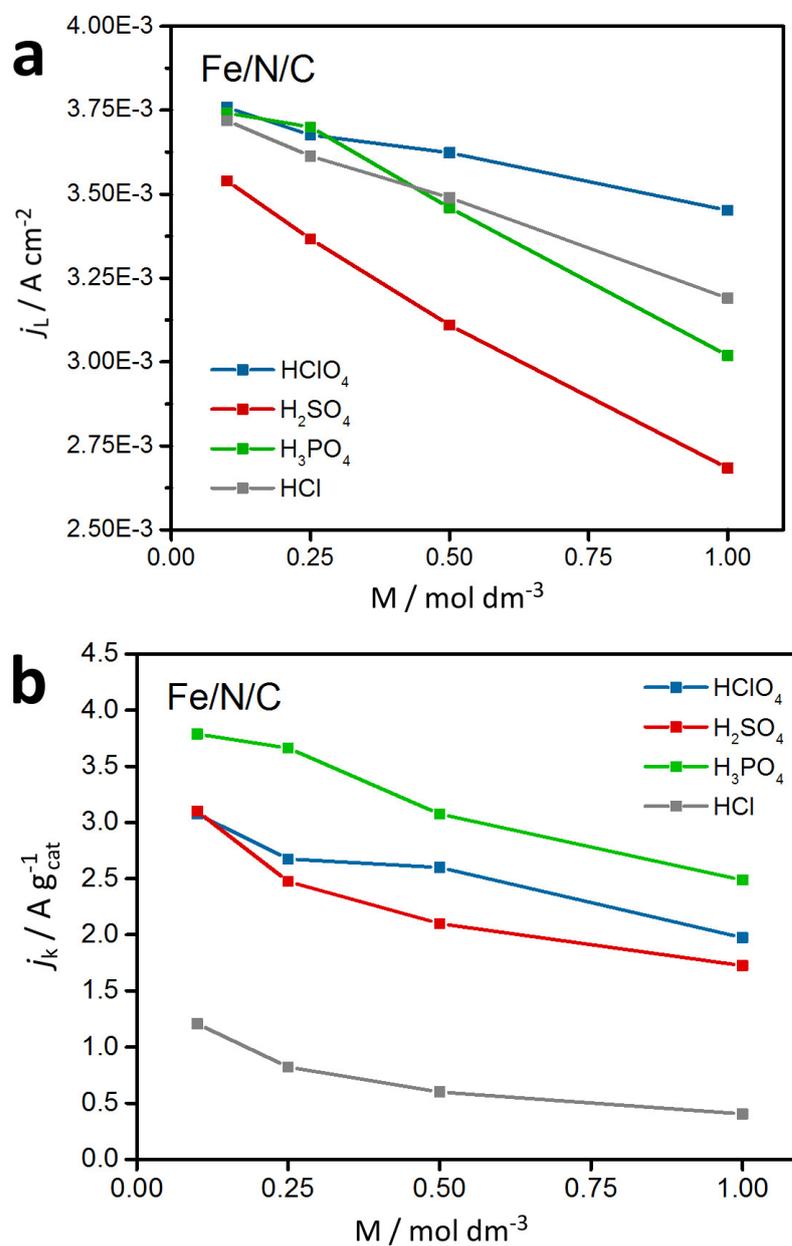


Figure 5.3: Effect of electrolyte molarity on (a) oxygen solubility expressed by j_L , (b) catalytic activity expressed by j_k .

lution and the effect on the ORR polarization curve recorded. This approach ensures that oxygen solubility and electrolyte viscosity are not significantly affected and hence changes in the observed ORR polarization curve must be due to site blocking from added anion species. The results presented in Fig. 5.4 support that even very small amounts of H_3PO_4 species have a negative effect on the ORR on Pt, while for the Fe-N-C catalyst the polarization curves in both solutions overlap indicating no significant change in the ORR rate. This supports the absence of any detrimental effect of H_3PO_4 to the activity of the active Fe-N-C sites. It also indicates that for a promotional effect a certain H_3PO_4 concentration is required.

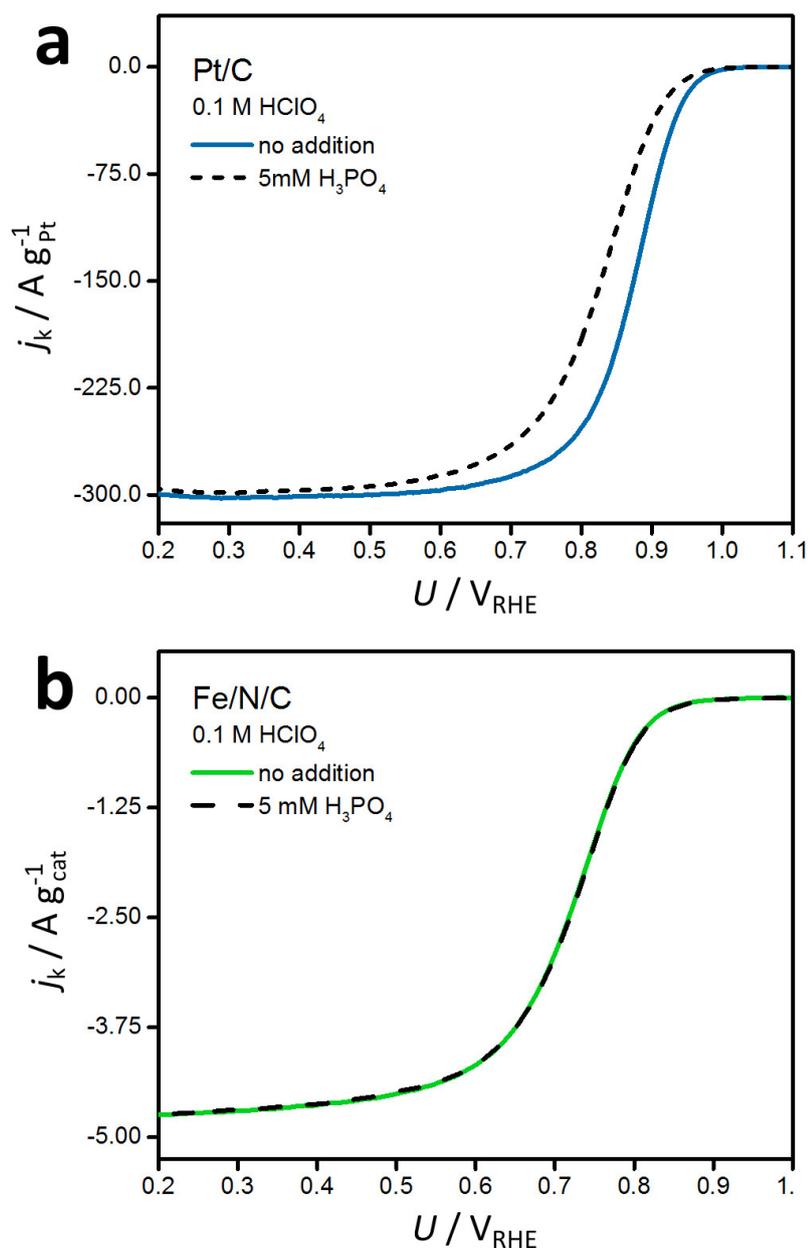


Figure 5.4: Effect of adding $5 \cdot 10^{-3}$ M H_3PO_4 to (a) Pt and (b) Fe-N-C catalyst in 0.1 M HClO_4 electrolyte solution.

5.2.2 Computational approach

To elucidate the phenomena behind the experimental observations, DFT calculations of the adsorption energy of anions present in the investigated electrolytes are performed. Then, the competition of anions and ORR intermediates for the active site is assessed.

The Pt(111) surface is modeled by periodically repeated (3×3) unit cell with three atomic layers, of which the bottom two are fixed in bulk configuration. The Fe-N-C catalyst model consists of a $\text{FeN}_4\text{C}_{12}$ moiety embedded in graphene structure with a surface cell size of $(8.170, 0.0) \times (0.0, 12.035)$ Å. Fe:N:C atomic ratio is 1:4:26.

Solvation of the surface and adsorbates is taken into account by using the implicit solvation model implemented in VASPsol [74, 75]. Comparison of implicit and explicit solvation approach can be found in Appendix A.1. Anion adsorption Gibbs free energy, $\Delta_{\text{ads}}G(\text{A}^{n-})$, is calculated as

$$\Delta_{\text{ads}}G(\text{A}^{n-}) = -\Delta_{\text{dilut}}G(\text{H}_n\text{A}_{(\text{solvated})}) - \Delta_{\text{solvation}}G(\text{H}_n\text{A}_{(\text{g})}) + \Delta_{\text{CHE}}G(U_{\text{vs.RHE}}, 1 \text{ bar}) \quad (5.1)$$

according to the thermodynamic cycle shown in Fig. 5.5. $\Delta_{\text{ads}}G(\text{A}^{n-})$ depends on the electrode potential through the $\Delta_{\text{CHE}}G(U_{\text{vs.RHE}}, 1 \text{ bar})$ term, which is calculated from DFT using the Computational Hydrogen Electrode model [9]. Solvation and dilution Gibbs free energies are calculated from standard thermodynamic relations using literature data of formation enthalpies, entropies and ions activity coefficients [58–60, 125, 126]. An example of the ClO_4^- adsorption free energy calculation on Fe-N-C catalyst at 0.75 V_{RHE} is given as Supplementary Note 1 to Paper B.2. As the gas phase entropies of HClO_4 and H_3PO_4 are not available in the literature, they were calculated from the partition function using molecular data [59] and treating internal degrees of freedom as harmonic vibrations. This approach has been validated for the case of H_2SO_4 , where the deviation of the calculated entropy from the experimental one is less than 0.3%. The calculated gas-phase entropies are 297.16 and 314.24 $\text{J mol}^{-1} \text{K}^{-1}$ for HClO_4 and H_3PO_4 , respectively.

Free energies are calculated as described in Section 2.2. To the best of the author’s knowledge, a reliable correction for the adsorbed O_2 has not been determined yet. Consequently, $^*\text{O}_2$ energy level on the free energy diagram (Fig. 5.7) may be slightly less accurate.

5.2.3 Discussion

Fig. 5.6 shows calculated potential-dependent Gibbs free energies of adsorption on the Pt surface. The figure includes adsorption energies of ORR intermediates (H_2O , OH , O) and each acid form present in the electrolyte solutions, *i.e.*, H_3PO_4 , H_2PO_4^- , HPO_4^{2-} and PO_4^{3-} for phosphoric acid, and ClO_4^- for perchloric acid. It is clearly seen that at ORR-relevant potentials ClO_4^- does not adsorb on the Pt(111) surface, and therefore does not influence the catalytic activity. Contrary to that, phosphate anions interact with Pt(111) much

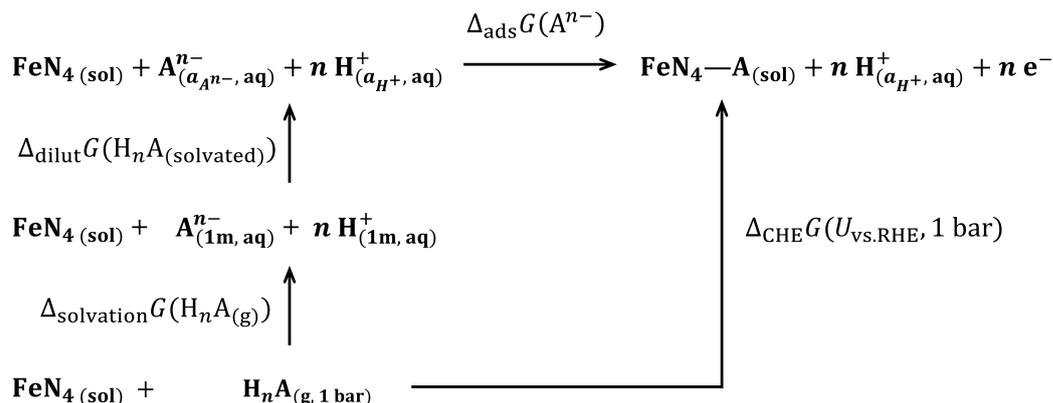


Figure 5.5: Thermodynamic cycle for calculation of the Gibbs free energy of A^{n-} anion adsorption from solution. Abbreviations and symbols in brackets: (g) – gas phase, (aq) – aqueous phase, (sol) – continuum solvent (VASPsol), a – activity, 1 m = 1 mol kg⁻¹ (standard molality).

stronger than the ORR intermediates and consequently displace them from the surface. This explains the observed drop of platinum ORR activity in phosphoric acid. At ORR-relevant potentials, the phosphate form that is most likely to be found on the Pt(111) surface is hydrogen phosphate (*HPO₄).

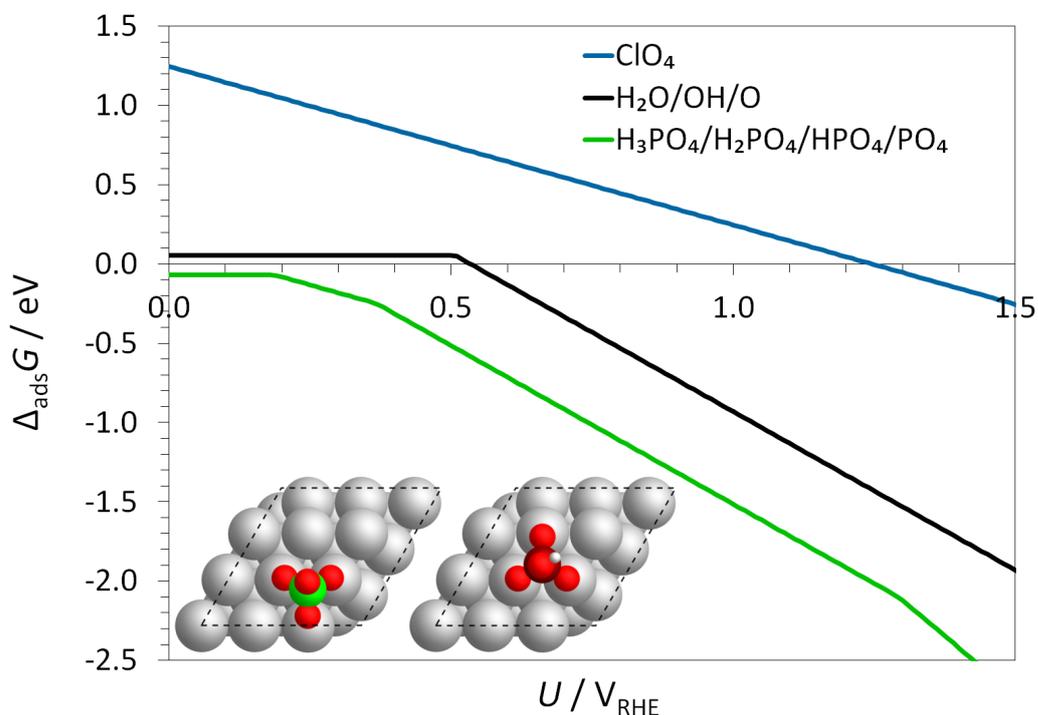


Figure 5.6: Anions adsorption Gibbs free energy on Pt(111) vs. electrode potential ($U_{\text{vs.RHE}}$) at 298.15 K and 0.5 M formal concentration. The insets show the model systems with optimized structures of *ClO₄ and *HPO₄. Color code for atoms: H – white, O – red, P – dark red, Cl – green, Pt – gray.

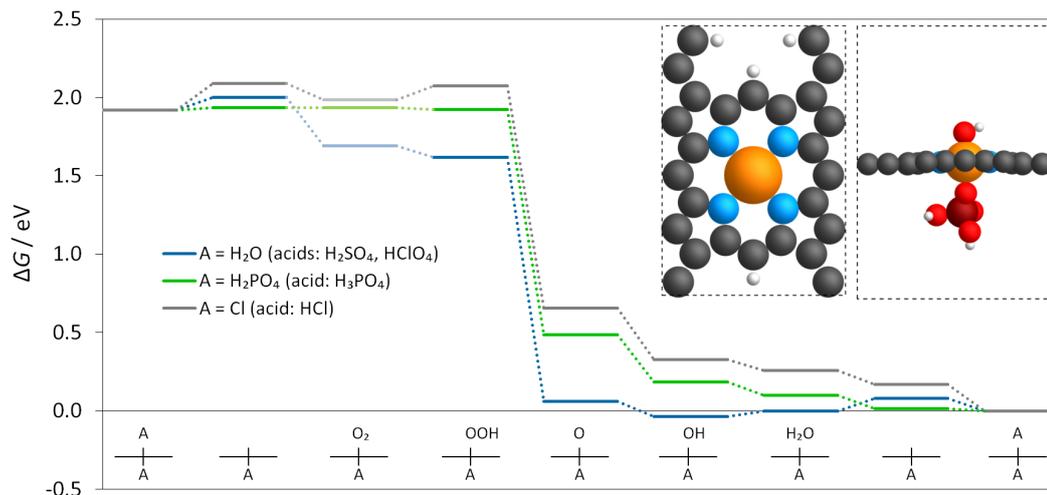


Figure 5.7: Free energy diagram of the oxygen reduction reaction on Fe-N-C catalyst at $U_{\text{vs.RHE}} = 0.75$ V in four acids: HClO_4 , H_2SO_4 , H_3PO_4 and HCl . Temperature: 298.15 K, acid formal concentration: 0.5 M. The insets in the upper-right corner show: (left) the catalyst model, top view; (right) $\text{H}_2\text{PO}_4\text{-FeN}_4\text{-OH}$ intermediate, side view. Color code for atoms: H – white, C – black, N – blue, O – red, P – dark red, Fe – orange.

The same analysis performed for the Fe-N-C catalyst model shows a similar trend: the perchloric group weakly interacts with the active site, while the dihydrogen phosphate (H_2PO_4^-) adsorption energy is slightly higher than the one of the ORR intermediates. However, in this case, stronger anion-catalyst interaction does not automatically result in a decrease in ORR activity. As mentioned previously, the Fe-N-C catalyst is a 2D material, where both sides of the catalyst are exposed to the electrolyte solution. If any of these sides is occupied by an anion rather than an ORR intermediate, the catalytic activity of the opposite side can be modified. Figure 5.7 shows the calculated ORR free energy diagrams along the minimum energy paths in the presence of the following acids: HClO_4 (in solution: ClO_4^-), H_3PO_4 (forms: H_3PO_4 , H_2PO_4^- , HPO_4^{2-} and PO_4^{3-}), H_2SO_4 (forms: HSO_4^- and SO_4^{2-}) and HCl (form: Cl^-). In HClO_4 and H_2SO_4 , the interaction of the FeN_4 moiety with anions is weaker than its interaction with water. Consequently, FeN_4 with H_2O ligand ($\text{H}_2\text{O-FeN}_4$) serves as the active site. The thermodynamically limiting step is OH removal, with a thermodynamic barrier of 0.115 eV at 0.75 V_{RHE} , therefore in these electrolytes, the catalyst is on the strong oxygen binding side of the ORR activity volcano. In H_3PO_4 and HCl , the interaction of the FeN_4 moiety with anions is stronger than its interaction with water. $\text{H}_2\text{PO}_4\text{-FeN}_4$ and Cl-FeN_4 serve as the active sites, respectively, and in both electrolytes, the Fe-O bond is weakened such that the OOH formation becomes the rate-limiting step (the catalyst is on the weak oxygen binding side of the activity volcano). Thermodynamic barriers for OOH formation at 0.75 V_{RHE} are 0.013 and 0.169 eV in H_3PO_4 and HCl , respectively. Summarizing, the thermodynamic barrier of the limiting step is lower in H_3PO_4 and higher in HCl , when compared to

HClO₄ and H₂SO₄. This indicates the following order of Fe-N-C ORR activity in acids: H₃PO₄ > HClO₄ = H₂SO₄ > HCl, which agrees very well with the experimental observations. It should be noted that the calculations cannot differentiate between the catalyst activity in HClO₄ and H₂SO₄ electrolyte. This is, however, also in agreement with the experimental results, where only small differences in ORR activity between these two electrolytes are observed. As seen in Fig. 5.3, these differences are most likely related to the solubility of oxygen (j_L), which at similar molar concentrations is smaller in H₂SO₄ than in HClO₄.

5.3 Conclusion

The results support previous investigations on anion adsorption on platinum surfaces while pointing towards interesting new effects on non-precious M-N-C catalysts. The strong activity inhibition caused by H₃PO₄ species on Pt is not observed on the Fe-N-C catalyst. On the contrary, the ORR activity is found to benefit from the presence of the H₃PO₄ electrolyte even though oxygen is poorly soluble in this solution. Moreover, the Fe-N-C catalyst appears more tolerant towards poisoning than Pt in general. These experimental results are supported by the computational modeling, which demonstrates that while the order of binding strength of the anions is the same on Pt and Fe-N-C, the catalytic effect on the latter is different. The effects of the weak binding HClO₄ and H₂SO₄ species are insignificant due to the stronger binding of H₂O to the FeN₄ moiety. However, the effect from the stronger binding H₃PO₄ and HCl species alter the FeN₄ site and the thermodynamic barrier of the limiting step, which is lowered in H₃PO₄ and increased in HCl, as compared to HClO₄ and H₂SO₄. The results shown are of particular interest for the so-called high-temperature proton exchange fuel cells (HT-PEMFCs). In this version of fuel cells, the electrolyte consists of phosphoric acid embedded into a polybenzimidazole (PBI) matrix, which forms a polymer electrolyte membrane. Catalyzing the ORR in HT-PEMFCs with Pt-based catalysts leads to relatively low reaction rates despite a relatively high operating temperature of about 150°C — an observation often related to anion poisoning (in addition to low oxygen solubility). The presented results indicate that with respect to the ORR activity, non-precious catalysts are a highly promising option as cathode material for HT-PEMFCs.

Chapter 6

Conclusions and outlook

6.1 Conclusions

The computational studies of the electrocatalytic oxygen reduction reaction presented in this thesis revolve around catalytic activity modifiers, which can be classified into two main groups:

- Effects that are immanently present in the catalytic system and not subject to any control. Considering these effects is necessary for reliable computational modeling of the catalysts under operating conditions. Solvation and spectator effects, studied in Chapters 3 and 4, belong to this category. It is shown that the oxygen reduction reaction occurs on N-doped graphene and its Fe₃C-supported counterpart at the adsorbate coverage between 0.5 and 1.0. Moreover, it is found that including explicit solvation is essential for the correct description of the ORR intermediates adsorption on the 2nd row elements.
- Activity modifiers that can be introduced into the system during synthesis (metallic support for N-doped graphene) or during the electrochemical cell operation (acid used as the electrolyte).

The second group is of particular interest. Understanding how the chemical environment affects material properties allows designing materials with optimal catalytic activity.

Over the past few decades, experimental and theoretical research has synergistically advanced our knowledge about the oxygen reduction reaction. Experimental studies have provided an accurate (up to the measurement uncertainty) description of the process in all its complexity. However, they have often offered only a limited possibility to control — or even merely determine — the actual structure and chemical environment of the active site. As opposed to that, computational studies have allowed testing well-defined structures of the active sites, although at the expense of introducing simplifications about the system structure and approximations in the theoretical methods. When these two different worlds meet by giving consistent results, we advance from a simple statement: “the catalyst works”, to “we know what catalytic site

likely makes it work”. And this is often just a step away from knowing “why it works”, which gives us a predictive power. In this thesis, experiments and computations have met in such a way twice:

1. Owing to the earlier experimental studies, the activity of the graphitic layer encapsulated iron-based catalyst is known to correlate with iron carbide (but not iron) content, as well as with the presence of the surface nitrogen dopants. Here, the iron carbide-supported nitrogen-doped graphene heterostructure ($\text{Fe}_3\text{C}/\text{NG}$) is found to exhibit activity superior to its Fe-supported counterpart (Fe/NG), as well as to the interfaces comprising undoped graphene (Fe/G , $\text{Fe}_3\text{C}/\text{G}$). Electron donating properties of the support appear to be the key factor deciding which heterostructure is active. Support possessing intermediate electron donating properties between iron and iron carbide is predicted to result in a catalyst more active than $\text{Fe}_3\text{C}/\text{NG}$.
2. Pt and Fe-N-C catalysts are experimentally found to respond differently when exposed to phosphoric acid (relative to measurements in HClO_4 electrolyte). The oxygen reduction reaction on platinum is significantly inhibited by the presence of H_3PO_4 , while the same acid is found to increase the onset potential of Fe-N-C catalyst, slightly promoting its activity. It is suggested that the 2-dimensional structure of the Fe-N-C catalyst is responsible for this difference. By adsorbing on one side of the FeN_4 moiety, dihydrogen phosphate anion slightly modifies properties of the other, active side. ORR intermediates bind slightly weaker in the presence of H_2PO_4 ligand, which shifts the catalytic activity closer to the top of the activity volcano. No such effect is possible on platinum, as the catalyst is a 3-dimensional nanoparticle. In this case, adsorption of phosphate anions leads inevitably to reducing the number of available active sites, which is equivalent to a reduction of the catalytic activity.

6.2 Outlook

Based on the combined experimental and theoretical insight into the catalysts studied in this thesis, the following topics are recognized as particularly worth studying in the future:

1. Supported N-doped graphene.

Electron donating properties of the support are likely closely related to the work function. Desirable materials would possess intermediate work functions between iron and iron carbide. This could be determined in a rather inexpensive computational screening study. Possible candidates are metals like cobalt, nickel, and copper, as their typical work functions are slightly higher than the work function of iron surfaces [58].

2. Anion effects in M-N-C catalysts.

Mineral acid remainders acting as ligands for the FeN_4 moiety in the Fe-N-C catalyst were shown to decrease binding energies of the ORR intermediates (relative to water ligand). The effect was more apparent in the case of chloride than a dihydrogen phosphate ligand. As a result, $\text{H}_2\text{PO}_4\text{-FeN}_4$ structure was more active, and Cl-FeN_4 was less active than $\text{H}_2\text{O-FeN}_4$.

ORR activity of the MN_4 moiety can be regulated by the central atom M. A specific combination of M and acid may result in an active site, which catalytic activity surpasses that of $\text{H}_2\text{PO}_4\text{-FeN}_4$. For example, MnN_4 is known to bind ORR intermediates stronger than FeN_4 [127]. It is possible that, combined with the weakening effect of the Cl ligand, the Cl-MnN_4 structure is very close to the top of the ORR activity volcano. Other transition metal atoms may also be studied, as well as other electrolytes (*e.g.*, hydrobromic acid).

Appendix A

Supplementary material

A.1 Implicit and explicit solvation of anions at the Fe-N-C catalyst

In Chapter 5, implicit solvation is employed to model interactions of solvent with ORR intermediates, as well as with adsorbed anions formed by acid deprotonation. This may raise the question whether solvation of species like ClO_4 , H_xSO_4 , and H_xPO_4 , which are bigger and more complex than ORR intermediates, can be described accurately without referring to the granular structure of the solvent.

To answer this question, adsorption Gibbs free energies of two anions, OH^- and HSO_4^- , are calculated using both the implicit and explicit solvation approach. For the latter, the method follows the same thermodynamic cycle as shown in Fig. 5.5, except that 10 H_2O molecules are used instead of continuum solvent. The water structure is optimized using the minima hopping method, as described in Section 2.3.1. Table A.1 shows that both approaches result in similar adsorption Gibbs free energies of the two anions.

Table A.1: Adsorption Gibbs free energies (in eV) of OH^- and HSO_4^- anions in implicit and explicit solvent.

Solvation	$\Delta_{\text{ads}}G(\text{OH}^-)$	$\Delta_{\text{ads}}G(\text{HSO}_4^-)$	$\Delta(\Delta_{\text{ads}}G)$
implicit	0.944	0.766	0.178
explicit, 10 H_2O	0.914	0.794	0.120
explicit, 14 H_2O	—	—	0.268
explicit, 22 H_2O	—	—	0.175

The difference $\Delta(\Delta_{\text{ads}}G) = \Delta_{\text{ads}}G(\text{OH}^-) - \Delta_{\text{ads}}G(\text{HSO}_4^-)$ was also calculated with 14 and 22 H_2O molecules (though with gas phase water reference, so the individual adsorption energies have not been calculated). The values of $\Delta(\Delta_{\text{ads}}G)$ obtained with explicit water model oscillate around the one from the implicit solvation model, which makes the use of the much less compu-

tationally demanding implicit solvation model legitimate. All the considered systems with explicit water molecules are shown in Fig. A.1.

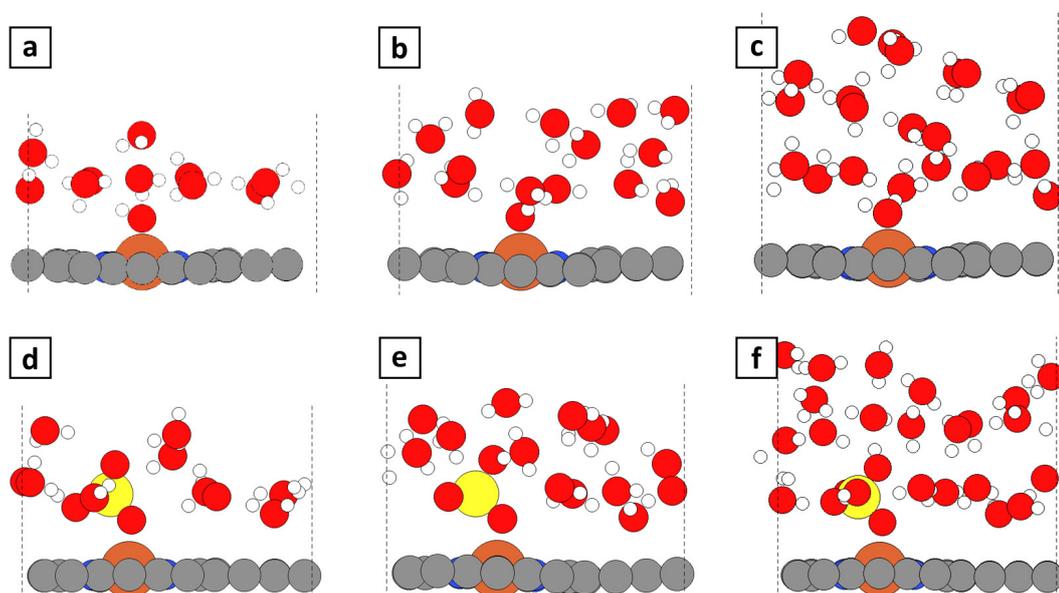


Figure A.1: Side views of the optimized structures of OH^- and HSO_4^- anions adsorbed on Fe-N-C catalyst model with explicit solvation: (a) $\text{FeN}_4\text{-OH}/10 \text{H}_2\text{O}$, (b) $\text{FeN}_4\text{-OH}/14 \text{H}_2\text{O}$, (c) $\text{FeN}_4\text{-OH}/22 \text{H}_2\text{O}$, (d) $\text{FeN}_4\text{-HSO}_4/10 \text{H}_2\text{O}$, (e) $\text{FeN}_4\text{-HSO}_4/14 \text{H}_2\text{O}$, (f) $\text{FeN}_4\text{-HSO}_4/22 \text{H}_2\text{O}$. Color code for atoms: H – white, C – gray, N – blue, O – red, S – yellow, Fe – orange.

References

- [1] W. Vielstich, A. Lamm, and H. Gasteiger. *Handbook of Fuel Cells: Fundamentals, Technology, Applications*. Wiley, Chichester, 2003.
- [2] EG & G Services Inc. and National Energy Technology Laboratory (U.S.). *Fuel cell handbook [electronic resource]*. U.S. Dept. of Energy, Office of Fossil Energy, National Energy Technology Laboratory Morgantown, WV, 7th ed. edition, 2004. URL <http://purl.access.gpo.gov/GPO/LPS115918>.
- [3] Yun Wang, Ken S. Chen, Jeffrey Mishler, Sung Chan Cho, and Xavier Cordobes Adroher. A review of polymer electrolyte membrane fuel cells: Technology, applications, and needs on fundamental research. *Appl. Energy*, 88(4):981–1007, 2011. doi: 10.1016/j.apenergy.2010.09.030. URL <http://www.sciencedirect.com/science/article/pii/S0306261910003958>.
- [4] Yao Nie, Li Li, and Zidong Wei. Recent advancements in Pt and Pt-free catalysts for oxygen reduction reaction. *Chem. Soc. Rev.*, 44:2168–2201, 2015. doi: 10.1039/C4CS00484A. URL <http://dx.doi.org/10.1039/C4CS00484A>.
- [5] Wei Xia, Asif Mahmood, Zibin Liang, Ruqiang Zou, and Shaojun Guo. Earth-abundant nanomaterials for oxygen reduction. *Angew. Chem. Int. Ed.*, 55(8):2650–2676, 2016. doi: 10.1002/anie.201504830. URL <http://dx.doi.org/10.1002/anie.201504830>.
- [6] Hoon T. Chung, David A. Cullen, Drew Higgins, Brian T. Sneed, Edward F. Holby, Karren L. More, and Piotr Zelenay. Direct atomic-level insight into the active sites of a high-performance PGM-free ORR catalyst. *Science*, 357(6350):479–484, 2017. doi: 10.1126/science.aan2255. URL <http://science.sciencemag.org/content/357/6350/479>.
- [7] Young Jin Sa, Dong-Jun Seo, Jinwoo Woo, Jung Tae Lim, Jae Yeong Cheon, Seung Yong Yang, Jae Myeong Lee, Dongwoo Kang, Tae Joo Shin, Hyeon Suk Shin, Hu Young Jeong, Chul Sung Kim, Min Gyu Kim, Tae-Young Kim, and Sang Hoon Joo. A general approach to preferential formation of active Fe-N_x sites in Fe-N/C electrocatalysts for efficient oxygen reduction reaction. *J. Am. Chem. Soc.*, 138(45):15046–15056, 2016. doi: 10.1021/jacs.6b09470. URL <https://doi.org/10.1021/jacs.6b09470>.

- [8] Ambarish Kulkarni, Samira Siahrostami, Anjali Patel, and Jens K. Nørskov. Understanding catalytic activity trends in the oxygen reduction reaction. *Chem. Rev.*, 2018. doi: 10.1021/acs.chemrev.7b00488. URL <https://doi.org/10.1021/acs.chemrev.7b00488>.
- [9] J. K. Nørskov, J. Rossmeisl, A. Logadottir, L. Lindqvist, J. R. Kitchin, T. Bligaard, and H. Jónsson. Origin of the overpotential for oxygen reduction at a fuel-cell cathode. *J. Phys. Chem. B*, 108(46):17886–17892, 2004. doi: 10.1021/jp047349j. URL <http://dx.doi.org/10.1021/jp047349j>.
- [10] H. J. Yan, B. Xu, S. Q. Shi, and C. Y. Ouyang. First-principles study of the oxygen adsorption and dissociation on graphene and nitrogen doped graphene for Li-air batteries. *J. Appl. Phys.*, 112(10):104316, 2012. doi: 10.1063/1.4766919. URL <http://dx.doi.org/10.1063/1.4766919>.
- [11] F. Abild-Pedersen, J. Greeley, F. Studt, J. Rossmeisl, T. R. Munter, P. G. Moses, E. Skúlason, T. Bligaard, and J. K. Nørskov. Scaling properties of adsorption energies for hydrogen-containing molecules on transition-metal surfaces. *Phys. Rev. Lett.*, 99:016105, Jul 2007. doi: 10.1103/PhysRevLett.99.016105. URL <http://link.aps.org/doi/10.1103/PhysRevLett.99.016105>.
- [12] J. Rossmeisl, A. Logadottir, and J.K. Nørskov. Electrolysis of water on (oxidized) metal surfaces. *Chem. Phys.*, 319(1-3):178–184, 2005. doi: 10.1016/j.chemphys.2005.05.038. URL <http://www.sciencedirect.com/science/article/pii/S0301010405002053>.
- [13] Isabela C. Man, Hai-Yan Su, Federico Calle-Vallejo, Heine A. Hansen, José I. Martínez, Nilay G. Inoglu, John Kitchin, Thomas F. Jaramillo, Jens K. Nørskov, and Jan Rossmeisl. Universality in oxygen evolution electrocatalysis on oxide surfaces. *ChemCatChem*, 3(7):1159–1165, 2011. doi: 10.1002/cctc.201000397. URL <http://dx.doi.org/10.1002/cctc.201000397>.
- [14] Joseph H. Montoya, Linsey C. Seitz, Pongkarn Chakthranont, Aleksandra Vojvodic, Thomas F. Jaramillo, and Jens K. Nørskov. Materials for solar fuels and chemicals. *Nat. Mater.*, 16:70, 2017. doi: 10.1038/nmat4778. URL <http://dx.doi.org/10.1038/nmat4778>.
- [15] Yonghong Bing, Hansan Liu, Lei Zhang, Dave Ghosh, and Jiujuun Zhang. Nanostructured Pt-alloy electrocatalysts for PEM fuel cell oxygen reduction reaction. *Chem. Soc. Rev.*, 39:2184–2202, 2010. doi: 10.1039/B912552C. URL <http://dx.doi.org/10.1039/B912552C>.
- [16] Ifan E. L. Stephens, Alexander S. Bondarenko, Ulrik Gronbjerg, Jan Rossmeisl, and Ib Chorkendorff. Understanding the electrocatalysis of oxygen reduction on platinum and its alloys. *Energy Environ. Sci.*, 5: 6744–6762, 2012. doi: 10.1039/C2EE03590A. URL <http://dx.doi.org/10.1039/C2EE03590A>.

- [17] Jianbo Wu and Hong Yang. Platinum-based oxygen reduction electrocatalysts. *Acc. Chem. Res.*, 46(8):1848–1857, 2013. doi: 10.1021/ar300359w. URL <https://doi.org/10.1021/ar300359w>.
- [18] Lin Li, Ask H. Larsen, Nichols A. Romero, Vitali A. Morozov, Christian Glinsvad, Frank Abild-Pedersen, Jeff Greeley, Karsten W. Jacobsen, and Jens K. Nørskov. Investigation of catalytic finite-size-effects of platinum metal clusters. *J. Phys. Chem. Lett.*, 4(1):222–226, 2013. doi: 10.1021/jz3018286. URL <http://dx.doi.org/10.1021/jz3018286>.
- [19] Raymond Jasinski. A new fuel cell cathode catalyst. *Nature*, 201(4925):1212–1213, 1964. doi: 10.1038/2011212a0. URL <http://dx.doi.org/10.1038/2011212a0>.
- [20] Eric Proietti, Frédéric Jaouen, Michel Lefèvre, Nicholas Larouche, Juan Tian, Juan Herranz, and Jean-Pol Dodelet. Iron-based cathode catalyst with enhanced power density in polymer electrolyte membrane fuel cells. *Nat. Commun.*, 2:416, 2011. doi: 10.1038/ncomms1427. URL <http://dx.doi.org/10.1038/ncomms1427>.
- [21] Juan Herranz, Frédéric Jaouen, Michel Lefèvre, Ulrike I. Kramm, Eric Proietti, Jean-Pol Dodelet, Peter Bogdanoff, Sebastian Fiechter, Irmgard Abs-Wurmbach, Patrick Bertrand, Thomas M. Arruda, and Sanjeev Mukerjee. Unveiling N-protonation and anion-binding effects on Fe/N/C catalysts for O₂ reduction in Proton-Exchange-Membrane Fuel Cells. *J. Phys. Chem. C*, 115(32):16087–16097, 2011. doi: 10.1021/jp2042526. URL <https://doi.org/10.1021/jp2042526>.
- [22] Gang Wu, Karren L. More, Christina M. Johnston, and Piotr Zelenay. High-performance electrocatalysts for oxygen reduction derived from polyaniline, iron, and cobalt. *Science*, 332(6028):443–447, 2011. doi: 10.1126/science.1200832. URL <http://www.sciencemag.org/content/332/6028/443.abstract>.
- [23] Ulrike I. Kramm, Juan Herranz, Nicholas Larouche, Thomas M. Arruda, Michel Lefèvre, Frédéric Jaouen, Peter Bogdanoff, Sebastian Fiechter, Irmgard Abs-Wurmbach, Sanjeev Mukerjee, and Jean-Pol Dodelet. Structure of the catalytic sites in Fe/N/C-catalysts for O₂-reduction in PEM fuel cells. *Phys. Chem. Chem. Phys.*, 14:11673–11688, 2012. doi: 10.1039/C2CP41957B. URL <http://dx.doi.org/10.1039/C2CP41957B>.
- [24] Ulrike I. Kramm, Michel Lefèvre, Nicholas Larouche, Dieter Schmeisser, and Jean-Pol Dodelet. Correlations between mass activity and physicochemical properties of Fe/N/C catalysts for the ORR in PEM Fuel Cell via ⁵⁷Fe Mössbauer spectroscopy and other techniques. *J. Am. Chem. Soc.*, 136(3):978–985, 2014. doi: 10.1021/ja410076f. URL <https://doi.org/10.1021/ja410076f>.
- [25] Csaba E. Szakacs, Michel Lefèvre, Ulrike I. Kramm, Jean-Pol Dodelet, and Francois Vidal. A Density Functional Theory study of catalytic sites

- for oxygen reduction in Fe/N/C catalysts used in H₂/O₂ fuel cells. *Phys. Chem. Chem. Phys.*, 16:13654–13661, 2014. doi: 10.1039/C3CP55331K. URL <http://dx.doi.org/10.1039/C3CP55331K>.
- [26] Andrea Zitolo, Vincent Goellner, Vanessa Armel, Moulay-Tahar Sougrati, Tzonka Mineva, Lorenzo Stievano, Emiliano Fonda, and Frédéric Jaouen. Identification of catalytic sites for oxygen reduction in iron- and nitrogen-doped graphene materials. *Nat. Mater.*, 14:937–942, 2015. doi: 10.1038/nmat4367. URL <http://dx.doi.org/10.1038/nmat4367>.
- [27] Edward F. Holby, Gang Wu, Piotr Zelenay, and Christopher D. Taylor. Structure of Fe–N_x–C defects in oxygen reduction reaction catalysts from first-principles modeling. *J. Phys. Chem. C*, 118(26):14388–14393, 2014. doi: 10.1021/jp503266h. URL <https://doi.org/10.1021/jp503266h>.
- [28] Edward F. Holby and Piotr Zelenay. Linking structure to function: The search for active sites in non-platinum group metal oxygen reduction reaction catalysts. *Nano Energy*, 29:54–64, 2016. doi: <https://doi.org/10.1016/j.nanoen.2016.05.025>. URL <http://www.sciencedirect.com/science/article/pii/S221128551630146X>.
- [29] Liming Dai, Yuhua Xue, Liangti Qu, Hyun-Jung Choi, and Jong-Beom Baek. Metal-free catalysts for oxygen reduction reaction. *Chem. Rev.*, 115(11):4823–4892, 2015. doi: 10.1021/cr5003563. URL <http://dx.doi.org/10.1021/cr5003563>.
- [30] Dingshan Yu, Qiang Zhang, and Liming Dai. Highly efficient metal-free growth of nitrogen-doped single-walled carbon nanotubes on plasma-etched substrates for oxygen reduction. *J. Am. Chem. Soc.*, 132(43):15127–15129, 2010. doi: 10.1021/ja105617z. URL <http://dx.doi.org/10.1021/ja105617z>.
- [31] Hideharu Niwa, Koji Horiba, Yoshihisa Harada, Masaharu Oshima, Takashi Ikeda, Kiyoyuki Terakura, Jun ichi Ozaki, and Seizo Miyata. X-ray absorption analysis of nitrogen contribution to oxygen reduction reaction in carbon alloy cathode catalysts for polymer electrolyte fuel cells. *J. Power Sources*, 187(1):93–97, 2009. doi: <https://doi.org/10.1016/j.jpowsour.2008.10.064>. URL <http://www.sciencedirect.com/science/article/pii/S0378775308019770>.
- [32] Ruili Liu, Dongqing Wu, Xinliang Feng, and Klaus Müllen. Nitrogen-doped ordered mesoporous graphitic arrays with high electrocatalytic activity for oxygen reduction. *Angew. Chem.*, 122(14):2619–2623, 2010. doi: 10.1002/ange.200907289. URL <http://dx.doi.org/10.1002/ange.200907289>.
- [33] Wenhui He, Chunhuan Jiang, Jiabo Wang, and Lehui Lu. High-rate oxygen electroreduction over graphitic-N species exposed on 3D hierarchically porous nitrogen-doped carbons. *Angew. Chem. Int. Ed.*,

- 53(36):9503–9507, 2014. doi: 10.1002/anie.201404333. URL <http://dx.doi.org/10.1002/anie.201404333>.
- [34] Nalini P. Subramanian, Xuguang Li, Vijayadurda Nallathambi, Swaminatha P. Kumaraguru, Hector Colon-Mercado, Gang Wu, Jong-Won Lee, and Branko N. Popov. Nitrogen-modified carbon-based catalysts for oxygen reduction reaction in polymer electrolyte membrane fuel cells. *J. Power Sources*, 188(1):38–44, 2009. doi: <https://doi.org/10.1016/j.jpowsour.2008.11.087>. URL <http://www.sciencedirect.com/science/article/pii/S0378775308022325>.
- [35] Chitturi Venkateswara Rao, Carlos R. Cabrera, and Yasuyuki Ishikawa. In search of the active site in nitrogen-doped carbon nanotube electrodes for the oxygen reduction reaction. *J. Phys. Chem. Lett.*, 1(18):2622–2627, 2010. doi: 10.1021/jz100971v. URL <https://doi.org/10.1021/jz100971v>.
- [36] Tan Xing, Yao Zheng, Lu Hua Li, Bruce C. C. Cowie, Daniel Gunzelmann, Shi Zhang Qiao, Shaoming Huang, and Ying Chen. Observation of active sites for oxygen reduction reaction on nitrogen-doped multilayer graphene. *ACS Nano*, 8(7):6856–6862, 2014. doi: 10.1021/nm501506p. URL <https://doi.org/10.1021/nm501506p>.
- [37] Linfei Lai, Jeffrey R. Potts, Da Zhan, Liang Wang, Chee Kok Poh, Chunhua Tang, Hao Gong, Zexiang Shen, Jianyi Lin, and Rodney S. Ruoff. Exploration of the active center structure of nitrogen-doped graphene-based catalysts for oxygen reduction reaction. *Energy Environ. Sci.*, 5:7936–7942, 2012. doi: 10.1039/C2EE21802J. URL <http://dx.doi.org/10.1039/C2EE21802J>.
- [38] Wei Ding, Zidong Wei, Siguo Chen, Xueqiang Qi, Tao Yang, Jinsong Hu, Dong Wang, Li-Jun Wan, Shahnaz Fatima Alvi, and Li Li. Space-confinement-induced synthesis of pyridinic- and pyrrolic-nitrogen-doped graphene for the catalysis of oxygen reduction. *Angew. Chem. Int. Ed.*, 52(45):11755–11759, 2013. doi: 10.1002/anie.201303924. URL <http://dx.doi.org/10.1002/anie.201303924>.
- [39] Donghui Guo, Riku Shibuya, Chisato Akiba, Shunsuke Saji, Takahiro Kondo, and Junji Nakamura. Active sites of nitrogen-doped carbon materials for oxygen reduction reaction clarified using model catalysts. *Science*, 351(6271):361–365, 2016. doi: 10.1126/science.aad0832. URL <http://science.sciencemag.org/content/351/6271/361>.
- [40] John W. F. To, Jia Wei Desmond Ng, Samira Siahrostami, Ai Leen Koh, Yangjin Lee, Zihua Chen, Kara D. Fong, Shucheng Chen, Jiajun He, Won-Gyu Bae, Jennifer Wilcox, Hu Young Jeong, Kwanypyo Kim, Felix Studt, Jens K. Nørskov, Thomas F. Jaramillo, and Zhenan Bao. High-performance oxygen reduction and evolution carbon catalysis: From mechanistic studies to device integration. *Nano*

- Res.*, 10(4):1163–1177, 2017. doi: 10.1007/s12274-016-1347-8. URL <http://dx.doi.org/10.1007/s12274-016-1347-8>.
- [41] Dehui Deng, Liang Yu, Xiaoqi Chen, Guoxiong Wang, Li Jin, Xiulian Pan, Jiao Deng, Gongquan Sun, and Xinhe Bao. Iron encapsulated within pod-like carbon nanotubes for oxygen reduction reaction. *Angew. Chem. Int. Ed.*, 52(1):371–375, 2013. doi: 10.1002/anie.201204958. URL <http://dx.doi.org/10.1002/anie.201204958>.
- [42] Jason A. Varnell, Edmund C. M. Tse, Charles E. Schulz, Tim T. Fister, Richard T. Haasch, Janis Timoshenko, Anatoly I. Frenkel, and Andrew A. Gewirth. Identification of carbon-encapsulated iron nanoparticles as active species in non-precious metal oxygen reduction catalysts. *Nat. Commun.*, 7:12582, 2016. doi: 10.1038/ncomms12582. URL <http://dx.doi.org/10.1038/ncomms12582>.
- [43] Lijie Zhong, Yang Hu, Lars Nilausen Cleemann, Chao Pan, Jakob Sværke, Jens Oluf Jensen, and Qingfeng Li. Encapsulated iron-based oxygen reduction electrocatalysts by high pressure pyrolysis. *Int. J. Hydrogen Energy*, 42(36):22887–22896, 2017. doi: <https://doi.org/10.1016/j.ijhydene.2017.07.093>. URL <http://www.sciencedirect.com/science/article/pii/S0360319917329191>.
- [44] Jiao Deng, Liang Yu, Dehui Deng, Xiaoqi Chen, Fan Yang, and Xinhe Bao. Highly active reduction of oxygen on a FeCo alloy catalyst encapsulated in pod-like carbon nanotubes with fewer walls. *J. Mater. Chem. A*, 1:14868–14873, 2013. doi: 10.1039/C3TA13759G. URL <http://dx.doi.org/10.1039/C3TA13759G>.
- [45] Hoon T. Chung, Jong H. Won, and Piotr Zelenay. Active and stable carbon nanotube/nanoparticle composite electrocatalyst for oxygen reduction. *Nat. Commun.*, 4, 2013. doi: 10.1038/ncomms2944. URL <http://dx.doi.org/10.1038/ncomms2944>.
- [46] Yang Hu, Jens Oluf Jensen, Wei Zhang, Lars N. Cleemann, Wei Xing, Niels J. Bjerrum, and Qingfeng Li. Hollow spheres of iron carbide nanoparticles encased in graphitic layers as oxygen reduction catalysts. *Angew. Chem. Int. Ed.*, 53(14):3675–3679, 2014. doi: 10.1002/anie.201400358. URL <http://dx.doi.org/10.1002/anie.201400358>.
- [47] Jean-Pol Dodelet, Régis Chenitz, Lijun Yang, and Michel Lefèvre. A new catalytic site for the electroreduction of oxygen? *ChemCatChem*, 6(7):1866–1867, 2014. doi: 10.1002/cctc.201402133. URL <http://dx.doi.org/10.1002/cctc.201402133>.
- [48] John P. Perdew and Karla Schmidt. Jacob’s ladder of density functional approximations for the exchange-correlation energy. *AIP Conf. Proc.*, 577(1):1–20, 2001. doi: 10.1063/1.1390175. URL <http://scitation.aip.org/content/aip/proceeding/aipcp/10.1063/1.1390175>.

- [49] John P. Perdew, Kieron Burke, and Matthias Ernzerhof. Generalized Gradient Approximation made simple. *Phys. Rev. Lett.*, 77:3865–3868, Oct 1996. doi: 10.1103/PhysRevLett.77.3865. URL <http://link.aps.org/doi/10.1103/PhysRevLett.77.3865>.
- [50] B. Hammer, L. B. Hansen, and J. K. Nørskov. Improved adsorption energetics within density-functional theory using revised Perdew-Burke-Ernzerhof functionals. *Phys. Rev. B*, 59:7413–7421, Mar 1999. doi: 10.1103/PhysRevB.59.7413. URL <http://link.aps.org/doi/10.1103/PhysRevB.59.7413>.
- [51] Jess Wellendorff, Keld T. Lundgaard, Andreas Møgelhøj, Vivien Petzold, David D. Landis, Jens K. Nørskov, Thomas Bligaard, and Karsten W. Jacobsen. Density functionals for surface science: Exchange-correlation model development with Bayesian error estimation. *Phys. Rev. B*, 85:235149, Jun 2012. doi: 10.1103/PhysRevB.85.235149. URL <http://link.aps.org/doi/10.1103/PhysRevB.85.235149>.
- [52] Kyuho Lee, Éamonn D. Murray, Lingzhu Kong, Bengt I. Lundqvist, and David C. Langreth. Higher-accuracy van der Waals density functional. *Phys. Rev. B*, 82:081101, Aug 2010. doi: 10.1103/PhysRevB.82.081101. URL <http://link.aps.org/doi/10.1103/PhysRevB.82.081101>.
- [53] Jess Wellendorff, Trent L. Silbaugh, Delfina Garcia-Pintos, Jens K. Nørskov, Thomas Bligaard, Felix Studt, and Charles T. Campbell. A benchmark database for adsorption bond energies to transition metal surfaces and comparison to selected DFT functionals. *Surf. Sci.*, 640:36–44, 2015. doi: 10.1016/j.susc.2015.03.023. URL <http://www.sciencedirect.com/science/article/pii/S0039602815000837>.
- [54] Andrew J. Medford, Jess Wellendorff, Aleksandra Vojvodic, Felix Studt, Frank Abild-Pedersen, Karsten W. Jacobsen, Thomas Bligaard, and Jens K. Nørskov. Assessing the reliability of calculated catalytic ammonia synthesis rates. *Science*, 345(6193):197–200, 2014. doi: 10.1126/science.1253486. URL <http://science.sciencemag.org/content/345/6193/197>.
- [55] P. A. M. Dirac. Note on exchange phenomena in the thomas atom. *Math. Proc. Cambridge Philos. Soc.*, 26:376–385, 7 1930. doi: 10.1017/S0305004100016108. URL http://journals.cambridge.org/article_S0305004100016108.
- [56] John P. Perdew and Yue Wang. Accurate and simple analytic representation of the electron-gas correlation energy. *Phys. Rev. B*, 45:13244–13249, Jun 1992. doi: 10.1103/PhysRevB.45.13244. URL <http://link.aps.org/doi/10.1103/PhysRevB.45.13244>.
- [57] Christopher J. Cramer. *Essentials of computational chemistry: Theories and models*. John Wiley & Sons Ltd, West Sussex, England, 2nd edition, 2004.

- [58] W.M. Haynes, editor. *CRC handbook of chemistry and physics: A ready-reference book of chemical and physical data*. CRC Press, Boca Raton, 95th edition, 2014.
- [59] NIST Computational Chemistry Comparison and Benchmark Database, NIST Standard Reference Database Number 101, Release 18, October 2016, Editor: Russell D. Johnson III. URL <http://cccbdb.nist.gov/>.
- [60] DIPPR, Project 801 – Full Version. Design Institute for Physical Property Research/AIChE. 2016.
- [61] R. O. Jones and O. Gunnarsson. The density functional formalism, its applications and prospects. *Rev. Mod. Phys.*, 61:689–746, Jul 1989. doi: 10.1103/RevModPhys.61.689. URL <http://link.aps.org/doi/10.1103/RevModPhys.61.689>.
- [62] Stefan Kurth, John P. Perdew, and Peter Blaha. Molecular and solid-state tests of density functional approximations: LSD, GGAs, and meta-GGAs. *Int. J. Quantum Chem.*, 75(4-5):889–909, 1999. doi: 10.1002/(SICI)1097-461X(1999)75:4/5<889::AID-QUA54>3.0.CO;2-8. URL [http://dx.doi.org/10.1002/\(SICI\)1097-461X\(1999\)75:4/5<889::AID-QUA54>3.0.CO;2-8](http://dx.doi.org/10.1002/(SICI)1097-461X(1999)75:4/5<889::AID-QUA54>3.0.CO;2-8).
- [63] Rune Christensen, Heine A. Hansen, and Tejs Vegge. Identifying systematic DFT errors in catalytic reactions. *Catal. Sci. Technol.*, 5:4946–4949, 2015. doi: 10.1039/C5CY01332A. URL <http://dx.doi.org/10.1039/C5CY01332A>.
- [64] Rune Christensen, Heine A. Hansen, Colin F. Dickens, Jens K. Nørskov, and Tejs Vegge. Functional independent scaling relation for ORR/OER catalysts. *J. Phys. Chem. C*, 120(43):24910–24916, 2016. doi: 10.1021/acs.jpcc.6b09141. URL <http://dx.doi.org/10.1021/acs.jpcc.6b09141>.
- [65] Felix Studt. The oxygen reduction reaction on nitrogen-doped graphene. *Catal. Lett.*, 143(1):58–60, 2013. doi: 10.1007/s10562-012-0918-x. URL <http://dx.doi.org/10.1007/s10562-012-0918-x>.
- [66] Ralph Koitz, Jens K. Nørskov, and Felix Studt. A systematic study of metal-supported boron nitride materials for the oxygen reduction reaction. *Phys. Chem. Chem. Phys.*, 17:12722–12727, 2015. doi: 10.1039/C5CP01384D. URL <http://dx.doi.org/10.1039/C5CP01384D>.
- [67] Martin Hangaard Hansen and Jan Rossmeisl. pH in grand canonical statistics of an electrochemical interface. *J. Phys. Chem. C*, 120(51):29135–29143, 2016. doi: 10.1021/acs.jpcc.6b09019. URL <http://dx.doi.org/10.1021/acs.jpcc.6b09019>.

- [68] Vladimir Tripković, Egill Skúlason, Samira Siahrostami, Jens K. Nørskov, and Jan Rossmeisl. The oxygen reduction reaction mechanism on Pt(111) from Density Functional Theory calculations. *Electrochim. Acta*, 55(27):7975–7981, 2010. doi: 10.1016/j.electacta.2010.02.056. URL <http://www.sciencedirect.com/science/article/pii/S0013468610003178>.
- [69] Liang Yu, Xiulian Pan, Xiaoming Cao, P. Hu, and Xinhe Bao. Oxygen reduction reaction mechanism on nitrogen-doped graphene: A Density Functional Theory study. *J. Catal.*, 282(1):183–190, 2011. doi: 10.1016/j.jcat.2011.06.015. URL <http://www.sciencedirect.com/science/article/pii/S0021951711002016>.
- [70] Vladimir Tripkovic and Tejs Vegge. Potential- and rate-determining step for oxygen reduction on Pt(111). *J. Phys. Chem. C*, 121(48):26785–26793, 2017. doi: 10.1021/acs.jpcc.7b07472. URL <http://dx.doi.org/10.1021/acs.jpcc.7b07472>.
- [71] Stefan Goedecker. Minima hopping: An efficient search method for the global minimum of the potential energy surface of complex molecular systems. *J. Chem. Phys.*, 120(21):9911–9917, 2004. doi: 10.1063/1.1724816. URL <http://scitation.aip.org/content/aip/journal/jcp/120/21/10.1063/1.1724816>.
- [72] Ask Hjorth Larsen, Jens Jørgen Mortensen, Jakob Blomqvist, Ivano E Castelli, Rune Christensen, Marcin Dułak, Jesper Friis, Michael N Groves, Bjørk Hammer, Cory Hargus, Eric D Hermes, Paul C Jennings, Peter Bjerre Jensen, James Kermode, John R Kitchin, Esben Leonhard Kolsbjerg, Joseph Kubal, Kristen Kaasbjerg, Steen Lysgaard, Jón Bergmann Maronsson, Tristan Maxson, Thomas Olsen, Lars Pastewka, Andrew Peterson, Carsten Rostgaard, Jakob Schiøtz, Ole Schütt, Mikkel Strange, Kristian S Thygesen, Tejs Vegge, Lasse Vilhelmsen, Michael Walter, Zhenhua Zeng, and Karsten W Jacobsen. The atomic simulation environment—a Python library for working with atoms. *J. Phys.: Condens. Matter*, 29(27):273002, 2017. URL <http://stacks.iop.org/0953-8984/29/i=27/a=273002>.
- [73] Andrew A. Peterson. Global optimization of adsorbate–surface structures while preserving molecular identity. *Top. Catal.*, 57(1):40–53, 2014. doi: 10.1007/s11244-013-0161-8. URL <http://dx.doi.org/10.1007/s11244-013-0161-8>.
- [74] Kiran Mathew, Ravishankar Sundararaman, Kendra Letchworth-Weaver, T. A. Arias, and Richard G. Hennig. Implicit solvation model for density-functional study of nanocrystal surfaces and reaction pathways. *J. Chem. Phys.*, 140(8):084106, 2014. doi: 10.1063/1.4865107. URL <http://scitation.aip.org/content/aip/journal/jcp/140/8/10.1063/1.4865107>.

-
- [75] K. Mathew and R. G. Hennig. Implicit self-consistent description of electrolyte in plane-wave density-functional theory. arXiv:1601.03346, 2016. URL <http://arxiv.org/abs/1601.03346>.
- [76] G. Kresse and J. Hafner. *Ab initio* molecular dynamics for liquid metals. *Phys. Rev. B*, 47:558–561, Jan 1993. doi: 10.1103/PhysRevB.47.558. URL <http://link.aps.org/doi/10.1103/PhysRevB.47.558>.
- [77] G. Kresse and J. Hafner. *Ab initio* molecular-dynamics simulation of the liquid-metal–amorphous-semiconductor transition in germanium. *Phys. Rev. B*, 49:14251–14269, May 1994. doi: 10.1103/PhysRevB.49.14251. URL <http://link.aps.org/doi/10.1103/PhysRevB.49.14251>.
- [78] G. Kresse and J. Furthmüller. Efficiency of ab-initio total energy calculations for metals and semiconductors using a plane-wave basis set. *Comput. Mater. Sci.*, 6(1):15–50, 1996. doi: 10.1016/0927-0256(96)00008-0. URL <http://www.sciencedirect.com/science/article/pii/0927025696000080>.
- [79] G. Kresse and J. Furthmüller. Efficient iterative schemes for *ab initio* total-energy calculations using a plane-wave basis set. *Phys. Rev. B*, 54:11169–11186, Oct 1996. doi: 10.1103/PhysRevB.54.11169. URL <http://link.aps.org/doi/10.1103/PhysRevB.54.11169>.
- [80] P. E. Blöchl. Projector augmented-wave method. *Phys. Rev. B*, 50:17953–17979, Dec 1994. doi: 10.1103/PhysRevB.50.17953. URL <http://link.aps.org/doi/10.1103/PhysRevB.50.17953>.
- [81] G. Kresse and D. Joubert. From ultrasoft pseudopotentials to the projector augmented-wave method. *Phys. Rev. B*, 59:1758–1775, Jan 1999. doi: 10.1103/PhysRevB.59.1758. URL <http://link.aps.org/doi/10.1103/PhysRevB.59.1758>.
- [82] Hendrik J. Monkhorst and James D. Pack. Special points for Brillouin-zone integrations. *Phys. Rev. B*, 13:5188–5192, Jun 1976. doi: 10.1103/PhysRevB.13.5188. URL <http://link.aps.org/doi/10.1103/PhysRevB.13.5188>.
- [83] Wissam A. Saidi. Oxygen reduction electrocatalysis using N-doped graphene quantum-dots. *J. Phys. Chem. Lett.*, 4(23):4160–4165, 2013. doi: 10.1021/jz402090d. URL <http://dx.doi.org/10.1021/jz402090d>.
- [84] Dohyun Kwak, Abhishek Khetan, Seunghyo Noh, Heinz Pitsch, and Byungchan Han. First principles study of morphology, doping level, and water solvation effects on the catalytic mechanism of nitrogen-doped graphene in the oxygen reduction reaction. *ChemCatChem*, 6(9):2662–2670, 2014. doi: 10.1002/cctc.201402248. URL <http://dx.doi.org/10.1002/cctc.201402248>.

- [85] Guo-Liang Chai, Zhufeng Hou, Da-Jun Shu, Takashi Ikeda, and Kiyoyuki Terakura. Active sites and mechanisms for oxygen reduction reaction on nitrogen-doped carbon alloy catalysts: Stone–Wales defect and curvature effect. *J. Am. Chem. Soc.*, 136(39):13629–13640, 2014. doi: 10.1021/ja502646c. URL <http://dx.doi.org/10.1021/ja502646c>.
- [86] Adolfo Ferre-Vilaplana and Enrique Herrero. Charge transfer, bonding conditioning and solvation effect in the activation of the oxygen reduction reaction on unclustered graphitic-nitrogen-doped graphene. *Phys. Chem. Chem. Phys.*, 17:16238–16242, 2015. doi: 10.1039/C5CP00918A. URL <http://dx.doi.org/10.1039/C5CP00918A>.
- [87] Graeme Henkelman, Andri Arnaldsson, and Hannes Jónsson. A fast and robust algorithm for Bader decomposition of charge density. *Comput. Mater. Sci.*, 36(3):354–360, 2006. doi: 10.1016/j.commatsci.2005.04.010. URL <http://www.sciencedirect.com/science/article/pii/S0927025605001849>.
- [88] G. S. Karlberg, J. Rossmeisl, and J. K. Nørskov. Estimations of electric field effects on the oxygen reduction reaction based on the Density Functional Theory. *Phys. Chem. Chem. Phys.*, 9:5158–5161, 2007. doi: 10.1039/B705938H. URL <http://dx.doi.org/10.1039/B705938H>.
- [89] Shizhong Liu, Michael G. White, and Ping Liu. Mechanism of oxygen reduction reaction on Pt(111) in alkaline solution: Importance of chemisorbed water on surface. *J. Phys. Chem. C*, 120(28):15288–15298, 2016. doi: 10.1021/acs.jpcc.6b05126. URL <http://dx.doi.org/10.1021/acs.jpcc.6b05126>.
- [90] Jing Sun, Ya-Hui Fang, and Zhi-Pan Liu. Electrocatalytic oxygen reduction kinetics on Fe-center of nitrogen-doped graphene. *Phys. Chem. Chem. Phys.*, 16:13733–13740, 2014. doi: 10.1039/C4CP00037D. URL <http://dx.doi.org/10.1039/C4CP00037D>.
- [91] Yan Jiao, Yao Zheng, Mietek Jaroniec, and Shi Zhang Qiao. Origin of the electrocatalytic oxygen reduction activity of graphene-based catalysts: A roadmap to achieve the best performance. *J. Am. Chem. Soc.*, 136(11):4394–4403, 2014. doi: 10.1021/ja500432h. URL <http://dx.doi.org/10.1021/ja500432h>.
- [92] Lu Wang, Huilong Dong, Zhenyu Guo, Liling Zhang, Tingjun Hou, and Youyong Li. Potential application of novel boron-doped graphene nanoribbon as oxygen reduction reaction catalyst. *J. Phys. Chem. C*, 120(31):17427–17434, 2016. doi: 10.1021/acs.jpcc.6b04639. URL <https://doi.org/10.1021/acs.jpcc.6b04639>.
- [93] Greg A. Kimmel, Jesper Matthiesen, Marcel Baer, Christopher J. Mundy, Nikolay G. Petrik, R. Scott Smith, Zdenek Dohnálek, and Bruce D. Kay. No confinement needed: Observation of a metastable

- hydrophobic wetting two-layer ice on graphene. *J. Am. Chem. Soc.*, 131(35):12838–12844, 2009. doi: 10.1021/ja904708f. URL <http://dx.doi.org/10.1021/ja904708f>.
- [94] Chang Hyuck Choi, Hyung-Kyu Lim, Min Wook Chung, Jong Cheol Park, Hyeyoung Shin, Hyungjun Kim, and Seong Ihl Woo. Long-range electron transfer over graphene-based catalyst for high-performing oxygen reduction reactions: Importance of size, N-doping, and metallic impurities. *J. Am. Chem. Soc.*, 136(25):9070–9077, 2014. doi: 10.1021/ja5033474. URL <http://dx.doi.org/10.1021/ja5033474>.
- [95] Elena Voloshina and Yuriy Dedkov. Graphene on metallic surfaces: Problems and perspectives. *Phys. Chem. Chem. Phys.*, 14:13502–13514, 2012. doi: 10.1039/C2CP42171B. URL <http://dx.doi.org/10.1039/C2CP42171B>.
- [96] Mie Andersen, Liv Hornekær, and Bjørk Hammer. Graphene on metal surfaces and its hydrogen adsorption: A meta-GGA functional study. *Phys. Rev. B*, 86:085405, Aug 2012. doi: 10.1103/PhysRevB.86.085405. URL <http://link.aps.org/doi/10.1103/PhysRevB.86.085405>.
- [97] Thomas Olsen, Jun Yan, Jens J. Mortensen, and Kristian S. Thygesen. Dispersive and covalent interactions between graphene and metal surfaces from the Random Phase Approximation. *Phys. Rev. Lett.*, 107:156401, Oct 2011. doi: 10.1103/PhysRevLett.107.156401. URL <http://link.aps.org/doi/10.1103/PhysRevLett.107.156401>.
- [98] Seung Hyo Noh, Do Hyun Kwak, Min Ho Seo, Takeo Ohsaka, and Byungchan Han. First principles study of oxygen reduction reaction mechanisms on N-doped graphene with a transition metal support. *Electrochim. Acta*, 140:225–231, 2014. doi: 10.1016/j.electacta.2014.03.076. URL <http://www.sciencedirect.com/science/article/pii/S0013468614005878>.
- [99] Yang Hu, Jens Oluf Jensen, Wei Zhang, Yunjie Huang, Lars N. Cleemann, Wei Xing, Niels J. Bjerrum, and Qingfeng Li. Direct synthesis of Fe₃C-functionalized graphene by high temperature autoclave pyrolysis for oxygen reduction. *ChemSusChem*, 7(8):2099–2103, 2014. doi: 10.1002/cssc.201402183. URL <http://dx.doi.org/10.1002/cssc.201402183>.
- [100] Yang Hu, Jens Oluf Jensen, Wei Zhang, Santiago Martin, Regis Chenitz, Chao Pan, Wei Xing, Niels J. Bjerrum, and Qingfeng Li. Fe₃C-based oxygen reduction catalysts: Synthesis, hollow spherical structures and applications in fuel cells. *J. Mater. Chem. A*, 3:1752–1760, 2015. doi: 10.1039/C4TA03986F. URL <http://dx.doi.org/10.1039/C4TA03986F>.
- [101] Yang Hu, Lijie Zhong, Jens Oluf Jensen, and Qingfeng Li. Graphene layer encapsulated metal nanoparticles as a new type of non-precious

- metal catalysts for oxygen reduction. *Asia-Pac. J. Chem. Eng.*, 11(3): 382–385, 2016. doi: 10.1002/apj.1986. URL <http://dx.doi.org/10.1002/apj.1986>.
- [102] Virtual NanoLab version 2016.2, QuantumWise A/S. URL www.quantumwise.com.
- [103] Wun C. Chiou Jr. and Emily A. Carter. Structure and stability of Fe₃C-cementite surfaces from first principles. *Surf. Sci.*, 530(1–2):88–100, 2003. doi: 10.1016/S0039-6028(03)00352-2. URL <http://www.sciencedirect.com/science/article/pii/S0039602803003522>.
- [104] P. Błoński and A. Kiejna. Structural, electronic, and magnetic properties of bcc iron surfaces. *Surf. Sci.*, 601(1):123–133, 2007. doi: 10.1016/j.susc.2006.09.013. URL <http://www.sciencedirect.com/science/article/pii/S0039602806009563>.
- [105] N. A. Vinogradov, A. A. Zakharov, V. Kocevski, J. Ruzs, K. A. Simonov, O. Eriksson, A. Mikkelsen, E. Lundgren, A. S. Vinogradov, N. Mårtensson, and A. B. Preobrajenski. Formation and structure of graphene waves on Fe(110). *Phys. Rev. Lett.*, 109:026101, Jul 2012. doi: 10.1103/PhysRevLett.109.026101. URL <http://link.aps.org/doi/10.1103/PhysRevLett.109.026101>.
- [106] Stefan Taubert and Kari Laasonen. The molecular and magnetic structure of carbon-enclosed and partially covered Fe₅₅ particles. *Phys. Chem. Chem. Phys.*, 16:3648–3660, 2014. doi: 10.1039/C3CP54491E. URL <http://dx.doi.org/10.1039/C3CP54491E>.
- [107] Omar Teschke. Imaging ice-like structures formed on HOPG at room temperature. *Langmuir*, 26(22):16986–16990, 2010. doi: 10.1021/la103227j. URL <http://dx.doi.org/10.1021/la103227j>.
- [108] Lijie Zhong, Cathrine Frandsen, Steen Mørup, Yang Hu, Chao Pan, Lars Nilausen Cleemann, Jens Oluf Jensen, and Qingfeng Li. 57Fe-Mössbauer spectroscopy and electrochemical activities of graphitic layer encapsulated iron electrocatalysts for the oxygen reduction reaction. *Appl. Catal., B*, 221:406–412, 2018. doi: <https://doi.org/10.1016/j.apcatb.2017.09.014>. URL <http://www.sciencedirect.com/science/article/pii/S0926337317308391>.
- [109] P. N. Ross and P. C. Andricacos. The effect of H₂PO₄⁻ anion on the kinetics of oxygen reduction on Pt. *J. Electroanal. Chem.*, 154:205–215, 1983.
- [110] M. A. Habib and J. O. Bockris. Adsorption at the solid/solution interface an FTIR study of phosphoric acid on platinum and gold. *J. Electrochem. Soc.*, 132:108–114, 1985.
- [111] F.C. Nart and T. Iwasita. On the adsorption of H₂PO₄⁻ and H₃PO₄ on platinum: An in situ FT-IR study. *Electrochim. Acta*, 37:385–391, 1992.

- [112] Qinggang He, Xiaofang Yang, Wei Chen, Sanjeev Mukerjee, Bruce Koel, and Shaowei Chen. Influence of phosphate anion adsorption on the kinetics of oxygen electroreduction on low index Pt(hkl) single crystals. *Phys. Chem. Chem. Phys.*, 12:12544–12555, 2010. doi: 10.1039/C0CP00433B. URL <http://dx.doi.org/10.1039/C0CP00433B>.
- [113] S. Ye, H. Kita, and A. Aramata. Hydrogen and anion adsorption at platinum single crystal electrodes in phosphate solutions over a wide range of pH. *J. Electroanal. Chem.*, 333:299–312, 1992.
- [114] J. T. Glass, G. I. Cahen, and G. E. Stoner. The effect of phosphoric acid concentration on electrocatalysis. *J. Electrochem. Soc.*, 136:656–660, 1989.
- [115] P. W. Faguy, N. Markovic, R. R. Adzic, C. A. Fierro, and E. B. Yeager. A study of bisulfate adsorption on Pt(111) single-crystal electrodes using in situ Fourier-Transform Infrared-Spectroscopy. *J. Electroanal. Chem.*, 289:245–262, 1990.
- [116] G. Horányi, J. Solt, and F. Nagy. Investigation of adsorption phenomena on platinized platinum electrodes by tracer methods. *Electroanal. Chem. Interfacial Electrochem.*, 31:95–102, 1971.
- [117] V. S. Bagotzky, Y. B. Vassilyev, J. Weber, and J. N. Pirtskhalava. Adsorption of anions on smooth platinum electrodes. *J. Electroanal. Chem.*, 27:31–46, 1970.
- [118] J. Clavilier. The role of anion on the electrochemical behaviour of a (111) platinum surface; an unusual splitting of the voltammogram in the hydrogen region. *J. Electroanal. Chem.*, 107:211–216, 1980.
- [119] N. M. Markovic, H. A. Gasteiger, and P. N. Ross. Oxygen reduction on platinum low-index single-crystal surfaces in sulfuric acid solution: Rotating ring-Pt(hkl) disk studies. *J. Phys. Chem.*, 99:3411–3415, 1995.
- [120] D. Malko, T. Lopes, E. Symianakis, and A. R. Kucernak. The intriguing poison tolerance of non-precious metal oxygen reduction reaction (ORR) catalysts. *J. Mater. Chem. A*, 4:142–152, 2016.
- [121] Qiang Wang, Zhi-You Zhou, Yu-Jiao Lai, Yong You, Jian-Guo Liu, Xia-Ling Wu, Ephrem Terefe, Chi Chen, Lin Song, Muhammad Rauf, Na Tian, and Shi-Gang Sun. Phenylenediamine-based FeN_x/C catalyst with high activity for oxygen reduction in acid medium and its active-site probing. *J. Am. Chem. Soc.*, 136(31):10882–10885, 2014. doi: 10.1021/ja505777v. URL <https://doi.org/10.1021/ja505777v>.
- [122] Alessandro Zana, Gustav K. H. Wiberg, Yu-Jia Deng, Thomas Østergaard, Jan Rossmeisl, and Matthias Arenz. Accessing the inaccessible: Analyzing the oxygen reduction reaction in the diffusion limit. *ACS Appl. Mater. Interfaces*, 9(44):38176–38180, 2017. doi: 10.1021/acsami.7b13902. URL <https://doi.org/10.1021/acsami.7b13902>.

- [123] M. Nesselberger and M. Arenz. In situ FTIR spectroscopy: Probing the electrochemical interface during the oxygen reduction reaction on a commercial platinum high-surface-area catalyst. *ChemCatChem*, 8: 1125–1131, 2016.
- [124] Dusan Strmcnik, Maria Escudero-Escribano, Kensaku Kodama, Vojislav R. Stamenkovic, Angel Cuesta, and Nenad M. Markovic. Enhanced electrocatalysis of the oxygen reduction reaction based on patterning of platinum surfaces with cyanide. *Nat. Chem.*, 2:880–885, 2010.
- [125] Jan M.L Martin. Heats of formation of perchloric acid, HClO_4 , and perchloric anhydride, Cl_2O_7 . Probing the limits of W1 and W2 theory. *J. Mol. Struct.: THEOCHEM*, 771(1):19–26, 2006. doi: <https://doi.org/10.1016/j.theochem.2006.03.035>. URL <http://www.sciencedirect.com/science/article/pii/S0166128006001655>.
- [126] R. F. Platford. Thermodynamics of aqueous solutions of orthophosphoric acid from the freezing point to 298.15°K. *J. Solution Chem.*, 4(7):591–598, Jul 1975. doi: 10.1007/BF00643381. URL <https://doi.org/10.1007/BF00643381>.
- [127] José H. Zagal and Marc T. M. Koper. Reactivity descriptors for the activity of molecular MN_4 catalysts for the oxygen reduction reaction. *Angew. Chem. Int. Ed.*, 55(47):14510–14521, 2016. doi: 10.1002/anie.201604311. URL <https://onlinelibrary.wiley.com/doi/abs/10.1002/anie.201604311>.

Appendix B

Papers

B.1 Paper 1

DFT study of stabilization effects on N-doped graphene for ORR catalysis

Mateusz Reda, Heine Anton Hansen, Tejs Vegge

Catalysis Today, 2018

In press.



Contents lists available at ScienceDirect

Catalysis Today

journal homepage: www.elsevier.com/locate/cattod

DFT study of stabilization effects on N-doped graphene for ORR catalysis

Mateusz Reda, Heine Anton Hansen*, Tejs Vegge

Department of Energy Conversion and Storage, Technical University of Denmark, DK-2800 Kgs. Lyngby, Denmark

ARTICLE INFO

Keywords:

Oxygen reduction reaction
Density functional theory
N-doped graphene
Explicit solvation

ABSTRACT

Noble metal free catalysts, such as N-doped graphene, have drawn a lot of attention as a promising replacement for platinum in low temperature fuel cells. Computational prediction of catalytic activity requires accurate description of the oxygen reduction reaction (ORR) intermediates adsorption energies. Two stabilizing effects, immanently present in experimental ORR setups with basal plane N-doped graphene catalyst, are studied systematically by means of density functional theory. Distant nitrogen with no adsorbates on neighboring carbon atoms selectively stabilizes *O and *O_2 adsorbates. Water solvation stabilizes all ORR intermediates, having a greater impact on *O and *O_2 , than on *OH and *OOH , in contrast to metal and oxide catalysts. Synergistic stabilization of *O caused by both effects reaches remarkably a high value of 1.5 eV for nitrogen concentrations above 4.2% N. Such a strong effect is explained by a high reactivity of *O and *O_2 , which possess empty O(sp) states. At 6.25% N, the reaction environment is found to comprise *O and free nitrogen spectators. Finally, strong *O solvation is found to be present in a broader class of systems, comprising all materials where the ORR occurs on a 2nd row element. Including at least a single explicit water layer is paramount to achieve the correct description of the ORR intermediates adsorption energies on these materials.

1. Introduction

Low temperature fuel cells have been recognized as one of the most attractive alternatives to combustion engines for automotive applications [1]. The promise of higher energy efficiency, independence from limited resources of fossil fuels and reduction in air pollution drives the research to overcome the obstacles to commercialization of this technology. Some of the difficulties are related to the development of auxiliary technologies, such as hydrogen production *via* water splitting and effective hydrogen storage [2], but the most troublesome issue directly related to the fuel cell stack is finding a durable material, which would efficiently catalyze the sluggish oxygen reduction reaction (ORR) [3].

Most commonly utilized cathodic materials for fuel cells are currently based on platinum [3,4]. However, due to its price and scarcity, methods of decreasing Pt loading, or completely replacing it with earth-abundant alternatives, are intensively explored [3,5,6,7–9]. The latter possibility is particularly attractive, as it may allow to further reduce the cost of the technology.

Setting aside arguably the most promising non-precious ORR catalysts containing a FeN_4 moiety [10,11], we draw attention to metal-free materials. This class of ORR catalysts is dominated by conductive carbon nanostructures, modified by various types of doping, especially nitrogen doping [7,9]. In recent years, N-doped carbon nanotubes and

graphene have been extensively studied both experimentally and computationally. Theoretical approaches investigated, among other things, effects such as: the type of nitrogen doping (graphitic, pyridinic, pyrrolic) [12], morphology and concentration of N-dopants [13], structural defects [14,15], curvature effect [14], solvation of *O_2 [16] and other ORR intermediates [17] by water, and the influence of additional nitrogen dopants on *O_2 [16] and *O [18] stability (where * is an active site on the catalyst's surface).

In the present paper, the latter two effects are revisited and reassessed. An unoccupied nitrogen dopant in the cell, referred to as “free nitrogen”, is a nitrogen atom, where neighboring carbon atoms are empty adsorption sites. Such nitrogen is particularly interesting due to its selective stabilization of *O over *OH and *OOH [18]. Similarly, the presence of water was found to stabilize *O_2 adsorbate by a uniquely high value of 0.83 eV, twice as much as *OH [17]. In what follows, the influence of these two effects on all ORR intermediates is systematically studied as a function of nitrogen concentrations, number of nitrogen atoms per adsorbate and number of water molecules per adsorbate. We employ Bader charge analysis [19] and projected density of states (PDOS) calculations to gain insight into the underlying phenomena and explain why different ORR intermediates respond differently to both effects. Finally, we include a case study of the oxygen reduction process on a selected catalytic system to show how our findings are applicable to the ORR modeling.

* Corresponding author.

E-mail address: heih@dtu.dk (H.A. Hansen).

<https://doi.org/10.1016/j.cattod.2018.02.015>

Received 18 December 2017; Received in revised form 2 February 2018; Accepted 9 February 2018
0920-5861/ © 2018 Elsevier B.V. All rights reserved.

2. Computational methods

All density functional theory (DFT) calculations are done using Atomic Simulation Environment (ASE) [20] coupled with the Vienna *Ab Initio* Simulation Package (VASP) [21–24]. The core electrons are described with the projector augmented wave method [25,26], and the basis set for the electronic wavefunctions are plane waves below a 400 eV energy cutoff. We use a Fermi smearing of electronic occupations with a width of 0.1 eV and Monkhorst-Pack [27] mesh for the Brillouin zone sampling of $(k_1, k_2, 1)$, with k_i such that $k_i v_i > 40$ for v_i being the corresponding lattice vector. The structure relaxation is performed until the maximum force on each atom drops below 0.01 eV/Å.

In this study, we consider systems in which water molecules interact with one another and with the hydrophobic surface of the catalyst. In such systems, dispersion forces can play a significant role, and semi-local exchange-correlation functionals like PBE [28] or RPBE [29] do not account for non-local van der Waals interactions. Here, we employ the BEEF-vdW [30] functional in which vdW-DF2 [31] non-local correlation is used. This approach proved to be successful in predicting adsorption bond energies both to transition metal surfaces [32] and carbon-based materials [30], as well as adsorption energy error estimation [33].

Solvation of the surface and adsorbates is taken into account by including water implicitly or explicitly. For implicit solvent calculations we use the continuum solvation model implemented in VASPsol [34,35] with a 600 eV plane wave cutoff. Explicit water layer structures are determined by the minima hopping algorithm implemented in ASE [36,37]. This global optimization method was accompanied by additional sampling of minimas, achieved by manual change of orientations of those H₂O molecules, which hydrogen atoms can point either towards or away from the surface. The vacuum layer region between periodic images of the system is about 10 Å. The dipole correction is used to decouple electrostatic potentials on the two sides of the two-dimensional structure.

The free energy corrections for adsorbed species are based on the quantum mechanical harmonic approximation and calculated vibrational frequencies. For calculations of the free energy diagrams, the total energy of the gas phase O₂ is corrected based on the formation Gibbs free energy of liquid H₂O as described previously [38], and the total energies of the systems with adsorbates are corrected according to the Christensen's correction scheme [39,40]: $\Delta E(\text{O}-\text{O}) = 0.2$ eV, $\Delta E(\text{H}_2\text{O}) = -0.03$ eV, and $\Delta E(\text{H}_2) = 0.09$ eV.

3. Results

All considered N-doped graphene models consist of graphitic nitrogen atoms uniformly dispersed in the graphene sheet. When a nitrogen atom is introduced into the system preserving its unit cell, it is placed in a position that maximizes the distance between nitrogen atoms. In that case, uniformity of N distribution cannot be strictly preserved. However, all the studied properties of the system are found to be insensitive to such deviations from uniformity. Non-uniform dopant distribution, such as nitrogen clustering, introduces another degree of freedom and is beyond the scope of this study.

The studied NG model systems are referred to in the following format:

$$\text{NG}_{xy}\text{N}/\text{ads}/z\text{H}_2\text{O},$$

where x – nitrogen concentration (atomic ratio), y – N/*ads ratio, ads – considered adsorbate (O, OH, OOH or O₂ for a specific adsorbate, or “ads” for general considerations), z – H₂O/*ads ratio. For example, NG_4.2%_2N/O/11H₂O denotes nitrogen-doped graphene with 4.2% of nitrogen, atomic oxygen adsorbate, N/*O ratio of 2 and H₂O/*O ratio of 11.

Adsorption energies are defined as the DFT energies of the following reactions:

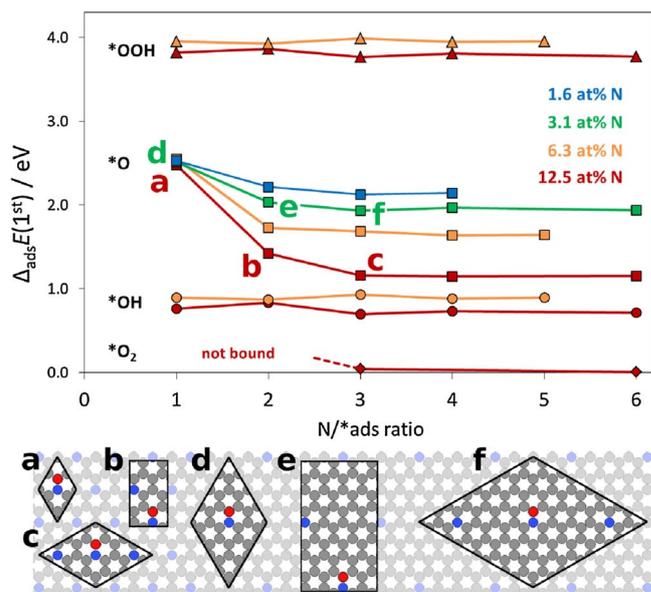
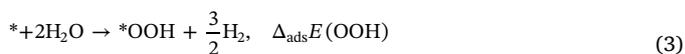
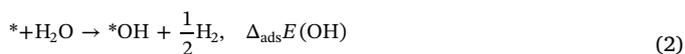


Fig. 1. First adsorption energy, $\Delta_{\text{ads}}E(1\text{st})$, vs. N/*ads ratio at different nitrogen concentrations; ads = {O, OH, OOH, O₂}. Sample unit cell structures are marked on the figure with letters (a)–(f). Color code for atoms: gray – carbon, blue – nitrogen, red – oxygen. (For interpretation of the references to color in this figure legend, the reader is referred to the web version of this article.)



Superscripts are added when considering adsorption energies in the presence of free nitrogen [$\Delta_{\text{ads}}^{\text{N}}E(\text{O})$], water [$\Delta_{\text{ads}}^{\text{W}}E(\text{O})$] or both [$\Delta_{\text{ads}}^{\text{N+W}}E(\text{O})$].

Stabilization by free nitrogen is the difference between the adsorption energy in the 1N/*ads system (no free nitrogen, e.g. Fig. 1 a or d) and > 1N/*ads systems:

$$\Delta_{\text{stab}}^{\text{N}}E(\text{X}) = \Delta_{\text{ads}}E(\text{X}) - \Delta_{\text{ads}}^{\text{N}}E(\text{X}) \quad (5)$$

The energy of stabilization *via* solvation is the difference between ORR adsorption energies in vacuum and in water, and equals the negative solvation energy:

$$\Delta_{\text{stab}}^{\text{W}}E(\text{X}) = -\Delta_{\text{solv}}E(\text{X}) = \Delta_{\text{ads}}E(\text{X}) - \Delta_{\text{ads}}^{\text{W}}E(\text{X}) \quad (6)$$

To calculate the adsorption energy in the presence of water, one H₂O molecule from the water layer is replaced with adsorbate. The energy of that water molecule is assumed to be the average energy of H₂O in the water layer.

3.1. Stabilization by free nitrogen

It is well known that a nitrogen dopant embedded in a graphene structure creates net positive charge on adjacent carbon atoms, making them more favorable for O₂ adsorption and facilitating the oxygen reduction reaction [41]. More recently, it was found that free nitrogen atoms which are located far away from the active site stabilize certain ORR adsorbates as well [18].

The effect of up to five free nitrogen atoms on the adsorption energy of ORR intermediates at different N concentrations is shown in Fig. 1. The OH and OOH adsorption energies are essentially independent of the N/*ads ratio, only fluctuations of ± 0.05 eV are observed. By contrast,

atomic oxygen is significantly stabilized by additional unoccupied nitrogen present in the cell. This effect is most apparent when the first free nitrogen appears in the cell: oxygen binding energy increases by up to 1.05 eV (for 12.5% N). Introduction of the second free nitrogen further stabilizes oxygen, especially at high nitrogen concentrations (0.26 eV stabilization of 3N/*O relative to 2N/*O at 12.5% N). A higher N/*O ratio than 3 has marginal effect on the stability of *O.

Stabilization by free N vanishes with decreasing nitrogen concentration. For systems with uniform N distribution this is understandable. In these systems, nitrogen concentration is strictly related to the N–N distance (d_{N-N}), so in the limit of $d_{N-N} \rightarrow \infty$ (equivalent to 0% N), the local environment around adsorption site is the same, irrespective of the N/*O ratio. Nonetheless, the influence of free nitrogen on oxygen binding proves to be a long-range effect. For instance, the stabilization of oxygen by two free nitrogen atoms at 1.6%N is around 0.4 eV, while the N–N distance is 14.8 Å. Moreover, we observe a hyperbolic decay of $\Delta_{\text{stab}}^N E(O)$ with N–N distance (Fig. S1, Supporting Information), which brings to mind electrostatic (Coulomb) potential between point charges. An explanation of this phenomenon is proposed in the discussion section.

The effect of stabilization by free nitrogen becomes even more significant for molecular oxygen, as the presence of at least 2 free nitrogen atoms ($N/*O_2 \geq 3$) appears to be a prerequisite for O_2 chemisorption at 12.5%N. We also note that for considered nitrogen concentrations, 12.5% N was the only one that assured O_2 chemisorption, whereas lower concentrations did not. * O_2 is similar to *O in that its binding energy strongly depends on the presence of free nitrogen atoms in the cell.

3.2. Stabilization via solvation

ORR intermediates adsorption energies depend on many parameters characterizing the environment near fuel cell cathode, such as the presence of water [42], pH of the electrolyte [43] or applied field [44]. Here we focus on the solvation effect caused by explicit water molecules.

The water effect is well-studied with Pt(111) as catalyst [42,45,46], and is often assumed to be transferable to other classes of materials [18,47]. There is some evidence, however, that $\Delta_{\text{stab}}^W E(X)$ can vary a lot between different catalyst materials. For instance, water has negligible effect on the stability of atomic oxygen found in fcc hollow sites on Pt (111) surface [42], but the same oxygen adsorbed on top of carbon atom in basal plane N-doped graphene is stabilized in aqueous environment by about 0.5 eV [17].

Here, we first study how a single water layer influences ORR intermediates adsorption at different water-to-adsorbate ratios ($H_2O/*\text{ads}$). The surface density of water in our model is 0.25 H_2O molecules per atom in the N-graphene sheet, which corresponds to about 5% average expansive strain on the water layer relative to hexagonal ice. This model allows to study water effect across many different N concentrations and $H_2O/*\text{ads}$ ratios. Hexagonal water arrangements were found to be the most stable by the minima-hopping algorithm both for clean and adsorbate-covered N-graphene surfaces (sample structures are shown in Fig. S2, Supporting Information). Unlike the case of the Pt (111) surface [48] and catalysts containing FeN_4 moieties [49], water molecules do not chemisorb on the active site of N-doped graphene. The average separation between the N-graphene sheet and water oxygen atoms is ca. 3.7 Å. The energy of a single water layer adhesion to graphene and N-graphene (6.25% N) is 79 and 82 meV per water molecule, respectively.

For both *OH and *OOH intermediates, the solvation-based stabilization energy is $\Delta_{\text{stab}}^W E(X) = 0.19 \pm 0.02$ eV, irrespective of nitrogen concentration, $H_2O/*\text{ads}$ ratio or N/*ads ratio. The situation is different for *O, where $\Delta_{\text{stab}}^W E(O)$ depends on the $H_2O/*O$ ratio. For systems without free nitrogen, the stabilization energy can be viewed as a difference between the 1N/*O and 1N/*O + H_2O curves in Fig. 2. At low

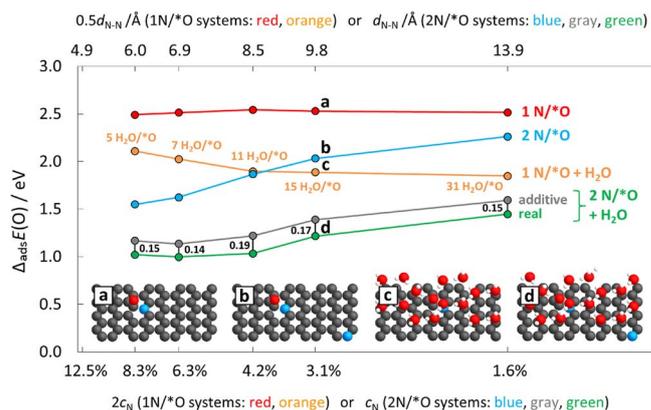


Fig. 2. Atomic oxygen adsorption energy on N-doped graphene as a function of N–N distance (or N concentration) in the following scenarios: (i) in vacuum, 1N/*O (red), (ii) in vacuum, 2N/*O (blue), (iii) in water, 1N/*O (orange), (iv) in water, 2N/*O (green), (v) in water, 2N/*O, assuming additivity of the free N and H_2O stabilizing effects (gray). Sample structures for systems containing 64 atoms in N-graphene unit cell are shown as inset. Color code for atoms: dark gray – carbon, blue – nitrogen, red – oxygen, white – hydrogen. (For interpretation of the references to color in this figure legend, the reader is referred to the web version of this article.)

water-to-adsorbate ratios ($H_2O/*O = 5$), the stabilization energy is 0.38 eV, and increases with increasing $H_2O/*O$ until reaching a plateau (ca. 0.65 eV) at 11 $H_2O/*O$. Increasing $H_2O/*O$ further has practically no effect on the stabilization energy (e.g. $\Delta_{\text{stab}}^W E(O) = 0.67$ eV at 31 $H_2O/*O$). The plateau suggests that 2–3 coordination shells of water participate in the stabilization of *O. A similar analysis for systems with free nitrogen (cf. the difference between the 2N/*O and 2N/*O + H_2O curves in Fig. 2) leads to the same conclusion, though in this case stabilization energies are about 0.17 eV higher.

A similar trend is found for the * O_2 adsorbate. The stabilization energy is 0.67 and 1.05 eV for NG_12.5%_3N/ O_2 /5 H_2O and NG_12.5%_6N/ O_2 /11 H_2O systems, respectively.

3.3. Synergy of the two effects

As mentioned previously, the solvation effect becomes stronger in the presence of free nitrogen. Equivalently, the free nitrogen effect becomes stronger in the presence of water, i.e. the two effects synergistically stabilize *O. This can be expressed as

$$\Delta_{\text{stab}}^{N+W} E(O) = \Delta_{\text{stab}}^N E(O) + \Delta_{\text{stab}}^W E(O) + \Delta_{\text{stab}}^{\text{syn}} E(O)$$

where the synergy component is $\Delta_{\text{stab}}^{\text{syn}} E(O) = 0.17 \pm 0.02$ eV (Fig. 2).

For high nitrogen concentration, the total stabilizing effect reaches a remarkably high value of 1.5 eV, and is approximately constant down to 4.2% N, due to the opposite changes of $\Delta_{\text{stab}}^N E(O)$ and $\Delta_{\text{stab}}^W E(O)$ with nitrogen concentration. Below 4.2% N, the solvation effect reaches its maximum and stabilizes, while free nitrogen effect continues to slowly vanish. However, even though the total stabilizing effect has to finally converge to the pure solvation effect at 0% N limit, the synergy component shows no clear evidence of fading over the considered nitrogen concentration range.

3.4. Increasing dimensionality

A computational approach to catalyst modeling often requires reduction of the real system size or dimensionality due to limited computational resources. This approach usually leads to meaningful results due to locality of adsorption phenomena [50], although it may be a source of errors. Here we estimate the inaccuracy of the description of real 3-dimensional (N-graphene or N-graphite)/water interface by a 2-dimensional model. This is done by applying three different modifications, one at a time to the base system, which is a single N-graphene

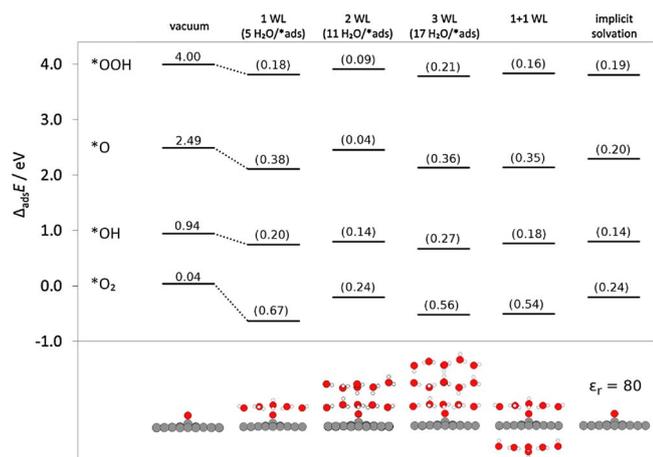


Fig. 3. ORR intermediate adsorption energies for different solvation models: 1–3 water layers (WL), one water layer on each side, and continuum solvation model. Adsorption energies and stabilization ($\Delta_{\text{stab}}^{\text{W}}E(X)$, in brackets) are included in eV above each $\Delta_{\text{ads}}E$ level. N-graphene models are: NG_12.5%_3N/ads for O₂ and NG_4.2%_1N/ads for *O, *OH and *OOH. Side-view structures of *O systems are included below the plot. Color code for atoms: gray – carbon, red – oxygen, white – hydrogen. (For interpretation of the references to color in this figure legend, the reader is referred to the web version of this article.)

sheet with a single water layer. The modifications are: (i) increasing the number of water layers (up to three) on the adsorbate side, (ii) including up to three N-graphene layers and (iii) including water layer on the other side of the N-graphene sheet.

3.4.1. Additional water layers on the adsorbate side

ORR intermediate adsorption and solvation energies for different models of solvation are summarized in Fig. 3. Adding a second water layer on the adsorbate side destabilizes all ORR adsorbates relative to the single water layer model. This is likely due to high stability of the reference, where water molecules adopt a special configuration with twice as many interlayer hydrogen bonds as in case of hexagonal ice, as shown in Fig. S3a (Supporting Information). The configuration is preserved to a large extent in systems with *OH and *OOH adsorbates (Fig. S3c and S3d), but differs significantly in *O and *O₂ systems (Fig. S3b and S3e), resulting in poor stabilization of these adsorbates. This special configuration of two water layers has been observed experimentally on graphene in ultrahigh vacuum [51], but is not expected to appear in experimental ORR setups, where the catalyst is immersed in a bulk electrolyte.

With 3 water layers, ORR adsorbate stability is similar to simulations with a single water layer within 0.11 eV. Although such differences may sometimes be non-negligible for ORR modeling, we can still conclude that the first water layer has a decisive influence on the

adsorbate solvation effects. A single water layer seems to be a reasonable compromise between accuracy and computational cost.

As discussed previously, in the single water layer model the H₂O/*O ratio influences *O solvation energy (Fig. 2). For example, increasing H₂O/*O ratio from 5 to 15 increases $\Delta_{\text{stab}}^{\text{W}}E(\text{O})$ from 0.38 to 0.64 eV. Similar increase of H₂O/*O ratio can be achieved by increasing the number of water layers from one (5 H₂O/*O) to three (17 H₂O/*O). Interestingly, $\Delta_{\text{stab}}^{\text{W}}E(\text{O})$ remains essentially constant in this process (0.38 and 0.36 eV, respectively). This suggests that from the practical point of view the effect of H₂O/*O ratio on solvation energy is limited to the first water layer.

3.4.2. Adding more N-graphene layers

Energetically, the most favorable stacking of multiple N-graphene layers containing 4.2% N is AA stacking with nitrogen atoms located one above another. In this case, the BEEF-vdW functional predicts similar (within 0.05 Å) interlayer distance as for graphite in the AB stacking. The adsorption and solvation energies for systems with single and multiple layers of N-graphene are summarized in Fig. S4 (Supporting Information). All solvation energies, as well as OH and OOH adsorption energies, are not affected by the presence of additional N-graphene layers. However, atomic and molecular oxygen adsorption energies exhibit non-monotonic variations with increasing number of N-graphene layers. Atomic oxygen binding becomes stronger by 0.08 and 0.06 eV, while molecular oxygen binding becomes weaker by 0.20 and 0.10 eV, for 2 and 3 graphene layers, respectively.

3.4.3. Water layer on both sides of N-graphene

Including water layer on both sides of N-graphene sheet marginally changes the *O, *OH and *OOH adsorption energy relative to having single water layer on the adsorbate side only (Fig. 3). The only affected ORR intermediate is O₂, which binding energy weakens by about 0.13 eV. Though not dramatic, this effect should be remembered while modeling oxygen reduction reaction, as vacuum on one side of a 2D catalyst is unlikely under experimental conditions.

4. Discussion

In this section we provide insight into the origin of the strong *O and *O₂ stabilization by free nitrogen and solvation effects. We also provide a case study of the oxygen reduction reaction on N-doped graphene with 6.25% N to demonstrate how our findings affect the predicted catalyst activity.

Fig. 4, showing the density of states projected onto adsorbed oxygen sp states for *O systems, forms the basis for the discussion. It illustrates that free nitrogen (transition from Fig. 4a and b) and water (Fig. 4a → c) cause O(sp) band filling. When both effects cooperate, essentially all the O(sp) states are located below the Fermi level.

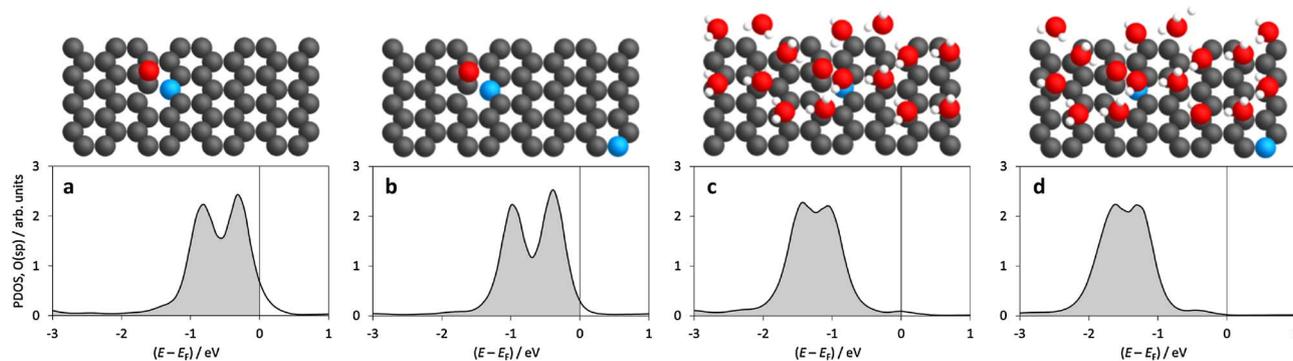


Fig. 4. Adsorbed oxygen projected density of states for: (a) NG_1.6%_1N/O, (b) NG_3.1%_2N/O, (c) NG_1.6%_1N/O/15H₂O, (d) NG_3.1%_2N/O/15H₂O. The corresponding structures are included above the plots. Color code for atoms is the same as in Fig. 2.

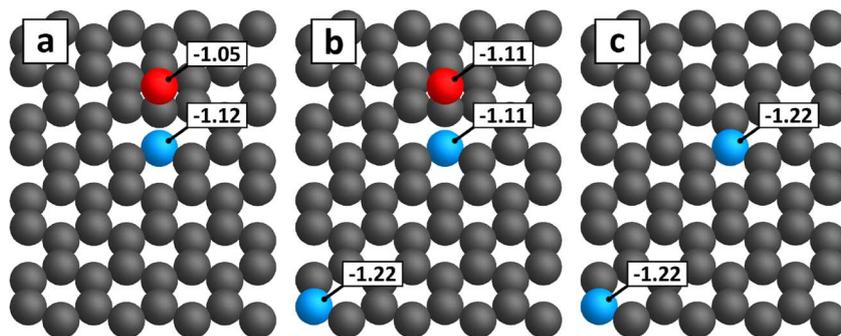


Fig. 5. Bader charge on atoms in: (a) NG_1.6_1N/O, (b) NG_3.1_2N/O and (c) NG_3.1. Color code for atoms is the same as in Fig. 2.

4.1. Stabilization due to free nitrogen

Free nitrogen selectively stabilizes *O and *O_2 . Both adsorbates have one dangling bond, since carbon, which is already bound to three other atoms, can provide only a single bond to oxygen. It is illustrated as unfilled O(sp) states (Fig. 4a), which makes *O and *O_2 quite reactive and unstable. The presence of free nitrogen in the system significantly stabilizes both adsorbates. In what follows, we study this effect on the example of the *O adsorbate.

Fig. 5 shows the Bader charge on oxygen and nitrogen for *O systems with and without free nitrogen, as well as the Bader charge on nitrogen in a pristine N-graphene sheet. It can be seen that a free nitrogen (Fig. 5b) causes the electron density on oxygen to raise by about $0.06 e^-$, compared to the system without free nitrogen (Fig. 5a). One possible reason for this increase could be electron density transfer from the introduced free nitrogen to oxygen via an inductive and/or mesomeric effect. In that case, we should see electron density depletion on the free nitrogen. However, Fig. 5c shows that this does not occur, and the Bader charge on nitrogen in the absence of any adsorbate is the same as the charge on free nitrogen in the presence of *O . We therefore propose another explanation, i.e. that a free nitrogen disrupts graphene's stable aromatic structure, which allows the more electronegative oxygen atom to withdraw electrons from the graphene carbon atoms more effectively.

The additional electron density on oxygen continues to fill the O(sp) band (Fig. 4b). The system becomes more strongly polarized: oxygen gains negative charge and graphene carbon atoms become positively charged. This shows that, as graphene loses electrons in favor of oxygen, the system becomes partly ionic, while at the same time retaining covalent bonds between respective parts, like in the case of zwitterions. We suggest variations in the Coulomb interaction between these parts (ions) are partly responsible for the variations in the stability of oxygen on the surface.

We find a correlation between the average Bader charge on oxygen and average oxygen binding energy for a set of NG_6.25% systems with varying N/ *O ratio (Fig. 6). In this case, the charge on oxygen is a measure of charge separation (varied by N/ *O ratio), while constant nitrogen concentration assures approximately constant distance between centers of positive and negative charges. The figure shows that the larger the charge donation into the O(sp) states, the more stable the system. We also note that above 2–3 N/ *O ratio, oxygen can no longer withdraw more electrons from the N-graphene sheet, and its adsorption energy stabilizes with respect to the number of free nitrogen atoms, as shown previously in Fig. 1.

It is worth noting that even though the *O binding energy correlates with the Bader charge on oxygen at a constant nitrogen concentration, these two properties do not correlate in general. For example, the Bader charge on oxygen is approximately constant (-1.10 ± 0.01) for the systems forming 2N/ *O curve in Fig. 2, where the nitrogen concentration changes. In light of the proposed explanation, the observed decrease of the oxygen binding with decreasing nitrogen concentration

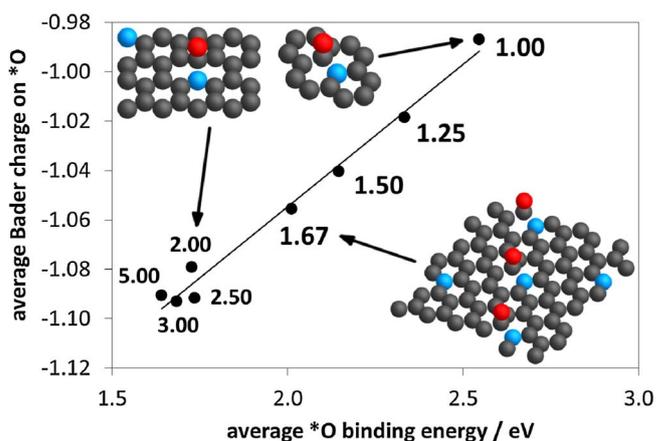


Fig. 6. Average $\Delta_{\text{ads}}E(O)$ vs. average Bader charge on *O at different N/ *O ratios for a set of NG_6.25% systems. Color code for atoms is the same as in Fig. 2.

is caused by the increase of the distance between fixed-charge ions. This dependence studied over a broader range of nitrogen concentrations reveals its hyperbolic character (Fig. S1, Supporting Information), which is expected for electrostatically interacting system.

4.2. Stabilization due to water

Water stabilizes all the ORR intermediates (Fig. 3). However, its influence on *O and *O_2 is clearly stronger than on *OH and *OOH . As noted previously, the difference between these two groups of adsorbates lies in the occupation of O(sp) states. *O and *O_2 have empty states, and their reactivity is thus much higher than that of *OH or *OOH .

The strong stabilizing effect of water on atomic and molecular oxygen can be explained by bond formation between water molecules and adsorbed species. In this process, water fills oxygen empty states, as can be seen from location of O(sp) band relative to Fermi level in vacuum (Fig. 4a and b) and in water (Fig. 4c and d). Bonds formed between *O and H_2O are about 0.18 \AA shorter (average of three bonds) than hydrogen bonds between water and *OH , suggesting they are much stronger than regular hydrogen bonds.

Describing water as a continuum polarizable medium ($\epsilon_r = 80$) results in unsatisfactory *O and *O_2 stabilization energies. For the system with low $H_2O/^*ads$ ratio considered in Fig. 3, implicit solvation underestimates $\Delta_{\text{stab}}^W E(O)$ and $\Delta_{\text{stab}}^W E(O_2)$ by 0.18 and 0.43 eV, respectively, relative to solvation by a single water layer. The situation becomes even worse for systems with higher $H_2O/^*ads$ ratio (e.g. underestimation of *O solvation by 0.40 eV in NG_4.2%_2N/O/11 H_2O system). At the same time, implicit water reproduces *OH and *OOH solvation with deviations smaller than 0.1 eV. Continuum solvation models can capture polarization effects in the system, but since they neglect granular structure of the solvent, they cannot describe all the

solvent-adsorbate interactions. This confirms that water-oxygen bond formation contributes significantly to *O and *O_2 stabilization. It also means that implicit solvation is not particularly suitable for ORR modeling on N-doped graphene.

Interestingly, the effect of strong *O solvation appears not to be limited to basal plane N-doped graphene. As long as the atomic oxygen is located at the atop adsorption site, significant *O stabilization (via solvation) energies of 0.5–1.2 eV are found on other types of materials, such as: B-doped graphene, N-doped graphene with Stone-Wales defect, Fe_3C -supported graphene, hydrogen-terminated graphite step zigzag edges (non-basal plane carbon material) and hexagonal boron nitride (non-carbon material). The structures and *O stabilization energies for these systems can be found in Tab. S1, Supporting Information. In all these cases, atop oxygen can form only a single bond with the 2nd row element (C or B), which is already bound to 3 other atoms. High stabilization energy can be explained by water-oxygen bond formation, like in the case of basal plane N-doped graphene.

4.3. Case study: ORR on N-graphene (6.25% N) with explicit water

To demonstrate how our findings affect predicted ORR activity, we take the example of N-doped graphene at 6.25% N. We assume the associative ORR pathway and neglect the *O_2 intermediate, as there is a strong evidence suggesting that the molecular oxygen adsorption is not necessarily required for the ORR to occur on N-doped graphene [52].

We first take a simple N-graphene model with one nitrogen and 15 carbon atoms in the unit cell, and 4 water molecules in single water layer (NG_6.25%_1N/ads/4H₂O). Its structure and free energy diagram at 0.8 V_{RHE} is shown in Fig. 7a. This system represents the simplest N-graphene/water interface model, that could be used for ORR modeling at this nitrogen concentration. The predicted thermodynamic overpotential is 0.78 V. However, this model is relevant for ORR modeling only under the assumption that adsorbate binding energies do not depend on coverage (θ_{ads}). While this is true for *OH and *OOH adsorbates, at low *O coverage (or, equivalently, high N/ *O ratio), atomic oxygen binds at least 0.8 eV stronger than at $\theta_{ads} = 1$ (Fig. 1). This will cause some nitrogen atoms in adjacent cells to remain unoccupied in order for the *O system to achieve a lower energy structure.

In the second step, we consider a ($\sqrt{2} \times \sqrt{2}$) version of the previous cell, and all the ORR steps occurring in the presence of a free nitrogen ($\theta_{ads} = 1/2$). The structure and the free energy diagram for this system are shown in Fig. 7b. This time *O binds so strong that its protonation becomes the potential-determining step. The resulting thermodynamic overpotential is 1.14 V.

Further increase of the N/ *ads ratio results in even more stable *O , with practically no change of the *OH and *OOH levels (see Fig. 1). It suggests that some amount of *O will be present on the catalyst surface throughout the entire oxygen reduction process in the form of *O spectators. Atomic oxygen stability starts to decrease for N/ $^*O < 2$ as shown in Fig. 6. Entering that range would increase *O free energy in Fig. 7b, such that *O protonation may no longer be a potential-determining step. In other words, increasing *O coverage above 1/2 allows the catalyst to explore free energy paths with lower overall thermodynamic barriers. We therefore suggest that, at 6.25%N, the oxygen reduction reaction occurs on basal plane N-doped graphene at *O coverages not lower than 1/2.

On the other hand, the coverage cannot be too close to 1. For example, introducing an *O spectator in the ($\sqrt{2} \times \sqrt{2}$) cell leaves only one catalytic site where the oxygen reduction reaction can take place, resulting in $\theta_{ads} = 1$. Adsorption of any ORR intermediate in such a position is highly unfavorable, as it significantly destabilizes spectator *O , which can no longer take the advantage of the free nitrogen effect (which is about 0.8 eV at 6.25%N, see Fig. 1). As a consequence, in order to minimize the barriers along the ORR free energy diagram, the system seeks to adopt a configuration in which both the *O and free nitrogen are simultaneously present in the catalytic environment.

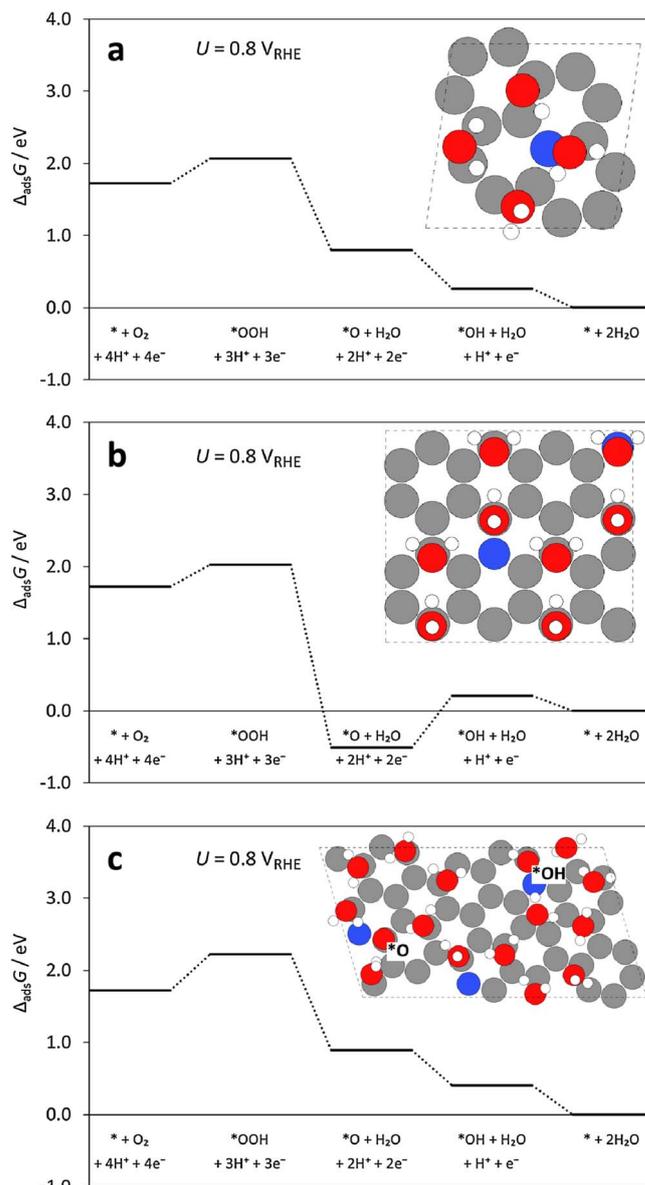


Fig. 7. Oxygen reduction reaction free energy diagrams at $U = 0.8 V_{RHE}$ for N-graphene (6.25%N): (a) one N atom in the unit cell; ORR occurs at $\theta_{ads} = 1$; inset shows the structure of a pristine catalyst, (b) two N atoms in the unit cell; ORR occurs at $\theta_{ads} = 1/2$; inset shows the structure of a pristine catalyst, (c) three N atoms in the unit cell; one adsorbed atomic oxygen and one free nitrogen act as spectators; ORR occurs at $\theta_{ads} = 2/3$; inset shows the structure of *OH in the catalytic environment defined by the spectators and a single water layer. Color code for atoms: gray – carbon, blue – nitrogen, red – oxygen, white – hydrogen.

Summarizing, the optimal adsorbate coverage is in the range of $1/2 < \theta_{ads} < 1$. The simplest realization of this scenario is a N-graphene cell containing three nitrogen atoms. A carbon near the first of the N atoms is permanently bound with atomic oxygen, the second N atom is free throughout the process, and a carbon near the third N serves as an adsorption site for ORR intermediates. The reaction occurs here at $\theta_{ads} = 2/3$. The free energy diagram and the catalyst structure with *OH adsorbate is shown in Fig. 7c. The thermodynamic overpotential is found to be 0.94 V, with potential-determining step being the *OOH formation on the surface.

It has to be noted that the predicted thermodynamic overpotential refers to the particular model studied here. In real systems, the distribution of nitrogen does not have to be regular, and nitrogen clustering may be observed. It is likely that there exist different adsorbate

coverages and different (*O spectator + free nitrogen + catalytic site) configurations, which result in lower thermodynamic barrier for the ORR, and thus dominate the basal plane N-doped graphene activity towards the oxygen reduction.

5. Conclusions

Two effects are found to be responsible for the unusually high stabilization of *O and *O₂ adsorbates on basal plane N-doped graphene compared to conventional metal-based ORR catalysts. These have been systematically studied here, *i.e.* the effect of additional, free nitrogen in the N-graphene sheet, and the solvation effect. The total stabilization from these two effects reaches values as high as 1.5 eV, including a 0.17 eV synergy component. Both effects are found to result from the high reactivity of *O and *O₂ adsorbates, caused by the presence of dangling bonds, which manifest themselves as unoccupied O(sp) states. Variations in the *O binding energy due to free nitrogen exhibit a long-range character, resembling electrostatic 1/*r* interactions between the charged parts of the system. The solvation effect is likely to be universal for materials where oxygen adsorbs on a 2nd row element in the atop position.

A case study of the oxygen reduction reaction at 6.25% N shows that the reaction occurs at an adsorbate surface coverage between $0.5 < \theta_{\text{ads}} < 1$, in the presence of *O and free nitrogen spectators.

Including explicit H₂O molecules is essential for a correct description of ORR intermediates adsorption energy on carbon materials. Continuum solvation models are unable to describe solvation of *O and *O₂ with sufficient accuracy, likely due to bond formation between these adsorbates and surrounding water molecules. We find that the first water layer has decisive influence on the adsorbate solvation. Including a single water layer to account for solvation effects seems to be a reasonable compromise between accuracy and computational cost.

Acknowledgements

The authors acknowledge support from the Innovation Fund Denmark for support through the Initiative Towards Non-Precious Metal Polymer Fuel Cells (NonPrecious), project no. 4106-00012A, as well as The Velux Foundations through the research center V-Sustain (Grant 9455). The authors would like to thank Colin F. Dickens (Stanford University) for fruitful discussions.

Appendix A. Supplementary data

Supplementary data associated with this article can be found, in the online version, at <https://doi.org/10.1016/j.cattod.2018.02.015>.

References

- G. Crabtree, M. Dresselhaus, The hydrogen fuel alternative, *MRS Bull.* 33 (4) (2008) 421–428, <http://dx.doi.org/10.1557/mrs2008.84> <https://www.cambridge.org/core/article/div-class-title-hydrogen-fuel-alternative-div/BFD3D2EBB36FEA8BDBDD539D537D616B>.
- E. Callini, K.-F. Aguey-Zinsou, R. Ahuja, J.R. Ares, S. Bals, N. Biliškov, S. Chakraborty, G. Charalambopoulou, A.-L. Chaudhary, F. Cuevas, B. Dam, P. de Jongh, M. Dornheim, Y. Filinchuk, J.G. Novaković, M. Hirscher, T.R. Jensen, P.B. Jensen, N. Novaković, Q. Lai, F. Leardini, D.M. Gattia, L. Pasquini, T. Steriotis, S. Turner, T. Vegge, A. Züttel, A. Montone, Nanostructured materials for solid-state hydrogen storage: a review of the achievement of COST action MP1103, *Int. J. Hydrogen Energy* 41 (32) (2016) 14404–14428, <http://dx.doi.org/10.1016/j.ijhydene.2016.04.025> <http://www.sciencedirect.com/science/article/pii/S0360319915319182>.
- Y. Nie, L. Li, Z. Wei, Recent advancements in Pt and Pt-free catalysts for oxygen reduction reaction, *Chem. Soc. Rev.* 44 (2015) 2168–2201, <http://dx.doi.org/10.1039/C4CS00484A>.
- V.R. Stamenkovic, B.S. Mun, M. Arenz, K.J.J. Mayrhofer, C.A. Lucas, G. Wang, P.N. Ross, N.M. Markovic, Trends in electrocatalysis on extended and nanoscale Pt-bimetallic alloy surfaces, *Nat. Mater.* 6 (3) (2007) 241–247, <http://dx.doi.org/10.1038/nmat1840>.
- R. Othman, A.L. Dicks, Z. Zhu, Non precious metal catalysts for the PEM fuel cell cathode, *Int. J. Hydrogen Energy* 37 (1) (2012) 357–372, <http://dx.doi.org/10.1016/j.ijhydene.2011.08.095> 11th China Hydrogen Energy Conference. <http://www.sciencedirect.com/science/article/pii/S0360319911020192>.
- D.C. Higgins, Z. Chen, Recent progress in non-precious metal catalysts for PEM fuel cell applications, *Can. J. Chem. Eng.* 91 (12) (2013) 1881–1895, <http://dx.doi.org/10.1002/cjce.21884>.
- L. Dai, Y. Xue, L. Qu, H.-J. Choi, J.-B. Baek, Metal-free catalysts for oxygen reduction reaction, *Chem. Rev.* 115 (11) (2015) 4823–4892, <http://dx.doi.org/10.1021/cr5003563> PMID: 25938707.
- D. Higgins, P. Zamani, A. Yu, Z. Chen, The application of graphene and its composites in oxygen reduction electrocatalysis: a perspective and review of recent progress, *Energy Environ. Sci.* 9 (2016) 357–390, <http://dx.doi.org/10.1039/C5EE02474A>.
- W. Xia, A. Mahmood, Z. Liang, R. Zou, S. Guo, Earth-abundant nanomaterials for oxygen reduction, *Angew. Chem. Int. Ed.* 55 (8) (2016) 2650–2676, <http://dx.doi.org/10.1002/anie.201504830>.
- E. Proietti, F. Jaouen, M. Lefèvre, N. Larouche, J. Tian, J. Herranz, J.-P. Dodelet, Iron-based cathode catalyst with enhanced power density in polymer electrolyte membrane fuel cells, *Nat. Commun.* 2 (2011) 416, <http://dx.doi.org/10.1038/ncomms1427>.
- G. Wu, K.L. More, C.M. Johnston, P. Zelenay, High-performance electrocatalysts for oxygen reduction derived from polyaniline, iron, and cobalt, *Science* 332 (6028) (2011) 443–447, <http://dx.doi.org/10.1126/science.1200832> <http://www.sciencemag.org/content/332/6028/443.full.pdf>.
- W.A. Saidi, Oxygen reduction electrocatalysis using N-doped graphene quantum-dots, *J. Phys. Chem. Lett.* 4 (23) (2013) 4160–4165, <http://dx.doi.org/10.1021/jz402090d> arXiv:https://doi.org/10.1021/jz402090d, <https://doi.org/10.1021/jz402090d>.
- D. Kwak, A. Khetan, S. Noh, H. Pitsch, B. Han, First principles study of morphology, doping level, and water solvation effects on the catalytic mechanism of nitrogen-doped graphene in the oxygen reduction reaction, *Chem. Cat. Chem.* 6 (9) (2014) 2662–2670, <http://dx.doi.org/10.1002/cctc.201402248>.
- G.-L. Chai, Z. Hou, D.-J. Shu, T. Ikeda, K. Terakura, Active sites and mechanisms for oxygen reduction reaction on nitrogen-doped carbon alloy catalysts: Stone–Wales defect and curvature effect, *J. Am. Chem. Soc.* 136 (39) (2014) 13629–13640, <http://dx.doi.org/10.1021/ja502646c>.
- J.W.F. To, J.W.D. Ng, S. Siahrostami, A.L. Koh, Y. Lee, Z. Chen, K.D. Fong, S. Chen, J. He, W.-G. Bae, J. Wilcox, H.Y. Jeong, K. Kim, F. Studt, J.K. Nørskov, T.F. Jaramillo, Z. Bao, High-performance oxygen reduction and evolution carbon catalysis: from mechanistic studies to device integration, *Nano Res.* 10 (4) (2017) 1163–1177, <http://dx.doi.org/10.1007/s12274-016-1347-8>.
- A. Ferre-Vilaplana, E. Herrero, Charge transfer, bonding conditioning and solvation effect in the activation of the oxygen reduction reaction on unclustered graphitic-nitrogen-doped graphene, *Phys. Chem. Chem. Phys.* 17 (2015) 16238–16242, <http://dx.doi.org/10.1039/C5CP00918A>.
- L. Yu, X. Pan, X. Cao, P. Hu, X. Bao, Oxygen reduction reaction mechanism on nitrogen-doped graphene: a density functional theory study, *J. Catal.* 282 (1) (2011) 183–190, <http://dx.doi.org/10.1016/j.jcat.2011.06.015>.
- F. Studt, The oxygen reduction reaction on nitrogen-doped graphene, *Catal. Lett.* 143 (1) (2013) 58–60, <http://dx.doi.org/10.1007/s10562-012-0918-x>.
- G. Henkelman, A. Arnaldsson, H. Jónsson, A fast and robust algorithm for bader decomposition of charge density, *Comput. Mater. Sci.* 36 (3) (2006) 354–360, <http://dx.doi.org/10.1016/j.commatsci.2005.04.010> <http://www.sciencedirect.com/science/article/pii/S0927025605001849>.
- A.H. Larsen, J.J. Mortensen, J. Blomqvist, I.E. Castelli, R. Christensen, M. Dułak, J. Friis, M.N. Groves, B. Hammer, C. Hargus, E.D. Hermes, P.C. Jennings, P.B. Jensen, J. Kermode, J.R. Kitchin, E.L. Kolsbjerg, J. Kubal, K. Kaasbjerg, S. Lysgaard, J.B. Maronsson, T. Maxson, T. Olsen, L. Pastewka, A. Peterson, C. Rostgaard, J. Schiøtz, O. Schütt, M. Strange, K.S. Thygesen, T. Vegge, L. Vilhelmsen, M. Walter, Z. Zeng, K.W. Jacobsen, The atomic simulation environment—a Python library for working with atoms, *J. Phys.: Condens. Matter* 29 (27) (2017) 273002 <http://stacks.iop.org/0953-8984/29/i=27/a=2730>.
- G. Kresse, J. Hafner, Ab initio molecular dynamics for liquid metals, *Phys. Rev. B* 47 (1993) 558–561, <http://dx.doi.org/10.1103/PhysRevB.47.558>.
- G. Kresse, J. Hafner, Ab initio molecular-dynamics simulation of the liquid-metal-amorphous-semiconductor transition in germanium, *Phys. Rev. B* 49 (1994) 14251–14269, <http://dx.doi.org/10.1103/PhysRevB.49.14251>.
- G. Kresse, J. Furthmüller, Efficiency of ab-initio total energy calculations for metals and semiconductors using a plane-wave basis set, *Comput. Mater. Sci.* 6 (1) (1996) 15–50, [http://dx.doi.org/10.1016/0927-0256\(96\)00008-0](http://dx.doi.org/10.1016/0927-0256(96)00008-0).
- G. Kresse, J. Furthmüller, Efficient iterative schemes for ab initio total-energy calculations using a plane-wave basis set, *Phys. Rev. B* 54 (1996) 11169–11186, <http://dx.doi.org/10.1103/PhysRevB.54.11169>.
- P.E. Blöchl, Projector augmented-wave method, *Phys. Rev. B* 50 (1994) 17953–17979, <http://dx.doi.org/10.1103/PhysRevB.50.17953>.
- G. Kresse, D. Joubert, From ultrasoft pseudopotentials to the projector augmented-wave method, *Phys. Rev. B* 59 (1999) 1758–1775, <http://dx.doi.org/10.1103/PhysRevB.59.1758>.
- H.J. Monkhorst, J.D. Pack, Special points for Brillouin-zone integrations, *Phys. Rev. B* 13 (1976) 5188–5192, <http://dx.doi.org/10.1103/PhysRevB.13.5188>.
- J.P. Perdew, K. Burke, M. Ernzerhof, Generalized gradient approximation made simple, *Phys. Rev. Lett.* 77 (1996) 3865–3868, <http://dx.doi.org/10.1103/PhysRevLett.77.3865>.
- B. Hammer, L.B. Hansen, J.K. Nørskov, Improved adsorption energetics within density-functional theory using revised Perdew–Burke–Ernzerhof functionals, *Phys. Rev. B* 59 (1999) 7413–7421, <http://dx.doi.org/10.1103/PhysRevB.59.7413>.
- J. Wellendorff, K.T. Lundgaard, A. Møgelhøj, V. Petzold, D.D. Landis, J.K. Nørskov,

- T. Bligaard, K.W. Jacobsen, Density functionals for surface science: exchange-correlation model development with Bayesian error estimation, *Phys. Rev. B* 85 (2012) 235149, <http://dx.doi.org/10.1103/PhysRevB.85.235149>.
- [31] K. Lee, E.D. Murray, L. Kong, B.I. Lundqvist, D.C. Langreth, Higher-accuracy van der Waals density functional, *Phys. Rev. B* 82 (2010) 081101, <http://dx.doi.org/10.1103/PhysRevB.82.081101>.
- [32] J. Wellendorff, T.L. Silbaugh, D. Garcia-Pintos, J.K. Nørskov, T. Bligaard, F. Studt, C.T. Campbell, A benchmark database for adsorption bond energies to transition metal surfaces and comparison to selected DFT functionals, *Surf. Sci.* 640 (2015) 36–44, <http://dx.doi.org/10.1016/j.susc.2015.03.023> <http://www.sciencedirect.com/science/article/pii/S0039602815000837>.
- [33] A.J. Medford, J. Wellendorff, A. Vojvodic, F. Studt, F. Abild-Pedersen, K.W. Jacobsen, T. Bligaard, J.K. Nørskov, Assessing the reliability of calculated catalytic ammonia synthesis rates, *Science* 345 (6193) (2014) 197–200, <http://dx.doi.org/10.1126/science.1253486> <http://science.sciencemag.org/content/345/6193/197.full.pdf>.
- [34] K. Mathew, R. Sundararaman, K. Letchworth-Weaver, T.A. Arias, R.G. Hennig, Implicit solvation model for density-functional study of nanocrystal surfaces and reaction pathways, *J. Chem. Phys.* 140 (8) (2014) 084106, <http://dx.doi.org/10.1063/1.4865107>.
- [35] K. Mathew, R.G. Hennig, Implicit Self-Consistent Description of Electrolyte in Plane-Wave Density-Functional Theory, (2016) [arXiv:1601.03346](https://arxiv.org/abs/1601.03346).
- [36] S. Goedecker, Minima hopping: an efficient search method for the global minimum of the potential energy surface of complex molecular systems, *J. Chem. Phys.* 120 (21) (2004) 9911–9917, <http://dx.doi.org/10.1063/1.1724816>.
- [37] A.A. Peterson, Global optimization of adsorbate-surface structures while preserving molecular identity, *Top. Catal.* 57 (1) (2014) 40–53, <http://dx.doi.org/10.1007/s11244-013-0161-8>.
- [38] J. Rossmeisl, A. Logadottir, J. Nørskov, Electrolysis of water on (oxidized) metal surfaces, *Chem. Phys.* 319 (1–3) (2005) 178–184, <http://dx.doi.org/10.1016/j.chemphys.2005.05.038> <http://www.sciencedirect.com/science/article/pii/S0301010405002053>.
- [39] R. Christensen, H.A. Hansen, T. Vegge, Identifying systematic DFT errors in catalytic reactions, *Catal. Sci. Technol.* 5 (2015) 4946–4949, <http://dx.doi.org/10.1039/C5CY01332A>.
- [40] R. Christensen, H.A. Hansen, C.F. Dickens, J.K. Nørskov, T. Vegge, Functional independent scaling relation for ORR/OER catalysts, *J. Phys. Chem. C* 120 (43) (2016) 24910–24916, <http://dx.doi.org/10.1021/acs.jpcc.6b09141>.
- [41] D. Yu, Q. Zhang, L. Dai, Highly efficient metal-free growth of nitrogen-doped single-walled carbon nanotubes on plasma-etched substrates for oxygen reduction, *J. Am. Chem. Soc.* 132 (43) (2010) 15127–15129, <http://dx.doi.org/10.1021/ja105617z>.
- [42] J.K. Nørskov, J. Rossmeisl, A. Logadottir, L. Lindqvist, J.R. Kitchin, T. Bligaard, H. Jónsson, Origin of the overpotential for oxygen reduction at a fuel-cell cathode, *J. Phys. Chem. B* 108 (46) (2004) 17886–17892, <http://dx.doi.org/10.1021/jp047349j>.
- [43] M.H. Hansen, J. Rossmeisl, pH in grand canonical statistics of an electrochemical interface, *J. Phys. Chem. C* 120 (51) (2016) 29135–29143, <http://dx.doi.org/10.1021/acs.jpcc.6b09019>.
- [44] G.S. Karlberg, J. Rossmeisl, J.K. Nørskov, Estimations of electric field effects on the oxygen reduction reaction based on the density functional theory, *Phys. Chem. Chem. Phys.* 9 (2007) 5158–5161, <http://dx.doi.org/10.1039/B705938H>.
- [45] V. Tripković, E. Skúlason, S. Siahrostami, J.K. Nørskov, J. Rossmeisl, The oxygen reduction reaction mechanism on Pt(1 1 1) from density functional theory calculations, *Electrochim. Acta* 55 (27) (2010) 7975–7981, <http://dx.doi.org/10.1016/j.electacta.2010.02.056>.
- [46] V. Tripkovic, T. Vegge, Potential- and rate-determining step for oxygen reduction on Pt(111), *J. Phys. Chem. C* 121 (48) (2017) 26785–26793, <http://dx.doi.org/10.1021/acs.jpcc.7b07472>.
- [47] R. Koitz, J.K. Nørskov, F. Studt, A systematic study of metal-supported boron nitride materials for the oxygen reduction reaction, *Phys. Chem. Chem. Phys.* 17 (2015) 12722–12727, <http://dx.doi.org/10.1039/C5CP01384D>.
- [48] S. Liu, M.G. White, P. Liu, Mechanism of oxygen reduction reaction on Pt(111) in alkaline solution: importance of chemisorbed water on surface, *J. Phys. Chem. C* 120 (28) (2016) 15288–15298, <http://dx.doi.org/10.1021/acs.jpcc.6b05126>.
- [49] J. Sun, Y.-H. Fang, Z.-P. Liu, Electrochemical oxygen reduction kinetics on Fe-center of nitrogen-doped graphene, *Phys. Chem. Chem. Phys.* 16 (2014) 13733–13740, <http://dx.doi.org/10.1039/C4CP00037D>.
- [50] L. Li, A.H. Larsen, N.A. Romero, V.A. Morozov, C. Glinsvad, F. Abild-Pedersen, J. Greeley, K.W. Jacobsen, J.K. Nørskov, Investigation of catalytic finite-size-effects of platinum metal clusters, *J. Phys. Chem. Lett.* 4 (1) (2013) 222–226, <http://dx.doi.org/10.1021/jz3018286>.
- [51] G.A. Kimmel, J. Matthiesen, M. Baer, C.J. Mundy, N.G. Petrik, R.S. Smith, Z. Dohnálek, B.D. Kay, No confinement needed: Observation of a metastable hydrophobic wetting two-layer ice on graphene, *J. Am. Chem. Soc.* 131 (35) (2009) 12838–12844, <http://dx.doi.org/10.1021/ja904708f>.
- [52] C.H. Choi, H.-K. Lim, M.W. Chung, J.C. Park, H. Shin, H. Kim, S.I. Woo, Long-range electron transfer over graphene-based catalyst for high-performing oxygen reduction reactions: importance of size, N-doping, and metallic impurities, *J. Am. Chem. Soc.* 136 (25) (2014) 9070–9077, <http://dx.doi.org/10.1021/ja5033474> PMID: 24905892.

Supporting information

DFT Study of Stabilization Effects on N-doped Graphene for ORR Catalysis

Mateusz Reda, Heine Anton Hansen*, Tejs Vegge

*Department of Energy Conversion and Storage, Technical University of Denmark,
DK-2800 Kgs. Lyngby, Denmark*

1. Supporting figures

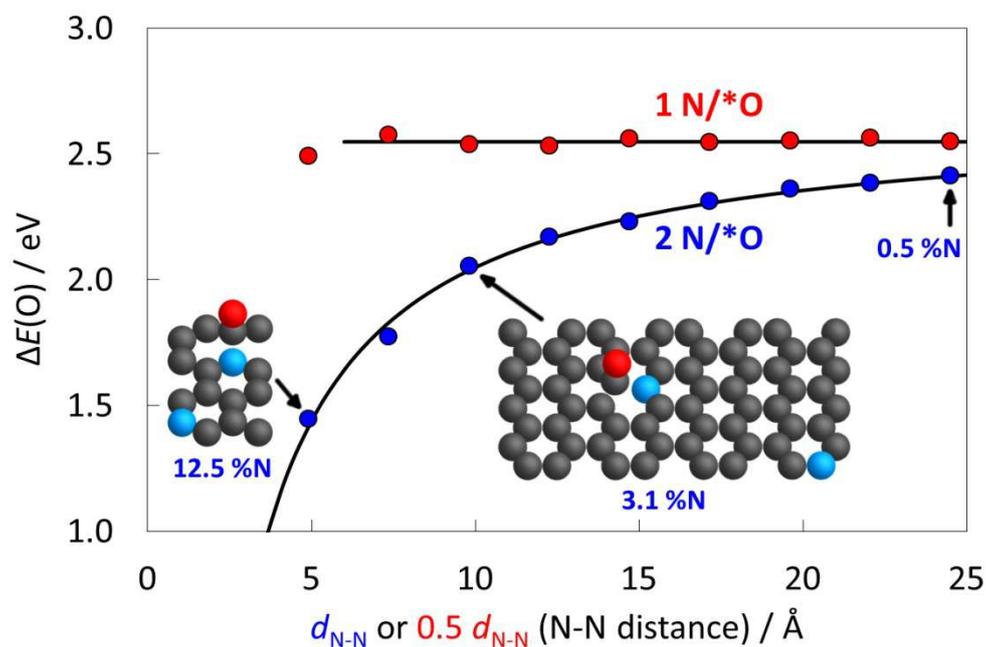


Figure S1: Oxygen adsorption energy as a function of N-N distance for systems with 1N/*O (constant function) and 2N/*O (hyperbola), showing the long-range character of the *O stabilization caused by a distant, free N. Color code for atoms: dark gray – carbon, blue – nitrogen, red – oxygen.

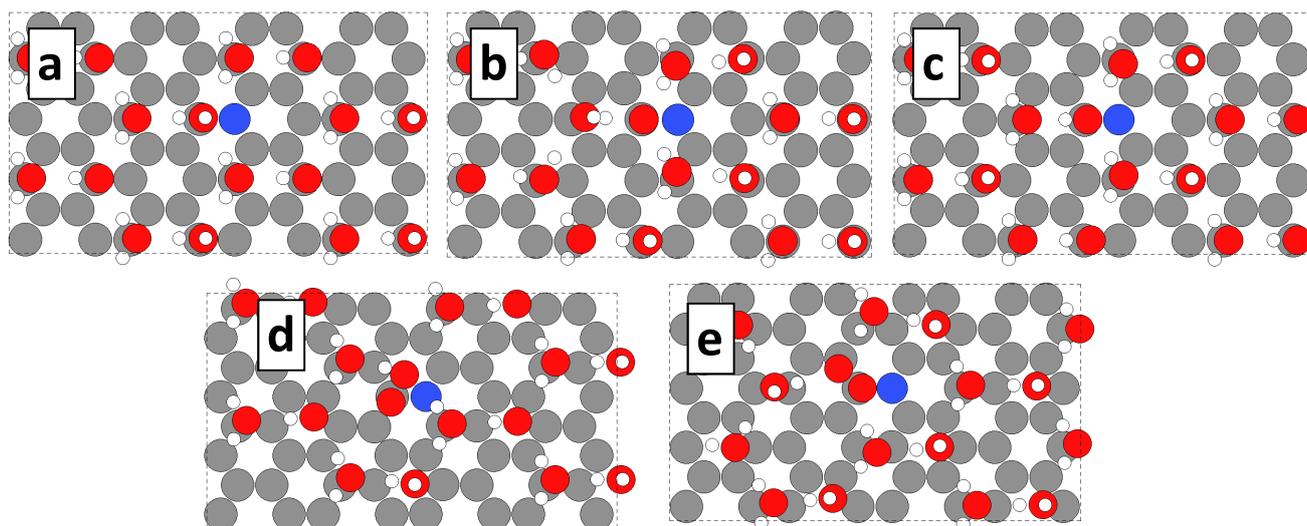


Figure S2: Top views of the optimized structures of pristine catalyst and ORR intermediates with single water layer. N-graphene models are: (a) pristine N-doped graphene with 1.6%N, (b) NG_1.6%_1N/O/15H₂O, (c) NG_1.6%_1N/OH/15H₂O, (d) NG_1.6%_1N/OOH/15H₂O and (e) NG_3.1%_2N/O₂/15H₂O. Color code for atoms: gray – carbon, blue – nitrogen, red – oxygen, white – hydrogen.

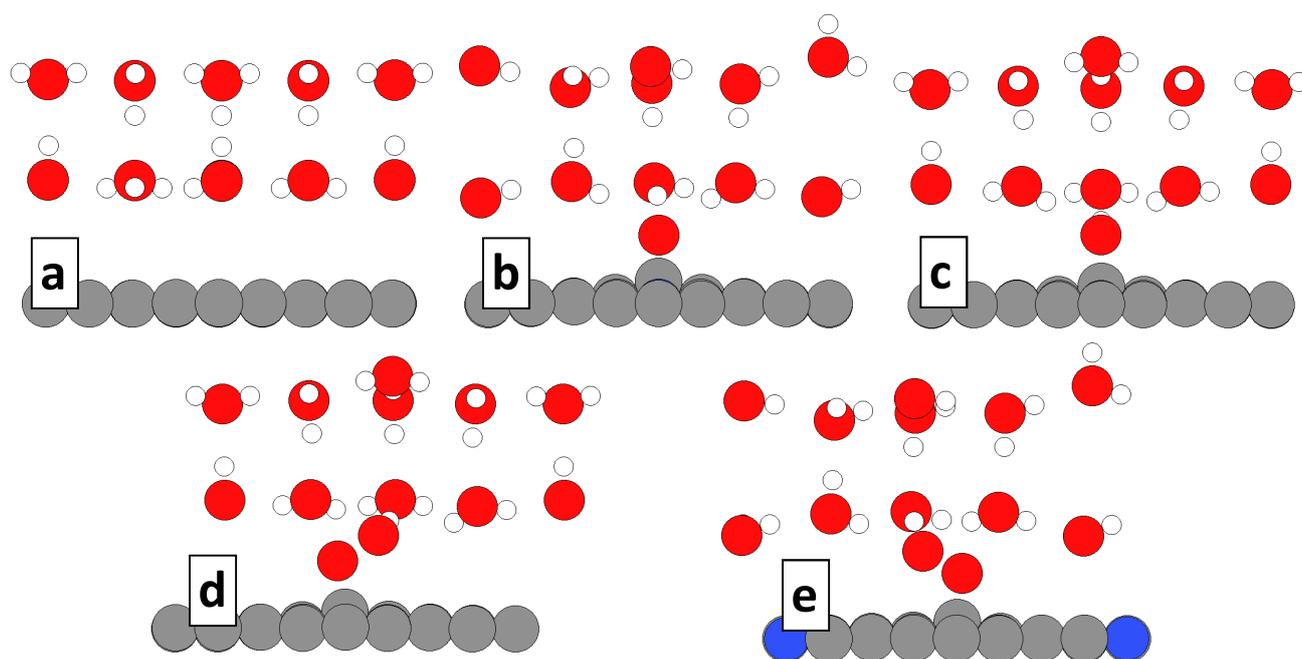


Figure S3: Side views of the optimized structures of pristine catalyst and ORR intermediates with double water layer. N-graphene models are: NG_12.5%_3N/ads for *O₂ and NG_4.2%_1N/ads for *O, *OH and *OOH. Color code for atoms: gray – carbon, blue – nitrogen, red – oxygen, white – hydrogen.

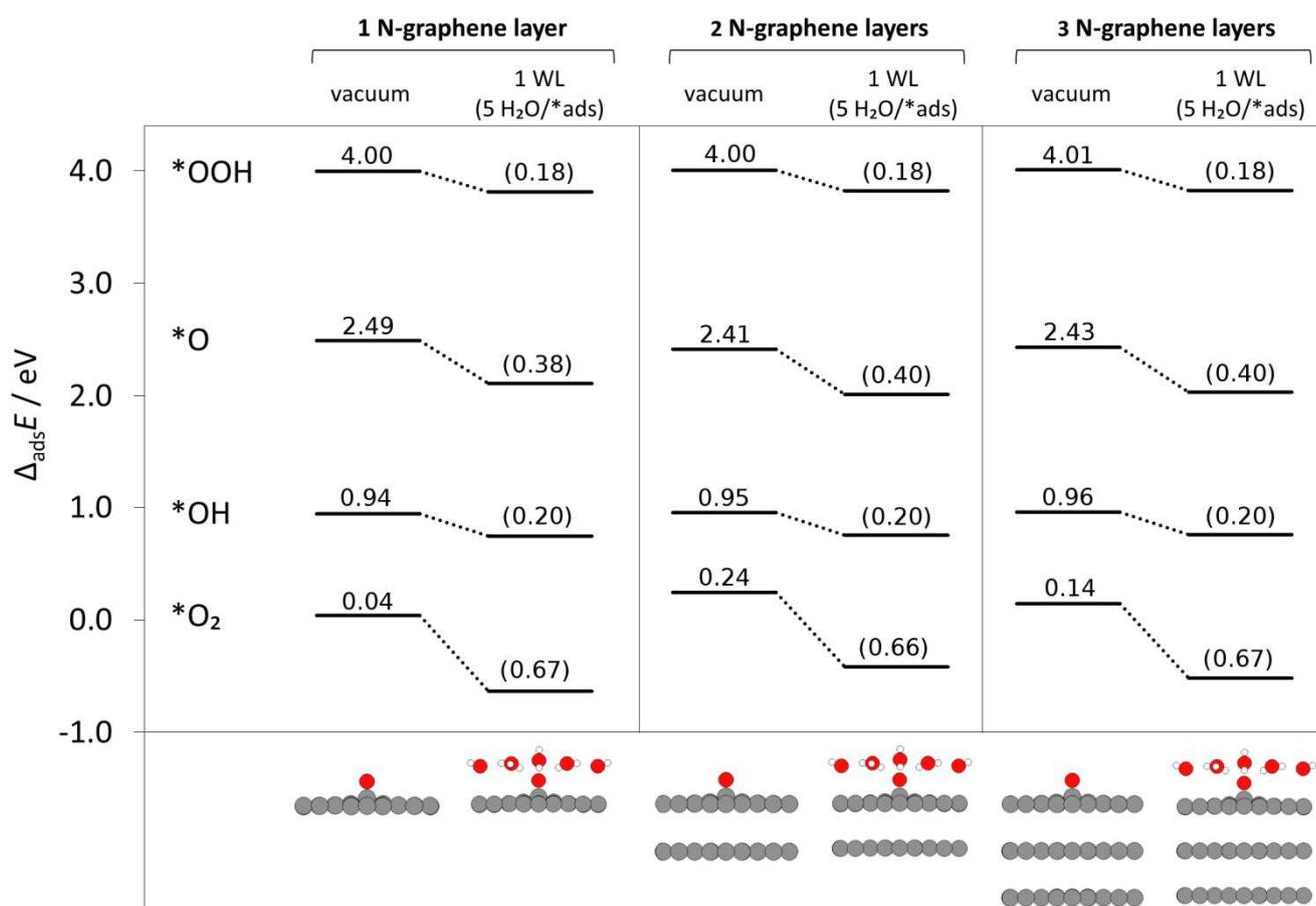
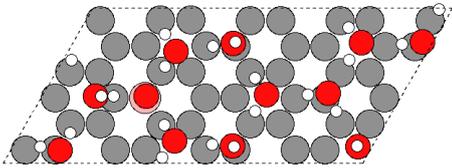
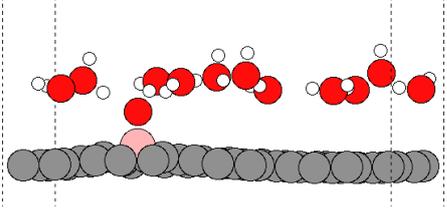
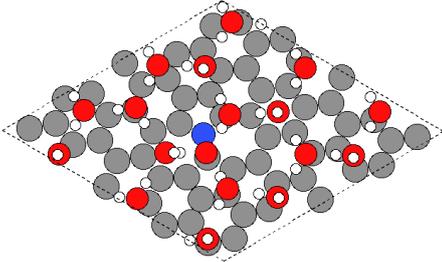
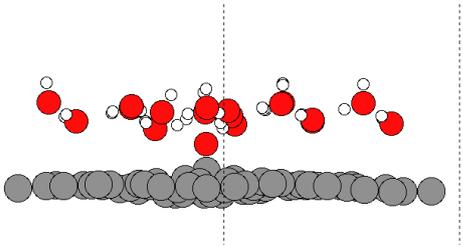
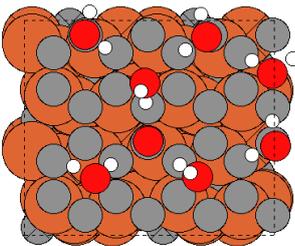
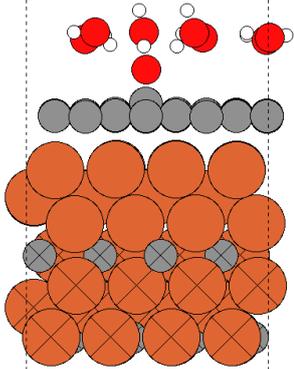
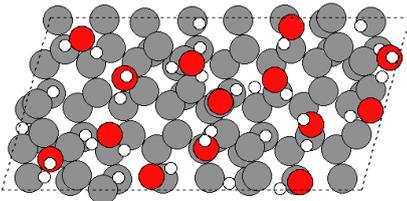
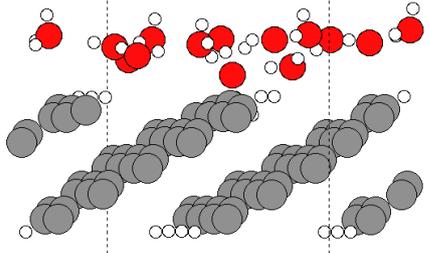
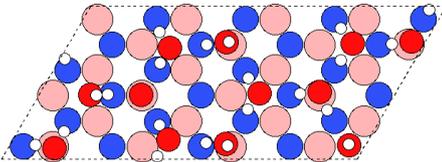
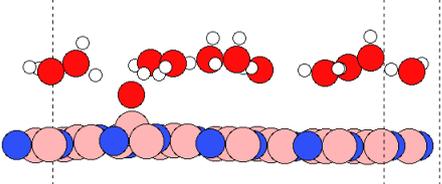


Figure S4: ORR intermediate adsorption energies for different numbers of N-graphene layers (1 to 3) in vacuum and with a single water layer. Adsorption energies and stabilization ($\Delta_{\text{stab}}^{\text{W}} E(X)$, in brackets) are included in eV above each $\Delta_{\text{ads}} E$ level. N-graphene models are: NG_12.5%_3N/ads for O₂ and NG_4.2%_1N/ads for *O, *OH and *OOH. Side-view structures of *O systems are included below the plot. Color code for atoms is the same as in Fig. S3.

Table S1. Additional structures exhibiting significant *O solvation energies. All calculations were performed at the same level of theory as described in Section 2 of the main manuscript: Computational methods. Energy of *O stabilization *via* solvation, $\Delta_{\text{stab}}^{\text{W}}E(\text{O})$, is defined in Eq. 6.

System	Structure – top view	Structure – side view
B-doped graphene $\Delta_{\text{stab}}^{\text{W}}E(\text{O}) = 0.85 \text{ eV}$		
N-doped graphene with Stone-Wales defect $\Delta_{\text{stab}}^{\text{W}}E(\text{O}) = 0.78 \text{ eV}$		
Fe ₃ C-supported graphene, Fe ₃ C strained (3.04%) $\Delta_{\text{stab}}^{\text{W}}E(\text{O}) = 0.63 \text{ eV}$		
Hydrogen-terminated graphite step zigzag edges $\Delta_{\text{stab}}^{\text{W}}E(\text{O}) = 1.27 \text{ eV}$		
Hexagonal boron nitride $\Delta_{\text{stab}}^{\text{W}}E(\text{O}) = 0.49 \text{ eV}$		

B.2 Paper 2

Enhanced Oxygen Reduction Activity by Selective Anion Adsorption on Non-Precious Metal Catalysts

Kaspar Holst-Olesen, Mateusz Reda, Heine Anton Hansen, Tejs Vegge, Matthias Arenz

Nature Communications, 2018

Under review.

Enhanced Oxygen Reduction Activity by Selective Anion Adsorption on Non-Precious Metal Catalysts

Kaspar Holst-Olesen¹, Mateusz Reda², Heine A. Hansen², Tejs Vegge^{2,*} & Matthias Arenz^{3,*}

ABSTRACT

Non-Precious Metal (NPM) catalysts are promising alternatives to platinum-based catalysts for the oxygen reduction reaction (ORR), the cathode reaction in fuel cells. In this paper, we focus on an iron-nitrogen-carbon (Fe/N/C) catalyst in comparison to platinum and investigate how these different types of catalyst behave towards selective anion poisoning. The catalysts are studied with respect to their ORR activity using the rotating disk electrode (RDE) technique in aqueous HClO₄, H₂SO₄, H₃PO₄ and HCl electrolytes and the results are supported by density functional theory (DFT) calculations. We find that the ORR on the Fe/N/C catalyst is less affected by anion poisoning than platinum. Surprisingly, it is seen that phosphoric acid not only does not poison the Fe/N/C catalyst but instead promotes the ORR; a finding in sharp contrast to the poisoning effect observed on platinum. This is a highly important finding as modern high-temperature proton exchange fuel cells (HT-PEMFCs) employ membranes consisting of phosphoric acid that is immobilized into a polybenzimidazole (PBI) matrix.

¹ Department of Chemistry, University of Copenhagen, Universitetsparken 5, 2100 Ø, Copenhagen, Denmark.

² Department of Energy Conversion and Storage, Technical University of Denmark, 2800 Kgs. Lyngby, Denmark.

³ Department of Chemistry and Biochemistry, University of Bern, Freiestrasse 3, 3012, Bern, Switzerland.

* Correspondence and requests for materials should be addressed to M.A. (e-mail: matthias.arenz@dcb.unibe.ch) or to T.V. (email: teve@dtu.dk)

INTRODUCTION

The oxygen reduction reaction (ORR) is known to be the most challenging catalytic reaction in low temperature hydrogen fuel cells¹. So far carbon supported platinum nanoparticles (Pt/C) have been the preferred catalytic material for the ORR, but the high cost and scarcity of platinum has triggered intensive research for alternative catalysts using only abundant materials. Since the work of Jasinski², it has been known that porphyrin structures with a metallic centre can catalyse the ORR. These materials utilize inexpensive transition metals such as Fe and Co, incorporated into a carbon support structure through nitrogen bonds. In literature, they are often referred to as Me/N/C or Non-Precious Metal Catalysts (NPMC).

The efficiency of fuel cells utilizing Pt/C is hampered by the low intrinsic ORR activity, but this process is also negatively influenced by impurities and anion adsorption on the catalytic sites. Because phosphoric acid fuel cells (PAFCs) were among the first commercially successful fuel cells, it is now well established that phosphoric acid electrolyte and its anions severely inhibit the catalytic sites on platinum³⁻⁸. This poisoning effect on platinum surfaces is also known for other anions such as sulphates and chlorides and has been intensively investigated in the past⁹⁻¹³. The basic principle of anion poisoning is a site blocking mechanism, where specific anion adsorption prevents the efficient interaction of the reactant with the active Pt sites. For NPMCs, considerably less is known about anion poisoning^{14,15}. Due to the different catalytic sites of Pt-based catalysts and NPMCs, it is worth investigating the differences towards poisoning effects. Pt/C is a 3D catalyst, where the active phase are Pt nanoparticles with a complex surface structure. In contrast, NPMCs are essentially 2D materials opening for the possibility of selective, partial ligand adsorption on the backside of the active centre to tune its catalytic activity; an option which is not possible on traditional Pt-based catalysts. Thus, in this study, we focus on the poisoning effect on NPMCs observed in four different aqueous electrolytes (i.e. H_3PO_4 , HClO_4 , H_2SO_4 and HCl) and compare the results to the known behaviour of Pt. Through electrochemical experiments and computational modelling, we find evidence that NPMCs and

Pt indeed behave differently towards anion poisoning. Most important, it is found that phosphoric acid, which has a strong poisoning effect on for Pt surfaces, promotes the ORR on NPMCs.

RESULTS

Electrochemical performance

The effect of anion adsorption on the ORR on Platinum

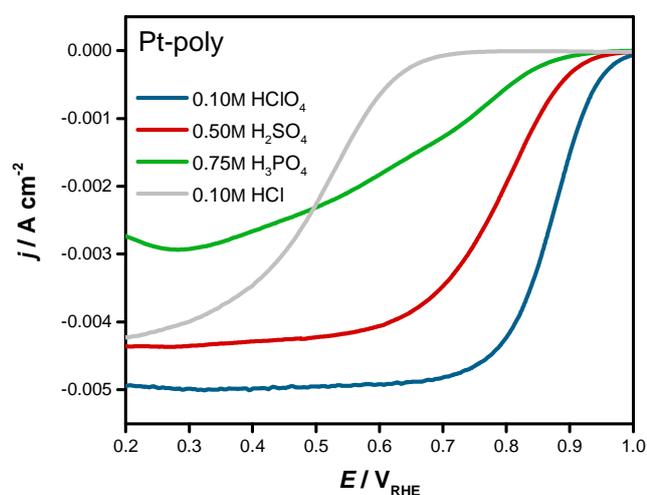


Figure 1 | Platinum polycrystalline RDE polarization curves. Pt-poly disk in 0.10 M HClO₄, 0.50 M H₂SO₄, 0.75 M H₃PO₄ and 0.10 M HCl electrolyte saturated with O₂ at 900 rpm and 10 mV s⁻¹.

In figure 1, the well-known inhibiting effect of anion adsorption on the ORR on platinum is demonstrated in RDE measurements of a polycrystalline Pt (Pt-poly) disk in aqueous HClO₄, H₂SO₄, H₃PO₄ and HCl electrolyte, respectively. Anion adsorption caused by these acidic electrolytes has been thoroughly investigated by voltammetry^{12,13,16-22} as well as other in-situ techniques such as FTIR²³ and is therefore well established for platinum. In acidic solution, the anionic (spectator) species inhibits the activity primarily due to the blocking of the catalytic surface. This can be observed in cyclic voltammetry particularly through changes in the features of hydrogen underpotential deposition (H_{upd}) below ~ 0.35 V_{RHE} and adsorption oxygenated species around ~ 0.9 V_{RHE} and also gives rise to the characteristic voltammetric profiles of Pt single crystals^{12,13,16-22}.

The degree of anion adsorption is potential dependent and becomes increasingly pronounced at more positive potential. This is problematic because for efficient energy conversion the ORR takes place in the positive potential range as well. For this reason, efforts have been made to mitigate the negative effects of blocking species on platinum²⁴⁻²⁹. Figure 1 illustrates that the ORR half-wave potential ($E_{1/2}$) decreases significantly in the order $\text{HClO}_4 > \text{H}_2\text{SO}_4 > \text{H}_3\text{PO}_4 > \text{HCl}$. This change of $E_{1/2}$ can be associated with a decrease in ORR activity. However, in accordance with the Levich equation of the diffusion limited current, I_L

$$I_L = 0.620 nFAD^{2/3} v^{-1/6} C_{\text{O}_2} \omega^{1/2}$$

the observed decrease in I_L also suggests that the concentration of dissolved oxygen in the respective electrolytes decreases in the same order³⁰, except for HCl. As the ORR is a first order reaction with respect to the oxygen concentration^{23,24}, the observed ORR activity is a result of anion blocking as well as oxygen concentration, see also below.

The effect of anion adsorption on the ORR on a NPMC

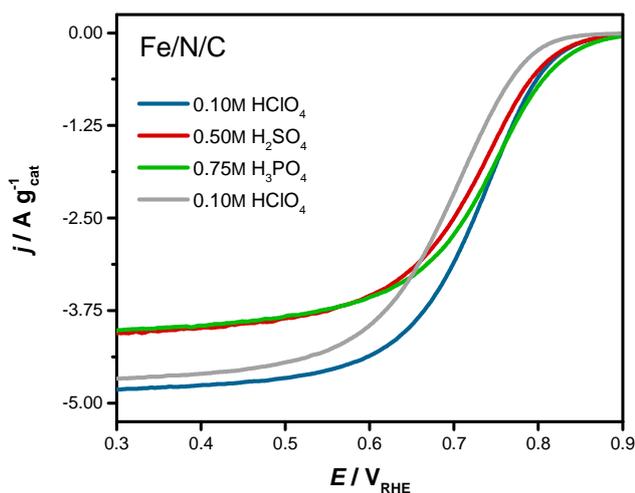
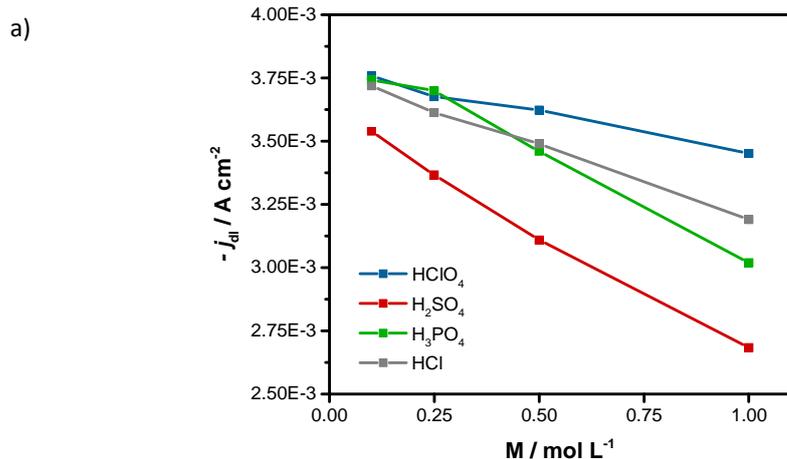


Figure 2 | Fe/N/C RDE polarization curves. HSAC Fe/N/C in 0.10 M HClO_4 , 0.50 M H_2SO_4 and 0.75 M H_3PO_4 electrolyte purged with O_2 at 900 rpm and 10 mV s^{-1} . Total catalyst load is $800 \mu\text{g cm}^{-2}$.

Performing the same measurements on NPMC is demonstrated in figure 2. The figure shows RDE results of a commercial Fe/N/C high surface area catalyst dispersed onto a glassy carbon (GC) disk in the same HClO₄, H₂SO₄, H₃PO₄ and HCl electrolyte solutions. To be meaningful, the ORR curves are not normalized to the surface area (as usually done for Pt based catalysts), but to the total amount of catalyst material. Analyzing the different half-wave potentials, it is evident that they are considerably less different (as compared to Pt) and all fall in a similar potential range. Noticeably, the polarization curve measured in H₃PO₄ electrolyte indicates a higher ORR activity at high potentials than in HClO₄. In this case, it appears that the decrease in j_L follows the trend of the increasing electrolyte concentration. This indicates, that the drop of activity seen on Pt-poly in H₃PO₄ (Figure 1) is not only related to oxygen solubility, but must also be due to other factors such as poisoning/anion adsorption, higher viscosity and possible depletion of oxygen at the Pt-electrolyte interface³³⁻³⁵. Comparing 0.1 M electrolyte solution³³⁻³⁵ with electrolytes of higher concentrations, the difference in oxygen solubility (j_L) leads to a difference in $E_{1/2}$ and thus in the measurements presented in figure 2, the ORR activity appears to be higher in HClO₄ electrolyte than in H₂SO₄. However, the onset potentials indicate that the ORR activity follows a different order than on Pt-poly, namely H₃PO₄ > HClO₄ ≈ H₂SO₄ > HCl.



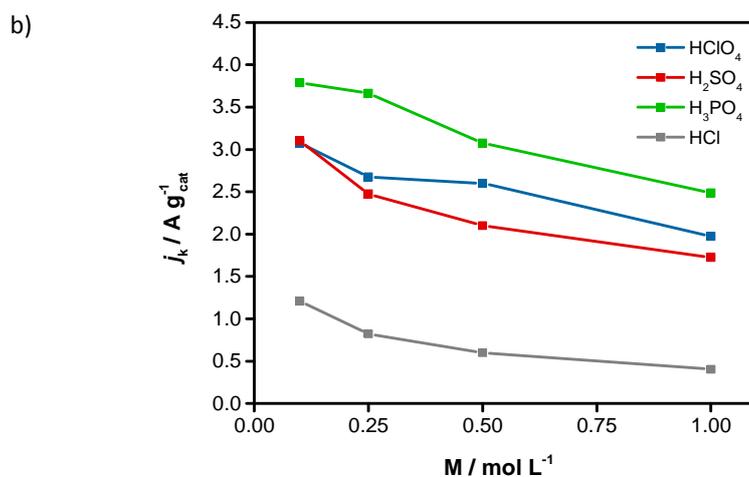


Figure 3 | Effect of increasing electrolyte molarity on a) oxygen solubility expressed by j_L and b) catalytic activity expressed by j_k

To disentangle the influence of oxygen concentration and anion adsorption on the Fe/N/C catalyst, the molarity of the four electrolytes HClO₄, H₂SO₄, H₃PO₄ and HCl was gradually increased and ORR polarization curves recorded. In figure 3a, j_L is used as a simple measure for the oxygen solubility and the viscosity of the electrolyte. It is seen that with increasing molarity, j_L and thus oxygen transport decreases. This trend is particular prominent for phosphoric acid. Calculating the mass averaged ORR rate j_k (Figure 3b), it can be seen that in all acidic solutions the ORR activity decreases with increasing electrolyte molarity in a similar manner as j_L . This suggests that increasing the molarity does not necessarily affect the catalytic activity of the Fe/N/C catalyst through site blocking. Instead, due to decreasing O₂ mass transport with increasing electrolyte molarity, the observed ORR rate decreases consistent with a first-order reaction with respect to C_{O₂}. Surprisingly, comparing the ORR on HClO₄ and H₃PO₄ electrolyte, it is seen that higher ORR rates are measured in the latter electrolyte, despite the lower O₂ solubility (j_L). Such behaviour is in sharp contrast to the observations on Pt/C catalysts, which always exhibit increased inhibition in H₃PO₄ electrolyte. Therefore, our results not only demonstrate that anion adsorption behaves differently on the Fe/N/C catalyst than on a Pt-surface. We observe a clear indication of a promotional effect of the anions in the H₃PO₄ electrolyte for Fe/N/C. The results for the ORR in HCl electrolyte imply that Fe/N/C is not completely

resistant to poisoning from species in the electrolyte solution, but that the promotional effect depends on the nature of the anions in the electrolyte.

Comparison of the influence of H_3PO_4 on Pt/C and Fe/N/C

In an effort to avoid the influence of oxygen solubility and electrolyte viscosity on the measured ORR rates, a different experiment was conducted as well; minute amounts of H_3PO_4 were added to a 0.1 M HClO_4 electrolyte solution and the effect on the ORR polarization curve recorded. This approach ensures that oxygen solubility and electrolyte viscosity are not significantly affected and hence changes in the observed ORR polarization curve must be due to site blocking from added anion species. The results presented in Figure 4 support that even very small amounts of H_3PO_4 species have a negative effect on the ORR on Pt, while for the Fe/N/C catalyst the polarization curves in both solutions overlap indicating no significant change in the ORR rate. This supports the absence of any detrimental effect of H_3PO_4 to the activity of the active Fe/N/C sites. It also indicates that for a promotional effect a certain H_3PO_4 concentration is required.

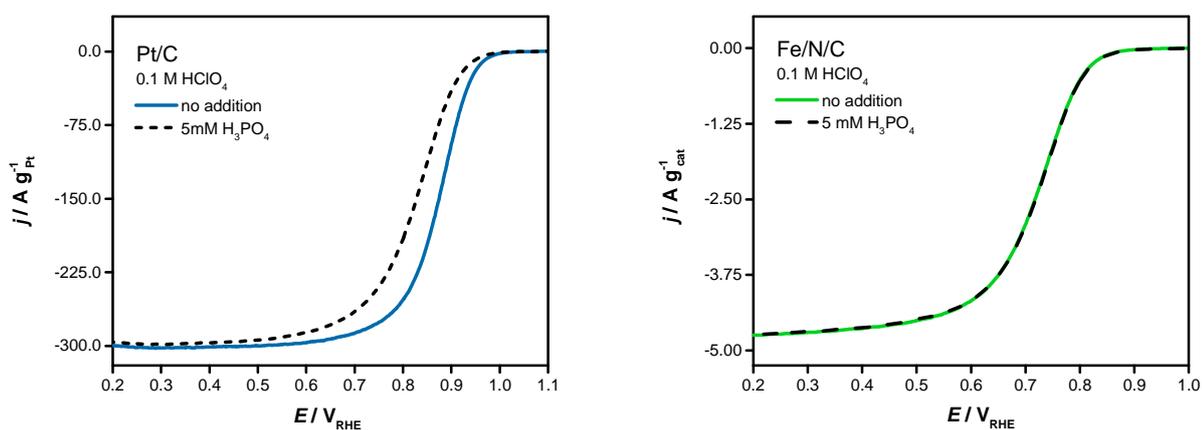


Figure 4 | Effect of H_3PO_4 . Carbon supported platinum TTK catalyst (Pt/C) and Fe/N/C catalyst in 0.1 M HClO_4 electrolyte with and without addition of 5×10^{-3} M H_3PO_4 .

DFT CALCULATIONS OF ANION ADSORPTION

To elucidate the responsible phenomena behind the presented experimental observations, we performed density functional theory (DFT) calculations of the adsorption energy of anions present in the investigated electrolytes and their competition with ORR intermediates for the active site. For the case of platinum, we calculated the potential-dependent adsorption Gibbs free energy of the ORR intermediates (H_2O , OH , O) and of each acid form present in the electrolyte solutions, i.e. H_3PO_4 , H_2PO_4^- , HPO_4^{2-} and PO_4^{3-} for phosphoric acid, and ClO_4^- for perchloric acid (Figure 5). It is clearly seen that at ORR-relevant potentials ClO_4^- does not adsorb on the Pt(111) surface, and therefore does not influence the catalytic activity. Contrary to that, phosphate anions interact with Pt(111) much stronger than the ORR intermediates and consequently displace them from the surface. This explains the observed drop of platinum ORR activity in phosphoric acid electrolyte. At ORR-relevant potentials, the phosphate form that is most likely to be found on the Pt(111) surface is hydrogen phosphate ($^*\text{HPO}_4$, where * denotes the active site).

The same analysis performed for the Fe/N/C catalyst model ($\text{FeN}_4\text{C}_{12}$ moiety, Fe:N:C atomic ratio of 1:4:26) shows a similar trend: the perchloric group weakly interacts with the active site, while the dihydrogen phosphate (H_2PO_4^-) adsorption energy is slightly higher than the one of the ORR intermediates. However, in this case, stronger anion-catalyst interaction does not automatically result in a decrease in ORR activity. As mentioned previously, the Fe/N/C catalyst is a 2D material, where both sides of the catalyst are exposed to the electrolyte solution. If any of these sides are occupied by an anion rather than an ORR intermediate, the catalytic activity of the opposite side can be modified. Figure 6 shows the calculated ORR free energy diagrams along the minimum energy paths in the presence of the following acids: HClO_4 (in solution: ClO_4^-), H_3PO_4 (forms: H_3PO_4 , H_2PO_4^- , HPO_4^{2-} and PO_4^{3-}), H_2SO_4 (forms: HSO_4^- and SO_4^{2-}) and HCl (form: Cl^-). In HClO_4 and H_2SO_4 , the interaction of the FeN_4 moiety with anions is weaker than its interaction with water. Consequently, $\text{H}_2\text{O-FeN}_4$ serves as the active site. The thermodynamically limiting step is OH removal, with a thermodynamic barrier of 0.115 eV at 0.75 V_{RHE} ³⁶, therefore in these electrolytes, the catalyst is on the strong oxygen binding side of the ORR activity volcano (Figure 7). In H_3PO_4 and HCl , the interaction of the

FeN₄ moiety with anions is stronger than its interaction with water. H₂PO₄-FeN₄ and Cl-FeN₄ serve as the active sites, respectively, and in both electrolytes the Fe-O bond is weakened such that the OOH formation becomes the rate limiting step (the catalyst is on the weak oxygen binding side of the activity volcano, see figure 7). Thermodynamic barriers for OOH formation at 0.75 V_{RHE} are 0.013 and 0.169 eV in H₃PO₄ and HCl, respectively. Summarizing, the thermodynamic barrier of the limiting step is lower in H₃PO₄ and higher in HCl, when compared to HClO₄/H₂SO₄. This indicates the following order of Fe/N/C ORR activity in acids: H₃PO₄ > HClO₄ = H₂SO₄ > HCl, which agrees very well with the experimental observations. It should be noted that the calculations cannot differentiate between the catalyst activity in HClO₄ and H₂SO₄ electrolyte. This is, however, also in agreement with the experimental results, where only small differences in ORR activity between these two electrolytes are observed. As seen in Figure 3 these differences are most likely related to the solubility of oxygen (*j_L*), which at similar molar concentrations is smaller in H₂SO₄ than in HClO₄.

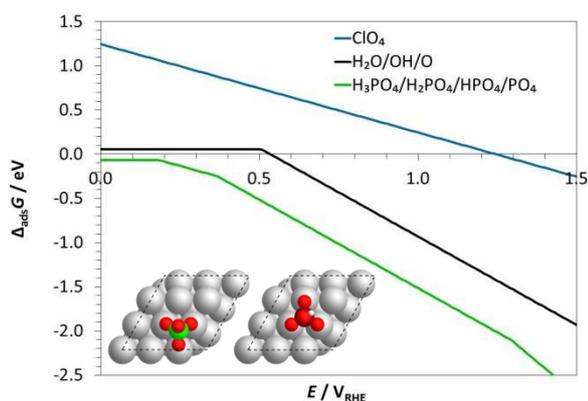


Figure 5 | Anion adsorption Gibbs free energy on Pt(111) vs. electrode potential (V_{RHE}) at 298.15 K and 0.5 M formal concentration. The inset shows the model systems with optimized structures of *ClO₄ and *HPO₄ (color code for atoms: Pt – gray, Cl – green, P – dark red, O – red, H – white).

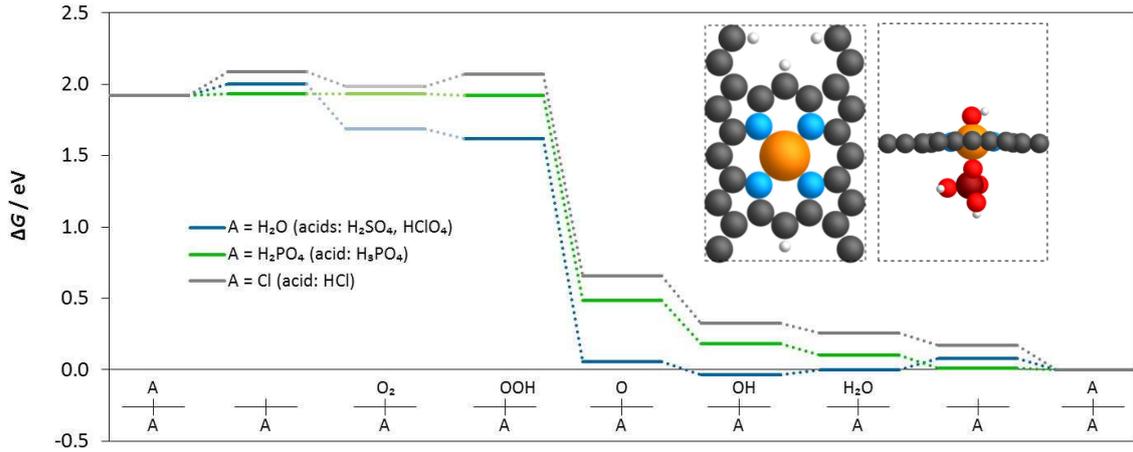


Figure 6 | Free energy diagram of the ORR on Fe/N/C catalyst, at $0.75 V_{RHE}$, in four acids: $HClO_4$, H_2SO_4 , H_3PO_4 and HCl . Temperature: 298.15 K, acids formal concentration: 0.5 M. The insets in the upper-right corner show: (left) the catalyst model, top view; (right) $H_2PO_4-FeN_4OH$ intermediate, side view. Colour code for atoms: H – white, C – black, N – blue, Fe – orange, P – dark red, O – red.

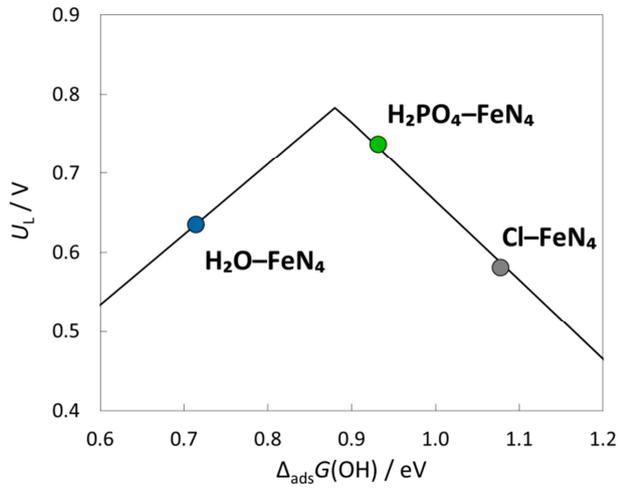


Figure 7 | Schematic ORR activity volcano, shown as relation between limiting potential (U_L) and OH adsorption free energy.

DISCUSSION

Our results support previous investigations on anion adsorption on platinum surfaces, while pointing towards interesting new effects on NPMCs. The strong activity inhibition caused by H_3PO_4 species on Pt is not observed on the Fe/N/C catalyst. On the contrary, the ORR activity is found to benefit from the presence of the H_3PO_4 electrolyte even though oxygen is poorly soluble in this solution. Moreover, the Fe/N/C catalyst appear more tolerant towards poisoning than Pt in general. These experimental results are supported by DFT-level computational modelling, which demonstrates that while the order of binding strength of the anions is the same on Pt and Fe/N/C, the catalytic effect on the latter is different. The effects from the weak binding HClO_4 and H_2SO_4 species are insignificant due to the stronger binding of H_2O to the FeN_4 moiety. However, the effect from the stronger binding H_3PO_4 and HCl species alter the FeN_4 site and the thermodynamic barrier of the limiting step, which is lowered in H_3PO_4 and increased in HCl , as compared to HClO_4 and H_2SO_4 . The results shown are of particular interest for so-called high temperature proton exchange fuel cells (HT-PEMFCs). In this modern version of PAFCs, the electrolyte consists of phosphoric acid, which embedded into a polybenzimidazole (PBI) matrix forms a polymer electrolyte membrane. Catalysing the ORR in HT-PEMFCs with Pt-based catalysts leads to relative low reaction rates despite of a relative high operation temperature of ~ 150 °C, an observation often related to anion poisoning (in addition to low oxygen solubility). Our results indicate that with respect to the ORR activity, NPMCs are a highly promising option as cathode catalyst for HT-PEMFCs.

METHODS

Electrochemical details

All electrochemical measurements were performed in an electrochemical 3-electrode setup. It consisted of an electrochemical double-walled glass cell, which enables precise temperature adjustment. The cell has a central glass joint, which supports the rotating disk electrode (RDE) and is fitted with a direct gas inlet made

of glass, a closed glass tube containing a thermo-logger, as well as a counter (CE) and reference electrode (RE). The CE was a glassy carbon rod and the RE consisted of an RHE in a closed glass tube equipped with a sealed in ceramic frit (Mettler) as liquid junction to the cell. The volume of electrolyte in the cell was ~225 ml. To keep a constant electrolyte temperature, a thermostat (Lauda, Germany) was connected to the outer jacket of the cell. The temperature of the electrolyte was monitored by a thermocouple Type J (RS Components). The electrolyte solutions were prepared from 70 % HClO₄, 96 % H₂SO₄, 85 % H₃PO₄ and 37 % HCl (suprapur quality, Merck) and ultra-pure water (Milli-Q, $\rho = 18.2 \text{ M}\Omega \text{ cm}$, Total organic carbon $\leq 5 \text{ ppb}$). Argon gas (purity $\geq 99.999\%$), oxygen gas and hydrogen gas (purity $\geq 99.995\%$) were from Air Liquide, Denmark. The RDE (EDI101, Radiometer) was combined with a software-controlled rotation control unit (CTV101, Radiometer) and the 3-electrode system was interfaced to an ECi-200 potentiostat operated with the EC4U software package (Nordic Electrochemistry). The WE was a 5 mm (\varnothing) polycrystalline platinum or glassy carbon disk, respectively, inserted into an 11 mm (\varnothing) PEEK cylinder. The WE was polished to a mirror finish on polishing pads with alpha alumina suspensions of 1.0 and 0.3 μm grain size respectively (Struers, Denmark). The NPMC ink was produced by adding 10 % Nafion solution (Sigma-Aldrich) and absolute ethanol (99.8 %) to dry Fe/N/C powder (Pajarito Powder). The mixture was then treated in an ultrasonic bath for 1 hour keeping the suspension cold. Thin films of the catalyst were made by adding 20 μl ink solution to a GC tip and dried for approximately 2 hours. Only uniform films with a loading of 800 $\mu\text{g cm}^{-2}$ were used for electrochemical experiments.

Computational details

All Density Functional Theory (DFT) calculations are done using Atomic Simulation Environment (ASE)³⁷ coupled with the Vienna *Ab Initio* Simulation Package (VASP)³⁸⁻⁴¹. Core electrons are described with the projector augmented wave method^{42,43}. We employ the BEEF-vdW exchange-correlation functional⁴⁴, a plane-wave basis set with 600 eV energy cut-off, Fermi smearing of the electronic occupations with a width of 0.1 eV and a $4 \times 3 \times 1$ Monkhorst-Pack⁴⁵ mesh for sampling of the Brillouin zone. The structure relaxation is performed until maximum force on each atom drops below 0.01 eV/Å.

The Pt(111) surface is modelled by periodically repeated (3 × 3) unit cell with three atomic layers, of which the bottom two are fixed in bulk positions. The Fe/N/C catalyst model consists of a FeN₄C₁₂ moiety embedded in graphene structure with surface cell size of (8.170, 0.0) × (0.0, 12.035) Å. Fe : N : C atomic ratio is 1 : 4 : 26.

Solvation of the surface and adsorbates is taken into account by using the implicit solvation model implemented in VASPsol^{46,47}. Vacuum layer region between atoms in the neighboring cells is at least 9 Å in each calculation. Dipole correction is used to decouple electrostatic potentials on the two sides of the two-dimensional structure. Anion adsorption Gibbs free energy, $\Delta_{\text{ads}}G(A^{n-})$, is calculated as

$$\Delta_{\text{ads}}G(A^{n-}) = -\Delta_{\text{dilut}}G(\text{H}_n\text{A}_{(\text{solvated})}) - \Delta_{\text{solvation}}G(\text{H}_n\text{A}_{(\text{g})}) + \Delta_{\text{CHE}}G(E_{\text{vs.RHE}}, p = 1 \text{ bar}) \quad (1)$$

according to the thermodynamic cycle shown in figure 8. $\Delta_{\text{ads}}G(A^{n-})$ depends on the electrode potential through the $\Delta_{\text{CHE}}G(E_{\text{vs.RHE}}, p = 1 \text{ bar})$ term, which is calculated from DFT using the Computational Hydrogen Electrode model³⁶. Solvation and dilution Gibbs free energies are calculated from standard thermodynamic relations using literature data of formation enthalpies, entropies and ions activity coefficients^{48–51}. An example of the ClO₄⁻ adsorption free energy calculation on Fe/N/C catalyst at 0.75 V_{RHE} is given as Supplementary Note 1. As the gas phase entropies of HClO₄ and H₃PO₄ are not available in the literature, they were calculated from the partition function using molecular data⁴⁹ and treating internal rotations as harmonic vibrations. This approach has been validated for the case of H₂SO₄, where the deviation of the calculated entropy from the experimental one is less than 0.3%. The calculated gas phase entropies are 297.16 and 314.24 J mol⁻¹ K⁻¹ for HClO₄ and H₃PO₄, respectively.

Free energy corrections for adsorbed species are based on the harmonic approximation and calculated vibrational frequencies. Total energy of gas phase O₂ is corrected based on the formation Gibbs free energy of liquid H₂O as described previously⁵², and total energies of the systems with adsorbates are corrected according to Christensen's correction scheme^{53,54}: $\Delta E(\text{O}-\text{O}) = 0.2 \text{ eV}$, $\Delta E(\text{H}_2\text{O}) = -0.03 \text{ eV}$, $\Delta E(\text{H}_2) = 0.09 \text{ eV}$.

To the best of our knowledge, a reliable correction for the adsorbed O₂ has not been determined yet. Consequently, *O₂ energy level on the free energy diagram (figure 6) may be slightly less accurate.

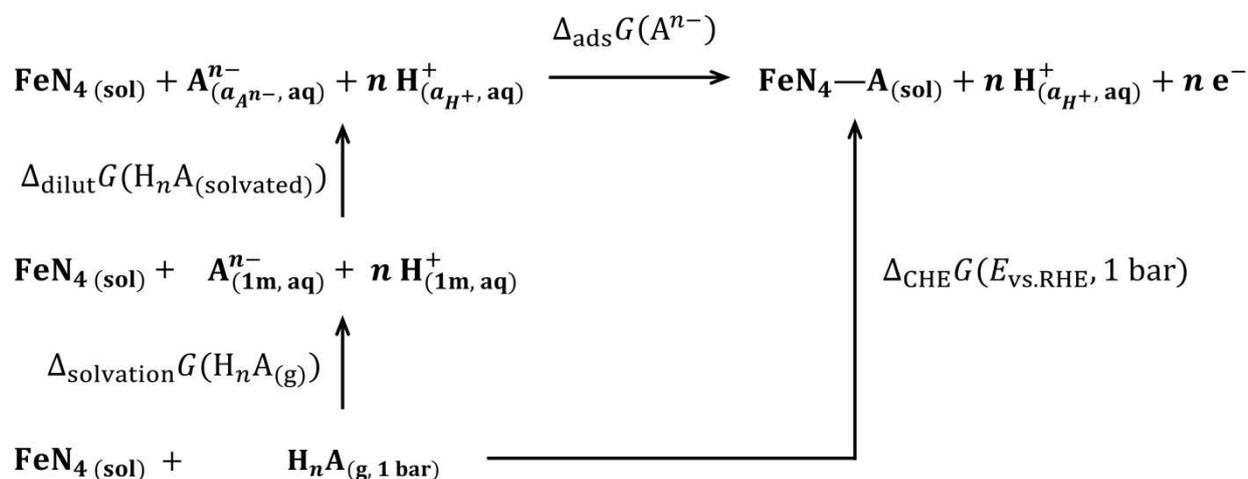


Figure 8 | Thermodynamic cycle for calculation of adsorption Gibbs free energy of Aⁿ⁻ anion from solution. Abbreviations and symbols in brackets: (g) – gas phase, (aq) – aqueous phase, (sol) – continuum solvent (VASPsol), a – activity, 1m = 1 mol kg⁻¹.

REFERENCES

1. Gasteiger, H. A., Kocha, S. S., Sompalli, B. & Wagner, F. T. Activity benchmarks and requirements for Pt, Pt-alloy, and non-Pt oxygen reduction catalysts for PEMFCs. *Appl. Catal. B Environ.* **56**, 9–35 (2005).
2. Jasinski, R. A New Fuel Cell Cathode Catalyst. *Nature* **201**, 1212–1213 (1964).
3. Ross, P. N. Andricacos, P. C. The Effect of H₂PO₄⁻ Anion on the Kinetics of Oxygen Reduction on Pt. *J. Electroanal. Chem.* **154**, 205–215 (1983).
4. Habib, M. A. & Bockris, J. O. Adsorption at the Solid/Solution Interface An FTIR Study of Phosphoric Acid on Platinum and Gold. *J. Electrochem. Soc.* **132**, 108–114 (1985).
5. Nart, F.C., Iwasita, T. On the Adsorption of H₂PO₄⁻ and H₃PO₄ on Platinum: An In Situ FT-IR Study. *Electrochim. Acta* **37**, 385–391 (1992).
6. He, Q. *et al.* Influence of phosphate anion adsorption on the kinetics of oxygen electroreduction on low index Pt(hkl) single crystals. *Phys. Chem. Chem. Phys.* **12**, 12544–55 (2010).

7. Ye, S., Kita, H. & Aramata, A. Hydrogen and anion adsorption at platinum single crystal electrodes in phosphate solutions over a wide range of pH. *J. Electroanal. Chem.* **333**, 299–312 (1992).
8. Glass, J. T., Cahen, G. I. & Stoner, G. E. The Effect of Phosphoric Acid Concentration on Electrocatalysis. *J. Electrochem. Soc.* **136**, 656–660 (1989).
9. Faguy, P. W., Markovic, N., Adzic, R. R., Fierro, C. A. & Yeager, E. B. A Study of Bisulfate Adsorption on Pt(111) Single-Crystal Electrodes Using In situ Fourier-Transform Infrared-Spectroscopy. *J. Electroanal. Chem.* **289**, 245–262 (1990).
10. Horányi, G., Solt, J. & Nagy, F. Investigation of Adsorption Phenomena on Platinized Platinum Electrodes by Tracer Methods. *Electroanal. Chem. Interfacial Electrochem.* **31**, 95–102 (1971).
11. Bagotzky, V. S., Vassilyev, Y. B., Weber, J. & Pirtskhalava, J. N. Adsorption of anions on smooth platinum electrodes. *J. Electroanal. Chem.* **27**, 31–46 (1970).
12. Clavilier, J. The Role of Anion on the Electrochemical Behaviour of a (111) Platinum Surface; An Unusual Splitting of the Voltammogram in the Hydrogen Region. *J. Electroanal. Chem.* **107**, 211–216 (1980).
13. Markovic, N. M., Gasteiger, H. A. & Ross, P. N. Oxygen Reduction on Platinum Low-Index Single-Crystal Surfaces in Sulfuric Acid Solution: Rotating Ring-Pt(hkl) Disk Studies. *J. Phys. Chem.* **99**, 3411–3415 (1995).
14. Malko, D., Lopes, T., Symianakis, E. & Kucernak, A. R. The intriguing poison tolerance of non-precious metal oxygen reduction reaction (ORR) catalysts. *J. Mater. Chem. A* **4**, 142–152 (2016).
15. Wang, Q. *et al.* Phenylenediamine-Based Fe_{Nx}/C Catalyst with High Activity for Oxygen Reduction in Acid Medium and Its Active-Site Probing. *J. Am. Chem. Soc.* **136**, 10882–10885 (2014).
16. Al Jaaf-Golze, K., Kolb, D. M. & Scherson, D. On the Voltammetry Curves of Pt (111) in Aqueous Solutions. *J. Electroanal. Chem.* **200**, 353–362 (1986).
17. Lawson, D. R., Whiteley, L. D., Martin, C. R., Szentirmay, M. N. & Song, J. I. Oxygen Reduction at Nafion Film-Coated Platinum Electrodes: Transport and Kinetics. *J. Electrochem. Soc.* 2247–2253 (1988).
18. Climent, M. a., Valls, M. J., Feliu, J. M., Aldaz, A. & Clavilier, J. The behaviour of platinum single-crystal electrodes in neutral phosphate buffered solutions. *J. Electroanal. Chem.* **326**, 113–127 (1992).
19. Woodard, F. E., Scortichini, C. L. & Reilley, C. N. Hydrogen Chemisorption and Related Anion Effects on Pt(110) Electrodes. *J. Electroanal. Chem.* **151**, 109–131 (1983).
20. Zolfaghari, A. & Jerkiewicz, G. Temperature-dependent research on Pt (111) and Pt (100) electrodes in aqueous H₂SO₄. *J. Electroanal. Chem.* **467**, 177–185 (1999).
21. Gisbert, R., García, G. & Koper, M. T. M. Adsorption of phosphate species on poly-oriented Pt and Pt(111) electrodes over a wide range of pH. *Electrochim. Acta* **55**, 7961–7968 (2010).
22. Markovic, N., Hanson, M., Mcdougall, G. & Yeager, E. The Effects of Anions on Hydrogen Electrosorption on Platinum Single-crystal Electrodes. *J. Electroanal. Chem.* **214**, 555–566 (1986).
23. Nesselberger, M. & Arenz, M. In Situ FTIR Spectroscopy: Probing the Electrochemical Interface during the Oxygen Reduction Reaction on a Commercial Platinum High-Surface-Area Catalyst. *ChemCatChem* **8**, 1125–1131 (2016).

24. Strmcnik, D. *et al.* Enhanced electrocatalysis of the oxygen reduction reaction based on patterning of platinum surfaces with cyanide. *Nat. Chem.* **2**, 880–5 (2010).
25. Ciapina, E. G. *et al.* Surface spectators and their role in relationships between activity and selectivity of the oxygen reduction reaction in acid environments. *Electrochem. commun.* **60**, 30–33 (2015).
26. Pa, I. A., Markovi, A., Gavrilov, N. & Mentus, S. V. Adsorption of Acetonitrile on Platinum and its Effects on Oxygen Reduction Reaction in Acidic Aqueous Solutions — Combined Theoretical and Experimental Study. *Electrocatalysis* **7**, 235–248 (2016).
27. He, Q., Shyam, B., Nishijima, M., Ramaker, D. & Mukerjee, S. Mitigating phosphate anion poisoning of cathodic Pt/C catalysts in phosphoric acid fuel cells. *J. Phys. Chem. C* **117**, 4877–4887 (2013).
28. Hong, S.-G., Kwon, K., Lee, M.-J. & Yoo, D. Y. Performance enhancement of phosphoric acid-based proton exchange membrane fuel cells by using ammonium trifluoromethanesulfonate. *Electrochem. commun.* **11**, 1124–1126 (2009).
29. Holst-Olesen, K., Nesselberger, M., Perchthaler, M., Hacker, V. & Arenz, M. Activity inhibition and its mitigation in high temperature proton exchange membrane fuel cells: The role of phosphoric acid, ammonium trifluoromethanesulfonate, and polyvinylidene difluoride. *J. Power Sources* **272**, (2014).
30. Zana, A. *et al.* Accessing the Inaccessible: Analyzing the Oxygen Reduction Reaction in the Diffusion Limit. *ACS Appl. Mater. Interfaces* **9**, 38176–38180 (2017).
31. Gottesfeld, S. & Zawodzinski, T. A. in *Advances in Electrochemical Science and Engineering* (1997).
32. Antoine, O., Bultel, Y. & Durand, R. Oxygen reduction reaction kinetics and mechanism on platinum nanoparticles inside Nafion (R). *J. Electroanal. Chem.* **499**, 85–94 (2001).
33. Appleby, A. J. & Baker, B. S. Oxygen Reduction on Platinum in Trifluoromethane Sulfonic Acid. *J. Electrochem. Soc.* **125**, 404–406 (1978).
34. Razaq, M., Razaq, A., Yeager, E. & Desmarteau, D. D. Perfluorosulfonimide as an Additive in Phosphoric Acid Fuel Cell. *J. Electrochem. Soc.* **136**, 7–12 (1989).
35. Deng, Y., Wiberg, G. K. H., Zana, A. & Arenz, M. On the oxygen reduction reaction in phosphoric acid electrolyte: Evidence of significantly increased inhibition at steady state conditions. *Electrochim. Acta* **204**, 78–83 (2016).
36. Nørskov, J. K. *et al.* Origin of the Overpotential for Oxygen Reduction at a Fuel-Cell Cathode. *J. Phys. Chem. B* **108**, 17886–17892 (2004).
37. Larsen, A. H. *et al.* The atomic simulation environment - a Python library for working with atoms. *J. Phys. Condens. Matter* **29**, 273002 (2017).
38. Kresse, G. & Furthmüller, J. Efficiency of ab-initio total energy calculations for metals and semiconductors using a plane-wave basis set. *Comput. Mater. Sci.* **6**, 15–50 (1996).
39. Kresse, G. & Furthmüller, J. Efficient iterative schemes for ab-initio total-energy calculations using a plane-wave basis set. *Phys. Rev. B* **54**, 11169–11186 (1996).
40. Kresse, G. & Hafner, J. Ab initio molecular-dynamics simulation of the liquid-metal-amorphous-semiconductor transition in germanium. *Phys. Rev. B* **49**, 14251–14269 (1994).
41. Kresse, G. & Hafner, J. Ab initio molecular dynamics for liquid metals. *Phys. Rev. B* **47**, 558–561 (1993).

42. Blöchl, P. E. Projector augmented-wave method. *Phys. Rev. B* **50**, 17953–17979 (1994).
43. Kresse, G. & Joubert, D. From ultrasoft pseudopotentials to the projector augmented-wave method. *Phys. Rev. B* **59**, 1758–1775 (1999).
44. Wellendorff, J. *et al.* Density functionals for surface science: Exchange-correlation model development with bayesian error estimation. *Phys. Rev. B* **85**, 235149 (2012).
45. Monkhorst, H. J. & Pack, J. D. Special points for Brillouin-zone integrations. *Phys. Rev. B* **13**, 5188–5192 (1976).
46. Mathew, K. & Hennig, R. G. Implicit self-consistent description of electrolyte in plane-wave density-functional theory. (2016). at <<http://arxiv.org/abs/1601.03346>>
47. Mathew, K., Sundararaman, R., Letchworth-Weaver, K., Arias, T. A. & Hennig, R. G. Implicit solvation model for density-functional study of nanocrystal surfaces and reaction pathways. *J. Chem. Phys.* **140**, 84106 (2014).
48. *CRC handbook of chemistry and physics: a ready-reference book of chemical and physical data.* (CRC Press, 2014).
49. NIST Computational Chemistry Comparison and Benchmark Database, NIST Standard Reference Database Number 101, Release 18, October 2016, Editor: Russell D. Johnson III. at <<http://cccbdb.nist.gov/>>
50. DIPPR, Project 801 - Full Version. Design Institute for Physical Property Research/AIChE, 2012.
51. Martin, J. M. L. Heats of formation of perchloric acid, HClO₄, and perchloric anhydride, Cl₂O₇. Probing the limits of W1 and W2 theory. *J. Mol. Struct. THEOCHEM* **771**, 19–26 (2006).
52. Rossmeisl, J., Logadottir, A. & Nørskov, J. K. Electrolysis of water on (oxidized) metal surfaces. *Chem. Phys.* **319**, 178–184 (2005).
53. Christensen, R., Hansen, H. A., Dickens, C. F., Nørskov, J. K. & Vegge, T. Functional Independent Scaling Relation for ORR/OER Catalysts. *J. Phys. Chem. C* **120**, 24910–24916 (2016).
54. Christensen, R., Hansen, H. A. & Vegge, T. Identifying systematic DFT errors in catalytic reactions. *Catal. Sci. Technol.* **5**, 4946–4949 (2015).

ACKNOWLEDGEMENTS

The authors would like to thank the Innovation Fund Denmark for funding through the Initiative Towards Non-Precious Metal Polymer Fuel Cells (NonPrecious), project no. 4106-00012A and the Velux Foundations through The VILLUM Center for the Science of Sustainable Fuels and Chemicals (#9455). We also thank Prof. Tadeusz Hofman (Warsaw University of Technology) for fruitful discussions.

AUTHOR CONTRIBUTIONS

All authors contributed to conceiving the investigations, to the writing and editing of the manuscript as well as to the discussion and interpretations of the results. K.H.O. performed all electrochemical measurements. M.R. formulated the computational approach and performed DFT calculations.

ASSOCIATED CONTENT

Supplementary Information

Competing financial interests: The authors declare no competing financial interests.

Supplementary Information

Enhanced Oxygen Reduction Activity by Selective Anion Adsorption on Non-Precious Metal Catalysts

Kaspar Holst-Olesen, Mateusz Reda, Heine Hansen, Tejs Vegge, Matthias Arenz

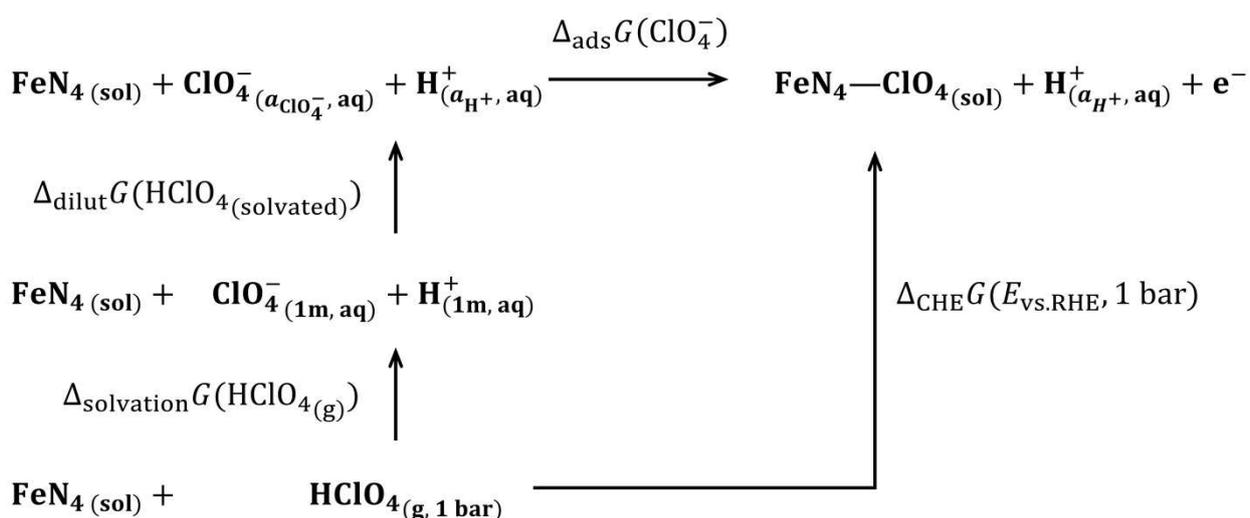
SUPPLEMENTARY NOTE 1: CALCULATION OF ClO_4^- ADSORPTION ON THE Fe/N/C CATALYST

Let us consider the process of ClO_4^- anion adsorption on the Fe/N/C catalyst with an empty backside:



In the equation, the catalyst is represented by the FeN_4 moiety. The thermodynamic cycle for this process is shown in Supplementary Fig. 1, and the adsorption energy is calculated according to the following equation (special case of equation (1)):

$$\Delta_{\text{ads}}G(\text{ClO}_4^-) = -\Delta_{\text{dilut}}G(\text{HClO}_4(\text{solvated})) - \Delta_{\text{solvation}}G(\text{HClO}_4(\text{g})) + \Delta_{\text{CHE}}G(E_{\text{vs.RHE}}, 1 \text{ bar}) \quad (\text{S2})$$



Supplementary Figure 1 | Thermodynamic cycle for calculation of adsorption Gibbs free energy of ClO_4^- anion from solution. Abbreviations and symbols in brackets: (g) – gas phase, (aq) – aqueous phase, (sol) – continuum solvent (VASPsol), a – activity, 1m = 1 mol kg^{-1} .

The third term on the right hand side of equation (S2), $\Delta_{\text{CHE}}G(E_{\text{vs.RHE}}, 1 \text{ bar})$, is the adsorption Gibbs free energy of gaseous $\text{HClO}_{4(\text{g})}$ at 1 bar and a given electrode potential $E_{\text{vs.RHE}}$, and is calculated by means of Density Functional Theory using the Computational Hydrogen Electrode scheme¹:

$$\Delta_{\text{CHE}}G(E_{\text{vs.RHE}}, 1 \text{ bar}) = \Delta_{\text{CHE}}G(0 \text{ V}_{\text{RHE}}, 1 \text{ bar}) - neE_{\text{vs.RHE}} \quad (\text{S3})$$

where: n – number of electrons transferred (here $n = 1$), e – elementary positive charge.

Adsorption Gibbs free energy of gaseous $\text{HClO}_{4(\text{g})}$ at 1 bar and 0 V_{RHE} is given by:

$$\Delta_{\text{CHE}}G(0 \text{ V}_{\text{RHE}}, 1 \text{ bar}) = G(\text{FeN}_4\text{-ClO}_{4(\text{sol})}) + \frac{1}{2}G(\text{H}_2(\text{g})) - [G(\text{FeN}_4(\text{sol})) + G(\text{HClO}_{4(\text{g})})] \quad (\text{S4})$$

where the Gibbs free energies of the reactants (X) are²:

$$G(X) = E_{\text{DFT}}(X) + E_{\text{ZPE}}(X) + \int_{0\text{K}}^T c_p(X)dT - TS(X, T, 1 \text{ bar}) \quad (\text{S5})$$

Here T is the temperature (298.15 K), $E_{\text{DFT}}(X)$ is the reactant DFT energy, $E_{\text{ZPE}}(X)$ is its zero point energy, $\int_{0\text{K}}^T c_p(X)dT$ is the integrated heat capacity (from 0 to 298.15 K) and $S(X)$ is the entropy. For the gas phase reactants, E_{ZPE} is calculated from the spectroscopic data, $\int_{0\text{K}}^T c_p dT$ is taken from the literature (for H_2) or calculated from the partition function using molecular data (for HClO_4 ; data and references are included in Supplementary Table 1), and $S(298.15 \text{ K}, 1 \text{ bar})$ is either taken from the literature ($\text{H}_2(\text{g})$) or calculated as described in the Methods section of the main manuscript ($\text{HClO}_{4(\text{g})}$). For the remaining systems, the last three terms on the right hand side of equation (S5) are calculated from DFT vibrational frequencies, allowing only the adsorbate atoms to vibrate, and assuming all the degrees of freedom can be described as independent quantum harmonic oscillators.

The second term on the right hand side of equation (S2), $\Delta_{\text{solvation}}G(\text{HClO}_{4(\text{g})})$, is the Gibbs free energy of dissolving gaseous HClO_4 in water to form ion solution in the standard state (ideal solution, $b = 1 \text{ mol/kg}$, $p = 1 \text{ bar}$) at 298.15 K:

$$\Delta_{\text{solvation}}G(\text{HClO}_{4(\text{g})}) = \Delta_f G^\circ(\text{ClO}_4^-(1\text{m,aq})) - \Delta_f G^\circ(\text{HClO}_{4(\text{g})}) \quad (\text{S6})$$

where $\Delta_f G^\circ(X)$ are the standard Gibbs free energies of formation, that can be found in the literature (data and referenced are included in Supplementary Table 2).

The first term on the right hand side of equation (S2), $\Delta_{\text{dilut}}G(\text{HClO}_{4(\text{solvated})})$, is the Gibbs free energy of dilution (in general: concentration change). It also captures deviations from ideal behavior:

$$\Delta_{\text{dilut}}G(\text{HClO}_4(\text{solvated})) = k_{\text{B}}T \ln(a_{\text{H}^+} a_{\text{ClO}_4^-}) \quad (\text{S7})$$

where $a_i = b_i \gamma_{\pm}$ is the ion activity, b_i is its molal concentration, and γ_{\pm} is the concentration-dependent mean activity coefficient.

Supplementary Table 1 | Values of the properties used to calculate $\Delta_{\text{CHE}}G(E_{\text{vs.RHE}}, 1 \text{ bar})$.

	FeN ₄ (sol)	HClO ₄ (g)	FeN ₄ -ClO ₄ (sol)	H ₂ (g)
$E_{\text{DFT}} / \text{eV}$	-247.655	-16.850	-261.357	-7.178
$E_{\text{ZPE}} / \text{eV}$	0	0.727 ³	0.429	0.273 ³
$\int_{0\text{K}}^{298.15\text{K}} c_p dT / \text{eV}$	0	0.155 ^a	0.135	0.088 ⁴
$S(298.15 \text{ K}, 1 \text{ bar}) / \text{meV K}^{-1}$	0	3.080 ^b	0.945	1.354 ⁴

^a calculated from the partition function² using molecular data³

^b calculated from the partition function² using molecular data³ and treating internal rotations as harmonic vibrations

Supplementary Table 2 | Values of the properties used to calculate $\Delta_{\text{solvation}}G(\text{HClO}_4(\text{g}))$ and $\Delta_{\text{dilut}}G(\text{HClO}_4(\text{solvated}))$.

	HClO ₄ (g)	ClO ₄ ⁻ (aq)	H ⁺ (aq)
$\Delta_f H^\circ(298.15 \text{ K}) / \text{eV}$	-0.0260 ⁵	-1.340 ⁴	0
$S^\circ(298.15 \text{ K}) / \text{meV K}^{-1}$	3.08 ^a	1.886 ⁴	0
$\Delta_f G^\circ(298.15 \text{ K}) / \text{eV}$	0.869	-0.0890	0
$b / \text{mol kg}_{\text{H}_2\text{O}}^{-1}$	N/A	0.5	0.5
$\gamma_{\pm} \left(0.5 \frac{\text{mol}}{\text{kg}_{\text{H}_2\text{O}}}\right)$	N/A	0.769 ⁴	0.769 ⁴

^a calculated from the partition function² using molecular data³ and treating internal rotations as harmonic vibrations

Using data included in Supplementary Tables 1 and 2, we calculate ClO₄⁻ adsorption Gibbs free energy on

Fe/N/C catalyst at $p = 1 \text{ bar}$, $T = 298.15 \text{ K}$, $E = 0.75 \text{ V}_{\text{RHE}}$ and $b_{\text{HClO}_4} = 0.5 \frac{\text{mol}}{\text{kg}_{\text{H}_2\text{O}}} \approx 0.5 \frac{\text{mol}}{\text{dm}^3}$:

$$\begin{aligned} \Delta_{\text{CHE}}G(E_{\text{vs.RHE}}, 1 \text{ bar}) &= -0.894 \text{ eV} \\ \Delta_{\text{solvation}}G(\text{HClO}_4(\text{g})) &= -0.958 \text{ eV} \\ \Delta_{\text{dilut}}G(\text{HClO}_4(\text{solvated})) &= -0.049 \text{ eV} \\ \Delta_{\text{ads}}G(\text{ClO}_4^-) &= +0.113 \text{ eV} \end{aligned}$$

SUPPLEMENTARY REFERENCES

1. Nørskov, J. K. *et al.* Origin of the Overpotential for Oxygen Reduction at a Fuel-Cell Cathode. *J. Phys. Chem. B* **108**, 17886–17892 (2004).
2. C.J. Cramer. *Essentials of Computational Chemistry*, Second Edition. Wiley, 2004.
3. NIST Computational Chemistry Comparison and Benchmark Database, NIST Standard Reference Database Number 101, Release 18, October 2016, Editor: Russell D. Johnson III. at <http://cccbdb.nist.gov/>
4. Haynes, W.M. (ed.), *CRC handbook of chemistry and physics: a ready-reference book of chemical and physical data*, 95th Edition. CRC Press, 2014.
5. Martin, J. M. L., Heats of formation of perchloric acid, HClO₄, and perchloric anhydride, Cl₂O₇. Probing the limits of W1 and W2 theory. *J. Mol. Struct. THEOCHEM* **771**, 19–26 (2006).

B.3 Paper 3

DFT Study of the Oxygen Reduction Reaction on Carbon-Coated Iron and Iron Carbide

Mateusz Reda, Heine Anton Hansen, Tejs Vegge

To be submitted.

DFT Study of the Oxygen Reduction Reaction on Carbon-Coated Iron and Iron Carbide

Mateusz Reda^a, Heine Anton Hansen^{a,*}, Tejs Vegge^a

^aDepartment of Energy Conversion and Storage, Technical University of Denmark, DK-2800 Kgs. Lyngby, Denmark

Abstract

Iron carbide encapsulated in graphitic layers has recently been recognized as an active Oxygen Reduction Reaction (ORR) catalyst made of earth-abundant elements. Here, the ORR activity of graphene (G) and N-doped graphene (NG) supported on Fe₃C(010) and Fe(110) is studied computationally by means of Density Functional Theory (DFT) calculations. Consistent with experiments, the calculations show higher activity of the Fe₃C-supported system than the Fe-supported one, as well as the importance of N-doping in achieving high ORR activity. The active sites are existing on a single N-doped graphitic layer placed on the Fe₃C surface. Like in the case of unsupported NG, the reaction on Fe₃C/NG interface proceeds at the atomic oxygen coverage between $0.5 < \theta_O < 1.0$. Charge on O adsorbate caused by the presence of support is found to correlate with oxygen binding strength. In case of Fe/NG system this results in the surface poisoning by oxygen. It is suggested that a heterostructure consisting of NG overlayer and a support with stronger electron donating properties than Fe₃C (but weaker than Fe) is likely to approach or exceed the ORR activity of Pt(111) surface.

Keywords: Oxygen reduction reaction, Density Functional Theory, Pt-group free ORR catalyst, N-doped graphene, Metal support

1. Introduction

Fuel cells are devices that directly convert chemical energy in fuels into electrical energy through an electrochemical reaction. They are theoretically much more efficient than heat engines. For example, direct utilization of hydrogen in an internal combustion engine has efficiency of about 10-20%, while the ideal thermodynamic efficiency of a H₂-O₂ fuel cell is about 83% at 25°C [1]. There are several types of fuel cells; among them, the Proton-Exchange Membrane Fuel Cells (PEMFC) are particularly promising for future use in light transport (*e.g.* cars) and certain portable applications [2]. However, the technology suffers from a serious issue, which is a sluggish kinetics of the Oxygen Reduction Reaction (ORR) taking place at the fuel cell cathode [3]. Over the past two decades, a considerable insight was gained into the phenomena underlying this obstacle, and the responsibility was found to lie on the side of an unfavorable scaling relation between OH and OOH binding energies. More in-depth discussion can be found in a very recent review article by Kulkarni *et al.* [4].

Currently, the greatest challenge in commercializing PEM fuel cells is finding a durable and inexpensive material, which would efficiently catalyze the oxygen electroreduction. One way to achieve this is to decrease the amount of precious metals, of which the most active known ORR catalysts are made [3, 5, 6, 7]. A different strategy is to synthesize the catalyst using precursors made entirely out of the earth-abundant elements [3, 8, 9]. The latter possibility is particularly attractive, as there is no fundamental difference between precious and non-precious catalysts regarding the highest achievable activity.

Arguably the most promising low-cost catalysts for ORR to date, both in terms of activity and long-term durability, are those containing FeN₄ moieties as active sites [10, 11]. Another notable class of catalysts are metal-supported 2-dimensional materials, which activity can be tuned both by the choice of the 2D overlayer (*e.g.* doped graphene,

*Corresponding author, heih@dtu.dk

hexagonal boron nitride) and the support [9]. These interfaces have rarely been studied computationally, and studies are challenging due to certain computational difficulties, such as problems with correct description of the support-overlayer interaction at a moderate computational cost [12, 13, 14, 15, 16].

Recently, a new metal-supported 2D material composed of iron carbide nanoparticles encased in graphitic layers was shown to have a notable activity and stability in acidic conditions [17, 18, 19, 20]. It has been suggested that a new type of catalytic site may have been discovered [21]. The catalyst activity was shown to correlate both with nitrogen [22] and iron carbide [23] content. The present work aims to provide insight into the possible nature of the ORR active sites at the iron/carbon interface, as well as to explain their catalytic activity and suggest how it may be improved.

2. Computational methods

Heterostructure interfaces are prepared using the Virtual NanoLab (VNL) software [24]. All Density Functional Theory (DFT) calculations are done using Vienna *Ab initio* Simulation Package (VASP) [26, 27, 28, 29] coupled with Atomic Simulation Environment (ASE) [25]. Core electrons are described with the projector augmented wave method [30, 31], and the basis set for the electronic wavefunctions are plane waves below a 400 eV energy cutoff. We use a Fermi smearing of electronic occupations with a width of 0.1 eV and a Monkhorst-Pack [32] mesh for the Brillouin zone sampling of $(k_1, k_2, 1)$, with k_i such that $k_i v_i > 30$ for v_i being the corresponding lattice vector. For systems containing iron, spin-polarized calculations are performed, as both iron and iron carbide are ferromagnetic. The structure relaxation is continued until the maximum force on each atom drops below 0.01 eV/Å.

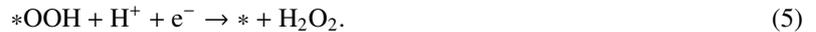
In our study, we consider systems such as multiple graphene layers stacked one on another, in which dispersion forces play a significant role. Many popular semilocal exchange-correlation functionals used in materials science, like PBE [33] or RPBE [34], do not account for non-local van der Waals interactions. Here we employ BEEF-vdW [35] functional in which vdW-DF2 [36] non-local correlation is used. This approach proved to be successful in predicting adsorption bond energies to transition metal surfaces [37], at the same time offering a very good description of metal/graphene heterostructures, such as Ni(111)/graphene [35].

Solvation of the surface and adsorbates is taken into account by including explicit water layer, which structure is determined by the minima hopping algorithm [38] implemented in ASE [39]. We use 14 Å of a vacuum + water layer region between periodic replicas. Dipole correction is used to decouple electrostatic potentials on the two sides of the two-dimensional structure.

Oxygen Reduction Reaction proceeds through four electron-proton transfer steps, called collectively a $4e^-$ associative pathway



where * denotes the active site on the surface of the catalyst. Competitively to reaction (2), the proton may attack the oxygen directly bound to the surface. This results in the parasitic formation of hydrogen peroxide and so-called $2e^-$ associative pathway [40]



$4e^-$ dissociative pathway, in which oxygen dissociates on the surface before accepting proton and electron, is less likely to occur due to high O_2 dissociation barrier on graphene and N-doped graphene (2.4 eV and 1.2 eV, respectively [41]).

We employ the Computational Hydrogen Electrode (CHE) scheme [42] to calculate free energies of the ORR steps as a function of the applied electrode potential. Adsorption energies are defined as the DFT energies of the following

reactions:



Gibbs free energies of the adsorbed species are calculated assuming they can be approximated by the quantum harmonic oscillators. Formation Gibbs free energy of liquid water is fixed at the experimental value of -2.46 eV to avoid calculation of O_2 energy, which is known to be poorly described by DFT [43]. Total energies of the systems with adsorbates are corrected according to the Christensen's correction scheme [44, 45]: $\Delta E(\text{O}-\text{O}) = 0.2$ eV (peroxide bond), $\Delta E(\text{H}_2\text{O}) = -0.03$ eV, $\Delta E(\text{H}_2) = 0.09$ eV. Free energy of H_2O_2 formation is fixed at the experimental value of -1.39 eV [46] by adjusting the energy level of hydrogen peroxide.

3. Results and discussion

3.1. Structures of the interfaces

3.1.1. $\text{Fe}_3\text{C}/\text{graphene}$

The iron carbide surface is modeled by use of the $\text{Fe}_3\text{C}(010)$ facet. The choice was made as a compromise between the surface energy [47], magnitude of the $\text{Fe}_3\text{C}/\text{graphene}$ ($\text{Fe}_3\text{C}/\text{G}$) lattice mismatch and the system size, with the aim to minimize all the three parameters. $\text{Fe}_3\text{C}(010)$ facet surface energy is only about $13 \text{ meV}/\text{\AA}^2$ (10%) higher than that of the most stable $\text{Fe}_3\text{C}(001)$ facet. The unit cell contains 16 graphene carbon atoms placed horizontally on top of the iron carbide slab, such that the graphene basal plane is exposed to the liquid phase (Fig. 1a–c). The carbide phase is compressed (3.0%) to match the lattice of graphene [13]. This is done to study the effect of support, without obscuring it by the effect of strained graphene. It has to be noted, however, that the actual (experimental) strain in the system due to the interaction between the two phases is not known. The effect of uniaxial, biaxial and shear strain on the OH adsorption energy on graphene is illustrated in Fig. S1 (Supporting Information).

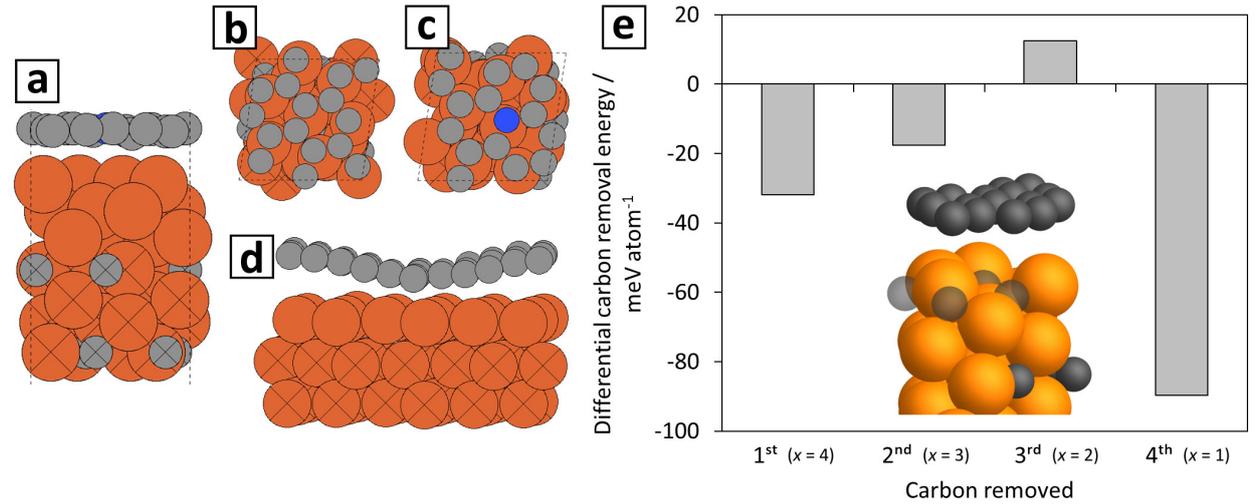


Figure 1: Interface models: (a) $\text{Fe}_3\text{C}(010)/\text{N-graphene}$, side view; (b) $\text{Fe}_3\text{C}(010)/\text{graphene}$, top view; (c) $\text{Fe}_3\text{C}(010)/\text{N-graphene}$, top view; (d) $\text{Fe}(110)/\text{graphene}$, side view; (e) differential energy of removing carbon atoms from the Fe_3C surface at the $\text{Fe}_3\text{C}/\text{G}$ interface; x is the parameter from Eq. (10); the four surface carbon atoms are shown as transparent in the inset. Crosses mark atoms which positions are fixed during structure relaxation. Color code for atoms: C – gray, N – blue, Fe – orange.

Considering the $\text{Fe}_3\text{C}(010)$ plane, the atomic layer pattern repeats every 6 layers. This results in a number of possible cleavages with different surface properties. Starting from a carbon-rich Fe_3C surface, we consider the stability of $\text{Fe}_3\text{C}/\text{graphene}$ interface as the carbon atoms are removed from the Fe_3C surface to form a separate graphite phase (Fig. 1e). The process is described by the following reaction:



where x is the number of carbon atoms on the Fe_3C surface in the model unit cell. We find that the lowest energy structure contains no carbon atoms on the Fe_3C surface. Although removal of the third carbon atom requires energy input (12 meV/atom, which amounts to $0.3 \text{ meV}/\text{\AA}^2$, or $5 \text{ mJ}/\text{m}^2$), this barrier, as well as the actual carbon removal barrier, is expected to be surmountable in the pyrolytic synthesis conditions [17]. We therefore use a model with Fe_3C surface without non-graphitic carbon at the $\text{Fe}_3\text{C}/\text{graphene}$ interface.

The model Fe_3C slab consists of 7 atomic layers (6.8 \AA), where the bottom 4 layers are fixed in the bulk positions during the structure relaxation (Fig. 1a). The surface cell dimensions are $(6.52, 0.00) \times (0.93, 6.45) \text{ \AA}$. This surface cell is utilized to model only the $\text{Fe}_3\text{C}/(\text{N-})\text{graphene}$ interface. The actual catalyst models, which are described in section 3.2, consist of in-plane-extended versions of the cell described here. Graphene chemisorbs on Fe_3C with an adhesion energy of 43 meV/(C atom), or $16.3 \text{ meV}/\text{\AA}^2$ ($260 \text{ mJ}/\text{m}^2$), and the Fe_3C -graphene distance is found to be 2.3 \AA . According to Bader charge analysis, each carbon atom in the graphene sheet withdraws $0.047 e^-$ from the carbide phase on average. Increased availability of electrons in the graphene sheet is expected to increase the $^*\text{O}$ adsorbate stability, which was observed before in N-graphene system with additional N dopant [48].

3.1.2. Fe/graphene

The iron surface is modeled by the lowest surface energy bcc-Fe(110) facet [49]. The slab consists of 3 atomic layers, where the two bottom layers are fixed in the bulk positions during the structure relaxation (Fig. 1d). The surface cell vectors are $(13.72, 0.00) \times (-2.21, 6.13) \text{ \AA}$, and each atomic layer consists of 16 iron atoms. Iron and graphene lattices are matched by applying mixed expansive/compressive strain (2.0 %) to the iron phase. The unit cell contains 32 graphene carbon atoms placed on top of the iron slab.

According to the calculations, graphene chemisorption energy on bcc-Fe(110) surface is slightly positive, +2.3 meV/(C atom), which suggests this heterostructure is metastable relative to separate phases. We have also found physisorbed state with a separation of 3.9 \AA and an adsorption energy of $-38 \text{ meV}/(\text{C atom})$. The potential energy surface of a similar shape was previously observed for fcc-Ni(111)/graphene interface calculated using GGA functionals: PBE [13] and BEEF-vdW [35]. In this case, repeating the calculations at a higher level of theory (meta-GGA [13] or Random Phase Approximation [14]) results in evident binding of the chemisorbed state. The problem appearing with GGA functionals, also when including nonlocal interaction corrections, is attributed to an inaccurate simultaneous description of the covalent and dispersive forces in such a weak binding systems [14]. Bearing that in mind, and having experimental evidence that bcc-Fe(110)/G forms a covalently bound heterostructure [50], we use the chemically bound bcc-Fe(110)/graphene interface as the ORR catalyst model.

We notice that a graphene sheet forms waves on the bcc-Fe(110) surface, with corrugation amplitude of 1.0 \AA (Fig. 1d). This effect was observed previously both in experiments and calculations, and was found to result from a combination of lattice mismatch and strong interfacial interaction [50]. The shortest distance between iron and graphene is 2.2 \AA .

A Bader charge analysis shows that each graphene carbon atom withdraws, on average, $0.041 e^-$ from the iron phase. This is significantly less than the $0.07 e^-/(\text{C atom})$ obtained by Taubert and Laasonen for iron nanoparticle enclosed in fullerene [51]. The discrepancy is likely due to larger separation between some parts of iron and graphene in the two dimensional Fe/G interface, caused by buckling of the graphene layer.

3.1.3. Nitrogen doping

Having established the $\text{Fe}_3\text{C}/\text{G}$ and Fe/G interface models, we investigate the effect of nitrogen doping. By replacing one carbon atom with nitrogen we obtain $\text{Fe}_3\text{C}/\text{N-graphene}$ ($\text{Fe}_3\text{C}/\text{NG}$, Fig. 1c) and $\text{Fe}/\text{N-graphene}$ (Fe/NG , Fig. 4b, inset) with 6.3 and 3.1 at%N in the graphene sheet, respectively. N-doped graphene is slightly more strongly bound to both supports. The chemisorption energy per N-graphene atom and the support-NG distance are -64 meV and 2.2 \AA for the Fe_3C support, and -3.4 meV and 2.1 \AA (NG wave trough) for the Fe support, respectively. A

Bader charge transfer from the carbide and iron phases to the N-graphene phase is 0.048 and 0.038 e^- /(NG atom), respectively, which is only slightly different from the one obtained for the undoped systems.

3.2. ORR catalyst models

In the previous study [48], we have considered spectator effect on the ORR intermediates stability on unsupported N-graphene. We have found that the presence of free nitrogen atoms (*i.e.* nitrogen, which neighboring carbon atoms are not occupied by any adsorbate) significantly stabilizes the *O intermediate (* stands for the active site). On the one hand the lack of free nitrogen results in artificially weak *O binding, but on the other hand too many free nitrogen atoms in the cell result in so strong *O binding that its reduction becomes the potential limiting step for the ORR. As a consequence, the reaction takes place in the presence of both *O and free nitrogen as spectators. In this study, we find the same to be true for the Fe₃C-supported N-graphene. In order to create such a reaction environment, we extend the previously described Fe₃C/NG unit cell in the surface plane to obtain a triple ($\sqrt{2} \times \sqrt{3}$) cell. The catalyst model contains 3 nitrogen atoms in the unit cell, of which one is occupied by *O, another one is free, and the last one serves as an active site for the ORR (Fig. 3b).

The catalytic properties of the Fe₃C/G interface are modeled using a double ($\sqrt{2} \times \sqrt{2}$) cell (Fig. 3a). The single cell resulted in artificially lowered stability of the water layer inserted on top of the heterostructure (solvation model is described in details in section 3.3).

The presence of free nitrogen is found not to influence the *O stability on Fe/NG interface. The previously described cell is thus also used as the catalyst model, both for N-doped and undoped systems.

For comparison, we use the same computational approach to model the oxygen reduction reaction on Pt(111) surface. The model consists of 3×3 surface cell and three atomic layers of platinum. The bottom two layers are fixed in the bulk positions during the structure relaxation.

3.3. The water layer

Since the oxygen reduction reaction catalysts are intended to work in an aqueous environment, it is desirable to include the water solvation effects in ORR modeling. Previously, we have shown that continuum solvation models cannot correctly account for interactions between water and adsorbed oxygen, hence including explicit H₂O molecules seems to be essential for the correct description of the ORR intermediates stability (especially for *O) [48]. The number of water molecules in each interface is enough to form at least a single water layer. This was found to sufficiently reproduce the ORR intermediates solvation on N-doped graphene [48].

Global optimization of the water layer structure is performed using the minima hopping algorithm [38, 39]. Here, the structure is determined for each ORR step in the appropriate environment (*e.g.* in the presence of spectators, when relevant). The support has minimal effect on the optimal structure of water. For the time of minima hopping runs the support is removed from the simulation cell and the (N-)graphene structure is fixed. All the water molecules and adsorbate atoms, except for the one directly bound to the (N-)graphene sheet, are allowed to move during the global optimization. The procedure is continued until at least 30 local minima are found for each system. Finally, we reinsert the support to the lowest energy structure, as well as to the structures which energy is up to 0.1 eV higher than the lowest energy one (usually 2 to 5 structures in total). The final geometry optimization is performed for these systems, allowing all the atoms to relax, except for the previously specified bottom part of the support slab. The lowest energy structure (Figs. S2 and S3, Supporting Information) is used to construct the free energy diagram of the corresponding catalytic system.

Only in a few cases, the water layer forms a regular hexagonal structure, similar to the one experimentally found on highly oriented pyrolytic graphite [52]. This is caused by difficulties in matching the support, graphene and hexagonal ice lattices at the same time at computationally affordable sizes of the unit cells. However, water layer stabilities relative to isolated H₂O molecules were found to be similar for all the considered systems, *i.e.* 0.490 ± 0.010 eV/H₂O molecule. Note that the difference between the water interaction energy with graphene and N-graphene (no support) was found to be only about 0.003 eV/H₂O molecule [48].

Adsorption energies in the presence of water are calculated by replacing one H₂O molecule from the water layer with an adsorbate. The energy of that water molecule is assumed to be the average energy of H₂O in the water layer without adsorbates. Similar to unsupported N-graphene [48], water molecules do not chemisorb on the active sites of Fe₃C/(N)G or Fe/(N)G interfaces. The presence of the aqueous environment stabilizes all ORR intermediates, *OH

and *OOH by 0.18-0.35 eV, and *O by 0.63-0.95 eV, relative to vacuum. This compares well with the solvation energies on an unsupported N-graphene [48].

The water layer structure utilized to model solvation effects on the Pt(111) surface is similar to the one previously described in the literature [53, 54], *i.e.* the half-dissociated water layer. The presence of *OH spectators in this model results from the fact that *OH reduction is the potential determining step for the oxygen reduction reaction on Pt(111). The structures of ORR intermediates embedded in the half-dissociated water layer on Pt(111) are shown in Fig. S4 (Supporting Information).

3.4. Free energy diagrams and the 2D volcano

Theoretical ORR free energy diagrams for the considered model catalysts at $U = 0.8 V_{\text{RHE}}$ are shown in Figs. 2–5, and the adsorption Gibbs free energies (at $U = 0 V_{\text{RHE}}$) are collected in Tab. S1 (Supporting Information).

In the figures, it is clearly seen that the Fe_3C support significantly stabilizes all the ORR intermediates, *i.e.* *OOH, *O and *OH, both on graphene (1.09, 1.68 and 1.07 eV, respectively) and N-graphene (0.15, 1.05 and 0.22 eV, respectively). The stabilizing effect is even stronger with the Fe support (1.47, 2.37 and 1.57 eV for graphene; 0.27, 1.71 and 0.42 eV for N-graphene, respectively). It is worth noting that the values for *O are much higher than those for the other ORR intermediates. As noted above, electron density is transferred from the support to the (N-)graphene sheet. We find a correlation between Bader charge on oxygen and *O binding energy (Fig. 6). The electron density likely stabilizes the adsorbed oxygen by filling its empty sp states, as found in a previous study on N-doped graphene [48]. Strong *O stabilization caused by support was observed earlier in Cu(111)/NG system [15].

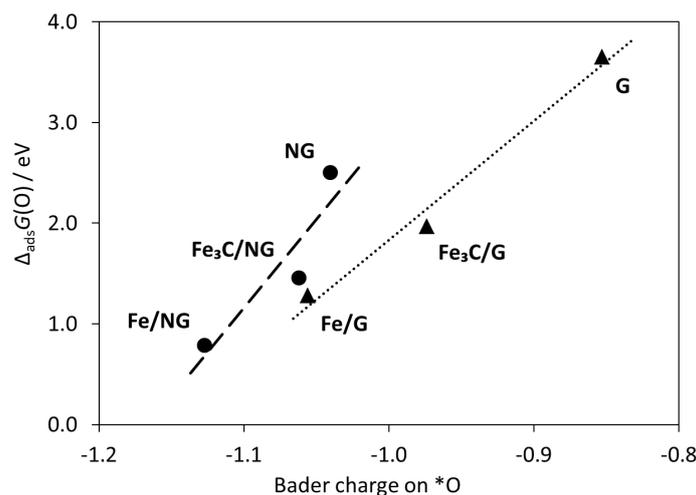


Figure 6: Correlation between oxygen adsorption Gibbs free energy and a Bader charge on *O for undoped (triangles, dotted line) and nitrogen-doped (circles, dashed line) systems.

Both Fe_3C and Fe supports significantly activate graphene surface towards ORR. The calculated ORR overpotential for Fe/G (Fig. 4a) and $\text{Fe}_3\text{C}/\text{G}$ (Fig. 3a) is 0.31 and 0.45 V higher than for the Pt(111) surface (Fig. 2a), respectively. This agrees with the experimental results, that encapsulated iron-based catalyst prepared from nitrogen-free precursors shows some but limited ORR activity [17, 22]. Interestingly, Fe/G heterostructure binds the *O intermediate so strong that its reduction to *OH becomes the potential-determining step — a situation rarely observed on transition metal surfaces [4]. The Fe/G, as well as the $\text{Fe}_3\text{C}/\text{G}$ heterostructures do not appear to follow the scaling relation between *O and *OH adsorption energies determined for the transition metal (111) surfaces [4]:

$$\Delta_{\text{ads}}G(\text{O}) = 2 \Delta_{\text{ads}}G(\text{OH}).$$

This is visualized on a 2D ORR activity volcano plot (Fig. 7).

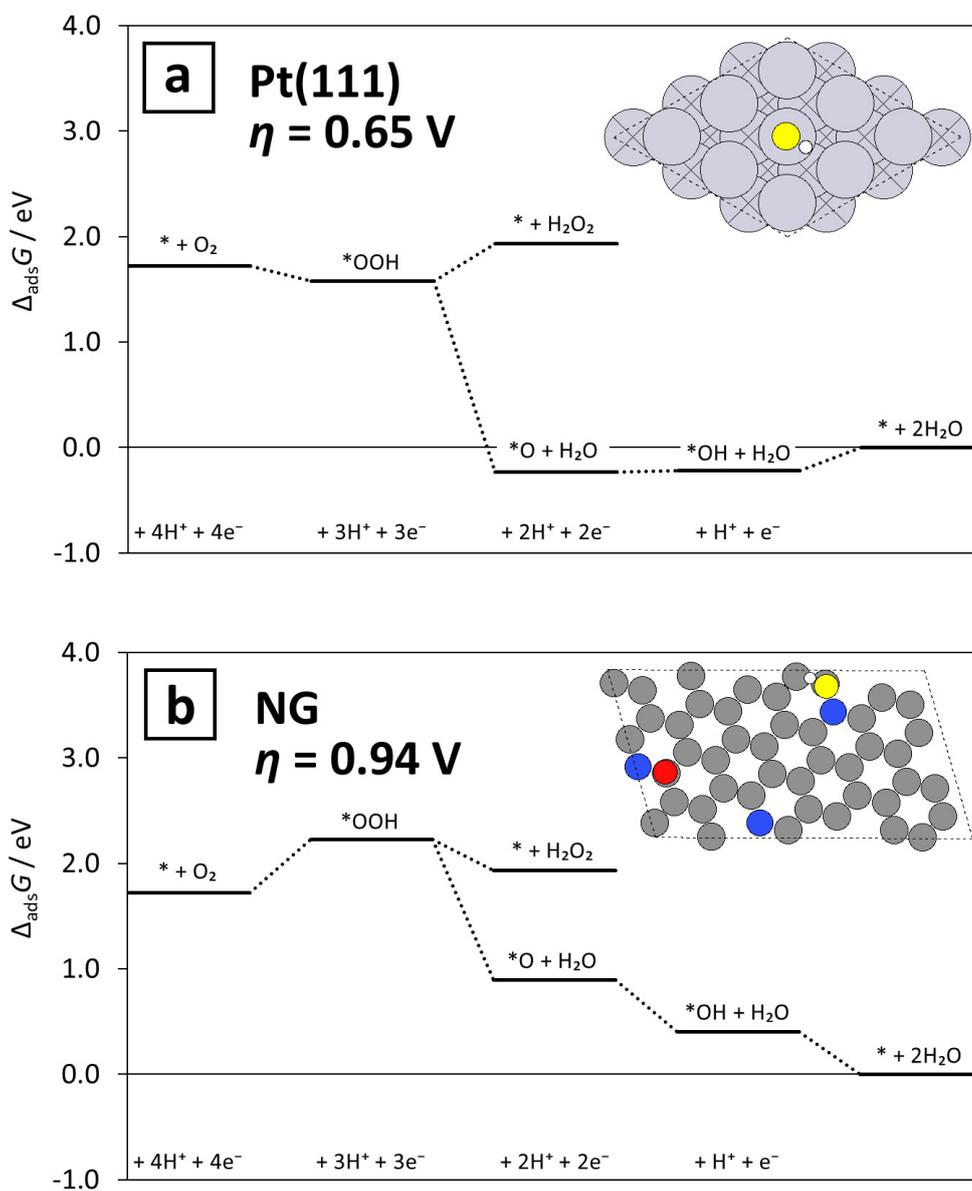


Figure 2: ORR free energy diagrams at $U = 0.8 \text{ V}_{\text{RHE}}$ for: (a) Pt(111), (b) NG. The insets show simulation cells of the corresponding systems with OH intermediate bound to the active site. Water layer is hidden for clarity. Crosses mark atoms which positions are fixed during structure relaxation. Color code for atoms: H – white, C – gray, N – blue, O – red (spectator) or yellow (adsorbate at the active site), Pt – light gray.

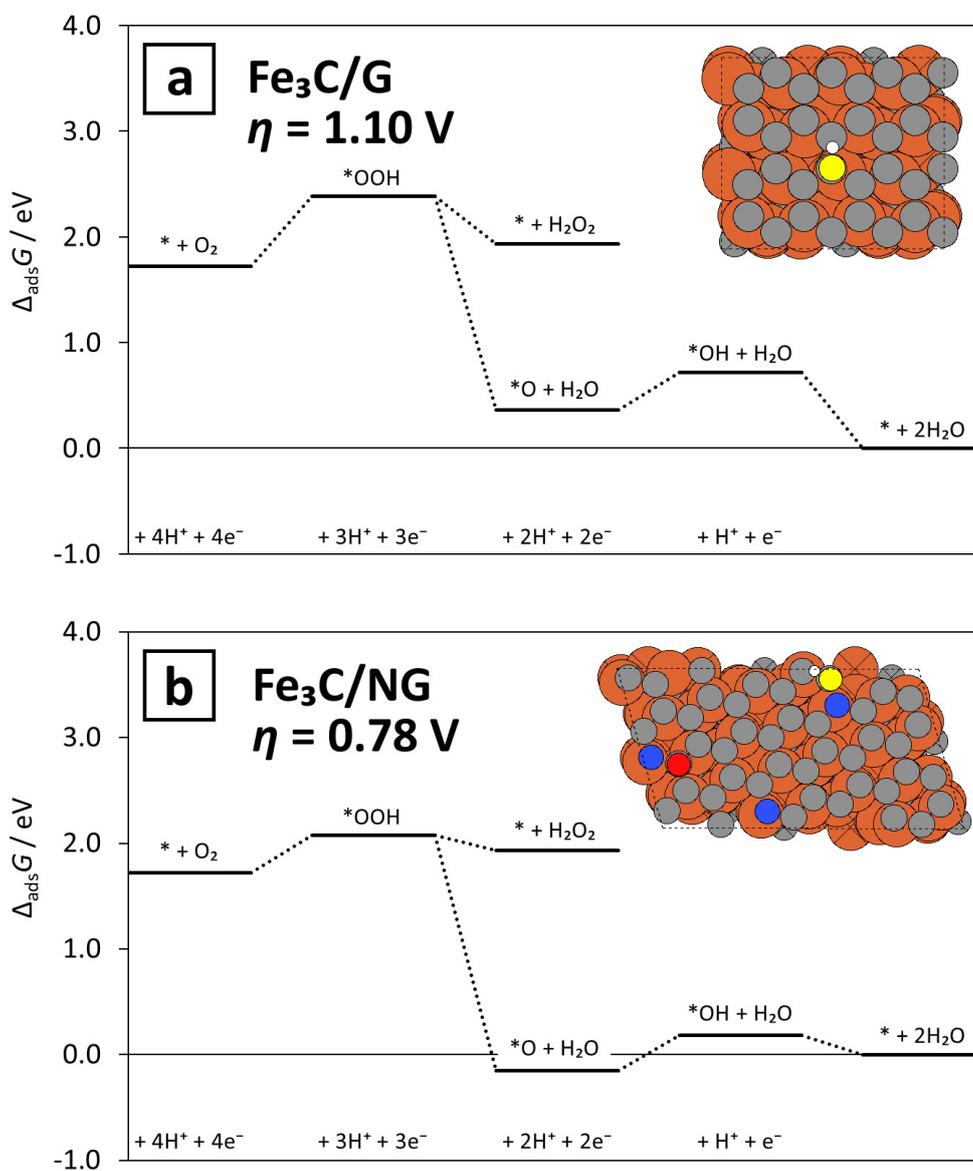


Figure 3: ORR free energy diagrams at $U = 0.8 \text{ V}_{\text{RHE}}$ for: (a) $\text{Fe}_3\text{C}/\text{G}$, (b) $\text{Fe}_3\text{C}/\text{NG}$. The insets show simulation cells of the corresponding systems with OH intermediate bound to the active site. Water layer is hidden for clarity. Crosses mark atoms which positions are fixed during structure relaxation. Color code for atoms: H – white, C – gray, N – blue, O – red (spectator) or yellow (adsorbate at the active site), Fe – orange.

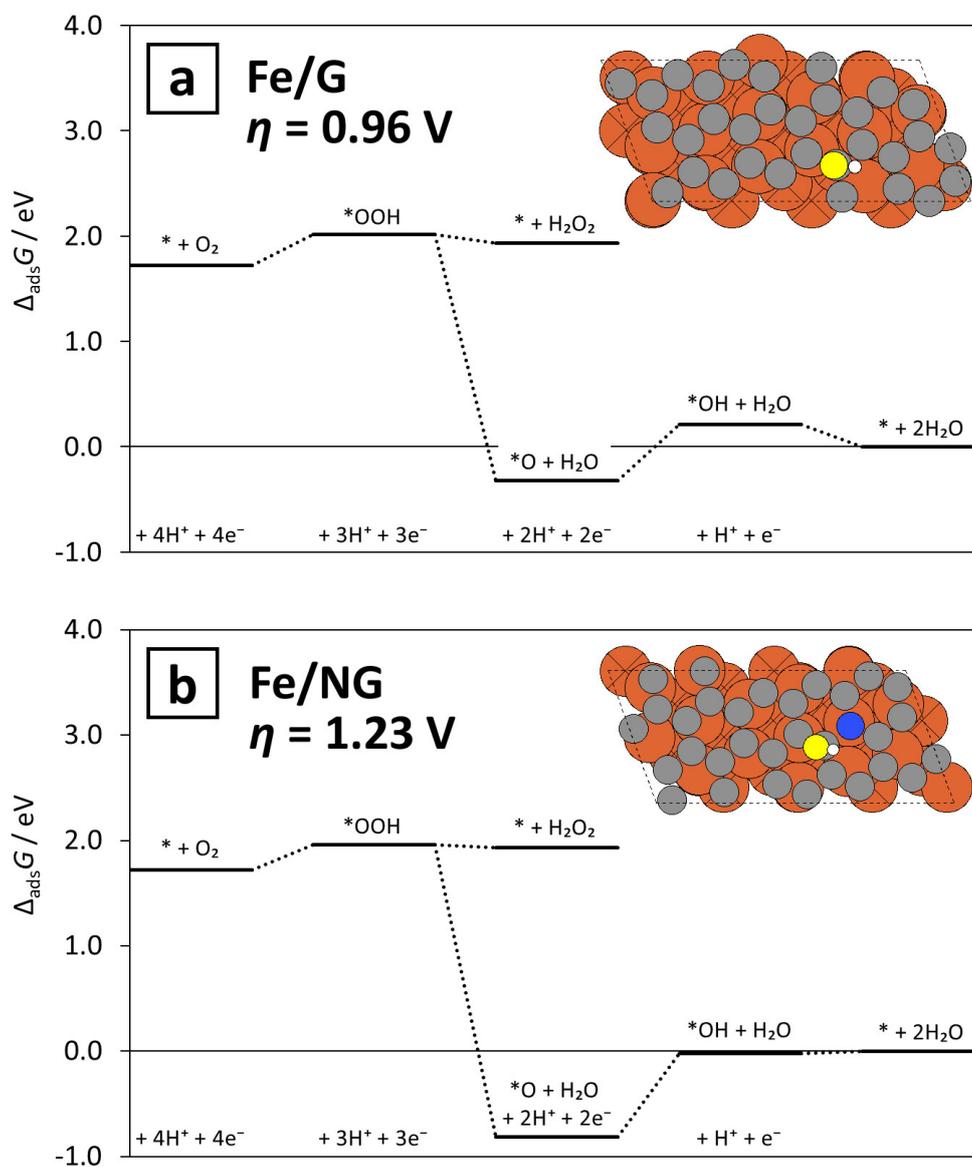


Figure 4: ORR free energy diagrams at $U = 0.8 \text{ V}_{\text{RHE}}$ for: (a) Fe/G, (b) Fe/NG. The insets show simulation cells of the corresponding systems with OH intermediate bound to the active site. Water layer is hidden for clarity. Crosses mark atoms which positions are fixed during structure relaxation. Color code for atoms is the same as in Fig. 3.

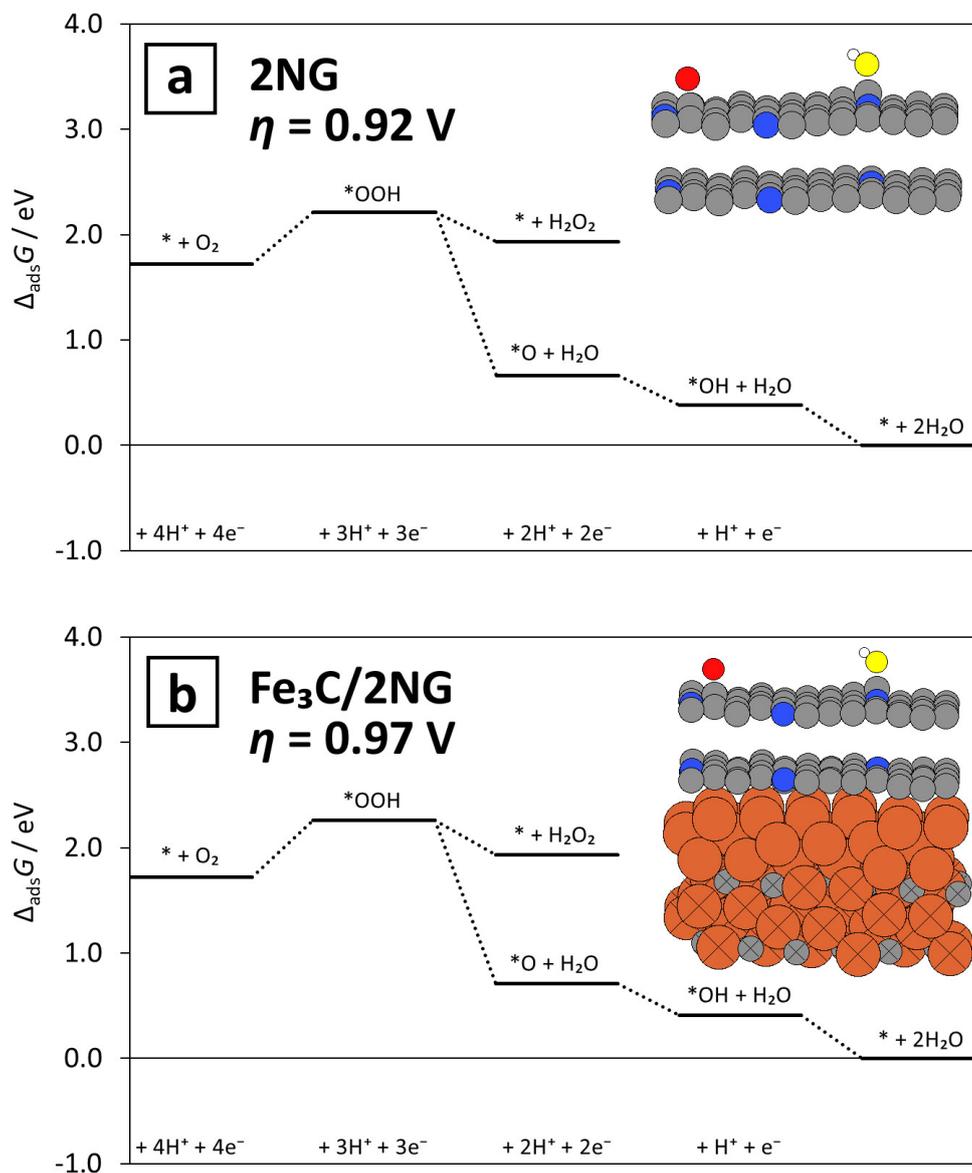


Figure 5: ORR free energy diagrams at $U = 0.8 \text{ V}_{\text{RHE}}$ for: (a) N-graphite with two NG layers (2×NG), (b) Fe₃C/N-graphite with two NG layers (Fe₃C/2×NG). The insets show simulation cells of the corresponding systems with OH intermediate bound to the active site. Water layer is hidden for clarity. Crosses mark atoms which positions are fixed during structure relaxation. Color code for atoms is the same as in Fig. 3.

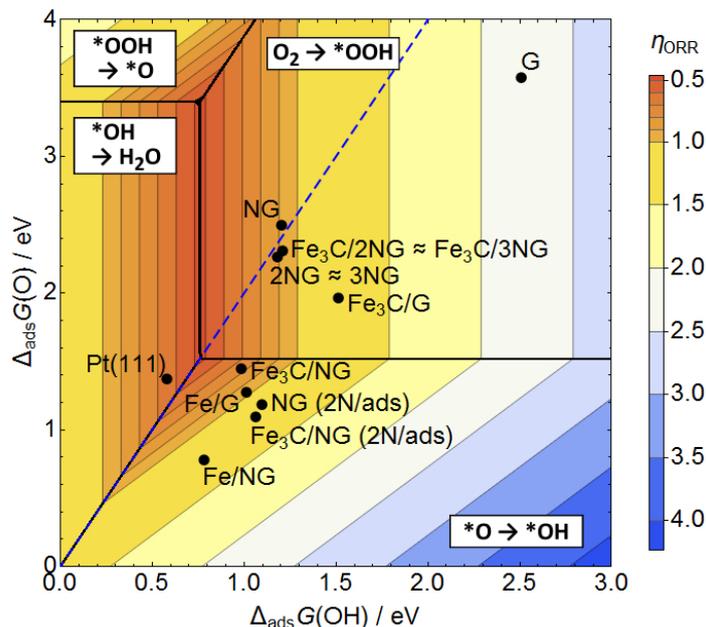


Figure 7: Theoretical ORR overpotential as a function of $\Delta_{\text{ads}}G(\text{OH})$ and $\Delta_{\text{ads}}G(\text{O})$. The scaling relation between $\ast\text{OH}$ and $\ast\text{OOH}$ adsorption energies, $\Delta_{\text{ads}}G(\text{OOH}) = \Delta_{\text{ads}}G(\text{OH}) + 3.4\text{eV}$, is determined from the data for the structures considered in this study (Tab. S1, Supporting Information). The plot is divided into four areas (separated by black solid lines) based on the potential determining steps, which are shown in white boxes. Blue dashed line denotes the scaling relation between $\ast\text{O}$ and $\ast\text{OH}$ adsorption energies observed on the transition metal (111) surfaces [4].

Unsupported N-doped graphene (Fig. 2b) belongs to the weak oxygen binding class of the ORR catalysts. Fe_3C support activates N-graphene towards ORR by making the bonds with ORR intermediates stronger, which decreases the calculated overpotential by 0.16 V (Fig. 3b). The resulting ORR overpotential is only 0.13 eV higher than that of the Pt(111) surface (Fig. 2a), lower than for any other heterostructure comprising undoped graphene investigated here. This is in line with experimental evidence that nitrogen plays an important role in the activity of encapsulated iron-based catalyst [22].

As mentioned in section 3.2, if the NG or $\text{Fe}_3\text{C}/\text{NG}$ structure contains sufficiently many unoccupied nitrogen atoms per adsorbate, $\ast\text{O}$ binding energy is so strong that $\ast\text{O}$ reduction becomes the ORR potential determining step. This already happens with 2 nitrogen atoms per adsorbate, *i.e.* with just one free nitrogen atom in the simulation cell (structures denoted as “NG (2N/ads)” and “ $\text{Fe}_3\text{C}/\text{NG}$ (2N/ads)” in Fig. 7; ORR free energy diagrams for these systems can be found in Fig. S5, Supporting Information). Under operational conditions, these structures immediately start to accumulate oxygen on the surface (*via* O_2 reduction or H_2O oxidation). This leads to destabilization of the next $\ast\text{O}$ adsorbates, and the $\ast\text{O}$ accumulation process is suspended as soon as another ORR step (*e.g.* O_2 reduction to $\ast\text{OOH}$) starts to limit the ORR potential.

Fe/NG heterostructure (Fig. 4b) binds oxygen species, especially $\ast\text{O}$, even stronger than $\text{Fe}_3\text{C}/\text{NG}$. In this case, however, accumulation of $\ast\text{O}$ on the surface does not destabilize next $\ast\text{O}$ adsorbates, and the process can continue until each nitrogen (or, more precisely, any carbon atom next to each nitrogen) in the NG sheet is occupied by oxygen. The theoretical overpotential required to reduce $\ast\text{O}$ is almost 0.6 V higher than for Pt(111), which means $\ast\text{O}$ effectively poisons the Fe/NG surface. This is again in agreement with experimental results, where the encapsulated iron-based catalyst’s ORR activity was found to correlate with the Fe_3C phase content, but not with the Fe phases content [23]. Fe/NG shows poor ORR activity due to an unfavorable breaking of the scaling relation between $\ast\text{O}$ and $\ast\text{OH}$ adsorption energy (Fig. 7).

Atomic oxygen adsorbed on top of a catalytic site being the 2nd row element (C, B) is particularly unstable due to the presence of empty O(sp) states [48]. It gains stability in the presence of water overlayer, free nitrogen atoms in N-doped graphene sheet [48], and, as shown in the present paper, an electron donating support. Excessive stabilization of $\ast\text{O}$ is, however, unfavorable for the ORR efficiency, as it increases the energy required to reduce $\ast\text{O}$ to $\ast\text{OH}$. To solve this problem, $\ast\text{O}$ has to be selectively destabilized. Since the spontaneous $\ast\text{O}$ accumulation on the catalyst

surface destabilizes the next *O adsorbates, the activity of NG and Fe₃C/NG systems increase. However, such an *O destabilization does not occur in case of Fe/NG system. Therefore, it cannot be expected that this effect will have a general application in establishing design rules for these systems.

Fe and Fe₃C supports differ in the amount of charge transferred to the N-graphene sheet, and subsequently to the *O adsorbate (Fig. 6). The Fe support donates enough charge to completely stabilize *O, even in the absence of free nitrogen. This results in the surface being fully covered by *O (all nitrogen atoms occupied) at the ORR-relevant potentials. Stronger electron donating supports than iron will most likely act similarly, causing the surface to be poisoned by *O as well. As opposed to that, Fe₃C support does not donate enough charge, and the presence of some amount of free nitrogen atoms is necessary. This leaves catalytic sites on the surface, where the ORR can proceed. Weaker electron donating supports than Fe₃C are expected to bind all the ORR adsorbates weaker, causing the drop in the ORR activity (moving it towards the pure NG activity). However, it can be expected that a support with electron donating properties between Fe and Fe₃C will bind the ORR adsorbates stronger, but not strong enough to let the N-graphene sheet be completely covered by *O. This may lead to a catalyst with ORR activity superior to that of the Fe₃C/NG heterostructure, possibly reaching or exceeding the activity of the Pt(111) surface.

3.5. Multiple graphene layers

Preparing well defined (N-)graphene layers on the support is a difficult task. As seen from TEM images, Fe₃C-based catalyst is often coated by a few graphitic layers [17, 20, 23]. For this reason, we computationally assess how adding more N-graphene layers change catalytic activity of the Fe₃C/NG catalyst. N-graphite model consists of two (2×NG) or three (3×NG) N-graphene sheets arranged in AA stacking, with nitrogen atoms located one above another [48]. Catalytic environment is the same as for NG and Fe₃C/NG systems, *i.e.* one *O and one free nitrogen act as spectators.

For the unsupported NG system, addition of the second N-graphene layer stabilizes the *O intermediate by about 0.2 eV, but the *OOH and *OH binding energies remain almost unaffected. The catalytic activity towards ORR does not change significantly, as O₂ reduction to *OOH is the potential determining step (Fig. 5a). The third N-graphene layer has a negligible effect on the ORR intermediates adsorption energies (Fig. S5c and Tab. S1, Supporting Information).

In case of the Fe₃C/NG system, the catalytic activity drops rapidly upon addition of the second N-graphene layer (Fig. 5b). Both the calculated overpotential and the adsorption energies of the ORR intermediates become close to the values obtained with the unsupported systems. With three N-graphene layers, any dissimilarities between supported and unsupported systems vanish (Fig. S5c and d, and Tab. S1, Supporting Information).

Our study shows that in systems comprising multiple N-graphene layers, the support would not be expected to enhance the ORR activity. However, a strong correlation between Fe₃C content and the activity is found in the experiments [23], and this correlation is fully consistent with the active sites existing on a single graphitic layer on Fe₃C.

4. Conclusions

ORR activity of four heterostructures, *i.e.* Fe₃C(010)/graphene, Fe₃C(010)/N-graphene, Fe(110)/graphene and Fe(110)/N-graphene is evaluated by means of Density Functional Theory and compared with earlier experimental studies. ORR intermediates solvation is taken into account by including an explicit water layer in each calculation. Both supports stabilize all the ORR intermediates, however the effect of Fe is noticeably stronger. The *O intermediate is stabilized particularly strongly, and its binding energy is found to correlate with charge on oxygen. Increasing O binding (and increasing negative charge on O) is found in the series: unsupported system < Fe₃C support < Fe support.

According to the calculations, the most active heterostructure is Fe₃C/N-graphene. Like in case of unsupported N-graphene system, Fe₃C/NG accumulates *O on the surface and the ORR takes place at the oxygen coverage between $0.5 < \theta_{\text{O}} < 1.0$. As opposed to that, Fe/NG system stabilizes *O intermediates so strong that its surface effectively becomes blocked by *O at ORR-relevant electrode potentials. The calculations are consistent with experimental evidence that: (i) Fe₃C support promotes ORR activity more than Fe support, (ii) N-doping is important for achieving high ORR activity.

The Fe₃C-supported system activity quickly converges to that of the unsupported one with increasing number of graphitic layers. Even two N-graphene layers effectively isolate adsorbates from influence of the support. Therefore,

the experimental activity of the iron carbide encased in graphitic layers likely comes from Fe₃C-supported single N-doped graphene layers. However, other effects like graphene defect promotion during synthesis caused by the presence of Fe₃C cannot be ruled out.

Finally, it was shown that electron donating support can increase the ORR activity of N-doped graphene (as in case of Fe₃C), but too strong electron donation properties of the support suppress the activity (as in case of Fe). It is therefore suggested that a heterostructure consisting of NG layer supported on a stronger electron donating material than Fe₃C (but weaker than Fe) is likely to have similar or better ORR activity than Pt(111) surface.

Acknowledgements

The authors acknowledge support from the Innovation Fund Denmark through the Initiative Towards Non-Precious Metal Polymer Fuel Cells (NonPrecious), project no. 4106-00012A.

References

- [1] W. Vielstich, A. Lamm, H. Gasteiger, *Handbook of Fuel Cells: Fundamentals, Technology, Applications*, Wiley, Chichester, 2003.
- [2] EG & G Services Inc., National Energy Technology Laboratory (U.S.), *Fuel cell handbook [electronic resource]*, 7th Edition, U.S. Dept. of Energy, Office of Fossil Energy, National Energy Technology Laboratory Morgantown, WV, 2004.
URL <http://url.access.gpo.gov/GPO/LPS115918>
- [3] Y. Nie, L. Li, Z. Wei, *Recent advancements in Pt and Pt-free catalysts for oxygen reduction reaction*, *Chem. Soc. Rev.* 44 (2015) 2168–2201. doi:10.1039/C4CS00484A.
URL <http://dx.doi.org/10.1039/C4CS00484A>
- [4] A. Kulkarni, S. Siahrostami, A. Patel, J. K. Nørskov, *Understanding catalytic activity trends in the oxygen reduction reaction*, *Chem. Rev.* doi:10.1021/acs.chemrev.7b00488.
URL <https://doi.org/10.1021/acs.chemrev.7b00488>
- [5] Y. Bing, H. Liu, L. Zhang, D. Ghosh, J. Zhang, *Nanostructured Pt-alloy electrocatalysts for PEM fuel cell oxygen reduction reaction*, *Chem. Soc. Rev.* 39 (2010) 2184–2202. doi:10.1039/B912552C.
URL <http://dx.doi.org/10.1039/B912552C>
- [6] I. E. L. Stephens, A. S. Bondarenko, U. Gronbjerg, J. Rossmeisl, I. Chorkendorff, *Understanding the electrocatalysis of oxygen reduction on platinum and its alloys*, *Energy Environ. Sci.* 5 (2012) 6744–6762. doi:10.1039/C2EE03590A.
URL <http://dx.doi.org/10.1039/C2EE03590A>
- [7] J. Wu, H. Yang, *Platinum-based oxygen reduction electrocatalysts*, *Acc. Chem. Res.* 46 (8) (2013) 1848–1857. arXiv:<https://doi.org/10.1021/ar300359w>, doi:10.1021/ar300359w.
URL <https://doi.org/10.1021/ar300359w>
- [8] L. Dai, Y. Xue, L. Qu, H.-J. Choi, J.-B. Baek, *Metal-free catalysts for oxygen reduction reaction*, *Chem. Rev.* 115 (11) (2015) 4823–4892, pMID: 25938707. arXiv:<http://dx.doi.org/10.1021/cr5003563>, doi:10.1021/cr5003563.
URL <http://dx.doi.org/10.1021/cr5003563>
- [9] W. Xia, A. Mahmood, Z. Liang, R. Zou, S. Guo, *Earth-abundant nanomaterials for oxygen reduction*, *Angew. Chem. Int. Ed.* 55 (8) (2016) 2650–2676. doi:10.1002/anie.201504830.
URL <http://dx.doi.org/10.1002/anie.201504830>
- [10] E. Proietti, F. Jaouen, M. Lefèvre, N. Larouche, J. Tian, J. Herranz, J.-P. Dodelet, *Iron-based cathode catalyst with enhanced power density in polymer electrolyte membrane fuel cells*, *Nat. Commun.* 2 (2011) 416. doi:10.1038/ncomms1427.
URL <http://dx.doi.org/10.1038/ncomms1427>
- [11] G. Wu, K. L. More, C. M. Johnston, P. Zelenay, *High-performance electrocatalysts for oxygen reduction derived from polyaniline, iron, and cobalt*, *Science* 332 (6028) (2011) 443–447. arXiv:<http://www.sciencemag.org/content/332/6028/443.full.pdf>, doi:10.1126/science.1200832.
URL <http://www.sciencemag.org/content/332/6028/443.abstract>
- [12] E. Voloshina, Y. Dedkov, *Graphene on metallic surfaces: problems and perspectives*, *Phys. Chem. Chem. Phys.* 14 (2012) 13502–13514. doi:10.1039/C2CP42171B.
URL <http://dx.doi.org/10.1039/C2CP42171B>
- [13] M. Andersen, L. Hornekær, B. Hammer, *Graphene on metal surfaces and its hydrogen adsorption: A meta-GGA functional study*, *Phys. Rev. B* 86 (2012) 085405. doi:10.1103/PhysRevB.86.085405.
URL <http://link.aps.org/doi/10.1103/PhysRevB.86.085405>
- [14] T. Olsen, J. Yan, J. J. Mortensen, K. S. Thygesen, *Dispersive and covalent interactions between graphene and metal surfaces from the Random Phase Approximation*, *Phys. Rev. Lett.* 107 (2011) 156401. doi:10.1103/PhysRevLett.107.156401.
URL <http://link.aps.org/doi/10.1103/PhysRevLett.107.156401>
- [15] S. H. Noh, D. H. Kwak, M. H. Seo, T. Ohsaka, B. Han, *First principles study of oxygen reduction reaction mechanisms on n-doped graphene with a transition metal support*, *Electrochim. Acta* 140 (2014) 225–231. doi:10.1016/j.electacta.2014.03.076.
URL <http://www.sciencedirect.com/science/article/pii/S0013468614005878>
- [16] R. Koitz, J. K. Nørskov, F. Studt, *A systematic study of metal-supported boron nitride materials for the oxygen reduction reaction*, *Phys. Chem. Chem. Phys.* 17 (2015) 12722–12727. doi:10.1039/C5CP01384D.
URL <http://dx.doi.org/10.1039/C5CP01384D>

- [17] Y. Hu, J. O. Jensen, W. Zhang, L. N. Cleemann, W. Xing, N. J. Bjerrum, Q. Li, **Hollow spheres of iron carbide nanoparticles encased in graphitic layers as oxygen reduction catalysts**, *Angew. Chem. Int. Ed.* 53 (14) (2014) 3675–3679. doi:10.1002/anie.201400358. URL <http://dx.doi.org/10.1002/anie.201400358>
- [18] Y. Hu, J. O. Jensen, W. Zhang, Y. Huang, L. N. Cleemann, W. Xing, N. J. Bjerrum, Q. Li, **Direct synthesis of Fe₃C-functionalized graphene by high temperature autoclave pyrolysis for oxygen reduction**, *ChemSusChem* 7 (8) (2014) 2099–2103. doi:10.1002/cssc.201402183. URL <http://dx.doi.org/10.1002/cssc.201402183>
- [19] Y. Hu, J. O. Jensen, W. Zhang, S. Martin, R. Chenitz, C. Pan, W. Xing, N. J. Bjerrum, Q. Li, **Fe₃C-based oxygen reduction catalysts: synthesis, hollow spherical structures and applications in fuel cells**, *J. Mater. Chem. A* 3 (2015) 1752–1760. doi:10.1039/C4TA03986F. URL <http://dx.doi.org/10.1039/C4TA03986F>
- [20] Y. Hu, L. Zhong, J. O. Jensen, Q. Li, **Graphene layer encapsulated metal nanoparticles as a new type of non-precious metal catalysts for oxygen reduction**, *Asia-Pac. J. Chem. Eng.* 11 (3) (2016) 382–385. doi:10.1002/apj.1986. URL <http://dx.doi.org/10.1002/apj.1986>
- [21] J.-P. Dodelet, R. Chenitz, L. Yang, M. Lefèvre, **A new catalytic site for the electroreduction of oxygen?**, *ChemCatChem* 6 (7) (2014) 1866–1867. doi:10.1002/cctc.201402133. URL <http://dx.doi.org/10.1002/cctc.201402133>
- [22] L. Zhong, Y. Hu, L. N. Cleemann, C. Pan, J. Sværke, J. O. Jensen, Q. Li, **Encapsulated iron-based oxygen reduction electrocatalysts by high pressure pyrolysis**, *Int. J. Hydrogen Energy* 42 (36) (2017) 22887–22896. doi:https://doi.org/10.1016/j.ijhydene.2017.07.093. URL <http://www.sciencedirect.com/science/article/pii/S0360319917329191>
- [23] L. Zhong, C. Frandsen, S. Mørup, Y. Hu, C. Pan, L. N. Cleemann, J. O. Jensen, Q. Li, **57Fe-Mössbauer spectroscopy and electrochemical activities of graphitic layer encapsulated iron electrocatalysts for the oxygen reduction reaction**, *Appl. Catal., B* 221 (2018) 406–412. doi:https://doi.org/10.1016/j.apcatb.2017.09.014. URL <http://www.sciencedirect.com/science/article/pii/S0926337317308391>
- [24] Virtual NanoLab version 2016.2, QuantumWise A/S. URL www.quantumwise.com
- [25] A. H. Larsen, J. J. Mortensen, J. Blomqvist, I. E. Castelli, R. Christensen, M. Dulak, J. Friis, M. N. Groves, B. Hammer, C. Hargus, E. D. Hermes, P. C. Jennings, P. B. Jensen, J. Kermode, J. R. Kitchin, E. L. Kolsbjerg, J. Kubal, K. Kaasbjerg, S. Lysgaard, J. B. Maronsson, T. Maxson, T. Olsen, L. Pastewka, A. Peterson, C. Rostgaard, J. Schiøtz, O. Schütt, M. Strange, K. S. Thygesen, T. Vegge, L. Wilhelmson, M. Walter, Z. Zeng, K. W. Jacobsen, **The atomic simulation environment—a Python library for working with atoms**, *J. Phys.: Condens. Matter* 29 (27) (2017) 273002. URL <http://stacks.iop.org/0953-8984/29/i=27/a=273002>
- [26] G. Kresse, J. Hafner, **Ab initio molecular dynamics for liquid metals**, *Phys. Rev. B* 47 (1993) 558–561. doi:10.1103/PhysRevB.47.558. URL <http://link.aps.org/doi/10.1103/PhysRevB.47.558>
- [27] G. Kresse, J. Hafner, **Ab initio molecular-dynamics simulation of the liquid-metal-amorphous-semiconductor transition in germanium**, *Phys. Rev. B* 49 (1994) 14251–14269. doi:10.1103/PhysRevB.49.14251. URL <http://link.aps.org/doi/10.1103/PhysRevB.49.14251>
- [28] G. Kresse, J. Furthmüller, **Efficiency of ab-initio total energy calculations for metals and semiconductors using a plane-wave basis set**, *Comput. Mater. Sci.* 6 (1) (1996) 15–50. doi:10.1016/0927-0256(96)00008-0. URL <http://www.sciencedirect.com/science/article/pii/0927025696000080>
- [29] G. Kresse, J. Furthmüller, **Efficient iterative schemes for ab initio total-energy calculations using a plane-wave basis set**, *Phys. Rev. B* 54 (1996) 11169–11186. doi:10.1103/PhysRevB.54.11169. URL <http://link.aps.org/doi/10.1103/PhysRevB.54.11169>
- [30] P. E. Blöchl, **Projector augmented-wave method**, *Phys. Rev. B* 50 (1994) 17953–17979. doi:10.1103/PhysRevB.50.17953. URL <http://link.aps.org/doi/10.1103/PhysRevB.50.17953>
- [31] G. Kresse, D. Joubert, **From ultrasoft pseudopotentials to the projector augmented-wave method**, *Phys. Rev. B* 59 (1999) 1758–1775. doi:10.1103/PhysRevB.59.1758. URL <http://link.aps.org/doi/10.1103/PhysRevB.59.1758>
- [32] H. J. Monkhorst, J. D. Pack, **Special points for Brillouin-zone integrations**, *Phys. Rev. B* 13 (1976) 5188–5192. doi:10.1103/PhysRevB.13.5188. URL <http://link.aps.org/doi/10.1103/PhysRevB.13.5188>
- [33] J. P. Perdew, K. Burke, M. Ernzerhof, **Generalized gradient approximation made simple**, *Phys. Rev. Lett.* 77 (1996) 3865–3868. doi:10.1103/PhysRevLett.77.3865. URL <http://link.aps.org/doi/10.1103/PhysRevLett.77.3865>
- [34] B. Hammer, L. B. Hansen, J. K. Nørskov, **Improved adsorption energetics within density-functional theory using revised Perdew-Burke-Ernzerhof functionals**, *Phys. Rev. B* 59 (1999) 7413–7421. doi:10.1103/PhysRevB.59.7413. URL <http://link.aps.org/doi/10.1103/PhysRevB.59.7413>
- [35] J. Wellendorff, K. T. Lundgaard, A. Møgelhøj, V. Petzold, D. D. Landis, J. K. Nørskov, T. Bligaard, K. W. Jacobsen, **Density functionals for surface science: Exchange-correlation model development with Bayesian error estimation**, *Phys. Rev. B* 85 (2012) 235149. doi:10.1103/PhysRevB.85.235149. URL <http://link.aps.org/doi/10.1103/PhysRevB.85.235149>
- [36] K. Lee, E. D. Murray, L. Kong, B. I. Lundqvist, D. C. Langreth, **Higher-accuracy van der Waals density functional**, *Phys. Rev. B* 82 (2010) 081101. doi:10.1103/PhysRevB.82.081101. URL <http://link.aps.org/doi/10.1103/PhysRevB.82.081101>
- [37] J. Wellendorff, T. L. Silbaugh, D. Garcia-Pintos, J. K. Nørskov, T. Bligaard, F. Studt, C. T. Campbell, **A benchmark database for adsorption bond energies to transition metal surfaces and comparison to selected DFT functionals**, *Surf. Sci.* 640 (2015) 36–44. doi:10.1016/j.susc.2015.03.023.

- URL <http://www.sciencedirect.com/science/article/pii/S0039602815000837>
- [38] S. Goedecker, **Minima hopping: An efficient search method for the global minimum of the potential energy surface of complex molecular systems**, *J. Chem. Phys.* 120 (21) (2004) 9911–9917. doi:10.1063/1.1724816.
URL <http://scitation.aip.org/content/aip/journal/jcp/120/21/10.1063/1.1724816>
- [39] A. A. Peterson, **Global optimization of adsorbate–surface structures while preserving molecular identity**, *Top. Catal.* 57 (1) (2014) 40–53. doi:10.1007/s11244-013-0161-8.
URL <http://dx.doi.org/10.1007/s11244-013-0161-8>
- [40] H. A. Hansen, V. Viswanathan, J. K. Nørskov, **Unifying kinetic and thermodynamic analysis of 2 e⁻ and 4 e⁻ reduction of oxygen on metal surfaces**, *J. Phys. Chem. C* 118 (13) (2014) 6706–6718. arXiv:<http://dx.doi.org/10.1021/jp4100608>, doi:10.1021/jp4100608.
URL <http://dx.doi.org/10.1021/jp4100608>
- [41] H. J. Yan, B. Xu, S. Q. Shi, C. Y. Ouyang, **First-principles study of the oxygen adsorption and dissociation on graphene and nitrogen doped graphene for Li-air batteries**, *J. Appl. Phys.* 112 (10) (2012) 104316. arXiv:<http://dx.doi.org/10.1063/1.4766919>, doi:10.1063/1.4766919.
URL <http://dx.doi.org/10.1063/1.4766919>
- [42] J. K. Nørskov, A. Logadottir, L. Lindqvist, J. R. Kitchin, T. Bligaard, H. Jónsson, **Origin of the overpotential for oxygen reduction at a fuel-cell cathode**, *J. Phys. Chem. B* 108 (46) (2004) 17886–17892. arXiv:<http://dx.doi.org/10.1021/jp047349j>, doi:10.1021/jp047349j.
URL <http://dx.doi.org/10.1021/jp047349j>
- [43] J. Rossmeisl, A. Logadottir, J. Nørskov, **Electrolysis of water on (oxidized) metal surfaces**, *Chem. Phys.* 319 (1-3) (2005) 178–184. doi:10.1016/j.chemphys.2005.05.038.
URL <http://www.sciencedirect.com/science/article/pii/S0301010405002053>
- [44] R. Christensen, H. A. Hansen, T. Vegge, **Identifying systematic DFT errors in catalytic reactions**, *Catal. Sci. Technol.* 5 (2015) 4946–4949. doi:10.1039/C5CY01332A.
URL <http://dx.doi.org/10.1039/C5CY01332A>
- [45] R. Christensen, H. A. Hansen, C. F. Dickens, J. K. Nørskov, T. Vegge, **Functional independent scaling relation for ORR/OER catalysts**, *J. Phys. Chem. C* 120 (43) (2016) 24910–24916. arXiv:<http://dx.doi.org/10.1021/acs.jpcc.6b09141>, doi:10.1021/acs.jpcc.6b09141.
URL <http://dx.doi.org/10.1021/acs.jpcc.6b09141>
- [46] W. Haynes (Ed.), **CRC handbook of chemistry and physics: a ready-reference book of chemical and physical data**, 95th Edition, CRC Press, Boca Raton, 2014.
- [47] W. C. Chiou Jr., E. A. Carter, **Structure and stability of Fe₃C-cementite surfaces from first principles**, *Surf. Sci.* 530 (1–2) (2003) 88–100. doi:10.1016/S0039-6028(03)00352-2.
URL <http://www.sciencedirect.com/science/article/pii/S0039602803003522>
- [48] M. Reda, H. A. Hansen, T. Vegge, **DFT study of stabilization effects on N-doped graphene for ORR catalysis**, *Catal. Today* (2018) –doi: <https://doi.org/10.1016/j.cattod.2018.02.015>.
URL <https://www.sciencedirect.com/science/article/pii/S092058611830066X>
- [49] P. Błoński, A. Kiejna, **Structural, electronic, and magnetic properties of bcc iron surfaces**, *Surf. Sci.* 601 (1) (2007) 123–133. doi:10.1016/j.susc.2006.09.013.
URL <http://www.sciencedirect.com/science/article/pii/S0039602806009563>
- [50] N. A. Vinogradov, A. A. Zakharov, V. Kocevski, J. Ruzs, K. A. Simonov, O. Eriksson, A. Mikkelsen, E. Lundgren, A. S. Vinogradov, N. Mårtensson, A. B. Preobrajenski, **Formation and structure of graphene waves on Fe(110)**, *Phys. Rev. Lett.* 109 (2012) 026101. doi:10.1103/PhysRevLett.109.026101.
URL <http://link.aps.org/doi/10.1103/PhysRevLett.109.026101>
- [51] S. Taubert, K. Laasonen, **The molecular and magnetic structure of carbon-enclosed and partially covered Fe₅₅ particles**, *Phys. Chem. Chem. Phys.* 16 (2014) 3648–3660. doi:10.1039/C3CP54491E.
URL <http://dx.doi.org/10.1039/C3CP54491E>
- [52] O. Teschke, **Imaging ice-like structures formed on hopg at room temperature**, *Langmuir* 26 (22) (2010) 16986–16990. doi:10.1021/la103227j.
URL <http://dx.doi.org/10.1021/la103227j>
- [53] V. Tripković, E. Skúlason, S. Siahrostami, J. K. Nørskov, J. Rossmeisl, **The oxygen reduction reaction mechanism on Pt(1 1 1) from density functional theory calculations**, *Electrochim. Acta* 55 (27) (2010) 7975–7981. doi:10.1016/j.electacta.2010.02.056.
URL <http://www.sciencedirect.com/science/article/pii/S0013468610003178>
- [54] V. Tripkovic, T. Vegge, **Potential- and rate-determining step for oxygen reduction on Pt(111)**, *J. Phys. Chem. C* 121 (48) (2017) 26785–26793. arXiv:<http://dx.doi.org/10.1021/acs.jpcc.7b07472>, doi:10.1021/acs.jpcc.7b07472.
URL <http://dx.doi.org/10.1021/acs.jpcc.7b07472>

Supporting information

DFT Study of the Oxygen Reduction Reaction on Carbon-Coated Iron and Iron Carbide

Mateusz Reda, Heine Anton Hansen*, Tejs Vegge

1. Supporting figures

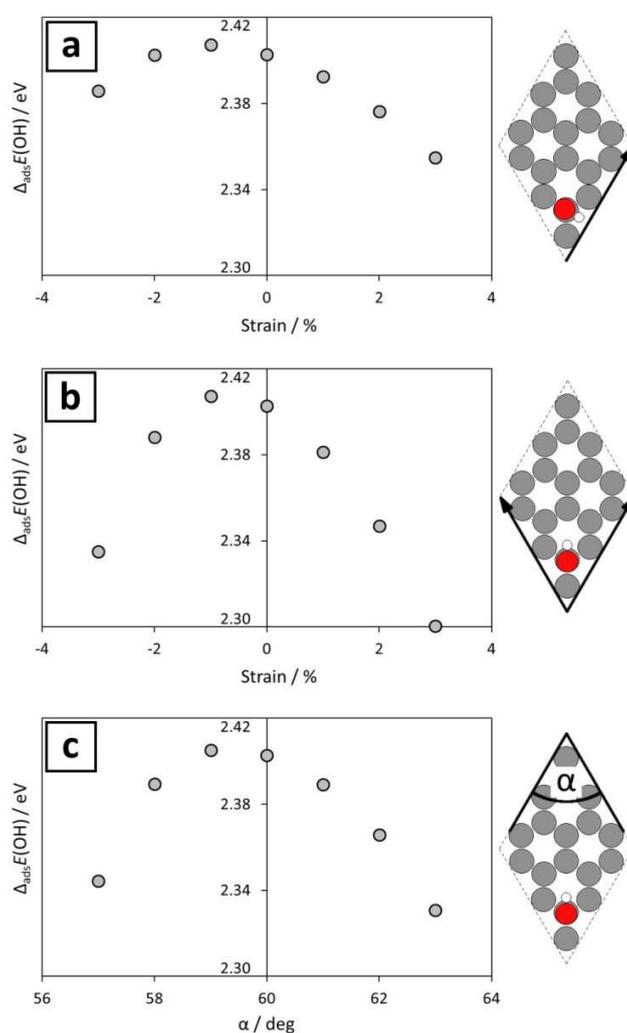


Figure S1. OH adsorption energy on graphene (Eq. 7) as a function of (a) uniaxial, (b) biaxial and (c) shear strain. The images show the unit cells, orientations of *OH and the varied lattice parameters. Color code for atoms: H – white, C – gray, O – red.

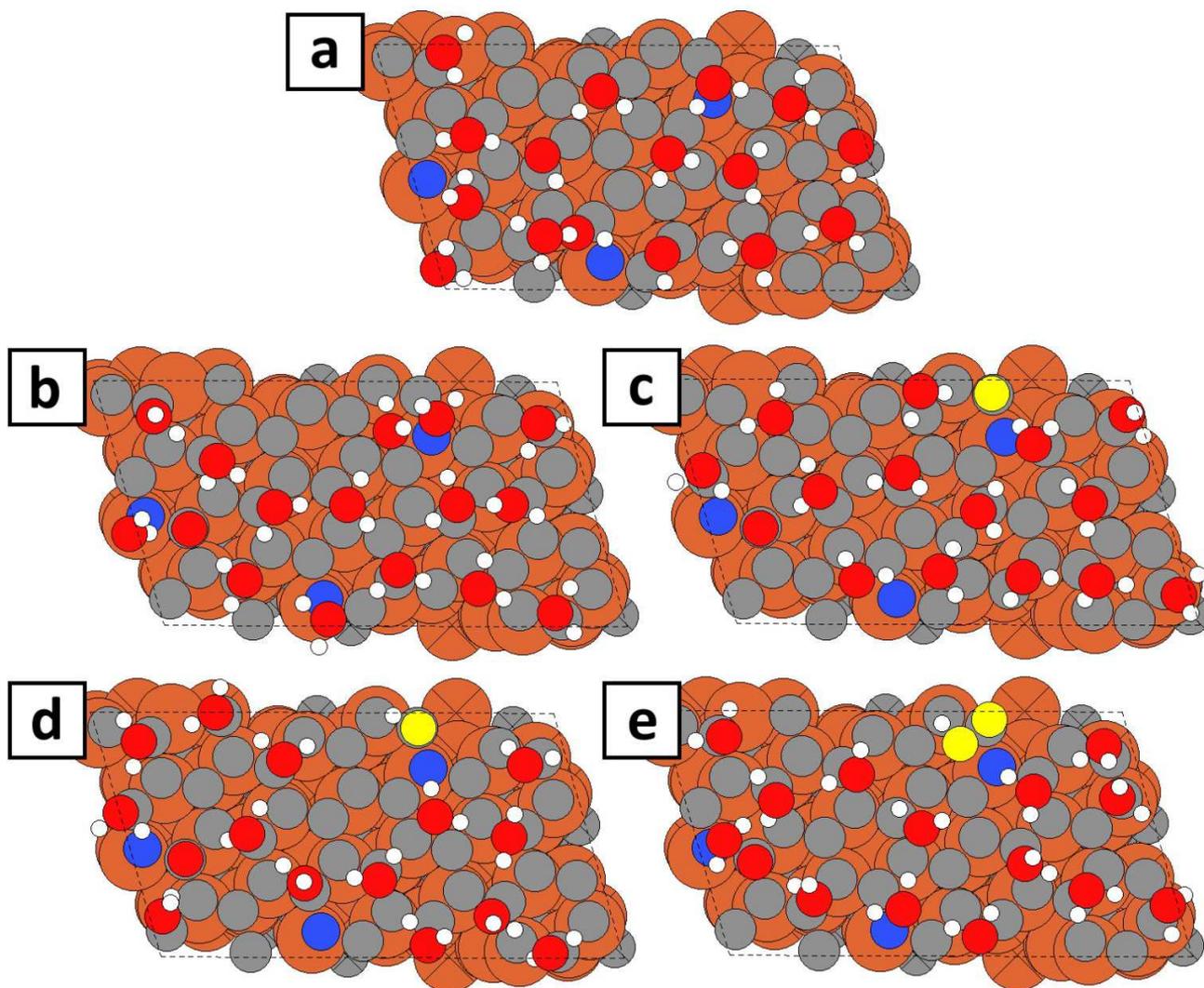


Figure S2. Water layer structures for the $\text{Fe}_3\text{C}/\text{NG}$ system. Same structures are used for NG and all (supported and unsupported) N-graphite systems. Water layer in (a) is shown in the absence of any adsorbate. The system in (b) consists of an empty active site *, one oxygen spectator and one free nitrogen spectator. Systems with the same spectators, additionally comprising ORR intermediates at the active site are: (c) *O, (d) *OH, (e) *OOH. Crosses mark atoms which positions are fixed during structure relaxation. Color code for atoms: H – white, C – gray, N – blue, O – red, Fe – orange. Oxygen atoms belonging to the adsorbates at the active site are highlighted in yellow.

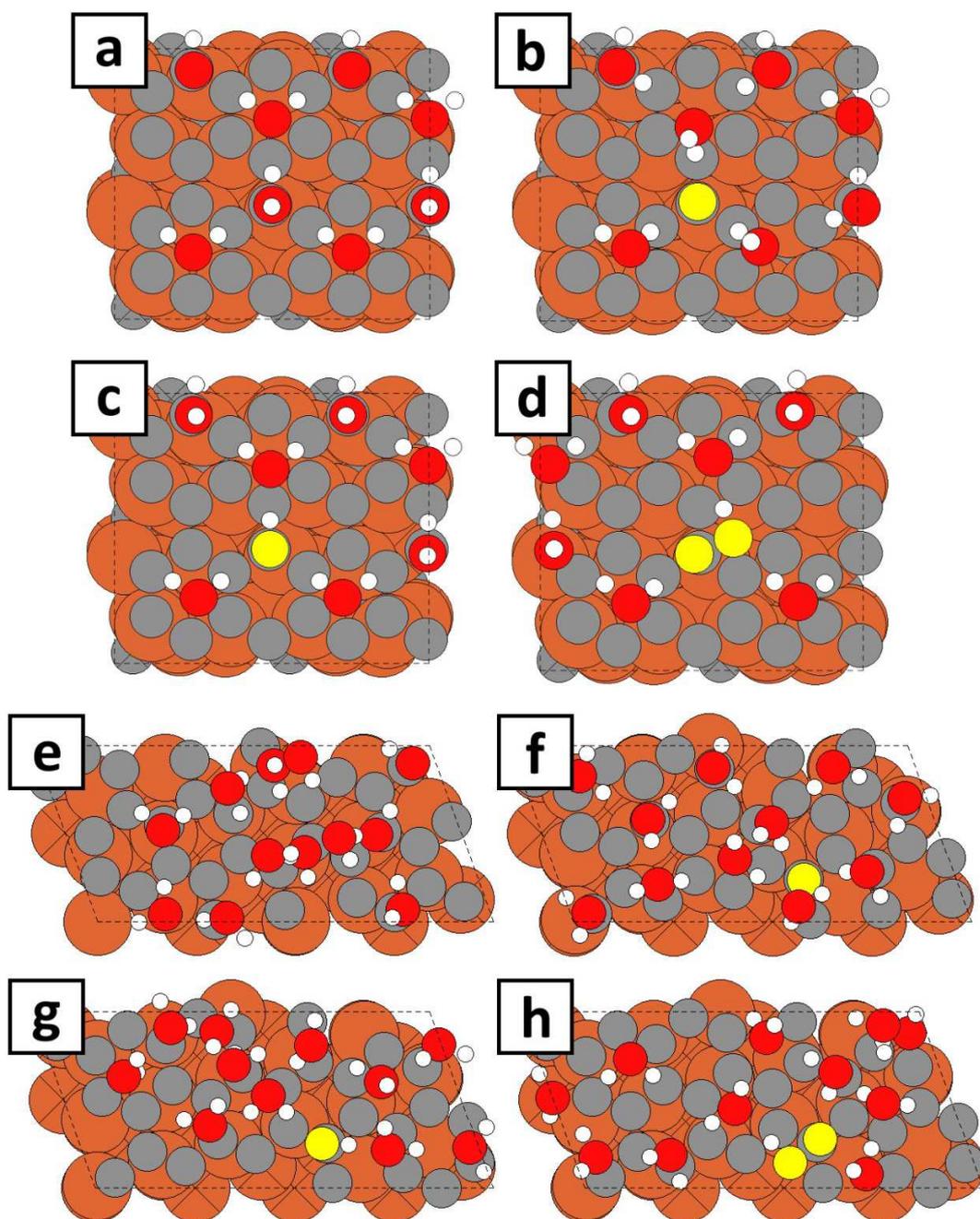


Figure S3. Water layer structures for $\text{Fe}_3\text{C}/\text{G}$: (a)-(d), and Fe/G : (e)-(h). The first four structures are also used for NG (2N/ads) and $\text{Fe}_3\text{C}/\text{NG}$ (2N/ads) systems. The last four structures are also used for Fe/NG system. Water layers in (a) and (e) are shown in the absence of any adsorbate. Systems with ORR intermediates at the active site: (b) and (f): $^*\text{O}$; (c) and (g): $^*\text{OH}$; (d) and (h): $^*\text{OOH}$. Color code for atoms is the same as in Fig. S2.

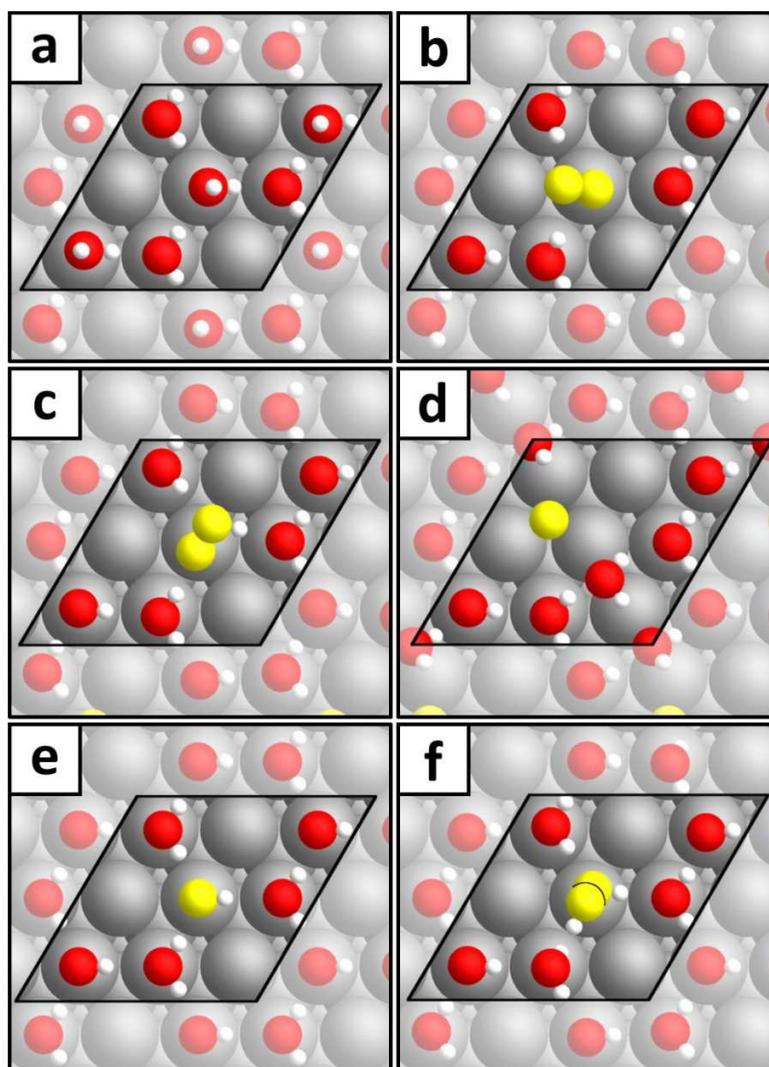


Figure S4. Structures of a single water layer (a) and ORR intermediates embedded in the half-dissociated water layer on Pt(111): (b) $*\text{O}_2$, (c) $*\text{OOH}$, (d) $*\text{O}$, (e) $*\text{OH}$ – the half-dissociated water layer, (f) H_2O_2^* . Color code for atoms: H – white, O – red, Pt – gray. Oxygen atoms belonging to the adsorbates at the active site are highlighted in yellow.

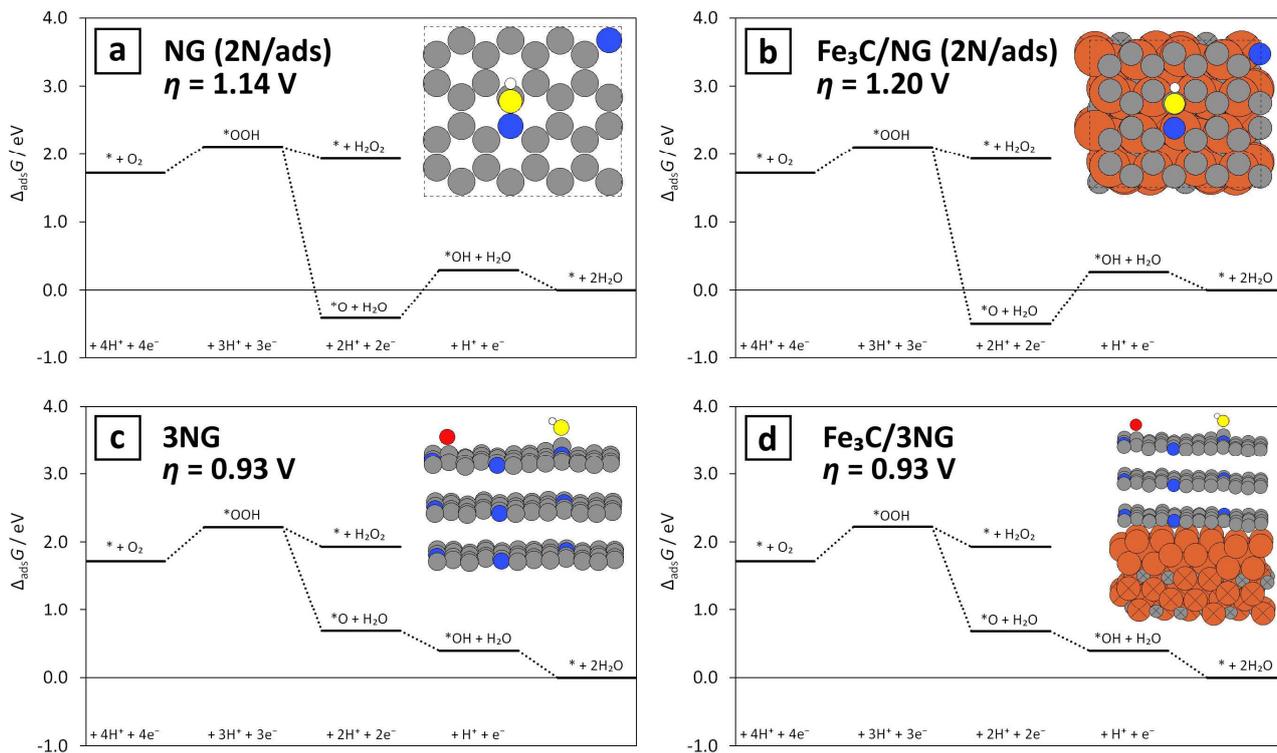


Figure S5. ORR free energy diagrams at $U = 0.8 \text{ V}_{\text{RHE}}$ for: (a) N-graphene with two N atoms per adsorbate [NG (2N/ads)], (b) Fe₃C/N-graphene with two N atoms per adsorbate [Fe₃C/NG (2N/ads)], (c) N-graphite with three N-graphene layers (3×NG), (d) Fe₃C/N-graphite with three N-graphene layers (Fe₃C/3×NG). The insets show simulation cells of the corresponding systems with OH intermediate bound to the active site. Water layer is hidden for clarity. Color code for atoms is the same as in Fig. S2.

2. Supporting tables

Table S1. ORR intermediates adsorption Gibbs free energies at $U = 0 V_{\text{RHE}}$ [$\Delta_{\text{ads}}G$, Eq. (6)-(9)] and the calculated ORR overpotential (η_{ORR}) on the considered surfaces in the presence of water, after applying the Christensen's correction (as described in the main manuscript).

System	Cell	$\Delta_{\text{ads}}G / \text{eV}$			$\eta_{\text{ORR}} / V_{\text{RHE}}$
		*OOH	*O	*OH	
Pt(111)	3×3	3.98	1.37	0.58	0.65
G	$\sqrt{2} \times \sqrt{2}$	5.98 ^a	3.65	2.58	2.19
Fe ₃ C/G	$\sqrt{2} \times \sqrt{2}$	4.79	1.96	1.51	1.10
Fe/G	1×1	4.41	1.28	1.01	0.96
NG	$\sqrt{2} \times \sqrt{3}$	4.63	2.50	1.20	0.94
Fe ₃ C/NG	$\sqrt{2} \times \sqrt{3}$	4.47	1.45	0.98	0.78
Fe/NG	1×1	4.36	0.78	0.78	1.23
NG (2N/ads)	$\sqrt{2} \times \sqrt{2}$	4.51	1.18	1.10	1.14
Fe ₃ C/NG (2N/ads)	$\sqrt{2} \times \sqrt{2}$	4.51	1.10	1.06	1.20
2×NG	$\sqrt{2} \times \sqrt{3}$	4.61	2.26	1.18	0.92
3×NG	$\sqrt{2} \times \sqrt{3}$	4.62	2.28	1.19	0.93
Fe ₃ C/2×NG	$\sqrt{2} \times \sqrt{3}$	4.66	2.31	1.21	0.97
Fe ₃ C/3×NG	$\sqrt{2} \times \sqrt{3}$	4.62	2.28	1.19	0.93

^a not bound; $\Delta_{\text{ads}}G$ estimated from $\Delta_{\text{ads}}G(\text{OOH}) = \Delta_{\text{ads}}G(\text{OH}) + 3.4 \text{ eV}$.